Massive MIMO channel characterization and propagation-based antenna selection strategies : application to 5G and industry 4.0

Frédéric Challita

To cite this version:

Frédéric Challita. Massive MIMO channel characterization and propagation-based antenna selection strategies : application to 5G and industry 4.0. Micro and nanotechnologies/Microelectronics. Université de Lille, 2019. English. NNT : 2019LILUI043 . tel-03624170v2

HAL Id: tel-03624170
https://theses.hal.science/tel-03624170v2

Submitted on 30 Mar 2022

iemn
Institut d'Electronique, de Microélectronique
et de Nanotechnologie
UMR CNRS 8520

Université
de Lille

THESE

THÈSE

pour obtenir le grade de docteur délivré par :

Université de Lille

École doctorale : "Sciences Pour L'Ingénieur (SPI)"

Spécialité doctorale : "Electronique, Microélectronique, Nanoélectronique et Micro-ondes"

Préparée à : "Institut d'Electronique et de Microélectronique et de Nanotechnologie"

Frédéric CHALLITA

Massive MIMO Channel Characterization and Propagation-based Antenna Selection strategies: Application to 5G and Industry 4.0

Caractérisation des Canaux Massive MIMO et Stratégies de Sélection d'Antenne: Application pour la 5G et l'Industrie 4.0

Soutenue publiquement le: 26 Septembre 2019

Directrice de thèse : Mme. Martine LIÉNARD, Professeur, Université de Lille
Co-directeur : M. Davy GAILLOT, Maître de Conférences-HDR, Université-Lille

Membres du Jury :

M. Jean-Francois DIOURIS, Professeur, Université de Nantes	Rapporteur
M. Pascal PAGANI, Ingénieur de Recherche- HDR, CEA CESTA	Rapporteur
M. Alain SIBILLE, Professeur, Telecom Paris Tech (*Président*)	Examinateur
Mme. Dinh-Thuy PHAN-HUY, Ingénieur de Recherche, Orange Labs	Examinateur
M. Wout JOSEPH, Professeur, UGent	Invité
M. José María MOLINA GARCÍA PARDO, Professeur, UPCT	Invité

Abstract

OVER the past decade, mobile connectivity and wireless systems have become a necessity for many applications and use-cases. Faster, smarter, safer and environment-friendlier networks are sought. Continuous efforts have been made to boost wireless systems performance, from analog to digital systems, bulky handheld cellular phone and user equipments to ever-small sensors and smart phones, from mechanization and basic automation systems to the smart industry of the future or Industry 4.0. However, current wireless networks are not yet able to fulfill the many gaps from 4G and address the requirements of 5G, or the fifth generation of mobile networks. Thus, significant technological breakthroughs are still required to strengthen wireless networks. For instance, in order to provide higher data rates and accommodate many types of equipment, more spectrum resources are needed and the currently used spectrum requires to be efficiently utilized.

5G is initially being labeled as an evolution, made available through improvements in LTE (Long-Term Evolution), but it will not be long before it becomes a revolution and a major step-up from previous generations.

Massive MIMO (Multiple-Input Multiple-Output) has emerged as one of the most promising physical-layer technologies for future 5G wireless systems. The main idea is to equip base stations with large arrays (100 antennas or more) to simultaneously communicate with many terminals or user equipments. Using smart pre-processing at the array, massive MIMO promises to deliver superior system improvement with improved spectral efficiency, achieved by spatial multiplexing and better energy efficiency, exploiting array gain and reducing the radiated power. Massive MIMO can fill the gap for many requirements in 5G use-cases notably industrial IoT (Internet of Things) in terms of data rates, spectral and energy efficiency, reliable communication, optimal beamforming, linear processing schemes and so on. Over the last 6 years, several scientific papers proved the theoretical aspects and promises of massive MIMO systems and many trials validated that this technology is not just an academic concept. However, the hardware and software complexity arising from the sheer number of radio frequency chains is a bottleneck and some challenges are still to be tackled before the full operational deployment of massive MIMO. For instance, reliable channel models, impact of polarization diversity,

optimal antenna selection strategies, mutual coupling and channel state information acquisition amongst other aspects, are all important questions worth exploring. Also, a good understanding of industrial channels is needed to bring the smart industry of the future ever closer. In this thesis, we try to address some of these questions based on radio channel data from a measurement campaign in an industrial scenario using a massive MIMO setup. The thesis main objectives are threefold:

1. Characterization of massive MIMO channels in Industry 4.0 (industrial IoT) with a focus on spatial correlation, classification and impact of cross-polarization at transmission side. The setup consists in multiple distributed user equipments in many propagation conditions. This study is based on propagation-based metrics such as Ricean factor, correlation, etc. and system-oriented metrics such as sum-rate capacity with linear precoding and power allocation strategies. Moreover, polarization diversity schemes are proposed and were shown to achieve very promising results with simple allocation strategies. This work provides comprehensive insights on radio channels in Industry 4.0 capable of filling the gap in channel models and efficient strategies to optimize massive MIMO setups are proposed.

2. Proposition of antenna selection strategies using the receiver spatial correlation, a propagation metric, as a figure of merit. The goal is to reduce the number of radio frequency chain and thus the system complexity by selecting a set of distributed antennas. The proposed strategy achieves near-optimal sum-rate capacity with less radio frequency chains. This is critical for massive MIMO systems if complexity and cost are to be reduced.

3. Proposition of an efficient strategy for overhead reduction in channel state information acquisition of FDD (frequency-division-duplex) systems. The strategy relies on spatial correlation at the transmitter and consists in solving a set of simple autoregressive equations (Yule-Walker equations). The results show that the proposed strategy achieves a large fraction of the performance of TDD (time-division-duplex) systems initially proposed for massive MIMO.

Résumé

Dans le domaine des télécommunications sans fil, des efforts importants se sont portés ces dix dernières années sur le développement de systèmes d'échange d'information rapides, intelligents, sûrs et respectueux de l'environnement. Les domaines applicatifs sont de plus en plus larges, s'étendant par exemple du grand public, à la voiture connectée, à l'internet des objets (IoT Internet of Things) et à l'industrie 4.0. Dans ce dernier cas, l'objectif est d'aboutir à une flexibilité et à une versatilité accrues des chaînes de production et à une maintenance prédictive des machines, pour ne citer que quelques exemples. Cependant, les réseaux sans fil actuels ne sont pas encore en mesure de répondre aux nombreuses lacunes de la quatrième génération des réseaux mobiles (4G) et aux exigences de la 5G quant à une connectivité massive, une ultra fiabilité et des temps de latence extrêmement faibles. L'optimisation des ressources spectrales est également un point très important. La 5G était initialement considérée comme une évolution, rendue possible grâce aux améliorations apportées à la LTE (Long-Term Evolution), mais elle ne tardera pas à devenir une révolution et une avancée majeure par rapport aux générations précédentes. Dans ce cadre, la technologie des réseaux massifs ou Massive MIMO (Multiple-Input Multiple-Output) s'est imposée comme l'une des technologies de couche physique les plus prometteuses. L'idée principale est d'équiper les stations de base de grands réseaux d'antennes (100 ou plus) pour communiquer simultanément avec de nombreux terminaux ou équipements d'utilisateurs. Grâce à un prétraitement intelligent au niveau des signaux d'émission, les systèmes massive MIMO promettent d'apporter une grande amélioration des performances, tout en assurant une excellente efficacité spectrale et énergétique. De nombreux articles scientifiques ont développé récemment les aspects théoriques de ces systèmes dont la faisabilité a été validée par des essais réalisés par des opérateurs. Cependant, certains défis doivent encore être relevés avant le déploiement complet des communications basées sur le massive MIMO. Par exemple, l'élaboration de modèles de canaux représentatifs de l'environnement réel, l'impact de la diversité de polarisation, les stratégies de sélection optimale d'antennes et l'acquisition d'informations d'état du canal, sont des sujets importants à explorer. En outre, une bonne compréhension des canaux de propagation en milieu industriel est nécessaire pour optimiser les

liens de communication de l'industrie intelligente du futur. Dans cette thèse, nous essayons de répondre à certaines de ces questions en nous concentrant sur trois axes principaux:

1. La caractérisation polarimétrique des canaux massive MIMO en environnement industriel. Pour cela, on étudie des scénarios correspondant à des canaux ayant ou non une visibilité directe entre émetteur et récepteur (Line-of-Sight – LOS) ou Non-LOS, et en présence de divers types d'obstacles. Les métriques associées sont soit celles utilisées en propagation telles que le facteur de Rice et la corrélation spatiale, soit orientées système comme la capacité totale du canal incluant des stratégies de précodage linéaire. De plus, les schémas de diversité de polarisation proposés montrent des résultats très prometteurs.

2. En massive MIMO, un objectif important est de réduire le nombre de chaînes de fréquences radio et donc la complexité du système, en sélectionnant un ensemble d'antennes distribuées. Cette stratégie de sélection utilisant la corrélation spatiale du récepteur, une métrique de propagation, comme facteur de mérite, permet d'obtenir une capacité totale quasi-optimale.

3. Une technique efficace de réduction des ressources temps-fréquence lors de l'acquisition d'informations du canal de propagation dans les systèmes FDD (frequency-division-duplex) est enfin proposée. Elle repose sur la corrélation spatiale au niveau de l'émetteur et consiste à résoudre un ensemble d'équations auto-régressives simples. Les résultats montrent que cette technique permet d'atteindre des performances qui ne sont pas trop éloignées de celles des systèmes TDD (time-division-duplex) initialement proposés pour le massive MIMO.

Acknowledgements

First of all, I would like to thank Mrs. Martine LIENARD, my thesis director, for accepting to guide me through these three years of thesis. Her patience, support, kindness and knowledge were most helpful during my thesis. I would like to thank her for her relevant remarks and support in writing this manuscript. I also learned a lot about gardening by listening to her passionately talk about the best ways to grow vegetables and fruits.

Also, thanks for Mr. Lionel BUCHAILLOT, director of the IEMN laboratory and all the members of the IEMN for all the help during these 3 years.

To my co-director Mr. Davy Gaillot, I am grateful and honored to have worked beside you. Lots of good moments were shared in these 3 years especially during conferences and presentations. I will never forget these times and I will never forget your patience, notes and help during the writing of this thesis and the different articles. I think it is important (I know you don't like this word), to express my sincere appreciation to you on both the professional and personal aspect.

Besides my advisor, I would like to thank the different members of my thesis committee, Mr. Jean-François Diouris, professor at Ecole Polytechnique de l'Université de Nantes, Mr. Pascal Pagani, research engineer HDR at CEA-CESTA, Mr. Alain Sibille , professor at TELECOM ParisTech and Mrs. Dinh-Thuy PHAN-HUY, research engineer at Orange Labs. Thank you for examining my work and for your insightful remarks that helped improve the quality of this manuscript.

I am also very greatful to Mr. Joseph Wout and Mr. José-Maria Molina Garcia-Pardo, invited members with whom we cooperated on many subjects and research areas. Thank you both for your comments and help during these 3 years.

I would also like to thank M. Degauque Pierre for his help, remarks and patience while processing measurement data for all the projects we worked on. His expertise and great mind were inspiring to me and helped me understand many concepts, especially in tunnel environments and wave propagation.

To Mr. Pierre Laly, it has been a great honor to work with you on the great MIMOSA. It helped me understand electronic systems and appreciate the complexity of channel sounders. Also, I will never forget the different measurement campaigns we did together, le Havre, Gant, Anvers. Thank you for the good times we shared together, thank you for teaching me lots and lots of things and thank you for your support.

I would also like to thank Mrs. Dégardin Virginie for welcoming me in the electronic department of University of Lille and for her trust, kindness and great spirit. Thank you Mr. Eric Simon for all the good discussions we had about NOMA and research aspects of my thesis. I appreciated these good times amongst others.

Last but not least, I would like to thank all my friends and colleagues who encouraged me and shared with me the good and the bad times: Ali, Navish, Grecia, Rose, Mauro, Gauthier, Shiqi, Mohammed C., Nicolas, Mahmoud, Elias, Rachel. I cannot mention them all, but I express my gratitude to you for making my stay in Lille a great one.

A special thanks to my family and Lamya for always being here when I needed you. Finally, thanks again to all the people I mentioned above and to the people whom I couldn't mention but helped me directly or indirectly during my study. Without you, I could not have achieved this success.

Contents

List of Figures

List of Tables

List of Publications

Accepted Papers in Peer-Review Journals

J1 **F. Challita**, M. Martinez-Ingles, M. Liénard, J. Molina-García-Pardo and D. P. Gaillot, “Line-of-Sight Massive MIMO Channel Characteristics in an Indoor Scenario at 94 GHz”, in:
IEEE Access, vol. 6, pp. 62361-62370, 2018.

J2 **F. Challita**, P. Laly, M. Liénard, E. Tanghe, W. Joseph and D. P. Gaillot, “Hybrid virtual polarimetric massive MIMO measurements at 1.35 GHz”, in:
IET Microwaves, Antennas and Propagation- Special Session, 2019.

J3 M. Yusuf, E. Tanghe, **F. Challita**, P. Laly, D. P. Gaillot, M. Liénard, L. Martens and W. Joseph, “Stationarity Analysis of V2I Radio Channel in a Suburban Environmen”, in:
IEEE Transactions on Vehicular Technology. (Accepted)

J4 **F. Challita**, VMR.Peñarrocha, L. Rubio, J. Reig, LJ. Llácer, JP. García, J. Molina-García-Pardo, M. Liénard and DP. Gaillot, “On the contribution of Dense Multipath Components in an intra-wagon environment for 5G mmW Massive MIMO channels”, in:
IEEE Antennas and Wireless Propagation Letters.

J5 **F. Challita**, P. Laly, M. Liénard, E. Tanghe, M. Yusuf, W. Joseph and D. P. Gaillot, “Channel Correlation-based approach for feedback overhead reduction in massive MIMO”, in:
IEEE Antennas and Wireless Propagation Letters, 2019.

Papers Under Review

J6 **F. Challita**, J. Molina-García-Pardo , M. Liénard, and D. P. Gaillot, “Evaluation of an antenna selection strategy for reduced massive MIMO complexity”, in:
Radio Science.

Accepted Papers in Peer-Review International Conferences

C1 **F. Challita**, P. Laly, M. Liénard, D. P. Gaillot, J. M. Molina-Garcia-Pardo and W. Joseph, “MIMO in Tunnel: Impact of Polarization and Array Orientation on the Channel Characteristics”, 2018 IEEE Radio and Antenna Days of the Indian Ocean (RADIO), Grand Port, 2018, pp. 1-2.

C2 **F. Challita**, P. Laly, M. Liénard, D. P. Gaillot, P. Degauque, W. Joseph, “Experimental Study of Depolarization and Antenna Correlation in Tunnels in the 1.3 GHz Band”, 2019 26th International Conference on Telecommunications (ICT), Ha Noi, Vietnam, pp. 1-5.

C3 M. Yusuf, E. Tanghe, **F. Challita**, P. Laly, D. P. Gaillot, M. Liénard, B. Lannoo, R. Berkvens, M. Weyn, L. Martens and W. Joseph, “Experimental Characterization of V2I Radio Channel in a Suburban Environment”, 2019 13th European Conference on Antennas and Propagation (EuCAP), Krakow, Poland, 2019, pp. 1-5.

C4 **F. Challita**, M. Martinez-Ingles, M. Liénard, J. Molina-García-Pardo and D. P. Gaillot, “Evaluation of an Antenna Selection Strategy for Reduced Massive MIMO Complexity”, 2018 12th European Conference on Antennas and Propagation (EuCAP 2018) ,London, UK, pp.1-5.

C5 **F. Challita**, M. Yusuf, E. Tanghe, P. Laly, M. Liénard, W. Joseph and D. P. Gaillot,“Impact of Polarization Diversity in Massive MIMO for Industry 4.0”, 2019 European Conference on Networks and Communications (EuCNC) 2019, Valencia, Spain, pp. 1-5.

IRACON-COST[1] Conference

P1 **F. Challita**, M. Martinez-Ingles, M. Liénard, J. Molina-García-Pardo and D. P. Gaillot, “Line-of-Sight Massive MIMO Channel Characteristics in an Indoor Scenario at 94 GHz”, 4th MCM and 4th Technical meeting, Lund, Sweden.

P2 **F. Challita**, M. Martinez-Ingles, M. Liénard, J. Molina-García-Pardo and D. P. Gaillot, “Evaluation of an Antenna Selection Strategy for Reduced Massive MIMO Complexity”, 5th MCM and 5th Technical meeting, Cartagena, Spain.

---

[1] The Inclusive Radio Communications (IRACON) COST ACTION CA15104 aims to introduce novel design and analysis methods for 5G and beyond-5G radio networks. The main goal of working group 1 is to develop accurate radio channel models for inclusive deployment scenarios at different frequencies and co-develop antenna systems that can cope with the the targeted deployments.

P3 **F. Challita**, P. Laly, M. Liénard, E. Tanghe, W. Joseph and D. P. Gaillot, “Impact of polarization in hybrid virtual polarimetric massive MIMO measurements at 1.35 GHz”, 6th MCM and 6th Technical meeting, Cartagena, Spain.

P4 **F. Challita**, E. Tanghe, , P. Laly, M. Liénard, W. Joseph and D. P. Gaillot, “Massive MIMO for Industrial Scenarios : Measurement-Based Polarimetric Analysis”, 9th MCM and 9th Technical meeting, Dublin, Ireland.

P5 M. Yusuf, E. Tanghe, **F. Challita**, P. Laly, D. P. Gaillot, M. Liénard, B. Lannoo, R. Berkvens, M. Weyn, L. Martens and W. Joseph, “Experimental Characterization of V2I Radio Channel in a Suburban Environment”, 9th MCM and 9th Technical meeting, Dublin, Ireland.

P6 M. Martinez-Ingles, **F. Challita**, D. P. Gaillot, JP. García, J. Molina-García-Pardo, “1-100 GHz Deterministic and Experimental Indoor Channel Modeling”, 9th MCM and 9th Technical meeting, Dublin, Ireland.

Other

Participation in European School of Antennas (ESoA) 2017- Université Catholique de Louvain (Summer School) and ranked first in the final exam.

Chapter 1

General Introduction and Motivations

Chapter Outline

In this introductory chapter, a general overview of 5G is presented in Sec. 1.1 while Sec. 1.2 focuses on the main features, use-cases and enabling technologies. A brief introduction of multi-antenna systems is given in Sec. 1.3. Massive MIMO (multiple-input multiple-output) systems, their key features, systems architecture and channel estimation are detailed in Sections 1.4, 1.5 and 1.7. Section 1.6 gives a summary of massive MIMO testbeds, first trials and challenges published in the literature. Lastly, Sections 1.8 and 1.9 present the different contributions of this work as well as the thesis organization, respectively. Other contributions during these 3 years of Ph.D. are listed in Sec. 1.10.

1.1 Introduction: Overview of The 5th Generation

1.1.1 5G: Evolution or Revolution ?

Mobile connectivity has become not only essential but a necessity for many network users. Technological advances and computer abilities are needed to provide faster, smarter and safer wireless networks [2]. The domain of application is wide and not limited to mobile devices and cellular networks [3] but also includes connected machines in industrial setups, vehicular communications (vehicle-to-everything or V2X) [4] and smart cities [5, 6]. Network architectures and generations have also evolved from the first digital generation (GSM or Global System for Mobile Communications) to the most recent generation network connectivity 4G (LTE or Long Term Evolution). The next 5 years are projected to supply unprecedented data rates and networks efficiency should follow along. The number of mobile subscribers is growing rapidly and the demand for more bandwidth (BW) and higher data rates continues to increase as reported by CISCO [7]. This explosion of mobile applications and adoption of mobile connectivity alongside the need for higher data rates, green energies and cutting-edge applications, is fueling the growth of 4G deployments, soon to be followed by 5G systems. All these points and many others lead to one conclusion: the need for cutting edge technologies [8] to support consumer usage trends and keep cost efficient solutions in terms of infrastructure. From this discussion, it appears that 5G would eventually be more of a revolution than an evolution of 4G, changing the way the world is perceived. However, although 5G is being marketed as a brand new technology, it will not be built from scratch [9, 10] and hybrid non-standalone configurations using both 5G and 4G technologies will co-exist.

1.1.2 Initial Vision: Use-cases for 5G New Radio

With the increasing requirements upon the new 5G communication standards, a new radio (NR) interface and radio access network (RAN) are being developed. 5G NR is the name that the third generation partnership project (3GPP) chose for 5G when Release 15 was announced. NR is the equivalent of LTE for 4G or UMTS technology for 3G technology. 5G NR's goal is to meet the performance requirements set by the international telecommunication union (ITU) for the year 2020. More specifically, recommendation ITU-T Y.3101 presents distinguishing features and requirements of the international mobile telecommunications 2020 (IMT-2020) for 5G networks. Promising technologies capable of fulfilling the gap from previous generations are sought. An overview of the NR interface standard under development by 3GPP is available in [11] with preliminary specifications for Release 15 approved in December 2017 [12]. Release 16 will provide further specifications for the second phase. The most central use-cases are not final and still being discussed both in ITU, 5G-PPP [13], the METIS project [14] and in 3GPP [12]. The main use cases to be supported span three different dimensions: enhanced mobile broadband (eMBB), massive machine type communications (mMTC) and ultra-reliable low latency communications (URLLC). Additional use-cases may naturally emerge in time with the evolution of the physical layer radio interface [15].

1.1.2.1 Use-Cases

Enhanced Mobile Broadband (eMBB):

Can be defined as the feature of 5G as the most relevant evolution of 4G. It is a data-driven use-case enabling new applications such as virtual reality (VR). Improved spectral efficiencies, cell-edge data rates and coverage, amongst other requirements, define the shape of eMBB in 5G networks. The relevant 5G requirements are:

- Peak throughput: 20 Gbps in Downlink (DL), 10 Gbps in Uplink (UL).
- Experienced data rates (5^{th} percentile user throughput): 100 Mbps (DL), 50 Mbps (UL).

- Area capacity (e.g. indoor hotspot): 10 Mbps/m^2.
- User plane latency: 4 ms

Massive Machine Type Communications (mMTC): Industry 4.0

IoT requires massive connectivity where tens of billions of interconnected low-cost devices and sensors communicate [16]. Recent advancements on machine-to-machine (M2M) communications in 4G networks are presented in [17]. This is being labeled as the fourth industrial revolution or Industry 4.0. There are many advantages brought by 5G cutting edge technologies for industrial automation scenarios in the drive for Industry 4.0 [18]. In [19], challenges and solutions for M2M communications are depicted. Relaxed data rates constraints are sought compared to eMBB but other strict requirements are still to be fulfilled:

- Density: 1 Million devices/km^2.
- Wide Coverage: 164 dB Maximum Coupling Loss (MCL).
- Device battery life: 10-15 years.

Ultra-Reliable Low Latency Communications (URLLC)

Critical applications (e.g. Intelligent V2X, remote surgery, smart grids, etc.) define very stringent latency and reliability requirements. For this ultra-reliable and low latency area communications, specific requirements are needed [20, 21]:

- Latency: less than 1 ms.
- Reliability : 99.999%.
- Control plane latency: tens of ms.
- User plane latency: less than 0.5 ms (one-way UL and DL).
- Mobility interruption time: 0 ms.

1.1.2.2 Multi-Layer Spectrum

Globally harmonized spectrum is needed for 5G systems to ensure the different requirements and satisfy future expectations and potential capabilities. 5G network deployments are converging to new frequency bands: 3.5 GHz (16% of total number of trials) and 24.25-27.5 GHz (19% of total number of trials) frequency ranges [22], two new frequencies to the cellular network industry. For instance, in France, Arcep (telecom regulator) announced it was planning to issue temporary frequency authorizations (in the 3.5 GHz band [3400 − 3800 MHz]) to develop 5G in France [23]. Also, it is expected that some applications of 5G networks will require very wide contiguous blocks of bandwidths (up to several GHz) to support high overall system capacities. To this end, high carrier frequencies (> 6 GHz) need to be considered. Maintaining a sustainable spectrum management environment is also critical for long term investments even if new techniques are envisaged. In Release 15 of 5G NR, two frequency ranges are defined [24]:

- 450 MHz - 6 GHz or the sub-6 GHz bands.
- 24.25 GHz - 52.6 GHz or the millimetr wave (mmW).

This multi-layer spectrum approach is vital to address the wide range of usage scenarios. The sub-6 GHz band is also divided into two parts as indicated below. According to Huawei in [25], 3 layers can be defined:

- Below 2 GHz: delivers high coverage for wide areas and deep indoor scenarios, useful for mMTC [26] to help support IoT services. It is also needed to extend high speed mobile broadband coverage across urban, suburban and rural areas. Mobile spectrum in this range can be used in the future for some use-cases. The European Commission has already expressed its wish to use the 700 MHz band to support 5G services in Europe. Similarly, the FCC (Federal Communications Commission) indicated that the 600 MHz band could be used in the United States and several other countries. Furthermore, the ITU is considering additional spectrum for mobile broadband from in 2023 (470-694 MHz), a good timing for 5G services.

- From 2 to 6 GHz (C-band): The 3.3-4.2 and 4.4-5 GHz ranges deliver the best compromise between wide coverage and spectral efficiency making them attractive for eMBB. The 3.3-3.8 GHz range is almost globally harmonized and used as the basis for initial commercial 5G services. A number of countries are exploring whether a portion of other bands could be used such as 3.8-4.2 GHz and spectrum in the 4-5 GHz range, in particular 4.8-4.99 GHz. The availability of at least 100 MHz BW per 5G network alongside the potential of massive MIMO will potentially boost throughputs (peak, average and cell-edge) with relatively affordable complexity.

- Above 6 GHz: delivers extremely high data rates (super data layer), and is widely recognized as a key component for hotspot areas, fixed broadband and fiber-like connectivity. mmW frequencies have particular propagation characteristics and are more sensible to blockage than lower frequencies. Accurate channel models and characteristics are needed to understand the different mechanisms at these frequency ranges [27]. The targeted spectrum above 6 GHz is expected to handle a mixture of licensed and unlicensed mobile bands. 24.25-29.5 GHz, 31.8-33.4 GHz, 37-43.5 GHz, 45.5-50.2, GHz, 50.4-52.6 GHz, 66-76 GHz and 81-86 GHz bands should be agreed in WRC-19. Studies concerning mmW mobile communications for 5G cellular networks can be found in [28]. The authors presented some measurement results at 28 and 38 GHz frequencies showing the possibility of employing steerable directional antennas at base stations (BS) and mobile devices. In [29], a theoretical feasibility study and prototype results on mmW beamforming are presented. In [30], the authors study the feasibility of spatial multiplexing and maximum ratio transmitter for mmW large MIMO.

From a cell point of view, this classification can be further generalized [9]:

- Macro-Cell : < 1 GHz: full coverage (rural scenarios and deep indoor).
- Dense urban: from 2 to 6 GHz: high date rates.
- Small cell 28/39 GHz (> 6 GHz generally): 10 Gbps hotspots.
- Ultra small cell: future mmW options and very high data rates.

1.1.3 Gaps and Challenges

The wireless industry has witnessed rapid growth in the last few decades. Nonetheless, many gaps and challenges should be addressed for the full development of 5G. Table 1.1 presents some differences between LTE and 5G, and the corresponding targeted applications and use-cases.

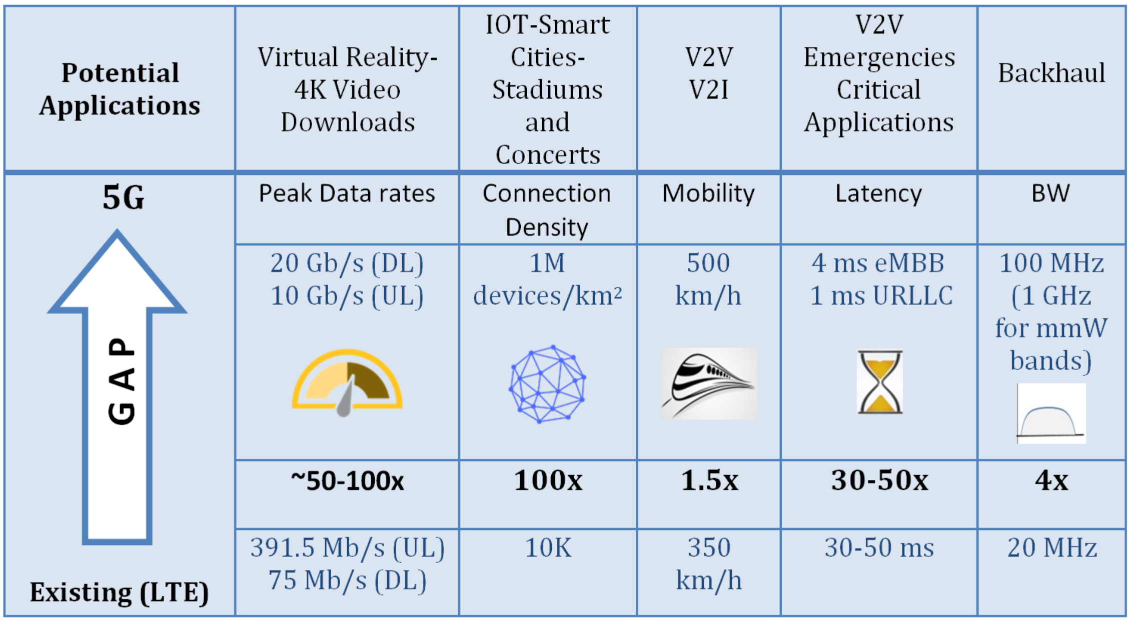

Potential Applications	Virtual Reality-4K Video Downloads	IOT-Smart Cities-Stadiums and Concerts	V2V V2I	V2V Emergencies Critical Applications	Backhaul
5G	Peak Data rates	Connection Density	Mobility	Latency	BW
	20 Gb/s (DL) 10 Gb/s (UL)	1M devices/km^2	500 km/h	4 ms eMBB 1 ms URLLC	100 MHz (1 GHz for mmW bands)
GAP	**~50-100x**	**100x**	**1.5x**	**30-50x**	**4x**
Existing (LTE)	391.5 Mb/s (UL) 75 Mb/s (DL)	10K	350 km/h	30-50 ms	20 MHz

Table 1.1: *Gaps and Challenges towards 5G.*

Other requirements related to technical performance for 5G radio interface such as energy efficiency (10 times longer battery life for low-power M2M), core network technologies, outage probability, interruption time, etc. can be found in [31, 26, 32, 33]. Spectrum policies and regulatory issues as already discussed need to be tackled before a worldwide deployment [34, 35]. NR Phase 1 and LTE share some common technical aspects such such as OFDM (orthogonal frequency-division multiplexing). However, PHY layer of NR phase 1 is scalable and supports new transmission modes in digital beamforming. This is illustrated in Table 1.2.

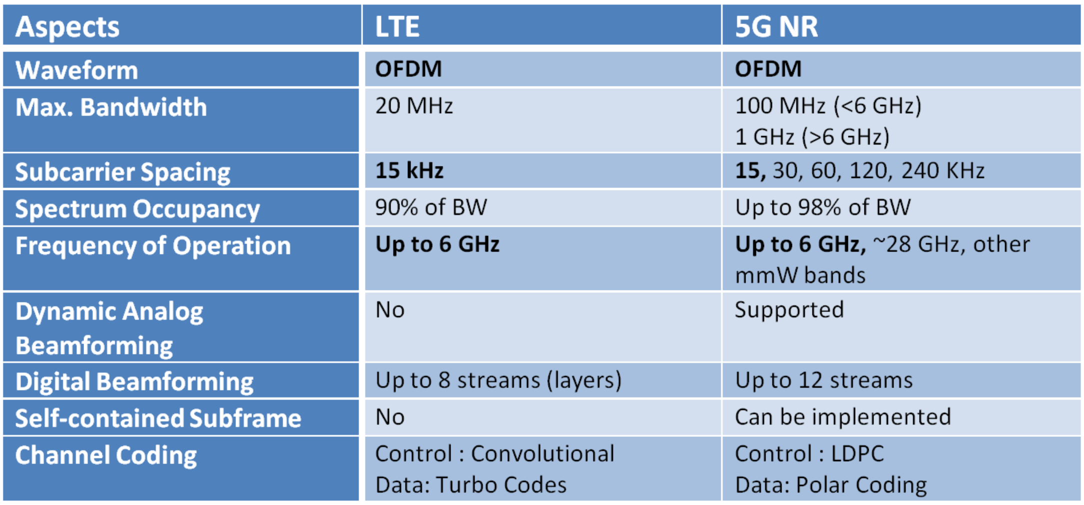

Aspects	LTE	5G NR
Waveform	**OFDM**	**OFDM**
Max. Bandwidth	20 MHz	100 MHz (<6 GHz) 1 GHz (>6 GHz)
Subcarrier Spacing	**15 kHz**	**15,** 30, 60, 120, 240 KHz
Spectrum Occupancy	90% of BW	Up to 98% of BW
Frequency of Operation	**Up to 6 GHz**	**Up to 6 GHz,** ~28 GHz, other mmW bands
Dynamic Analog Beamforming	No	Supported
Digital Beamforming	Up to 8 streams (layers)	Up to 12 streams
Self-contained Subframe	No	Can be implemented
Channel Coding	Control : Convolutional Data: Turbo Codes	Control : LDPC Data: Polar Coding

Table 1.2: *Main Differences in PHY layer of LTE and 5G-NR.*

1.2 Impacting technologies of 5G

In order to satisfy the different requirements for 5G systems, improvements of existing technologies and emerging techniques should be evaluated [3, 36]. The 5 main impacting technologies of 5G are:

- mmW: A gold mine of spectrum and contiguous blocs of bandwidths.
- Cloud-based radio access network (C-RAN): centralized baseband units (BBU) are separated from remote radio heads (RRHs). Different RRHs are connected to a centralized cloud with all the signal processing [37, 38].
- M2M communications and Industry 4.0: support of a large number of low-rate devices at very low latency data-transfer.
- Device-centric architectures: small-cells (micro, femto) in a heterogeneous network (HETNETs), traffic offload, better coverage, etc.
- **Massive MIMO**: allowing the densification of BS or access points (AP) by deploying massive Tx arrays capable of multiplexing many user equipments (UEs) in the same time-frequency resource. It is a cutting-edge technology capable of filling the gap for many 5G systems requirements [32] by increasing system capacity of new wireless systems [39].

Many demonstrations have already highlighted the effectiveness of massive MIMO systems implementation, mostly for cellular communications, indoor scenarios, etc. and will be discussed later. Table 1.3 lists the different technologies and aspects of 5G NR highlighting the emergence of massive MIMO .

Densification	Massive Connexion	Antenna	Spectrum
• Self Backhauling • Energy Efficiency • Interoperability • **Massive MIMO**	• **Massive MIMO** • Long battery life • Protocol optimization • Signaling techniques • Resource allocation	• **Massive MIMO** • Long range • Deep coverage • Antenna packaging and integration	• < 1GHz : IoT, mobile broadband • 1 GHz to 6 GHz : mobile broadband • > 6 GHz : extreme mobile broadband, indoor, backhaul point to point • **Spectral efficiency (Massive MIMO)**
			

Table 1.3: *Mobile Technologies for 5G.*

1.2.1 Massive MIMO: Why Now ?

Multi-antenna systems are a must to address the different requirements of 5G-NR. Extra antennas used in massive MIMO help focusing energy into ever smaller regions of space to bring huge improvements in throughput and radiated energy efficiency [40]. Other benefits such as cheaper parts, lower latency, reliability, amongst others, make massive MIMO an interesting candidate for 5G. System throughput, defined as the sum of data rates delivered to all users in a given cell and measured in bits per second (bits/s or bps), is a key parameter for performance evaluation. Throughput is directly related to BW and spectral efficiency (SE) as illustrated in Eq. 1.1. The SE measured in bits/s/Hz (bps/Hz), is a deterministic number and gives direct insight into expected data rates for a given system:

$$Throughput(bits/s) = BW(Hz) \times SE(bits/s/Hz). \tag{1.1}$$

The maximum SE is determined by the channel capacity defined by Claude Shannon is his seminal paper from 1948 [41]. Clearly, in order to increase data rates, higher bandwidths are needed and/or better SE. Due to congestion in cellular frequencies (below 6 GHz), the second option is more adapted for this frequency range. For mmW bands, the first option can be easily applied because of large contiguous blocs of spectrum. In the following, some key points address the “Why Now ” question:

- Congestion of macro networks, base sites will run out of capacity by 2020 for sub-6 GHz spectrum: *capacity requirements* fulfilled by spatial multiplexing in massive MIMO.
- Large BW above 6 GHz but complicated propagation conditions : *coverage requirements* fulfilled by high gain adaptive arrays in massive MIMO.
- Massive MIMO is now supported (primary versions) in release 13-14 for LTE and 15 for 5G-NR: *3GPP specifications support.*
- Low cost and high efficiency components for active antenna arrays are becoming technically and commercially feasible: *Technology capability.*
- In Rel. 15-NR, diversity schemes are not explicitly supported: *Spatial multiplexing is becoming more and more essential.*

1.3 Multi-antenna System Communications

Multiple antennas at either both ends or one end of the communication link have been widely used in wireless systems to address different challenges such as link reliability (diversity techniques) or SE (multiplexing techniques). In order to understand massive MIMO, MIMO and MU-MIMO are first introduced.

1.3.1 MIMO Communications

MIMO systems gained considerate attention for the past decades [42, 43] and are now incorporated into most of the new generation wireless standards. Transmission with MIMO antennas is a well-known method to overcome fading and enhance link reliability: this is categorized as diversity. Also, simultaneous communication of multiple data streams over the same radio channel by exploiting the multipath nature of the radio channel started a considerate evolution in data rates and system capacity. This paves the way for a wide variety of use-cases and applications. More recently, MIMO has been applied to power line communications (PLC) [44, 45, 46].

1.3.1.1 Fundamentals and system model

A simple system model with M transmitting antennas (Tx) and N receiving antennas (Rx) is presented in Fig. 1.1. The $N \times M$ channel matrix $\mathbf{H}$ contains the channel coefficients linking each Tx antenna to each Rx antenna of a single-user (SU).
For diversity schemes, each Rx antenna combines the Tx signals which coherently add up to provide signal-to-ratio (SNR) gains on one hand, or to increase reliability on the other hand. MIMO systems have the capability to multiply systems throughput by $\min(M, N)$ in ideal rich multipath conditions: this is spatial multiplexing. The memoryless MIMO flat fading channel (narrowband model) is given by :

$$\mathbf{y} = \mathbf{H}\mathbf{x} + \mathbf{n}, \tag{1.2}$$

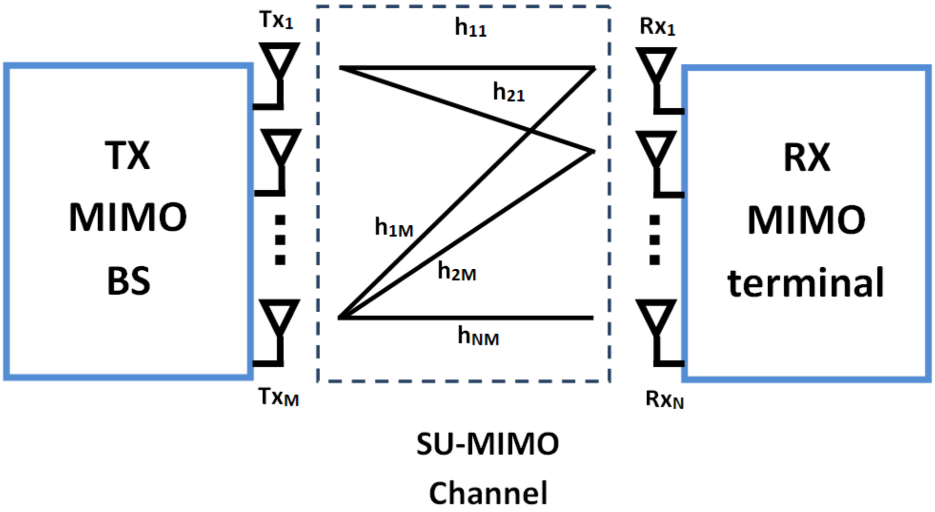

Figure 1.1: *SU-MIMO system model.*

- $\mathbf{H}$ is the $N \times M$ complex channel matrix given by :

$$\begin{bmatrix} h_{11} & h_{12} & \dots & h_{1M} \\ h_{21} & h_{22} & \dots & h_{2M} \\ \vdots & \dots & \ddots & \vdots \\ h_{N1} & h_{N2} & \dots & h_{NM} \end{bmatrix}$$

- h_{ij} is the complex channel gain between Tx and Rx elements with $i = 1, ..., M$ and $j = 1, , ..., N$
- $\mathbf{x}$ is the $M \times 1$ complex transmitted signal vector
- $\mathbf{y}$ is the $N \times 1$ complex received signal vector
- $\mathbf{n}$ is the $N \times 1$ complex additive noise signal vector with variance σ_n^2.

1.3.2 Multi-User MIMO

MU-MIMO have been attracting considerable interest [47]-[48] and is still a hot topic for wireless communication systems [49]-[50]. A BS or AP equipped with M antennas (up to 16) communicating with a number of distributed users K (equipped with $N \geq 1$ antennas) falls into the MU-MIMO systems category. Generally, the transmitter should be equipped (as a minimum) with as many antennas as the total number of served users antennas. A sketch of the MU-MIMO (multi-user MIMO) scenario with K users equipped with $N = 1$ is illustrated in Fig. 1.2.

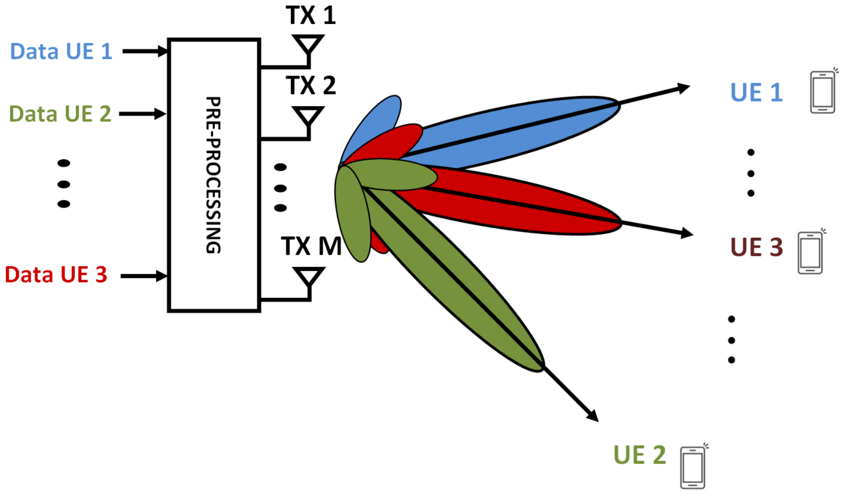

Figure 1.2: *MU-MIMO scenario.*

The research on MU-MIMO is not recent and have witnessed some impactful array processing papers [51, 52, 53, 54]. These systems can harmonize the high capacity achieved using standard MIMO processing techniques with the benefits of space-division multiple access (SDMA) for which the spatial degrees of freedom (DoF) are used as multiplexing dimension. This technique supports multiple connections on a single channel where different users are spotted by their spatial signatures inside the network. SDMA also helps mitigate the effects of adjacent cell interference.

1.3.2.1 Advantages of MU-MIMO

Traditionally, the time-frequency resources are divided into resource blocks (RB) and one user is active per RB for which the SISO (single-input single-output) SE is quantified as $\log_2(1 + SNR)$ with SNR an average signal-to-noise ratio. In a suitable and rich multipath environment, multiple users can be simultaneously assigned multiple parallel streams. The total SE is thus scaled up by a factor G, known as **Multiplexing Gain**, the number of potential parallel streams. The total SE becomes $G\log_2(1 + SNR)$ for an interference-free case. This is a general approach to quantify the SE, details on power allocation and other systems aspect are given in Ch. 2. The need to harvest multiplexing gains has motivated the effort to switch from MIMO systems to MU-MIMO. It is noteworthy that SDMA does not require multiple antenna at the UE [55]. The MU-MIMO main advantages are listed below:

- Possibility of using one antenna at Rx for each user: less constraints on the physical size of UE and cost requirements.

- MU-MIMO is better equipped than MIMO to overcome most of propagation limitations such as ill-conditioned channels or strong line-of-sight (LOS) by using advanced scheduling schemes.

- Enhanced sum-rates inside a given cell: better use of spectrum resources.

However, these advantages come at a price:

- MU interference can be mitigated through precoding (widely discussed in Ch. 2) and cancellation techniques such as ML (Maximum Likelihood) detection for UL [56], dirty paper coding (DPC) [57, 58] for DL or interference alignment [59, 60]. Some approaches are based on beamforming techniques such as in [61, 62].
- Availability of channel state information at the transmitter (CSIT) is challenging especially in high mobility scenarios.
- User scheduling and resource allocation schemes lead to an increase in implementation complexity.

1.3.3 Evolution of multi-antenna systems with 3GPP

Multiple antennas can increase capacity and reliability but also provide spatial resolvability, spatial DoF for multiple users to share and higher SE. MIMO systems have evolved lately to include MU-MIMO systems (via the introduction of new transmission modes TM) before the arrival of massive MIMO [63]. This transition was motivated by many factors:

- In the 1-6 GHz range of cellular communication, the number of antennas that can be deployed in compact user terminals is limited.
- The wireless channel to a given terminal can have, in some configurations or scenarios, few contributing paths, limiting the ability to send parallel data streams.
- Advanced signal processing schemes are sometimes needed in point to point MIMO to detect multiple streams.
- For MU-MIMO, users should be spatially well-separated to avoid co-channel interference.
- Small-scale fading can still affect the link reliability.
- Massive MIMO can be a solution to focus, in an efficient manner, the energy towards the intended users.

The following figure illustrates the evolution of multi-antenna systems under the scope of 3GPP standards and releases.

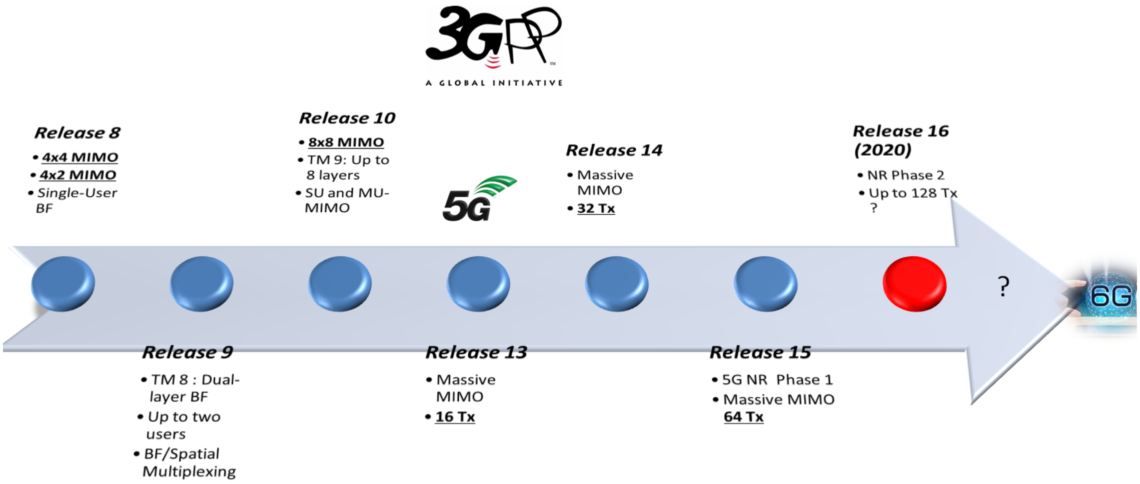

Figure 1.3: *3GPP Releases-From MIMO to massive MIMO. This figure displays the evolution from Release 8 to the up-coming Release 16.*

1.4 Massive MIMO: Massive Breakthrough

1.4.1 History and Brief Introduction

The massive MIMO concept was first mentioned in the seminal paper: **"Non-cooperative Cellular Wireless with Unlimited Numbers of Base Station Antennas"** [64] by Thomas Marzetta, published in 2010. This paper only talks about MU-MIMO systems with very large antenna arrays, but over the years, massive MIMO became a catchy term in all the published scientific papers.

From this paper, it is understood that massive MIMO is a form of MU-MIMO, an asymptotic extension where M is very large and many UEs are simultaneously served (see Fig. 1.4). The transition from MIMO, MU-MIMO to massive MIMO, according to IEEE, is a clean break with current practice through the use of a large excess of service Tx antennas over active terminals. Generally speaking, the receivers (UEs, machines, industrial robots, etc.) in 5G use-cases are equipped with one antenna [9, 22, 25]. Transmission signals are adjusted by the physical layer using phase/gain control. The basic information, theoretical aspects and limits were presented in early works such as [65]-[66].

Massive MIMO is generally defined as "useful and scalable version of MU-MIMO" [67], or "a MU-MIMO system with M antennas and K users per BS. The system is characterized by $M \gg K$ and operates in time-division duplexing (TDD) mode (discussed later) using linear UL and DL processing" [68].

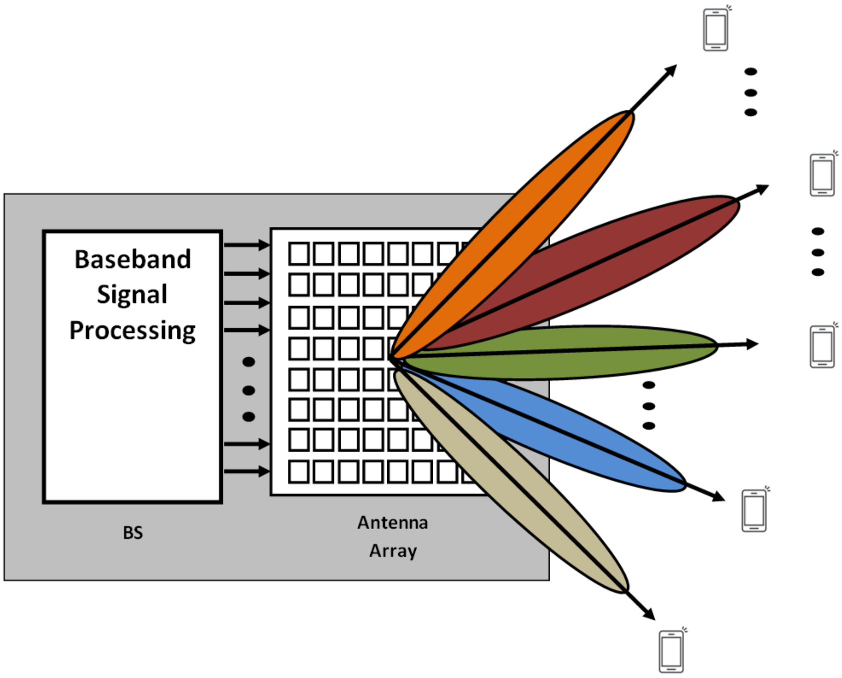

Figure 1.4: *Overall Massive MIMO System.*

These definitions cover most systems but are very general. In order to bring out the characteristics of such systems, some essential caracteristics covering the definition of massive MIMO are given hereafter. Massive MIMO:

- is an extensive raise in the number of transmitting antennas M packed into an array (see Fig. 1.5),
- relies on the spatial dimension to form orthogonal sub-channels and simultaneously serve K users,
- communicates over a channel with ***favorable propagation conditions***,
- benefits from ***channel hardening*** provided by the large number of antennas,
- Uses TDD relying on channel reciprocity and UL pilots to obtain channel state information (CSI).

Different antenna array geometries for the Tx are presented in Fig. 1.5 from [69]. Mostly recognized, the URA (uniform rectangular array) because of its horizontal and vertical aperture and the possibility of adjusting both elevation and azimuth angles. For instance, vertical alignment of the array elements is beneficial for users on different floors using elevation beamforming as shown in Fig. 1.6.

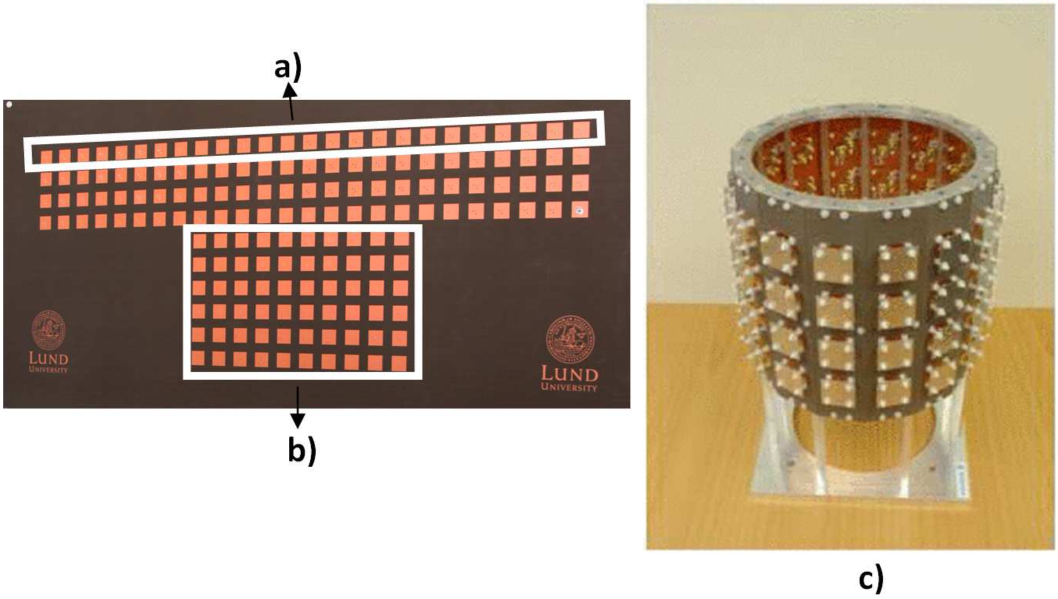

Figure 1.5: *Different Array Configurations: a) Linear, b) Rectangular and c) Cylindrical (Lund University).*

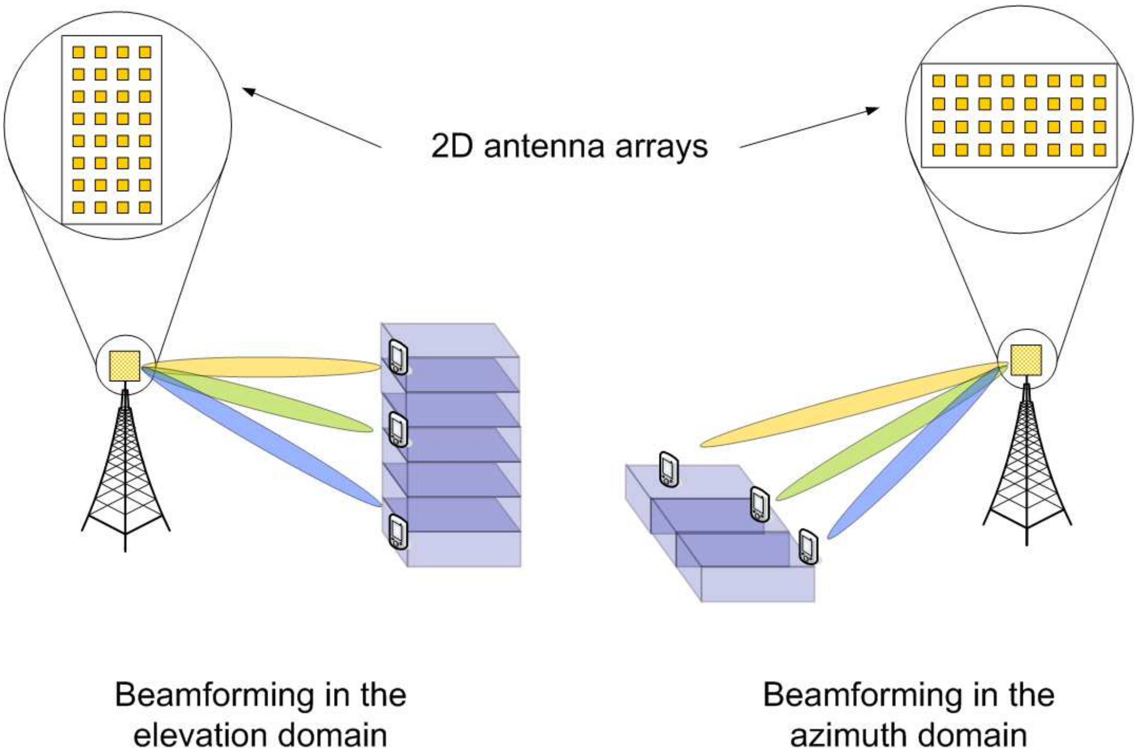

Figure 1.6: *Massive MIMO in the elevation and azimuth domain.*

Channel hardening and favorable propagation condition (widely discussed in Ch. 2) can be illustrated mathematically as the following:
Suppose a simple Rayleigh environment, a $K \times M$ massive MIMO channel $\mathbf{H}$ with channel vectors $\mathbf{h_{ij}} \in \mathcal{N}_{\mathbb{C}}^{1 \times N_{obs}}$ and N_{obs} the number of observations. The product $\mathbf{H}\mathbf{H}^H \rightarrow \sigma^2 \mathbf{I}_K$, with $\sigma^2 \mathbf{I}_K$ a $K \times K$ scaled identity matrix. The diagonal elements converge to a deterministic value (channel hardening) and off-diagonal elements converge to 0 (indicating favorable propagation or zero inter-user interference). Channel hardening and favorable propagation condition are two main pillars of massive MIMO. In the following, some key definitions from a 5G system point of view are presented:

1.4.2 General Definitions

- **BS** or **AP** will designate the Tx massive MIMO transmitter in this manuscript.

- **UE** or user, receiver, will designate one Rx of the massive MIMO setup.

- **RF Chain**: A radio frequency chain is a set of electronic modules designed to transmit and/or receive radio signals. RF chains usually contain amplifiers, low-noise amplifiers (LNA), etc.

- **Physical Radiating Element**: emits radio waves in a given direction with a given power depending on a predefined radiation pattern. It can also be called physical antenna [9].

- **Antenna**: consists in one or more m radiating elements (dipoles, patches, etc.) fed with the same signal. For instance, one antenna is capable of sending one stream at a time even if many radiating elements exist. This is the key aspect of phased arrays and analog beamforming discussed later. It can also be called logical antenna port [12].

- An **Antenna Array** consists in multiple antennas, each with an individual RF chain. In this case, the number of multiplexed streams equals the number of antennas. An antenna array consists in M antennas (consequently M RF chains) which in turn can consist in m radiating elements.

- A **Radiation Pattern** describes the directivity of a radiating element or antenna array. The directivity is the ratio between the radiated power in a given direction and the power radiated by an isotropic antenna. Directivity is measured in dBi (with respect to the isotropic antenna).

- **Array Gain**: When multiple radiating elements are associated, the resulting signal has a strong directivity. In cellular communications, large vertical antenna panels with 120^o horizontal sector have a strong directivity. It is made up of many radiating elements, each having a directivity of a few dBi. If a panel consists in 8 patch antenna elements, each having typical 7 dBi, the total array gain is the individual gain + 10 × $\log_{10}(8)$= 16 dBi gain per panel.

- **Multiplexing Gain**: It is generally measured as the rank of the channel matrix and indicates how many users can be simultaneously served (number of layers in LTE). The multiplexing gain is limited by $min(M, N_{Rx})$, with N_{Rx} the total number of users antennas ($K \times N$).
- **Beamforming (BF)** uses multiple antennas to adjust the phase and amplitude of the wavefront by appropriately weighing individual antenna signals to form a directional signal transmission. At mmW bands, beamforming will be mostly used to increase range by energy focusing while at lower bands it will be key to spatial multiplexing especially in increasing the SE. There has been a considerate amount of research concerning beamforming techniques for massive MIMO as illustrated in the next section. Beamforming architectures and features will be thoroughly discussed later on.

1.4.3 Key Features

A great deal of interest in massive MIMO has been emerging [39, 64, 70, 71, 72]. In [73] and references therein, an overview of massive MIMO technology is thoroughly presented. In [64], Marzetta demonstrated that the use of excessive number of radiating elements at the transmitting side paired with a number of active users permits the use of simple linear precoders such as maximum-ratio-combining (MRC) in the UL and maximum-ratio-transmitter (MRT) in the DL. Massive MIMO key enabler is the asymptotic orthogonality of users channel vectors. Large array gains, low complexity precoding and detection techniques, savings in term of radiated energy per bit, hardware-friendly waveform shaping, reduced sensitivity to hardware imperfections and non-linearity distortions are all potential improvements from massive MIMO. The many DoF provided by massive MIMO via spatial multiplexing and high diversity orders can provide high data rates over a reliable channel.

1.4.4 Main Advantages

A review of the main advantages of massive MIMO is presented hereafter:

Inter-user Interference:

$[\mathbf{HH}^H]_{i,i}$ values grow with M but the off-diagonal elements are also of importance for the overall system evaluation. The values of $[\mathbf{HH}^H]_{i,j}$ with $i \neq j$ grow far slower than diagonal elements. In i.i.d. Rayleigh channels, distributions of both diagonal and off-diagonal elements converge to Gaussian distributions when M $\rightarrow \infty$.

Spectral Efficiency:

With M BS antennas and K single-antenna users, a diversity order of M and a multiplexing gain of K can be achieved. In [74], SE optimization methods with pilot and users considerations are presented. In [75], the effect of increasing M and its impact on SE is discussed while centralized and decentralized massive MIMO systems are evaluated in [76].

Energy Efficiency:

With large arrays, increasing M can be harvested in terms of reduced transmit energy per element. This is discussed in [77, 78]. These DoF make massive MIMO a viable candidate for green communications [40, 79, 80]. In the DL, large arrays can focus the transmitted energy in the directions of the users (using precoding techniques discussed later) achieving high energy efficiency [39]. It is possible to maintain the same SE for K users while doubling M and reducing Tx power by a factor of 2; energy efficiency thus doubles. A survey on energy-efficient techniques for massive MIMO is presented in [81]. In [82], the advantages and challenges of massive MIMO for energy-efficient MU systems are discussed.

Large array gains:

Using more antennas can be interpreted as more samples in the spatial domain. If these samples are constructively combined, the SNR can be improved with respect to SISO systems. The signal strength for a targeted user becomes larger. However, radio regulators set limitations on the effective transmitted power of wireless devices, including array gain which cannot increase indefinitely. In Fig. 1.7, the radiation pattern of a massive MIMO linear array of variable size is presented with omnidirectional antennas. This is to underline how increasing M can benefit wireless systems: narrower beamwidths, less spillage and attenuation of side lobes. This is a simple example with one user located at angle $\theta = 0°$ and using phased array principle to steer the beam in the wanted direction. Generally with massive MIMO, multiple users are simultaneously served, thus multiple streams are sent from the array (a superposition of beams) as shown in Fig. 1.8.

A complementary list of general advantages of massive MIMO:

- The effects of fast fading and uncorrelated noise vanishes with the increasing M: **channel hardening**.
- High communication reliability.
- Capability to focus energy in small regions of space.
- Simple linear signal processing.
- Efficient diversity and multiplexing techniques in favorable propagation conditions.

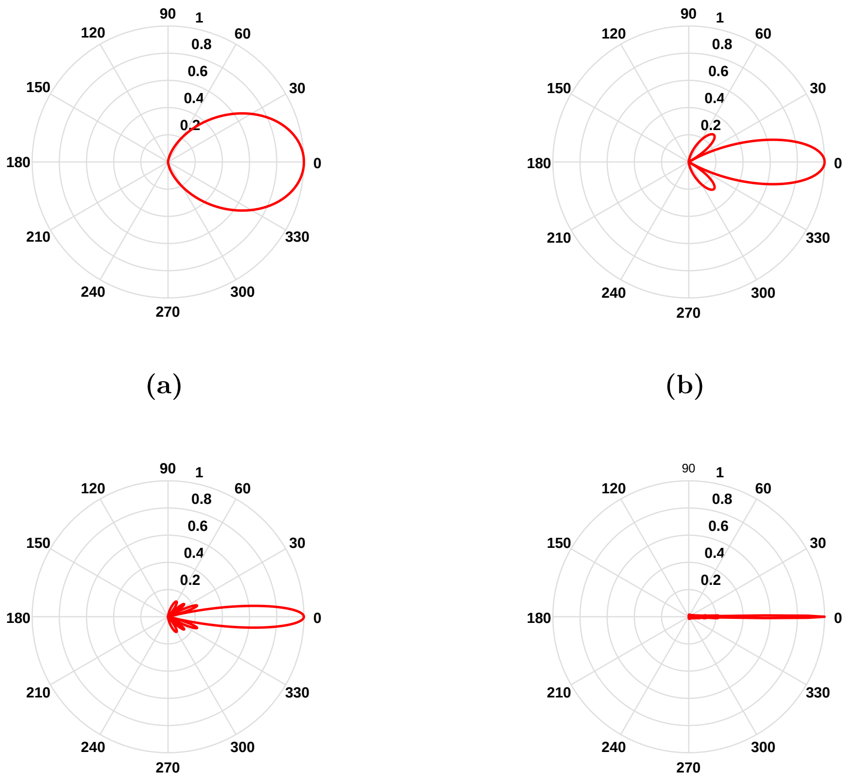

(a) (b) (c) (d)

Figure 1.7: *Radiation Pattern of multiple-antenna setups a) $M = 2$, b) $M = 4$, c) $M = 8$ and d) $M = 64$ radiating elements with normalized gain.*

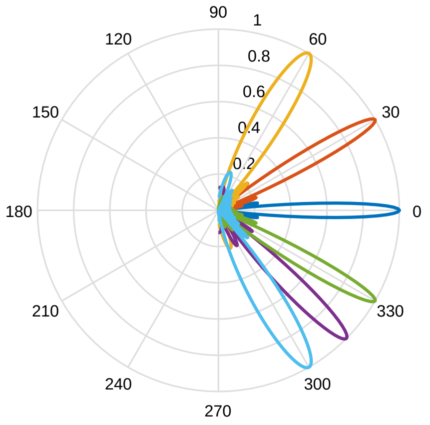

Figure 1.8: *Radiation Pattern for 6 users with different spatial signatures and $M = 16$ Tx antennas.*

1.5 Massive MIMO System Architecture

In this section, we introduce the concepts of analog, digital and hybrid beamforming. The advantages of each scheme and their applications with massive MIMO setups are also discussed. The three different architectures are illustrated in Fig. 1.9(a), (b) and Fig. 1.10 for analog, digital and one example of hybrid beamforming, respectively. These figures show a simplified schematic since carrier oscillator, baseband modulator, power amplifiers, and other typical RF components should also be integrated. As a general notation and from Sec. 1.4.2:

- **Digital Beamforming (DBF)**: $m = M = N_{RF}$
- **Analog Beamforming (ABF)**: $m > 1$ and $M = 1$
- **Hybrid Beamforming**: $m > 1$ and $M < m$

1.5.1 Digital Beamforming (DBF)

In a full digital architecture, each radiating element is connected to one RF chain. The signal is pre-processed at baseband before RF transmission. Multiple beams can be simultaneously formed from the same set of elements in the array. This allows a full flexibility of the system and makes DBF attractive for spatial multiplexing with massive MIMO. However, this also requires a RF chain for each element. DBF is referred to as MU-MIMO in LTE/5G. It is already used in transmission modes 7, 8 and 9 in LTE Advanced Pro.

1.5.2 Analog Beamforming (ABF)

ABF [83] is simpler but can accommodate one user (no SDMA). The same signal is fed to each physical antenna element and the signal phases are adjusted in the RF domain using analog phase-shifters to steer the radiating pattern of the array in a given direction. The different copies of the signal from different array elements are constructively summed at the Rx to form the in-beam direction. This is the principle of phased arrays which has been known for a while now. The main difference with DBF is mainly the processing wherein the DBF is applied on the baseband signal (on K data streams) whilst phase shifting in the analog beamformer is applied after digital-to-analog conversion (DAC) for the single stream user.

1.5.3 No Compromise ?

ABF is the best compromise between coverage and power/cost constraints but not adequate for massive MIMO scenarios with a large number of receivers. However, it can be associated with mmW for potential wireless backhaul design applications or use-cases where link reliability and high data rates are a must [84, 85].

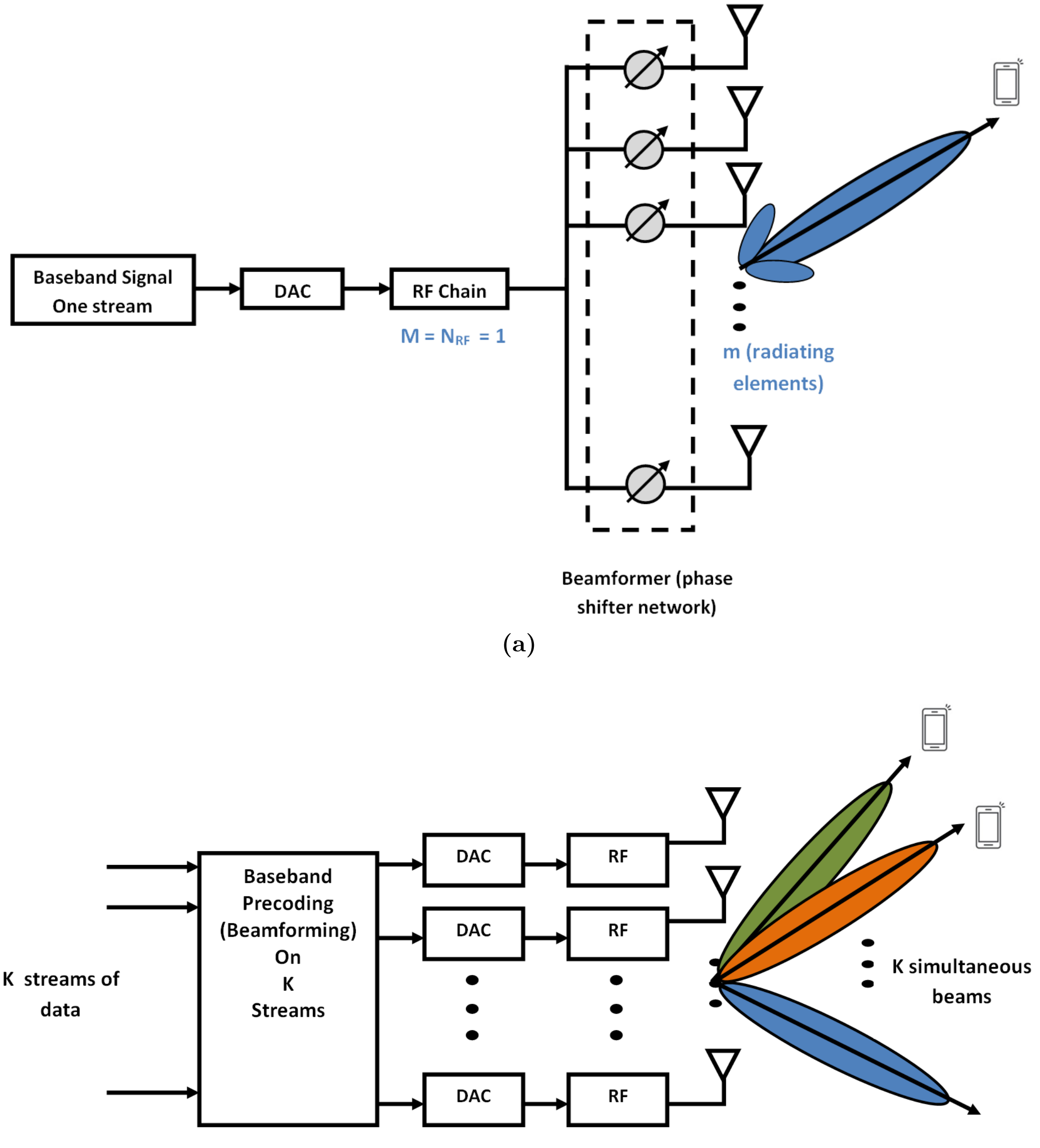

(a)

(b)

Figure 1.9: *(a) Tx Analog Beamformer (b) Tx Full Digital Beamformer.*

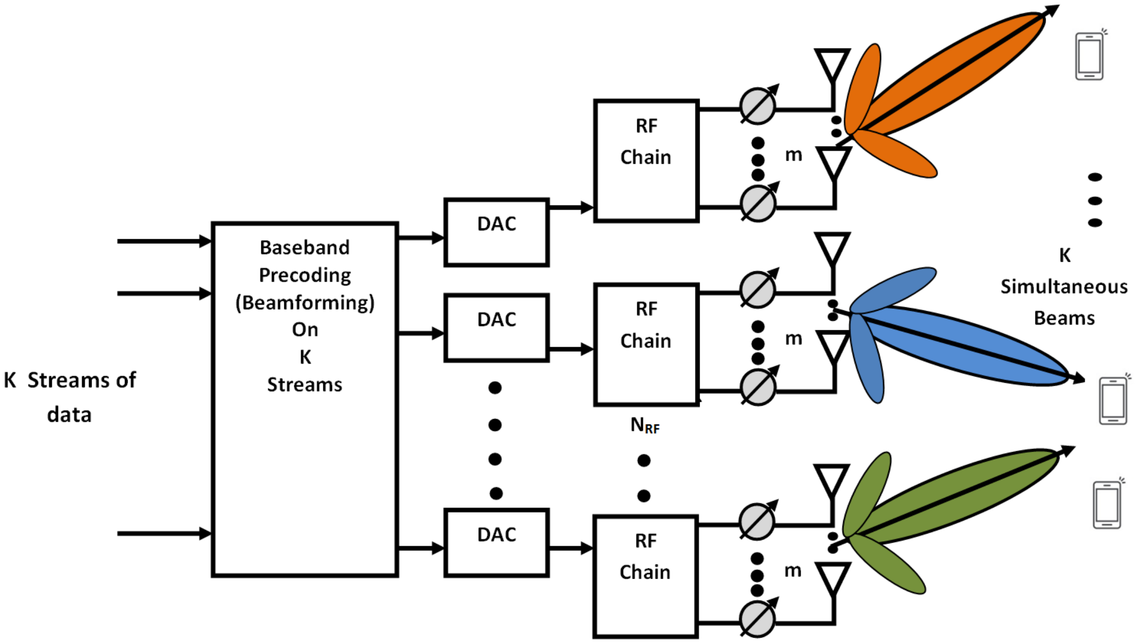

Figure 1.10: *Example of a Hybrid Beamforming Architecture.*

DBF is convenient for capacity enhancements and flexibility in MU scenarios. However, its complexity increases with M. Hybrid beamforming is a compromise between the two where the number of RF chains is less than the number of antennas [86] but still large to accommodate a given number of streams. Hybrid beamforming can also be thought of as a phased array adapted for the transmission of simultaneous beams. A survey on hybrid beamforming architectures for massive MIMO is available in [87]. A comparison between hybrid analog-digital and full digital schemes is presented in [88] and the trade-off between throughput and needed training is depicted in [89]. As shown in Fig. 1.10, N_{RF} is less than the number of total radiating elements m but should be equal or greater than the number of antennas or K data streams (simultaneous sent beams). This is one of the proposed architectures (partially connected architecture) of hybrid beamforming but many others exist [90] such as fully connected architectures where the RF beamformer of each RF chain make use of all the array elements. It should be underlined that one RF chain in hybrid beamforming can be considered as one logical antenna port. Typically, there are more physical antenna elements than logical antenna ports. There can be as many simultaneous beams as there are logical antenna ports .

1.5.4 What is precoding then ?

In massive MIMO, it is popular to use the term precoding or pre-filtering. Precoding is equivalent to DBF. The transmitted signal can be matched to the multipath signature of the channel and is not limited to LOS conditions. The 5G BS (AP) computes the spatial information for each user based on CSI-RS (Channel State

Information- Reference Signal). It uses this information to compute the precoding matrix where the data symbols are mapped to array elements. The multiple data streams have their own weights which include phase offsets to each stream to enable the waveforms to combine constructively at the receiver. This maximizes the signal strength to the user whilst also minimizing the interfering signals. In this way the 5G BS is able to communicate with multiple UEs concurrently and independently by using spatial information. The three different precoding techniques: MRT, zero forcing (ZF) and minimum-mean-squared estimator (MMSE) will be described in Ch. 2. Under this umbrella, it should be noted that all the system complexity in massive MIMO is reported at the transmitting side.

1.6 Massive MIMO in practice

1.6.1 Real-time Testbeds

Real-time testbeds for massive MIMO systems are the best solutions to validate the different concepts and promises of this technology. Lund University, in collaboration with National Instruments (NI), introduced the 100 antenna LuMaMi (Lund University Massive MIMO) testbed in [69], the first real-time implementation of massive MIMO. Specifications of the design, implementation and validation of the system can be found in [91]. In [92], a 128-element testbed, developed by the University of Bristol in collaboration with NI and Lund University was presented. The ArgosV2 testbed [93] developed at Rice University is a TDD based system and reported some cell capacity and signal-to-interference and noise (SINR) measurements. ZTE also reported TDD massive MIMO field trial in [94] with 64 Tx and 8 LTE commercial handsets in a rise building achieving a 300 Mbps sum-rate with 20 MHz BW. The Titan massive MIMO system [95] provides a ready to use MU massive MIMO testbed with real-time processing up to 250 MHz BW with up to 1000 antennas, but no details of the implementation were provided. The Ngara demonstrator in Australia uses low-cost equipment in frequency-division duplexing (FDD) fashion and have reported an UL SE of 67.26 bps/Hz in a lab at 638 MHz. It was reported in [96], using the LuMaMi , through LOS measurements at 3.51 GHz in an indoor environment with 12 receivers, an uncoded system sum-rate of 1.59 Gbps using a single 20 MHz LTE band, equating a SE of 79.4 bps/Hz. In a subsequent indoor trial, 22 receivers were simultaneously served, achieving a SE of 145.6 bps/Hz, claimed to be the highest SE achieved for any wireless system to date. The results of different field trials demonstrated that massive MIMO can be adopted as a key enabling technology for 5G.

1.6.2 Trials and Deployments

Although 5G is still in its exploratory phase, some operators have already advertised some 5G technologies [97]-[98]. An overview of trials, challenges and deployments for

5G in practice can be found in [99]. Recently, the Russian telecom operator MTS has deployed more than 40 state-of-the-art LTE sites with massive MIMO functionality in seven cities where the 2018 FIFA World Cup took place [100]. Orange and Ericsson demonstrated in Châtillon that high data rates (greater than 10 Gbit/s) can be achieved thanks to bricks of the future 5G technology. Some field trials [98] reported peak speeds of 330 Mbps per channel using a 20 MHz channel at 2.5 GHz. It also demonstrated a four-fold increase in capacity per channel, a three-fold increase in cell edge performance and an improvement in the overall coverage area, compared to current commercial deployment. In [97], DeutscheAG reported LTE TDD massive MIMO field trials at 3.5 GHz with 20 MHz BW combining massive MIMO, 256QAM where a 750 Mbps peak speed was reported. In [101], a FDD-LTE massive MIMO field trial was reported for the first time but no technical details were given. Etisalat has conducted a live on-air trial of massive MIMO technology with Ericsson including latency, speed and beamsteering tests. The test reported an aggregate site throughput of over 24 Gbps at 15 GHz with 800 MHz BW. Bouygues Telecom reported a 5G test under real-world conditions [23]. The test was based on non-standalone (NSA) 5G technology. In partnership with Huawei, various tests were conducted in Bordeaux which saw a peak DL speed of 2.3 Gbps and latencies as low as 7.5 ms. These tests and trials amongst others demonstrate the benefits of massive MIMO and justify the race for deployment between different European and international operators.

1.6.3 Challenges

Despite the merit of massive MIMO, a number of issues still need to be tackled before fully bringing massive MIMO to practice [102, 103, 104]. Many challenges [105, 106, 107, 108, 73, 109, 32] should be addressed, and original contributions are sought. In the following, some general challenges are presented, then, we focus on relevant challenges to this thesis.

- Pilot contamination issue in a multi-cell scenario investigated in [110, 103] through a wide survey. Blind methods for non-linear estimation [111] are proposed for instance and channel predictions to overcome channel aging [112].

- Low complexity hardware, impact and mitigation of hardware imperfections [113]. Massive MIMO performance with hardware-constrained BS is investigated in [114] and the effect of non-ideal hardware on capacity limits and energy efficiency is depicted in [65].

- Mutual coupling between antennas can be beneficial when reciprocity calibration is considered in TDD. This effect has been widely studied for MIMO systems [115]. Power loss [116] and higher spatial correlations [117] due to coupling between closely-packed antenna elements [118] can degrade the system performance of a simple MIMO system. For massive MIMO, mutual coupling can generate power loss and reduction in DoF. The effect of element mutual coupling on the capacity of fixed length linear arrays is presented in [119] for instance. This parameter should be seriously considered when evaluating the overall performance of a massive MIMO setup. Effect of antenna spacing and mutual coupling on the system are studied in [106, 120].

- Resource allocation schemes.
- Network optimization and deployment strategies.
- Channel modeling for high mobility scenarios, industrial scenarios and model proposition for massive MIMO parameters.
- TDD or FDD and efficient feedback methods for FDD deployments.
- Efficient antenna selection strategies to reduce N_{RF} and M.

1.7 Channel Estimation

Massive MIMO relies on quasi-perfect CSI at the BS to coherently pre-process the signals [121]. However, channel acquisition is a challenging aspect and estimating the channel by sending pilots consumes resources. In this paragraph, two techniques, TDD and FDD, are discussed.

1.7.1 Time Division Duplexing

In TDD, UL and DL communication are performed over the same frequency band, using different time slots. This technique has been initially proposed for massive MIMO [64, 122].

- UL transmission : K users send K orthogonal pilot sequences and the channel is estimated based on the received pilot signals. This operation is known as training and requires K channel uses.
- DL transmission : BS needs CSI to precode the transmitted signals in order to make sure each user recovers its own data. Due to the assumed channel reciprocity[1], the estimated channel at the BS from UL pilots can be used to precode the transmit symbols. Limitations on the channel coherence time may create a pilot contamination problem [64] where pilot sequences employed by users in neighboring cells are no longer orthogonal to those within the cell. Also, when M is large, the effective channel gains become nearly deterministic due to channel hardening. This property improves the DL channel gain estimation and alleviates the need for DL pilots [123, 124].

---

[1] The impulse response between two elements is the same in both directions.

1.7.2 Frequency Division Duplexing

In FDD systems, UL and DL use two different frequency bands to estimate the corresponding channel. In this case, the UL and DL channel are not reciprocal.

- UL transmission: same procedure as in TDD and the process will need K channel uses.
- DL transmission: The M BS antennas transmit M orthogonal pilot sequences to K users and each user estimates the channel based on the received pilot signal then the estimation is fed back to the BS via a control channel.

1.7.2.1 Coherence Interval

In the time-frequency domain (similar to the ressource grid in LTE), a coherence interval τ_c is defined as the number of complex-valued samples (or ressource elements RE) within a time interval corresponding to the coherence time T_c and a BW equal to the coherence BW B_c. A coherence interval has $T_c B_c$ complex-valued samples within the time-frequency domain. It is the largest time-frequency space within which the channel is supposed stationary and thus should be estimated. These samples are distributed between UL and DL pilots (for training) and payload (useful data). We denote τ_{dl}, τ_{ul}, the DL and UL payload data samples and $\tilde{\tau}_{dl}$, $\tilde{\tau}_{ul}$ the number of samples allocated for DL and UL pilots, respectively. The two structures are illustrated in Fig. 1.11(a) for TDD and (b) for FDD, respectively. Note that for simplicity, the feedback process is not shown for FDD. In order to send and receive data, the training burden should not consume a lot of resources. From this, we can define constraints for TDD and FDD systems:

- TDD : $\tilde{\tau}_{ul} < \tau_c$
- FDD : $\tilde{\tau}_{ul} + \tilde{\tau}_{dl} < \tau_c$

Hence, it can be seen that the training burden in TDD is independent of DL pilots thus independent of M. This is not the case in FDD where the training overhead scales up with M reducing the payload as seen in Fig. 1.11(b).

Generally, we assume $\tilde{\tau}_{ul} = K$ samples and $\tilde{\tau}_{dl} = M$. The constraints becomes:

- TDD : $K < \tau_c$
- FDD : $K + M$ (DL pilots) + M (feedback) $= K + 2M < \tau_c$

1.7.2.2 5G Frame Structure

In Fig. 1.12, the number of resource elements for training (training pilots) is illustrated as a function of K and M. Based on LTE [125], 2 RBs consist in 14 OFDM symbols spanning 12 sub-carriers in frequency domain (168 complex samples on the time-frequency resource grid).

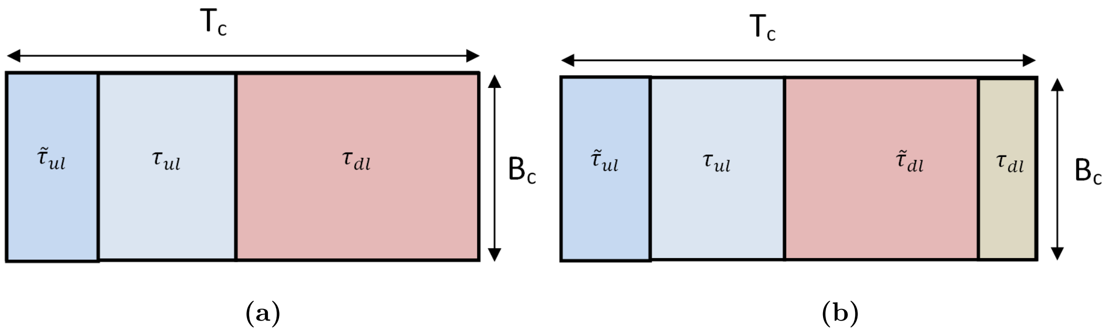

Figure 1.11: *a) TDD Vs b) FDD frame structure inside a coherence interval* τ_c*.*

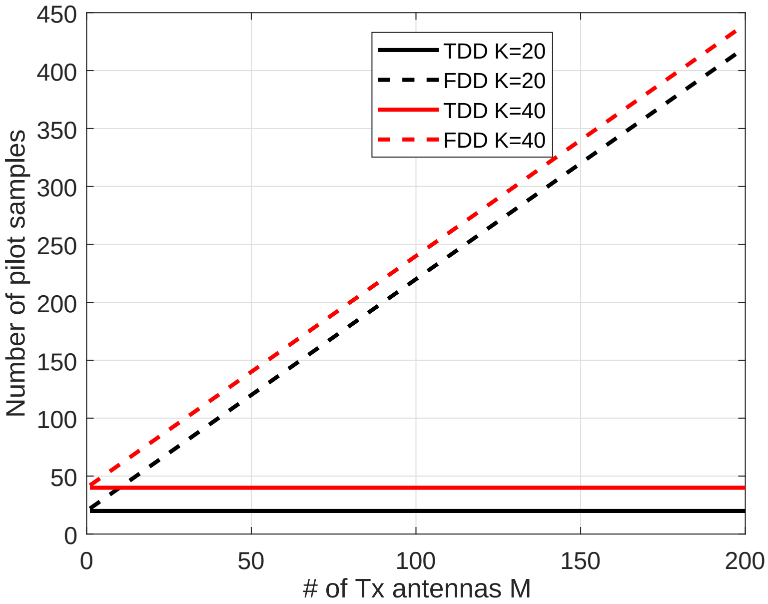

Figure 1.12: *Comparison between TDD and FDD : number of allocated pilots for channel estimation procedure with* K *=20,* K*=40 and* M *varying from 1 to 200.*

The channel is assumed to be constant inside a RB. In 5G NR, multiple frame structures are supported, the main difference being subcarrier spacing and the number of OFDM symbols. The number of subcarriers is also 12. If a BS with $M = 200$ elements is deployed, the entire RB is spent on DL pilots in FDD since pilots are used for channel estimation at each antenna. Thus, to harvest massive MIMO gains with FDD, new design schemes are needed to reduce the performance gap with TDD. This illustration confirms the advantage of TDD over FDD wherein for a given K, when M increases, the number of allocated pilots is constant while in FDD, the evolution depends mostly on M. It is concluded from this analysis that TDD is the preferable mode for massive MIMO since it requires less pilots than FDD and is highly scalable with M. However, significant interest in massive MIMO-FDD versions have emerged [126] and FDD systems were reported to achieve better results than TDD systems in specific situations, for instance symmetric traffic and delay-sensitive applications [127, 128]. Under this umbrella, massive MIMO FDD-based solutions are needed.

1.8 Motivations and Contributions

An essential question for massive MIMO is to validate the theoretical predictions with experimental results. Unlike Rayleigh channels, real scenarios such as large indoor industrial channels have specific characteristics that can influence the performance of massive MIMO. In the following, the different relevant challenges are presented.

1.8.1 Special Focus on Industry 4.0

Works for Release 16 already began with some trends such as support for Industrial IoT channel models for frequencies up to 100 GHz. A new study item entitled "Study on NR industrial Internet of Things (IoT)" has been proposed [129] and contributions are sought starting from the RAN1 meeting in April 2019. The study item aims to develop a channel model to support studies on URLLC and industrial IoT enhancements for industrial scenarios and use cases. In order to achieve this, the study item should fulfill the following objectives:

- Review existing literature and new propagation measurements in industrial environments.
- Identify key differences with existing channel models such as the model in technical report TR 38.901.
- Define new industrial propagation scenarios, corresponding propagation parameters and new model components if needed.
- Priority for frequency ranges below 52.6 GHz.

These points underline the importance of channel modeling for M2M in industrial scenarios. As no channel models are yet published, a geometrical-based channel model is proposed in Ch. 2.

1.8.2 Polarimetric Channel Characteristics and Propagation Conditions

Inter-user interference and channel hardening will depend on the massive MIMO channel matrix $\mathbf{H}$ and thus on the environment and propagation conditions. When i.i.d. Rayleigh is assumed, transmission is interference-free and optimal performance can be achieved with relatively simple precoding. In practice, channels hardly satisfy the i.i.d. assumption and M is limited. For instance, if the number of scatterers is small compared to K or if users channels are highly correlated, propagation conditions are unfavorable leading to performance degradation. A good understanding of propagation conditions is needed if optimal strategies are to be developed. Under this umbrella, cross-polarization impact, a scarcely studied subject for massive MIMO, is exploited in Ch. 3. A good understanding of polarization effects will help to propose novel transmission strategies to achieve most of the performance of massive MIMO. These subjects are studied for an industrial scenario with a massive MIMO setup, an environment where massive MIMO studies are also scarce in the literature.

1.8.3 CSI Feedback Overhead Reduction

Capacity improvements depend on CSI. Massive MIMO, originally uses the calibrated TDD strategy, to estimate the instantaneous channel from UL pilots. However, motivated by spectrum regulation issues, significant interest in FDD-based systems have emerged [126, 130]. In this manuscript, a novel method for CSI feedback overhead reduction is proposed in Ch. 4.

1.8.4 Antenna Selection Strategies

Unlike i.i.d. scenarios where all array elements contribute equally, in real scenarios [84], adaptive antenna selection strategies may be used to reduce the implementation complexity by decreasing the number of RF chains and the number of active antennas. Antenna selection strategies have yet to be fully defined and evaluated. A novel strategy is proposed in Ch. 4.

1.9 Thesis Organization

The main scope of the thesis will be the evaluation of the performance of a massive MIMO setup in an industrial scenario for potential M2M communication in the scope of Industry 4.0. To achieve this goal, Ch. 2 introduces some system metrics, main massive MIMO channel and system characteristics, and an overview of channel modeling. Using a geometrical-based channel model, a massive MIMO system is evaluated through a parametric analysis. In Ch. 3, the studied industrial scenario is described and polarimetric channel measurements are presented. A propagation-based method for user classification is proposed. Performance of precoding techniques are evaluated according to the propagation scenario and polarimetric channel. Lastly, using polarimetric analysis, new strategies exploiting polarization diversity and reducing infrastructure complexity, are proposed. Ch. 4 is dedicated to CSI feedback reduction on one side, by proposing a correlation-based approach for feedback overhead reduction in FDD, and on the other side, an original antenna selection strategy at Tx based on the receiver spatial correlation is described, detailed, validated and evaluated. These strategies are assessed using propagation parameters and sum-rate capacity analysis. In Ch. 5 and 6, the different conclusions of this manuscript and future research directions are given.

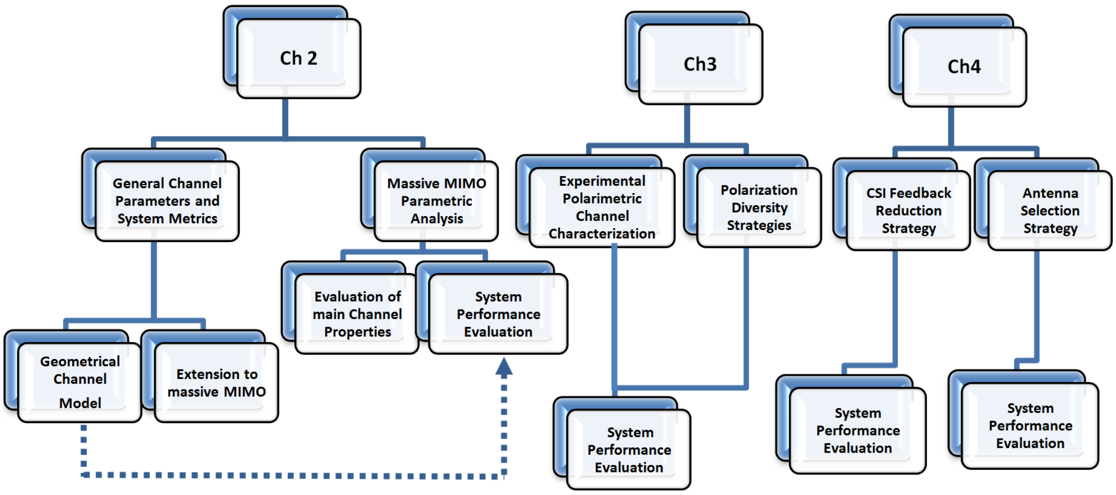

Figure 1.13: *Structure of the thesis.*

1.10 Other Contributions

The previous paragraphs briefly introduced the main contributions obtained during the preparation of this Ph.D. thesis and which will be described in the next chapters. It must be emphasized that, in parallel to this work, I have also contributed to other studies presenting complementary aspects and always dealing with MIMO or massive MIMO systems. The corresponding results have been published (5 papers) either in journals or in proceedings of conferences, detailed references being given in the **List of Publications**. Since it can be interesting to present a short overview of what has been done in this frame, this section presents context and objectives of this additional work, emphasizing my own contribution. The different results are deduced from measurement campaigns and the corresponding papers are classified according to the geometry of the indoor environment in which they took place: laboratory room, meeting room, subway carriage and tunnel. Note that, in these cases, frequency may cover a band extending from 1.3 GHz up to 94 GHz, while in the following chapters the main focus is on frequencies around 3.5 GHz. The different sections are associated with the corresponding paper number in the **List of Publications**.

Laboratory Room

In collaboration with Univ. Politecnica di Cartagena (UPCT, Spain), a series of experiments in LOS conditions were carried out in a laboratory of about 45 m^2 furnished whith tables, cupboards and desktops. The frequency-dependence of channel correlation was first studied in the 5 -94 GHz band, spacing between array elements of the 6×6 virtual URA varying from a few millimeters to 27 mm in [P6]. To simulate a massive MIMO configuration, the size of the Tx array was increased up to 50×50, for a frequency of 94 GHz, and 4 positions of the receiver (Rx) were considered. It was demonstrated that mmW massive MIMO systems allows reaching orthogonal Tx-Rx streams even for a small 7×7 antenna array subset with correlation between users < 0.2. Moreover, strong phase variations at Tx are highlighted through channel phase correlation studies. These phase variations also contribute to the decorrelation at Rx between close users, paving the way for further massive MIMO system enhancements [J1].

Meeting Room

In this room, 7.92 m wide and 6.82 m long, the polarimetric massive MIMO radio channel of a LOS scenario was investigated at 1.35 GHz, using a real-time MIMO radio channel sounder with dual-polarized patch antennas. The 8×12 massive MIMO Tx array was based on a hybrid architecture including a vertical uniform linear array translated at different horizontal positions, then forming an URA. The performance of the system was evaluated for different polarization schemes and Rx antenna orientations using propagation channel-based metrics, as receiver spatial correlation, and system-oriented metrics such as sum-rate capacity. Results have indicated a clear dependence of the performance to the polarization schemes and receiver orientation. It clearly appeared that the additional degree of freedom brought by polarization diversity can contribute to improve spectral efficiency by a factor of about 20%. Also, coupling effects were discussed and shown to decrease the overall system performance by increasing spatial correlation. The latter parameter was also modeled using a Burr statistical distribution [J2].

Subway carriages

In the frame of a collaboration between our laboratory, UPCT and Univ. of Valencia (Spain), we have interpreted results of measurements that took place in a long subway carriage in the 25-40 GHz band, Tx being a 7×7 URA, 8 users being uniformly distributed in the carriage. One of the main objectives was to study the dependence of the specular (SMC) and dense multipath components (DMC) to the inter-user spatial correlation and sum-rate capacity. It appears that the inter-user spatial correlation computed with DMC offers the best favorable propagation for a massive MIMO setup whereas SMC contribute to the users correlation. These results highlight the need to include DMC in 5G massive MIMO channel models and emulators to improve their accuracy at the system level [J4].

Road tunnel

Measurements have been carried out in a low traffic road tunnel to investigate the influence of the polarization of the Tx and Rx antennas on the channel characteristics. The same channel sounder as in [J2] for the meeting room measurements was used. In a first step, emphasis was on the cross-polarization discrimination factor

(XPD) and, for a MIMO configuration, on the correlation between Tx and Rx array elements, depending on the array orientation and on the polarization [C2].
In a second step, various combinations of polarization at both Tx and Rx have been tested to minimize spatial correlation while keeping the size of the array as small as possible. Indeed, to maintain a high MIMO capacity with a compact array, and based on an association of co- and cross-polarized antennas, a compromise must be found between loss of power due to XPD and decrease of correlation [C5].

1.11 Summary of Key Points

- Technological breakthroughs are needed in the wireless community to accommodate the requirements of 5G.
- 5G will not be built from scratch right away. Configurations using both 5G and 4G technologies will co-exist.
- Multiple antenna systems such as MIMO and MU-MIMO addressed many challenges but still not sufficient.
- Massive MIMO is presented as a paradigm shift to fulfill many milestones of 5G.
- Massive MIMO can achieve both high SE and EE by multiplexing many UEs which share the energy costs and achieve high sum SE.
- Field trials have confirmed the potential benefits of massive MIMO systems, specially for outdoor scenarios.
- Massive MIMO can enhance coverage using high gain adaptive arrays ($>$ 6 GHz) and provides high orders of interference-limited spatial multiplexing ($<$ 6 GHz).
- Massive MIMO can be used under ABF (beamsteering) technique. It is mostly intended for backhaul or very high data rate applications.
- Massive MIMO's full advantages are harvested when full digital systems are used.
- FDD channel estimation becomes challenging due to induced substantial overhead (such as feedback) that scales up with the number of antennas.
- Many challenges still have to be addressed before fully exploiting the advantages of massive MIMO.

Chapter 2

Massive MIMO Channel and System Aspects

Introduction

In order to design wireless communication systems, a first step is the understanding of the medium between the transmitter and the receiver. The multipath channel and its characteristics will help determine hardware and software requirements for system design. Propagation models are generally used in network planning tools and tuned for new frequency ranges to improve network planning accuracy. This is particularly true for massive MIMO where channel models based on measurements are a must to optimize the overall performance in any use-case. Moreover, from the Tx array side, spatial and temporal stationarity assumptions of the channel are often not verified in real massive MIMO environments. Under this umbrella, the objectives of this chapter are twofold : (i) provide an overview of the wireless channel and main propagation metrics of the SISO channel and (ii) extend this body of knowledge to massive MIMO channels and systems with the specific set of impacting parameters using a geometrical-based channel model.

This chapter is organized as follows: The SISO wireless channel and general propagation characteristics are first presented in Sec. 2.1. The different parameters are then extended to the massive MIMO case and additional parameters such as Gram's power ratio are presented in Sec. 2.2. A geometrical-based channel model for massive MIMO is proposed and validated in Sec. 2.3. The massive MIMO system model, precoding schemes and power allocation concepts are detailed in Sec. 2.4. Finally, sum-rate capacity analysis using the proposed channel model are discussed in Sec. 2.5. This chapter is concluded in Sec. 2.6.

2.1 SISO Wireless Propagation Channel

Radio waves interact with the medium via reflexion, refraction, diffraction and other variants of these physical phenomena (see Fig. 2.1(a). Different replicas of the original signal are combined at the receiver (constructively or destructively) with different directions, delays and amplitudes resulting in rapid fluctuations of the signal amplitude. A constructive interference causes a signal peak while a destructive one results in a valley or a deep fade. These replicas define the multipath components (MPC) of the wireless channel. Propagation channel models aim at translating as accurately as possible all or part of the different MPC taking into account time-frequency-space variations. It is a very active research area for developing effective tools used by standardization organisms.

2.1.1 Characteristics of Propagation Channels

Radio propagation phenomena yield to amplitude and phase variations on the received signal. Two types of fading can be distinguished: (1) large scale and (2) small scale fading.

2.1.1.1 Large scale propagation

In the case of free space propagation with direct LOS between the transmitter and receiver, power loss is distance-dependent. It decreases proportionally with the square of the distance d between Tx and Rx. Generally, the received power P_r from one antenna with gain G_r when a signal with power P_t is transmitted from antenna with gain G_t is calculated using Friis' transmission equation.

$$P_r = \frac{P_t G_t G_r c^2}{(4\pi d f)^2}, \tag{2.1}$$

with f the operating frequency and c the speed of an electromagnetic wave in vacuum. It can be seen that P_r decreases with larger distance and for higher frequencies due to the small size of the Rx antenna. Generally, with the presence of obstacles, the free-space assumption does not hold and P_r decreases as $\frac{1}{d^n}$ where n is the pathloss exponent. n is a real positive parameter that depends on the propagation environment and determines how fast the power decays with distance. The latter can take values smaller than 2 (indoor) or between 2 (free space propagation) and 5 (totally obstructed environment). Also, local shadowing effects between Tx and Rx can occur, giving rise to large deep fading. In order to account for different propagation conditions for different users, the large scale coefficient can be modeled at user k located at distance d_k from the Tx as:

$$\beta_k(dB) = \gamma(d_0) + 10n \log\left(\frac{d_k}{d_0}\right) + \kappa, \tag{2.2}$$

where $\gamma(d_0)$ is the reference path loss at distance d_0 and n the pathloss exponent. κ is the only non-deterministic term drawn from $\sim \mathcal{N}(0, \sigma_f^2)$. This parameter represents the shadow fading creating log-normal random variations around $\gamma(d_0)+10n\log(\frac{d_k}{d_0})$. It can indicate physical blockage from objects and provides a more realistic channel description.

2.1.1.2 Small scale propagation

Contrary to large scale, small scale fading (or microscopic fading) refers to rapid fluctuations of P_r around its average. Multipath is a key feature for multi-antenna communications where diversity is exploited. It also has many effects on the radio channel:

1. Fast changes in signal strength over relatively small distances and time-intervals.
2. Echoes in the time domain (time dispersion) caused by propagation delays.
3. Random frequency modulation due to different Doppler shifts on different MPC.

It should be noted that multipath propagation does not only occur in NLOS conditions. Even when a LOS exists, reflections from the ground and surrounding structures still exist. The detection of fading mainly depends on system properties, its resolvability is determined by the system bandwidth BW. These different discussed mechanisms in this section are illustrated in Fig. 2.1(b).

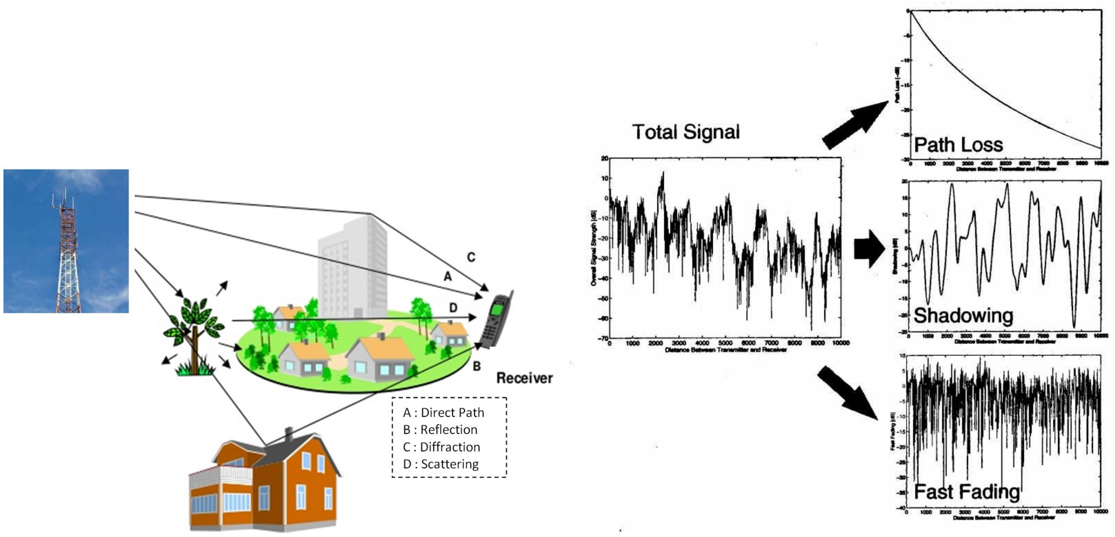

(a) **(b)**

Figure 2.1: *(a) Example of MPC propagation mechanisms and (b) Radio Signal Distortion (example from [1]).*

2.1.2 Time-Frequency Domain SISO Channel Model

The discrete channel impulse response (CIR) is function of the absolute time t and the delay bin $\Delta\tau$ whithin which different MPC are combined. Different time instants t are snapshots of the observed event. t and $\Delta\tau$ are two independent variables where $t \gg \Delta\tau$. t is generally in the order of ms or s whilst $\Delta\tau = \frac{1}{BW}$ is in the order of μs or ns depending on the transmission BW. The baseband discrete impulse response of a SISO multipath channel under WSS (wide-sense-stationary) assumption can be written as:

$$h(t, \Delta\tau) = \sum_{l}^{M_f} a_l(t)\delta(\tau - l\Delta\tau)), \tag{2.3}$$

where $l\Delta\tau$ and a_l represent the l^{th} delay bin and complex amplitude, respectively. $\delta(.)$ is the Dirac or unit impulse function. The channel gain at time t is the sum over l of $|a_l|^2$. If the CIR is time-invariant (static user and environment), or at least WSS where $a_l(t)$ is constant over the duration of the CIR ($M_f\Delta\tau$), with M_f the number of frequency samples in BW, Eq. 2.3 can be simplified as:

$$h(\tau) = \sum_{l}^{M_f} a_l\delta(\tau - l\Delta\tau). \tag{2.4}$$

For the special case where the channel is time-variant, other parameters are necessary to fully describe the radio channel such as the Doppler spread B_D and coherence time T_c. B_D is a measure of the spectral broadening generally caused by relative motion between Tx and Rx while T_c is the time domain dual of B_D and is a measure of the time range over which the CIR can be considered invariant. Channel responses are correlated at different snapshots within T_c. For the rest of the chapter, as only static channels are considered, the index t is dropped.

2.1.2.1 Delay Domain Analysis

The power delay profile (PDP) represents the relative received power as a function of excess delays and can be directly derived from the CIR as follows:

$$PDP(\tau) = 10\log_{10}|h(\tau)|^2. \tag{2.5}$$

Basic parameters of the multipath channel can be directly derived from the PDP. The rms delay spread (σ_τ) is the square root of the second central moment of the PDP and largely depends on the studied environment.

The rms delay spread is expressed as :

$$\sigma_\tau = \sqrt{\bar{\tau^2} - (\bar{\tau})^2}, \tag{2.6}$$

with

$$\bar{\tau} = \frac{\sum_l P(\tau_l)\tau_l}{\sum_l P(\tau_l)}, \tag{2.7}$$

where $P(\tau_l) = |a_l|^2$. Delays are measured with respect to the first detectable path (depending on the BW), and generally taking a 20 dB threshold referred to the highest peak. Typical values of σ_τ are on the order of μs for outdoor radio channels and on the order of ns for indoor settings. It should be noted that the CIR and the frequency response (or channel transfer function CTF) are related through the Fourier transform.

2.1.2.2 Frequency domain analysis

In the frequency domain, the coherence bandwidth B_c is the dual parameter of the delay spread. B_c is a measure of the similarity of the radio channel frequency response ($h(f)$). It gives quantitative information about the maximum allowed transmission BW for which the channel can be considered frequency-flat. The autocorrelation complex function $R_h(\Delta f)$ is defined as :

$$R_h(\Delta f) = \frac{\mathbb{E}\{h(f)h(f+\Delta f)^*\}}{\mathbb{E}\{|h(f)|^2\}}. \tag{2.8}$$

B_c corresponds to a Δf value for which $|R_h(\Delta f)| = \eta$, a percentage of the maximum value of the module of the autocorrelation function ($R_h(0) = 1$). Typical values of η are generally 0.7 or 0.9. For instance, $\eta = 0.7$ is the limit between frequency flat fading and frequency selective channels. $\eta = 0.9$ is applied for nearly flat channels, generally useful for OFDM sub-carrier spacing.

2.2 Massive MIMO Channel Characteristics

In this section, we first present the main notations used for the massive MIMO channel matrix. The two main consequences of massive MIMO are explained and the additional channel propagation parameters and their application to massive MIMO systems are described. *Reminder:* A massive MIMO system is a multi-user system with a large number of transmitting elements. The number of receivers is usually large (but less than the number of array elements) and each receiver is generally a user with one receiving antenna. In this manuscript, only the DL part of the radio channel is considered[1].

2.2.1 Notations

Different multiple-antenna scenarios are shown in Fig. 2.2. Consider M the number of BS antennas (denoted as Tx), K the number of receivers (denoted as Rx), N the number of antennas per receiver and M_f the number of frequency points. The following matrix definitions are used throughout the manuscript:

---

[1] In fact, using UL-DL duality properties, the different results can be directly translated to the UL [74, 131].

- $K = 1, N = 1, M = 1$: SISO Channel $\mathbf{h} \in \mathbb{C}^{1 \times M_f}$ (green).
- $K = 1, N > 1, M > 1$: SU-MIMO or point-to-point MIMO Channel $\mathbf{H} \in \mathbb{C}^{N \times M \times M_f}$ (red).
- $K > 1, N \geq 1, M > 1$: MU-MIMO Channel $\mathbf{H} \in \mathbb{C}^{KN \times M \times M_f}$ (orange).
- $K \gg 1, N \geq 1, M >> K$: Massive MIMO Channel defined hereafter (blue).

Note that the antenna array can be formed by M co-polarized elements (physical antennas) or $M/2$ dual-polarized elements (M logical ports or RF chain as defined in Ch. 1.4.2).

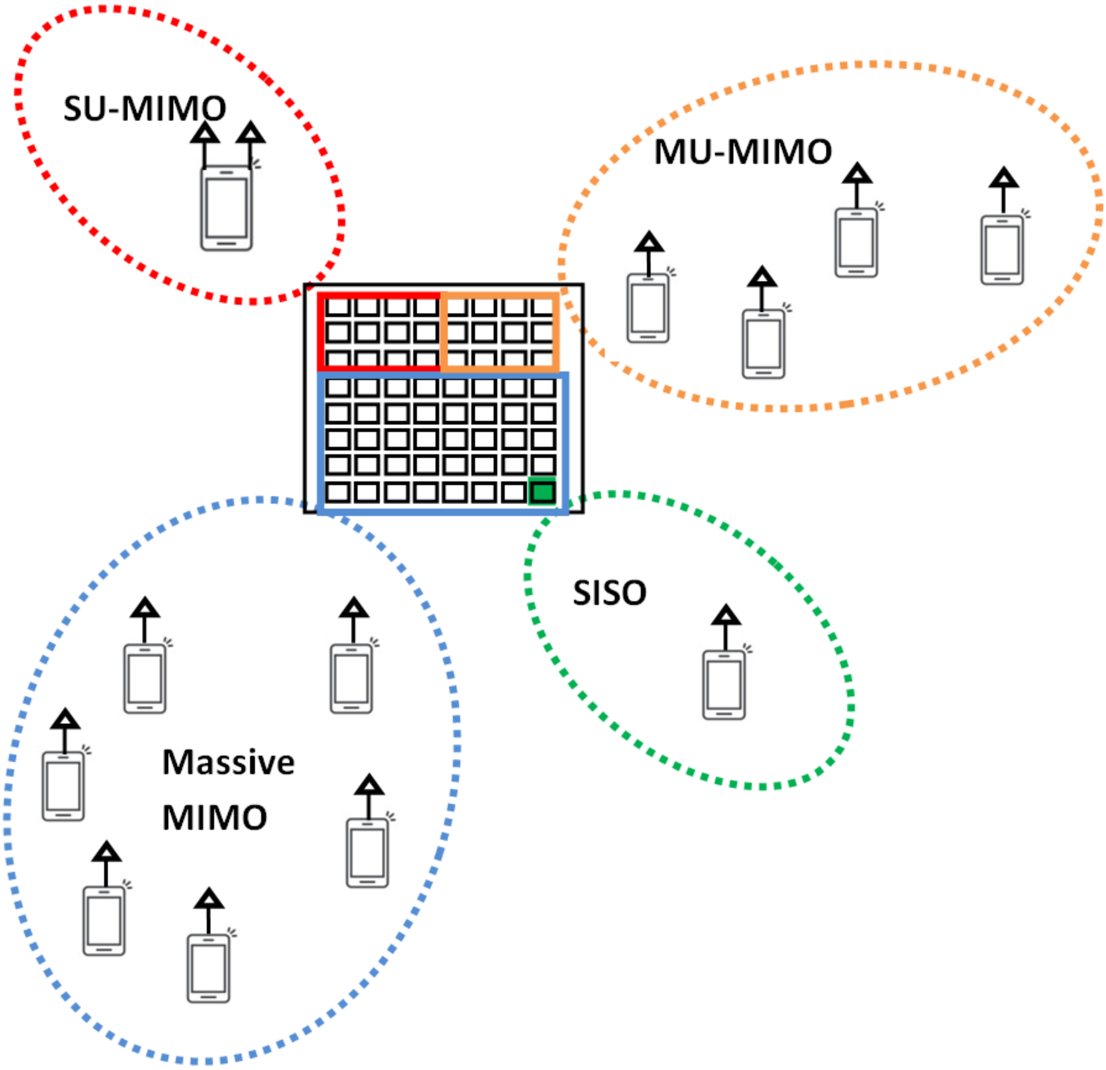

Figure 2.2: *Multiple Antennas Configurations: SISO, SU-MIMO, MU-MIMO and massive MIMO.*

For MU and massive MIMO systems, the particular case of $N = 1$ is considered. The massive MIMO channel matrix structure is a generalized MIMO matrix with K users. The channel between a single-antenna receiver and an M-antenna BS can be represented by an M-dimensional channel vector that contains the contributions of all M Tx elements: $\mathbf{h} \in \mathbb{C}^{1\times M\times M_f}$. The K SU channel vectors are concatenated to form the K$\times M \times M_f$ massive MIMO matrix. $\mathbf{H} = [\mathbf{h}_1, \mathbf{h}_2, ..., \mathbf{h}_K]$ as illustrated in Fig. 2.3 where the user channel vector $\mathbf{h}_{k,m} \in \mathbb{C}^{1\times M_f}$. If one time-frequency resource is considered, the subscript M_f is omitted and $\mathbf{h}_k \in \mathbb{C}^{1\times M}$.

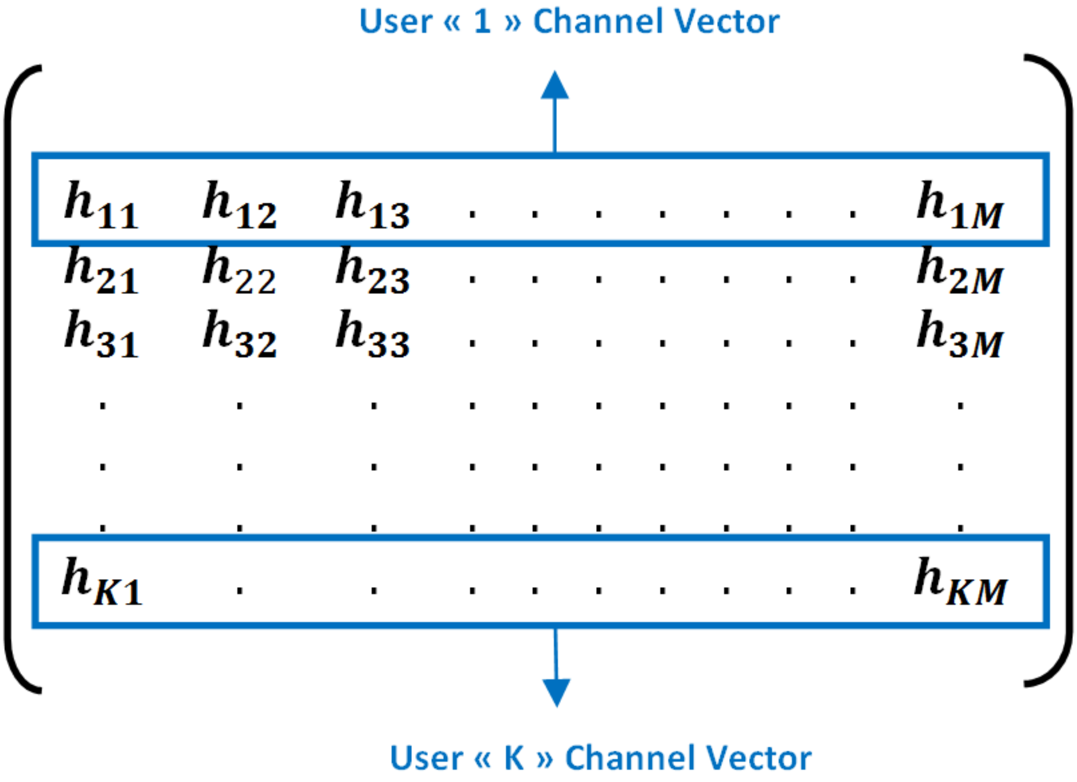

Figure 2.3: *Massive MIMO channel matrix with* $\mathbf{h}_{k,m} \in \mathbb{C}^{1\times M_f}$.

2.2.2 General Propagation Parameters

In this section, the different useful propagation metrics are introduced.

2.2.2.1 Average Channel Gain

The average channel gain for each Tx-Rx SISO link $\mathcal{G}$ is first computed in the bandwidth BW and is given by :

$$\mathcal{G} = \mathbb{E}\{|\mathbf{h}|^2\} = \frac{\|\mathbf{h}\|^2}{M_f}, \tag{2.9}$$

with the expectation operator applied over frequencies, unless otherwise indicated. This parameter is not specific to massive MIMO systems, but evaluates the strength of the signal. For multi-antenna systems, the channel gain is generally computed for each link :

$$\mathcal{G}_{k,m} = \mathbb{E}\{|\mathbf{h}_{k,m}|^2\}. \tag{2.10}$$

Extension to massive MIMO

However, one particularity for massive MIMO is the spatial variability of $\mathcal{G}_{k,m}$ over the antenna array with $k = 1, 2, ..., K$ and $m = 1, 2, ..., M$. This point will be discussed in Ch. 3.

2.2.2.2 Cross-Polarization Discrimination

As discussed in Ch. 1, polarimetric massive MIMO measurements are scarce in the literature. For such measurements, it is critical to characterize the channel depolarization effects to understand the different mechanisms impacting the system performance. Cross-polarization discrimination (XPD) is defined as the ratio between average channel gain in co-polarization mode to the average channel gain in cross-polarization mode and can be expressed as:

$$XPD(dB) = 10\log_{10}\left(\frac{\mathcal{G}^{co-polar}}{\mathcal{G}^{cross-polar}}\right). \tag{2.11}$$

Large XPD values indicate low depolarization in the scenario whilst small values indicate strong depolarization effects.

Extension to massive MIMO

Depolarization effects can provide an additional DoF for signals multiplexing. The advantages of polarization diversity associated with spatial multiplexing will be widely discussed in Ch. 3. For MU setups, XPD is computed for user k:

$$XPD_k(dB) = 10\log_{10}\left(\frac{\mathcal{G}_k^{co-polar}}{\mathcal{G}_k^{cross-polar}}\right). \tag{2.12}$$

2.2.2.3 Ricean Factor

In wireless communications, the Ricean factor K^{Rice} is identified as the ratio between the LOS power component and the sum of the powers of all the NLOS components [132, 133]. K^{Rice} is a useful metric for multipath propagation and channel classification. The relative strength of the dominant component and the rest of the N_{ray} received MPC is expressed as in [134]: .

$$K^{Rice}(\text{dB}) = 10\log_{10}\left(\frac{|h(\tau_m)|^2}{\sum_{i\neq m}^{N_{ray}}|h(\tau_i)|^2}\right), \tag{2.13}$$

where τ_m is the associated delay of the shortest path, τ_i is the delay of the i^{th} NLOS component. In [135], the author describes K^{Rice} as the ratio between the deterministic signal power and the variance of the MPC power and can be formulated as:

$$K^{Rice}(\mathrm{dB}) = 10\log_{10}\left(\frac{A^2}{2\sigma^2}\right), \tag{2.14}$$

with A the peak amplitude of the dominant signal and σ the variance of the MPC amplitude. As $A \to 0$, the dominant path decreases in amplitude and the Ricean distribution tends towards a Rayleigh distribution. The MLE (maximum-likelihood-estimator) extracts A and σ from the channel distributions [134], and its limitations are discussed in Appendix C.

<u>Extension to massive MIMO</u>

K^{Rice} is an insightful parameter when dealing with multiple receivers in different propagation conditions. A receiver in LOS would have a larger K^{Rice} value than partially or totally obstructed receivers. However, the computation of K^{Rice} is particularly challenging in massive MIMO systems because of the large array dimension [136]. The assumption of spatial stationarity could not be verified [137] leading to variability of K^{Rice} along the array.

2.2.2.4 Spatial Correlation

Correlation, a basic parameter for MIMO systems, is a measure of similarity between two vectors. The degree of correlation between antennas gives a good insight on the possibility of using spatial multiplexing or spatial diversity. Spatial correlation appears naturally in all communication systems, and using signal processing techniques, it can be used to enhance the overall capacity performance. Generally, spatially correlated users cause more inter-user interference. In massive MIMO, spatial correlation at Tx or Rx, was found to dictate the performance of the system. The correlation characteristics of the massive MIMO channel $\mathbf{H}$ are split into an analysis of the Rx inter-user correlation and Tx correlation per user.

Tx spatial correlation

The Tx correlation $\mathbf{R}_{Tx}$ (or intracorrelation) highlights the dependence between the channel coefficients for each user and provides information about the fading characteristics that could participate in the decorrelation process of the massive MIMO channel from the Tx side. It is reported in Ch. 4 that it is also a useful parameter for potential feedback reduction for channel acquisition techniques. $\mathbf{R}_{Tx,k}$ can be computed on the different frequency observations from the $M_f \times M$ matrix of user k denoted $\mathbf{H}_k$:

$$\mathbf{R}_{Tx,k} = \frac{\mathbb{E}\{\mathbf{H}_k^H \mathbf{H}_k\}}{\mathbb{E}\{|\mathbf{H}_k|^2\}}. \tag{2.15}$$

$\mathbf{R}_{Tx,k}$ results in a $M \times M$ matrix containing all the correlation coefficients between all Tx elements combinations. Taking $k = 1, ..., K$, the full channel correlation matrix $\mathbf{R}_{Tx}$ of size $K \times M \times M$ can be deduced.

Extension to massive MIMO

The distribution of the correlation values ρ_{Tx} of each Rx across array elements is a key aspect for parametric analysis, for scenario classification methods in Ch. 3 and for the proposed strategy to reduce feedback for CSI aspects in Ch. 4.

Rx spatial correlation

$\mathbf{R}_{Rx}$ (or intercorrelation) is the main metric to assess the performance of the massive MIMO system. It helps predicting the precoding matrix and its complexity as well as many signal processing techniques. The Rx spatial correlation properties highlight the capability of a massive MIMO system to simultaneously serve a number of users and thus give valuable insight on whether the propagation is favorable or not by evaluating the orthogonality between channel vectors. The receiving correlation matrix $\mathbf{R}_{Rx}^{m}$ computation for two special cases is shown:

1. **For any two users i and j**, the intercorrelation ρ_{ij} as a function of the number of antennas of a subset in the array M_t ($1 \leq M_t \leq M$) and for a given frequency $f \in [1...M_f]$, is given by:

   $$\rho_{ij}(M_t, f) = \frac{|\mathbf{h}_i \mathbf{h}_j^H|}{\|\mathbf{h}_i\| \|\mathbf{h}_j\|}. \tag{2.16}$$

   $\mathbf{h}_i$ and $\mathbf{h}_j$ are two channel vectors of user i and j respectively. It is possible to average on the different frequency observations.

2. **For all users and a fixed subset of M_t elements from the Tx array**. Considering one frequency sample, f, using the $K \times M_t$ matrix denoted $\mathbf{H}^t$, a general equation for the computation of the total spatial correlation matrix:

   $$\mathbf{R}_{Rx}^{t}(f) = \frac{\mathbb{E}\{\mathbf{H}^t \mathbf{H}^{t^H}\}}{\mathbb{E}\{|\mathbf{H}^t|^2\}}. \tag{2.17}$$

   Note that in this case, the expectation is over M_t and not M_f. When $M_t = M$ and after the averaging process on all samples, the correlation matrix will be denoted $\mathbf{R}_{Rx}$. The off-diagonal elements of the upper triangular part of $\mathbf{R}_{Rx}$ (because of Hermitian symmetry) contain all the correlation values between all receivers combinations as shown in Fig. 2.4 and as defined in Eq. 2.16.

   In order to represent the result of the operation in Eq. 2.17, a scalar value for $\mathbf{R}_{Rx}$ should be derived. A macroscopic Rx correlation coefficient ρ_{Rx} is deduced from $\mathbf{R}_{Rx}$ by averaging the off-diagonal upper triangular part of $\mathbf{R}_{Rx}$(values in the blue triangle of Fig. 2.4):

   $$\rho_{Rx}(M_t, f) = \frac{\sum_{i=1}^{K-1} \sum_{j=i+1}^{K} |\rho_{ij}|}{(K^2-K)/2}. \tag{2.18}$$

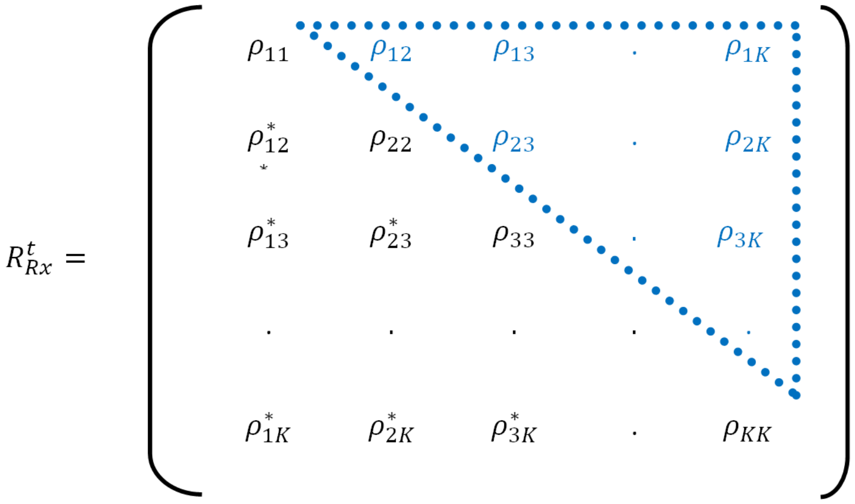

Figure 2.4: *Massive MIMO Spatial Receiver Correlation Matrix* $\mathbf{R}_{Rx}^{t}$.

It should be noted that ρ_{Rx} does not always reflect the correlation behavior (because of the averaging process) and should be analyzed carefully. When users have very different channel conditions (leading to different correlation values), it is more prudent to take the cumulative distribution function (CDF) of the values in $\mathbf{R}_{Rx}$.

3. **Asymptotic behavior**. In order to highlight the influence of an increasing M on the correlation properties in a massive MIMO system, the value of M_t (from Eq. 2.17) is varied between 1 and M.

Extension to massive MIMO

The Rx correlation will be widely used throughout the manuscript to evaluate the expected performance of a massive MIMO setup from a receiver point of view. It will also be shown that this parameter is a key factor for an antenna selection strategy proposed in Ch. 4 to reduce the number of RF chains in a massive MIMO system. Also, the definition in Eq. 2.16 can be used to illustrate the two pillars of massive MIMO system: (1) channel hardening and (2) favorable propagation condition as illustrated hereafter.

2.2.3 The Two Characteristics of Massive MIMO

The theoretical mathematical aspect of massive MIMO is based on the law of large numbers (very long random vectors [138]) and the theorem of Lindeberg-Levy. Let $\mathbf{h_i}$ and $\mathbf{h_j}$ be two mutually independent $1 \times M$ channel vectors whose elements are zero-mean random variables with σ_i^2, σ_j^2 their corresponding variances. For a SU case, channel hardening can be mathematically illustrated as:

$$\frac{1}{M}(\mathbf{h}_i\mathbf{h}_i^H) \overset{a.s.}{\rightarrow} \sigma_i^2 \quad as\ M \rightarrow \infty. \tag{2.19}$$

And favorable propagation for two users:

$$\frac{1}{M}(\mathbf{h}_i\mathbf{h}_j^H) \overset{a.s.}{\rightarrow} 0 \quad as\ M \rightarrow \infty. \tag{2.20}$$

where $\overset{a.s.}{\rightarrow}$ denotes almost sure convergence. Eq. 2.20 shows that the two vectors become orthogonal as the number M increases.

Finally, from the Lindeberg-Levy central theorem :

$$\frac{1}{\sqrt{M}}\mathbf{h_i h_j^H} \overset{\mathrm{d}}{\rightarrow} \mathcal{N}_{\mathbb{C}}(0, \sigma_i^2\sigma_j^2) \ \ as\ M \rightarrow \infty, \tag{2.21}$$

where $\overset{\mathrm{d}}{\rightarrow}$ denotes convergence of distribution.

2.2.3.1 Channel Hardening

One of the main impairments in wireless propagation is small-scale fading causing random fluctuations in the channel gain over a brief period of time (as opposed to large-scale fading). These fluctuations render the channel non-deterministic and CSI estimation becomes more challenging. This aspect is well-known in wireless communications and fading mitigation techniques have been proposed, for instance in CDMA[2] communications using a compact array receiver to provide space diversity gain [139]. With massive MIMO, fast fading is naturally reduced similarly to traditional spatial diversity schemes [140]. With M antennas, the probability of getting a deep fade is p^M where p is the probability of getting a deep fade with a single antenna system. This corresponds to channel hardening. It naturally leads to improved reliability when M increases resulting in lower latency and alleviating the need for DL pilots in massive MIMO TDD schemes [67, 123, 124]. Massive MIMO channel measurements have confirmed the channel hardening effect as shown in [141, 142]. Note that, on the contrary of favorable propagation condition, channel hardening can be evaluated for a SU scenario. Given a user channel vector, the average received gain at user k when M antennas are transmitting converges to a deterministic value denoted β_k, the large-scale coefficient. Mathematically, for a given observation, it can be written for user k as:

$$\frac{\|\mathbf{h}_k\|^2}{M} \overset{a.s.}{\rightarrow} \beta_k\ as\ M \rightarrow \infty. \tag{2.22}$$

Eq. 2.22 shows that channel variations are reduced when more antennas are added .

---

[2] Code division multiple access

2.2.3.2 Favorable Propagation Condition

To analyze the favorable propagation condition, the joint behavior of K channel vectors $\mathbf{h} \in \mathbb{C}^{1\times M}$ should be considered. When channel vectors become pairwise orthogonal, the effect of MU-interference and noise can be eliminated with simple techniques [143, 144, 145]. The ultimate favorite propagation condition occurs for two users when $\mathbf{h_i h_j^H} = 0$. This makes the directions of the two channels orthogonal. In this case, the BS can completely separate signals s_i and s_j. Generally, this condition is very hard to satisfy and asymptotically favorable propagation [67] is used instead as illustrated in Eq. 2.20. For any two user channel vectors, the channel directions $\frac{\mathbf{h}_i}{\sqrt{\|\mathbf{h}_i\|^2}}$ and $\frac{\mathbf{h}_j}{\sqrt{\|\mathbf{h}_j\|^2}}$ become asymptotically orthogonal. This is a consequence of the law of large numbers, a direct proof being provided in [67].

2.2.4 The Gram Matrix

In Fig. 2.5, the advantages of increasing the number of Tx elements is displayed in a simple way. The module of the elements of $\mathbf{G}$ defined as the product $\mathbf{HH}^H$ is presented, normalized with respect to the largest value of $\mathbf{G}$ in order to obtain values between 0 and 1. K is fixed to 8 and M is chosen to be 4, 16, 32 and 64.

Massive MIMO leads to two important aspects cleared from the analysis of the Gram matrix $\mathbf{G}$: (1) the diagonal elements converge to deterministic constants β_k proving *channel hardening* and (2) the off-diagonal elements converge to 0 proving *favorable propagation condition.* Values close to one (after normalization) on the diagonal indicate the channel is well-conditioned amongst the different receivers. Off-diagonal element values close to 0 provide further insight on the degree of separation between the different users and indicate good orthogonality between channel vectors. It can be seen that when increasing M, not only inter-user interference is reduced, but also channel gains (diagonal elements) converge to a deterministic value, in this case, $\sigma^2 = 1$. In summary, for i.i.d. user channels, when M increases, inter-user interference vanishes, and simultaneous transmission is potentially achieved using linear precoding schemes.

2.2.4.1 Gram's matrix Power Ratio

Gram's matrix power ratio is the ratio between the intended power for user k and the total power. It indicates the percentage of received interference from different users. From the $K \times K$ Gram matrix $\mathbf{G}$, the ratio $\gamma(\mathbf{G})$ for user k can be formulated as :

$$\gamma_k(\mathbf{G}) = \frac{|g_{k,k}|^2}{\sum_{j=1}^{K} |g_{k,j}|^2}. \tag{2.23}$$

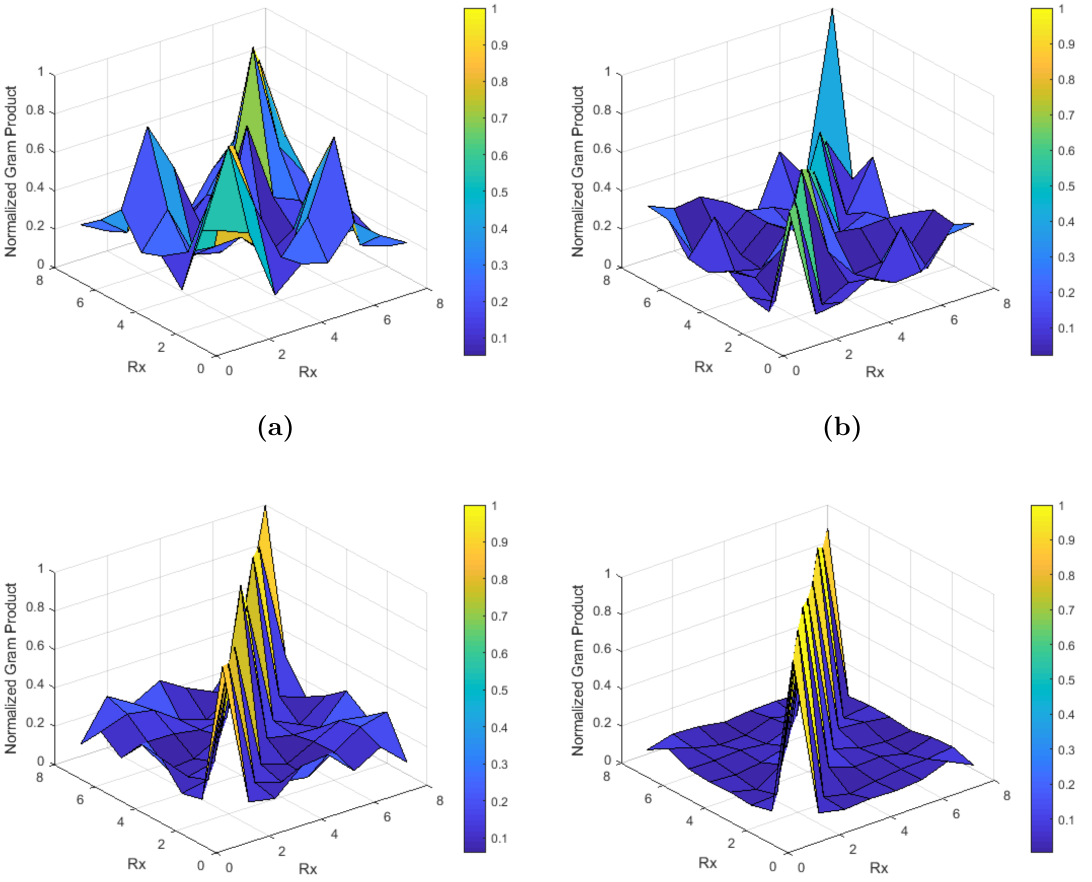

(a) **(b)**

(c) **(d)**

Figure 2.5: *Gram Product for* $K = 8$ *and a)* $M = 4$*, b)*$M = 16$*, c)* $M = 32$*, d)* $M = 64$ *and 1000 observations are considered for the averaging.*

This can be further generalized to obtain a single value or matrix power ratio by averaging over all K users[3]. Values vary between 1 (very good separation) to 0 (highly correlated users).

2.3 Massive MIMO Channel Model

In order to evaluate the performance of a massive MIMO system, channel models that reflect propagation characteristics are essential. However, standardized massive MIMO channel models are still not available. A review of channel model shows that two main types of channel models are considered: correlation-based stochastic models and geometry-based stochastic models (2D and 3D). The former regroups

---

[3] This should be carefully done to avoid misinterpretation of results due to the averaging process.

i.i.d. channels and Kronecker-based model and have been used to provide theoretical performance analysis for massive MIMO. However, its accuracy is limited especially when modeling non-stationary phenomenon. The latter regroups accurate COST and WINNER models but at the expense of higher computational complexity. A thorough survey on massive MIMO channel models is available in [146] and references therein. Performance comparison of preliminary massive MIMO channel models is also available in [147, 148]. In order to evaluate the impact of massive MIMO channel characteristics on system performance aspects, we will focus on geometrical channel models, from which massive MIMO correlation properties can be determined.

2.3.1 Review of Correlation-based Channel Models

Correlated channel models (also referred to as Kronecker-based stochastic models KBSM) are popular for performance analysis of massive MIMO systems [149]-[150] due to their simplicity and consideration on spatial correlations. The total correlation matrix is derived using the Kronecker product of the spatial correlation matrices at both Tx and Rx [133]. However, this model relies on WSS assumption and that both Tx and Rx correlation matrices are independent which is not always true. The general system model is presented in Eq. 2.24:

$$\mathbf{H}_{kron} = \mathbf{R}_{Rx}^{1/2}\mathbf{H}_{iid}\mathbf{R}_{Tx}^{1/2}, \tag{2.24}$$

with $\mathbf{R}_{Rx}$, the $K \times K$ Rx correlation matrix and $\mathbf{R}_{Tx}$, the $M \times M$ Tx correlation matrix. This model is suitable for local point-to-point SU-MIMO where $\mathbf{R}_{Tx}$ is supposed constant. $\mathbf{R}_{Tx}$ is generally a Toeplitz matrix defined in LTE [151] for a 4-element ULA as:

$$\mathbf{R}_{Tx} = \begin{bmatrix} 1 & \rho^{1/9} & \rho^{4/9} & \rho \\ \vdots & \ddots & \ddots & \vdots \\ \rho & \dots & \dots & \end{bmatrix}, \tag{2.25}$$

with ρ the correlation factor for element separation $3\lambda/2$. However, this model is adapted to specific scenarios and for ULA. As massive MIMO systems are mostly URA-based, $\mathbf{R}_{Tx}$ can be determined from canonical geometrical channel models discussed hereafter.

2.3.2 Geometrical based Propagation Channel Model

The proposed model is based on the Ricean channel model developed for SU-MIMO. The propagation channel is composed of the sum of two contributions corresponding to the LOS and NLOS components associated to a plane wave and the sum of N_{ray} plane waves, respectively. Each plane wave impinging the URA of size $M_x \times M_y$ is characterized by its complex amplitude a, angle of arrival (AoA) and delay. By introducing the Ricean factor for each user k, K_k^{Rice} (defined in Sec. 2.2.2.3),

$\mathbf{H}_k(Mx, My)$ can be expressed for the k^{th} user and at frequency f as:

$$\mathbf{H}_k = \sqrt{\frac{K_k^{Rice}}{K_k^{Rice}+1}} \frac{\sqrt{M_x M_y}\mathbf{H}_{LOS,k}}{\|\mathbf{H}_{LOS,k}\|_F} + \sqrt{\frac{1}{K_k^{Rice}+1}} \frac{\sqrt{M_x M_y}\mathbf{H}_{NLOS,k}}{\|\mathbf{H}_{NLOS,k}\|_F}. \tag{2.26}$$

The amplitude of the LOS component is drawn from a Rayleigh distribution. If the LOS component is normalized to 1, $\mathbf{H}_{LOS,k}$ is given by the steering matrix of the URA whose elements $h_{m_x,m_y}(f)$ are the phases of the plane wave impinging the array element m_x, m_y with an angle (θ, ϕ), the phase reference being defined at element $(0,0)$:

$$h_{m_x,m_y}^{LOS}(f) = \exp\left(-2\pi j \frac{d_i}{\lambda}[(m_x-1)\sin\theta\cos\phi + (m_y-1)\sin\theta\sin\phi]\right).\exp\left(-2\pi j f \tau_i\right). \tag{2.27}$$

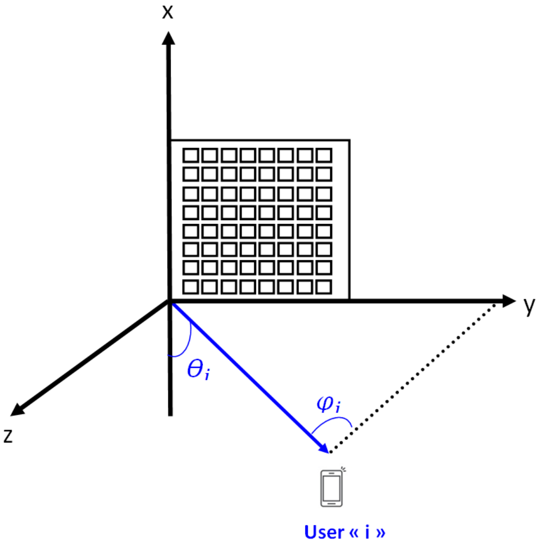

Figure 2.6: *Steering vector with elevation θ and azimuth angle ϕ.*

In the proposed geometrical model, θ and ϕ, the elevation and azimuth angle of the plane wave, are randomly chosen in a uniform distribution within the interval $[\theta_{min}\ \theta_{max}]$, and $[\phi_{min}\ \phi_{max}]$, respectively. These distributions can also be characterized by the elevation and azimuth angular intervals $\Delta\theta$ and $\Delta\phi$, respectively. In Eq. 2.27, d_i is the antenna spacing, f the frequency, λ the wavelength and τ_i is the absolute delay of the LOS component. The elements of $\mathbf{H}_{NLOS,k}$ are easily deduced from Eq. 2.27 and are given by:

$$h_{m_x,m_y}^{NLOS}(f) = \\ \sum_{i=1}^{N_{ray}} a_i^{NLOS} \exp\left(-2\pi j \frac{d_i}{\lambda}[(m_x-1)\sin\theta_i\cos\phi_i + (m_y-1)\sin\theta_i\sin\phi_i]\right).\exp\left(-2\pi j f \tau_i\right). \tag{2.28}$$

In this formula, a_i^{NLOS} is the complex amplitude of the plane wave i, normalized to the amplitude of the LOS component (chosen equal to 1). In the following, a vectorization of the $\mathbf{H}_k$ matrix is applied, leading to a $1 \times M$ vector with $M = M_x \times M_y$. This approach can be generalized to any number of users K, with the channel vector corresponding to the k^{th} user: $\mathbf{h}_k = vec(\mathbf{H}_k)^T$. The total massive MIMO channel is constructed as indicated in Fig. 2.3 after vectorization of all URA user channel matrices. For K users, K channel vectors are concatenated to form the $K \times M$ full massive MIMO channel matrix $\mathbf{H}$ at frequency f:

$$\mathbf{H}(f) = [\mathbf{h}_1(f) \;\; \mathbf{h}_2(f) \;\; ... \;\; \mathbf{h}_K(f)]. \tag{2.29}$$

For $f = 1, ..., M_f$, the full $K \times M \times M_f$ channel can be constructed (normalizing with respect to frequency as well). This geometrical model can be used to simulate various scenarios where the users are partly or not, collocated or distributed. Note that collocated users correspond to the worst scenario due to strong correlation between users which is still a challenging problem in the context of massive MIMO. Depending on the geometrical configuration of the environment and on the relative position of the Tx and Rx antennas to the obstacles, the various parameters in the model can be adequately tuned as, for example, the interval of the AoA of the waves impinging Rx, the number of rays and K^{Rice}. Note that N_{obs} channel realizations can be performed but the subscript is dropped for simplicity. The proposed channel model was validated using measurements from Ch. 3 and the results are reported in Appendix D.

2.3.2.1 Special Case: Rayleigh Channel Model

The uncorrelated Rayleigh channel, widely used as a canonical model for massive MIMO, is obtained from Eq. 2.26 when $K^{Rice} = 0$. This model is attractive because closed-form expressions can be computed for capacity, bit-error-rate, etc. It can also be categorized as a NLOS case where the the normalized channel vectors are uniformly distributed over the unit sphere.

2.3.2.2 Improving Stochastic Models

For MU and massive MIMO setups, each user, depending on its propagation condition (LOS, NLOS, or obstructed LOS), can have a distinct correlation matrix. To this purpose, $\mathbf{R}_{Tx,k}$ for the k^{th} user should be accounted for in the model in Eq. 2.24. Also, analytical definitions for $\mathbf{R}_{Rx}$ and $\mathbf{R}_{Tx}$ are either based on statistical distributions as indicated in [152] or analytical expressions that can be cumbersome. It appears the best approach to tune stochastic models and improve their accuracy would be to compute these correlation matrices from the geometrical model. However, this part is outside the scope of the manuscript.

2.3.3 Parametric Analysis

Using the established channel model in Eq. 2.26, a parametric analysis is applied and results validating the proposed approach are presented. To this purpose, two different aspects of the massive MIMO channel are verified: (1) channel hardening effect for a SU scenario and (2) favorable propagation condition for a MU setup using Gram's matrix power ratio. The different parameters used for each simulation are listed each time in a table. M, N_{ray} and N_{obs} are fixed to 100, 13 and 500, respectively, for all simulations.

2.3.3.1 Channel Hardening

Referring to Eq. 2.26, the effect of K^{Rice} is evaluated. Figure 2.7 shows the standard deviation σ, for $K = 1$ using different K^{Rice} values.

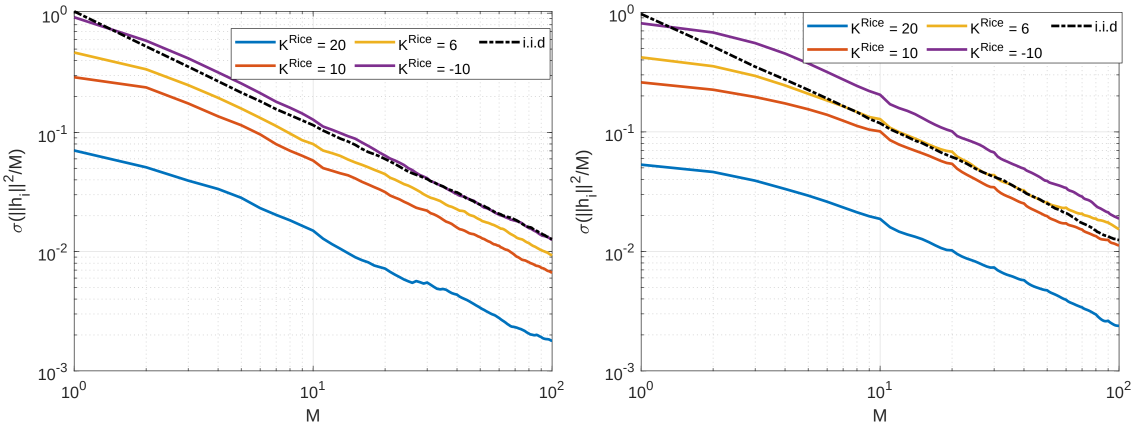

(a) **(b)**

Figure 2.7: *Influence of K^{Rice} on Channel Hardening for (a) $(\Delta\theta, \Delta\phi) = (30^o, 30^o)$ and (b) $(\Delta\theta, \Delta\phi) = (60^o, 60^o)$.*

Table 2.1 summarizes the channel model parameters, the Tx correlation $\rho_{Tx,3\lambda/2}$ being deduced from $\mathbf{R}_{Tx}$ for an element separation of $3\lambda/2$ and can be found in the charts in Appendix D.

Table 2.1: *Model parameters for channel hardening simulations.*

$(\Delta\theta,\Delta\phi)$	K^{Rice}	$\rho_{Tx,3\lambda/2}$
$(30^o, 30^o)$	[20 10 6 -10]	[0.93, 0.90,0.88,0.67]
$(60^o, 60^o)$	[20 10 6 -10]	[0.85, 0.79 , 0.75, 0.31]

The values of the channel gain standard deviation decrease with M for all cases indicating channel hardening effect in massive MIMO. For $M = 100$, the smallest value of σ (0.001) is observed for $K^{Rice} = 20$ dB and $(\Delta\theta,\Delta\phi) = (30^o,\ 30^o)$. This value increases with K^{Rice} and reaches 0.01 for the i.i.d. case. It also increases when $(\Delta\theta,\ \Delta\phi)$ increases. For $K^{Rice} = 6$ dB, $\sigma = 0.009$ when $(\Delta\theta,\ \Delta\phi) = (30^o,\ 30^o)$ and $\sigma = 0.015$ (higher than i.i.d.) when $(\Delta\theta,\ \Delta\phi) = (60^o,\ 60^o)$. It can be concluded that the channel gain standard deviation decreases when K^{Rice} increases and thus when $\rho_{Tx,3\lambda/2}$ increases. This indicates that strong Ricean channels and highly correlated Tx elements are both favorable for channel hardening. This is expected since strong K^{Rice} generally implies a dominant LOS component whose value is more deterministic than NLOS components, thus generating less variability in channel gain.

2.3.3.2 Gram's Power Ratio

The average Gram's power ratio as a function of the number of antennas M is presented for different K^{Rice} values in Fig. 2.8(a), for different angles in (b) and compared for LOS, NLOS and mixed LOS/NLOS scenario in (c). Table 2.2 summarizes the channel model parameters for this scenario, the Rx correlation being deduced from the charts in Appendix D.

Table 2.2: *Model parameters for favorable propagation conditions simulation.*

K	**$(\Delta\theta,\Delta\phi)$**	K^{Rice}	$\rho_{Tx,3\lambda/2}$	ρ_{Rx}
12	$(60^o, 60^o)$	[10 6 0 -10]	[0.8, 0.74, 0.53, 0.31]	[0.81,0.69,0.46, 0.26]
12	$([60^o, 60^o, 30^o],[120^o, 60^o, 30^o]\ )$	-10	[0.29, 0.31, 0.59]	[0.18, 0.26,0.41]
6/6	$60^o, 60^o$	[6/-10]	0.73/0.35	0.46

Similarly to channel hardening, increasing M leads to better power ratios. Nonetheless, from Fig. 2.8(a) it is observed that for $K^{Rice} = -10$ dB, $\gamma(\mathbf{G})$ reaches ∼60% and only ∼20% for $K^{Rice} = 10$ dB. Figure 2.8(b) shows that $\gamma(\mathbf{G})$ is closer to i.i.d. (80%) for $(\Delta\theta, \Delta\phi) =(60^o, 120^o)$ and $K^{Rice} = -10$ dB compared to $(\Delta\theta, \Delta\phi) = (60^o, 60^o)$ and $(\Delta\theta, \Delta\phi) = (30^o, 30^o)$ where $\gamma(\mathbf{G})$=60% and 30%, respectively. Also, when the angular interval increases and K^{Rice} decreases, correlation values at both Tx and Rx are very small, similar to what is generally found in the uncorrelated i.i.d. case.

These parameters are inter-dependant and affect the general behavior of channel characteristics. Channels with similar characteristics than i.i.d. (small correlation values) present higher power ratio values. Finally, from Fig. 2.8, adding UEs with strong K^{Rice} decreases $\gamma(\mathbf{G})$ (40%) compared to UEs with small K^{Rice} (60%) but larger than scenarios where UEs have strong K^{Rice} (25%). As opposed to channel hardening, favorable propagation condition is mostly satisfied for small K^{Rice} and large angular intervals, meaning more diversity and leading to strong decorrelations at both Tx and Rx side. This does not mean that channels are either favorable or harden, since correlated channels with strong K^{Rice} still harden without necessarily having favorable propagation condition and vice-versa.

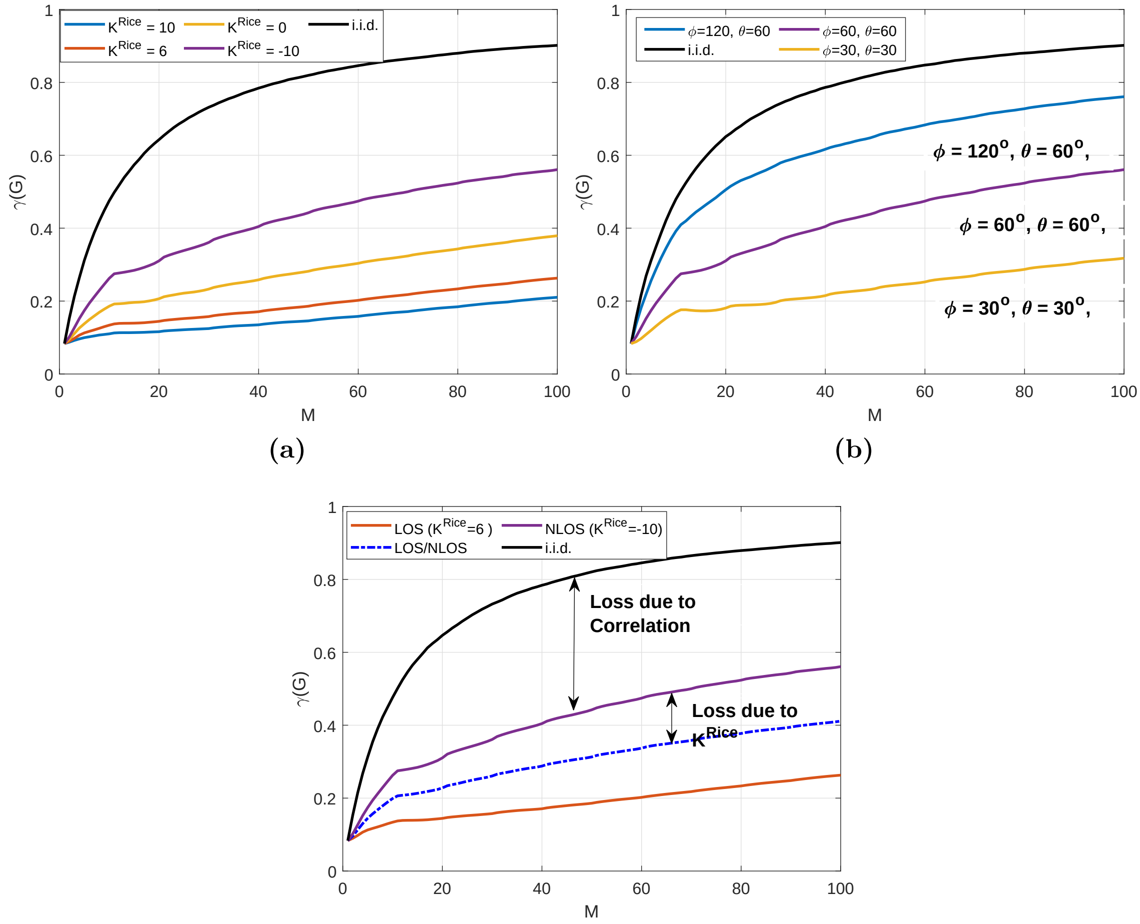

(a) **(b)**

(c)

Figure 2.8: *Impact of (a) K^{Rice} and (b) $(\Delta\theta,\Delta\phi)$ on Gram's power ratio. (c) Comparison between LOS, NLOS and LOS/NLOS scenarios.*

2.4 System Model for DL Massive MIMO

In this section, the widely used system model for DL massive MIMO case studies is presented. The standard MIMO system model is a special case of massive MIMO scenario with $K = 1$ and N the number of receive antennas. Perfect channel knowledge is assumed for the computation of the capacity of MIMO channels and sum-rate capacity for MU-cases.

Here, K users with $N = 1$ are simultaneously served from the M-element array BS. Let $\mathbf{x} \in \mathbb{C}^{M\times 1}$ the transmitted signal vector from the BS antenna array to the intended K users. The channel can be described as flat-band at each subcarrier or frequency point. The received signal at user k is given by:

$$y_k = \mathbf{h}_k\mathbf{x} + n_k, \tag{2.30}$$

where y_k is the received DL signal for user k, $\mathbf{H}$ is the composite $K \times M$ channel matrix and $\mathbf{h}_k \in \mathbb{C}^{1\times M}$ is the k^{th} complex raw vector of $\mathbf{H}$ from the M BS antennas to the k^{th} user. n_k is the noise for user $k \sim \mathbb{C}\mathcal{N}(0, \sigma^2)$. $\mathbf{x}$ contains a precoded version of the $K \times 1$ data symbol vector (payload symbol) and given by:

$$\mathbf{x} = \mathbf{W}\sqrt{\mathbf{P}}\mathbf{s}, \tag{2.31}$$

where $\mathbf{s}$ is the $K \times 1$ data symbol row vector with unit energy ($\mathbb{E}\{\mathbf{s}\mathbf{s}^H\} = 1$):

$$\mathbf{s} = [s_1, s_2, ..., s_K]^T. \tag{2.32}$$

$\mathbf{P}$ is a diagonal matrix with elements p_k $(k = 1, 2, ..K)$ and describes the transmit power allocated to a particular user k and depends on the applied strategy discussed later. $\mathbf{W}$ is the $M \times K$ precoding matrix formed by the beamforming vectors for each user $\mathbf{W} = [\mathbf{w}_1, \mathbf{w}_2, ..., \mathbf{w}_K]$ detailed later. $\mathbf{W}$ is normalized to satisfy the power constraint $\mathbb{E}\{\mathbf{x}\mathbf{x}^H\} = 1$:

$$\mathbf{W} = \frac{\tilde{\mathbf{W}}}{\sqrt{\mathbb{E}\{tr(\tilde{\mathbf{W}}\tilde{\mathbf{W}}^H)\}}}, \tag{2.33}$$

with $\tilde{\mathbf{W}}$ the non-normalized version of $\mathbf{W}$.
It should be noted that when both $\mathbf{x}$ and $\mathbf{n}$ have unit power, p_k can be interpreted as average transmit signal to noise ratio (SNR). Eq. (2.30) can be rewritten to explicitly highlight the interference between the different users:

$$y_k = \sqrt{p_k}\mathbf{h}_k\mathbf{w}_k s_k + \sum_{i=1,\ i\neq k}^{K} \sqrt{p_i}\mathbf{h}_k\mathbf{w}_i s_i + n_k, \tag{2.34}$$

The first part of the equation is the desired part of the signal for the k^{th} user and the second part shows the interference from other users as well as the noise. From this definition, the system performance metrics such as $SINR$ (signal to interference and noise ratio) can be defined. A block diagram of the DL massive MIMO system is provided in Fig. 2.9

2.4.1 System performance: Capacity of MIMO systems

MIMO technology improves the capacity of the communication link without increasing transmission power. Improvements depend largely on the propagation environment. In a SU scenario, capacity is a useful metric and gives the maximum amount of data information that can be transmitted as a function of the available bandwidth given a power constraint [153]. It is measured in bits/s/Hz or bps/Hz. In the following, we provide a theoretical background on the capacity of MIMO channels and then extend the discussion for MU setups and massive MIMO systems.

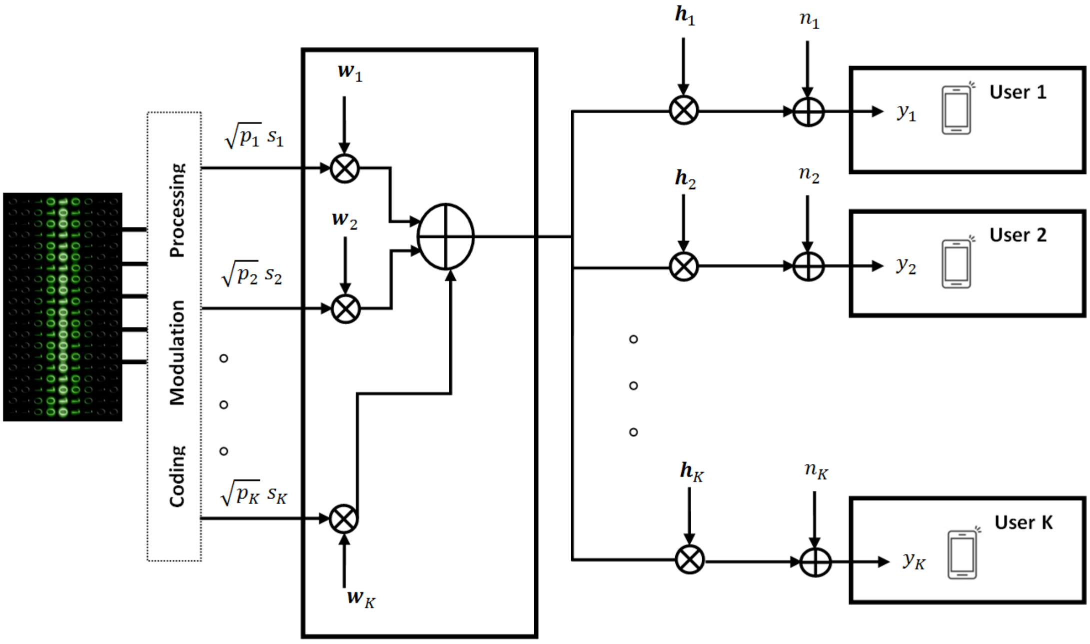

Figure 2.9: *Block Diagram of the Massive MIMO DL System.*

2.4.1.1 Capacity of SU-MIMO

Mutual information capacity between input $\mathbf{x}$ and output $\mathbf{y}$ is written for a SU-MIMO system (with N, M receiving and transmitting antennas, respectively as in [42]:

$$\mathcal{I}(\mathbf{x};\mathbf{y}) = \log_2 \det[\mathbf{I}_N + \mathbf{H}\mathbf{Q}\mathbf{H}^{\mathbf{H}}] = \log_2 \det[\mathbf{I}_M + \mathbf{Q}\mathbf{H}^{\mathbf{H}}\mathbf{H}], \tag{2.35}$$

where the second equality follows from Sylvester's determinant identity ($\det(I+AB) = \det(I+BA)$). $\mathbf{Q}$ is the $M \times M$ positive definite input covariance matrix ($Tr(\mathbf{Q}) = \mathbb{E}\{\mathbf{x}\mathbf{x}^H\} \leq P$) with $\mathbf{x}$ the input signals and P the total transmitted power. $\mathcal{I}(\mathbf{x};\mathbf{y})$ can be referred to as $C(\mathbf{H},\mathbf{Q})$ and will be more simply denoted as $C(\mathbf{H})$ due to perfect channel knowledge assumption.

In Fig. 2.10, the capacity of $\mathbf{H}$ is presented as a function of the SNR for normalized i.i.d. channels and different N and M values. Here, equal power allocation is used with MRT (presented later).

2.4.2 Capacity of MU-MIMO

SU-MIMO systems are a special case of MU-MIMO channels where $K=1$. In MU systems, we assume K users with potentially one antenna ($N=1$). For this reason, in MU-MIMO scenarios, the capacity/user, the users mean capacity or the sum-rate capacity are common used terms. The latter is widely used because it provides an insight on the total reachable performance for all users in a given scenario. From

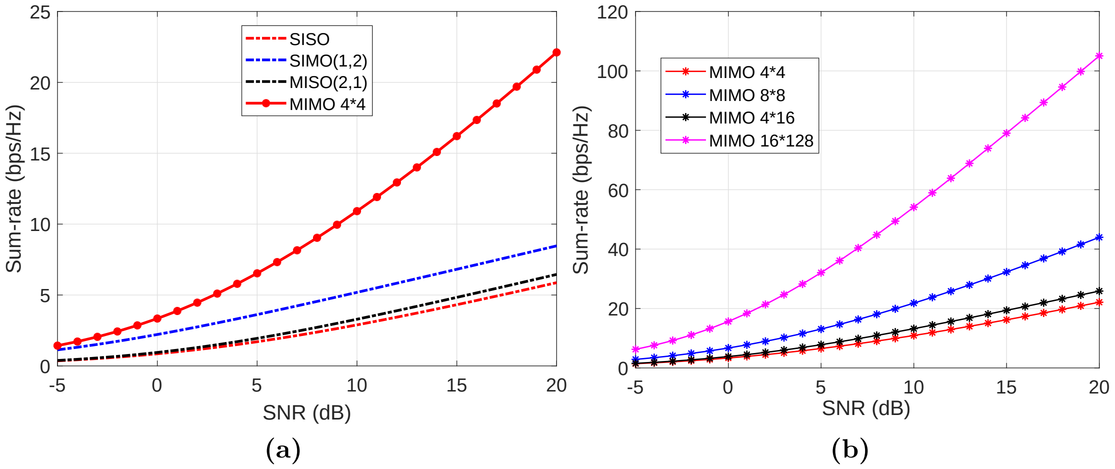

Figure 2.10: *(a) $C(\mathbf{H})$ of SISO, MISO, SIMO, 4×4 MIMO and (b) $C(\mathbf{H})$ for different MIMO configurations in i.i.d. channels.*

a pure mathematical point of view, Eq. 2.35 is valid for MU and massive MIMO scenarios. For the K-user case, we consider capacity bounds :

- Capacity bound per user:

$$C_k \leq \log_2 \left(1 + \frac{p_k}{\sigma_n^2} \|\mathbf{h}_k\|^2 \right). \tag{2.36}$$

- Sum-rate capacity

$$C = \sum_{k=1}^{K} C_k \leq \log_2 \det \left(\mathbf{I}_K + \sum_{k=1}^{K} \frac{p_k}{\sigma_n^2} \|\mathbf{h}_k\|^2 \right). \tag{2.37}$$

These bounds define the capacity regions for MU-scenarios. In order to reach these bounds and optimize the overall capacity, power allocation techniques and precoding schemes (for interference management) are needed.

2.4.2.1 Power Allocation

In order to maximize the sum-capacity, $\mathbf{Q}$ should be chosen to maximize $\mathcal{I}(\mathbf{x}; \mathbf{y})$. This optimization problem is illustrated as in [154]:

$$C(\mathbf{H}) = \max_{\mathbf{Q}} \log_2 \det[\mathbf{I}_K + \rho \mathbf{H}\mathbf{Q}\mathbf{H}^{\mathbf{H}}], \tag{2.38}$$

with $\mathbf{Q} \geq 0$ and $Tr\{\mathbf{Q}\} = 1$ here and $\rho = \frac{P}{\sigma_n^2}$ is the SNR. In a non-optimal equal power allocation scheme over all transmit antennas M, $\mathbf{Q} = \frac{\mathbf{I}_M}{M}$. The sum-capacity in Eq. 2.38 can be achieved using the dirty-paper coding technique in the DL and

SIC (successive interference cancellation) for the UL. In order to obtain the optimum covariance matrix denoted $\tilde{\mathbf{Q}}$ the transmission is decoupled along individual channel modes forming K parallel data streams (or data pipes) in the directions of the singular vectors of $\mathbf{H}$ at both Tx and Rx side. A vital requirement to accomplish this task is finding the optimal power allocation $\{p_1^*, ..., p_{min(K,M)*}\}$ across these modes and express $\tilde{\mathbf{Q}}$ under the following form:

$$\tilde{\mathbf{Q}} = \mathbf{V}\ diag\{\tilde{p}_1, ..., \tilde{p}_{min(K,M)}\}\mathbf{V}^H, \tag{2.39}$$

where $\mathbf{V}$ is given by the SVD of $\mathbf{H}$:

$$\mathbf{H} = \mathbf{USV}^H, \tag{2.40}$$

and $\mathbf{S} = diag\{\sigma_1, ..., \sigma_{min(K,M)}\}$. The diagonal entries of $\mathbf{S}$ are the singular values of $\mathbf{H}$. Also, $\sigma_k^2 = \lambda_k(\mathbf{G})$ with $\mathbf{G} = \mathbf{HH}^H$ for $K > M$. Eq. 2.38 becomes:

$$C(\mathbf{H}) = \max_{p_k} \sum_{k=1}^{min(K,M)} \log_2[1 + \rho p_k \lambda_k]. \tag{2.41}$$

Considering optimal power allocation from the power-constrained maximization given by the waterfilling algorithm [42, 155, 156, 154], Eq. 2.41 can be written such as:

$$C(\mathbf{H}) = \sum_{k=1}^{min(K,M)} \log_2[1 + \rho \tilde{p}_k \lambda_k], \tag{2.42}$$

with $\{\tilde{p}_1, .., \tilde{p}_{min(K,M)}\}$, the vector of optimal power allocation. This technique is applicable for MIMO systems as well as for MU-MIMO systems. Generally, equal power allocation is applied when no CSIT is available and waterfilling is possible only under the assumption of CSIT.

2.4.2.2 Precoding Strategies

Power allocation as mentioned before is important for capacity optimization but not sufficient when the channel suffers from inter-user interference. Hence, precoding is a necessary step in a MU setups to separate data streams while minimizing inter-user interference as much as possible. Different precoders will be discussed in the next section, their characteristics and particularities. The transmitted signal from M antennas is a linear combination of the symbols intended to the K users (consists in a superposition of multiple beams corresponding to multiple data streams using spatial multiplexing). In the DL, DPC is optimal because it achieves the maximum sum-rate capacity [157]. However, DPC requires high computational power and complexity, two factors to avoid when implementing massive MIMO systems. To that purpose, linear schemes such as Matched Filtering also known as MRT, ZF or MMSE are used due to their simplicity. Linear detection in the UL is similar to linear precoding in the DL [158]. A comparison is established in [159].

2.4.2.3 Maximum-Ratio-Transmission

The objective of MRT is to maximize the receive SNR at each user. It can be obtained by solving the optimization problem illustrated in [159] and the solution is given by the Hermitian transpose of the channel matrix:

$$\mathbf{W}_{MF} = \mathbf{H}^{H}. \tag{2.43}$$

This solution shows a maximized receive signal for the k^{th} user, but also the existence of cross-talk.

- Advantages: simple signal processing, achieves the array gain of a SU system at low SNR when interference is limited.
- Challenges: Performs poorly when correlation between users is high and should be treated with caution at high SNR to avoid high inter-user interference.

2.4.2.4 Zero-Forcing

By contrast to MRT, ZF precoder aims at nulling out inter-user interference but neglects the effect of noise. The optimization problem [157] searches for $\mathbf{W}$ that completely removes cross-talk while maintaining minimum transmit energy. The solution is the Moore-Penrose pseudoinverse of the channel :

$$\mathbf{W}_{ZF} = \mathbf{H}^{\dagger} = \mathbf{H}^{H}(\mathbf{H}\mathbf{H}^{H})^{-1}. \tag{2.44}$$

This scheme requires that $M > K$ for $\mathbf{H}$ to be invertible. A simple example to understand the ZF operation is illustrated in Fig. 2.11.

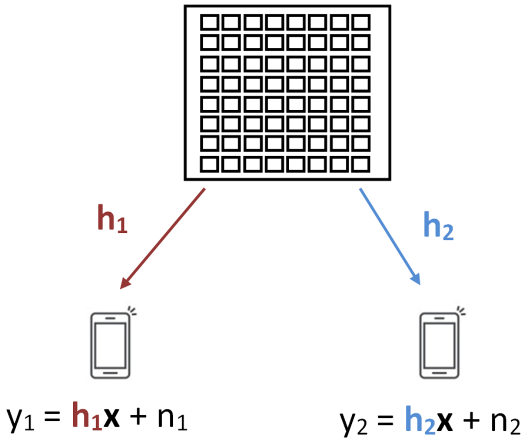

Figure 2.11: *Exemple of a transmission using ZF for two users.*

Consider $K = 2$ (see Fig. 2.11), the superposition of two data streams gives:

$$\mathbf{x} = \mathbf{w}_1 s_1 + \mathbf{w}_2 s_2, \tag{2.45}$$

and the design goal is to achieve 2 spatial DoF with $\mathbf{w}_1 \perp \mathbf{h}_2$ and $\mathbf{w}_2 \perp \mathbf{h}_1$.

- Advantages: relatively simple signal processing, works well in interference-limited scenarios.
- Challenges: ZF ignores noise enhancement problems and may suffer a great power penalty due to the nulling effect. It also strongly depends on the channel conditioning. If the channel is ill-conditioned, the pseudo-inverse can significantly amplify the noise, degrading the performance. If $\mathbf{H}$ has full rank and the Gram matrix ($\mathbf{H}\mathbf{H}^H$) is diagonal, p_k can be fully used on user signals. When some user channels are spatially correlated [140, 160], the nulling operation absorbs more energy leaving little to the user signals.

2.4.2.5 Minimum Mean-Squared Error

ZF is suitable for high SNR scenarios while MRT outperforms ZF at low SNRs. Across the whole SNR range, a tradeoff is necessary between maximizing signal strength and reducing interference. MMSE precoding relies on the estimation of noise covariance at the receiver and feeding it back to the transmitter to help design a better precoder for the whole SNR range. MMSE is obtained by minimizing the mean-square error (MSE) between the transmitted and the estimated received signal. The MMSE solution is given by:

$$\mathbf{W}_{MMSE} = \mathbf{H}^H(\mathbf{H}\mathbf{H}^H + \kappa.\mathbf{I})^{-1}, \tag{2.46}$$

where $\kappa = \dfrac{K.\sigma_n^2}{p_k}$. At very high SNRs, $\kappa = 0$ and MMSE converges towards ZF. When $\kappa \rightarrow \infty$ (i.e. p_k is very low), MMSE converges towards MRT. In between, MMSE outperforms the two methods in terms of sum-rate capacity.

2.4.3 Performance Analysis: Simplified System Model

The computation of the optimal sum capacity is a particularly complex task since the power allocation needs to be numerically optimized. This clearly indicates the benefit of the presented linear schemes alongside heuristic strategies such as water-filling in practice. This is specifically true for massive MIMO systems for which channel hardening [142] is more pronounced compared to classical MIMO systems. Taking into account Eq. 2.34, the corresponding signal to interference plus noise ratio ($SINR$) for user k is given as the ratio between the desired signal (first part of the equation) and the cross-talk with noise (second part of the equation) for a given user k.

$$SINR_k = \frac{p_k|\mathbf{h}_k\mathbf{w}_k|^2}{\sum_{i=1,\ i\neq k}^{K} p_i|\mathbf{h}_k\mathbf{w}_i|^2 + \sigma_n^2}. \tag{2.47}$$

Note that in this manuscript, the noise is assumed to have unit variance σ_n^2, meaning the noise power is actually taken into account in p_k that reflects the SNR. The corresponding capacity for user k is:

$$C_k = \log_2(1 + SINR_k), \quad \textit{in bits/s/Hz} \tag{2.48}$$

and the sum-rate in the considered cell or scenario will be:

$$C = \sum_{k=1}^{K} C_k. \tag{2.49}$$

This definition will be widely used throughout this manuscript for the spectral efficiency evaluation with the different presented precoders.

2.4.3.1 Massive MIMO and Linear Processing

When M increases, the users channels become nearly orthogonal reducing inter-user interference and as a result, DPC (complex non-linear scheme explained in Appendix B.1) maximum rates can be approached by using simpler linear schemes [114]. If M is very large such that inter-user interference is eliminated, the individual capacities of K users can be added since all users channels are now interference-free. In this case, if M is increased for a fixed K, the gain from beamforming is obtained. If K is also increased the gain from spatial multiplexing appears. Clearly, the largest gains in terms of spectral efficiency come from spatial multiplexing but increasing M is necessary to facilitate spatial multiplexing by eliminating or at least reducing the denominator in Eq. 2.47. This discussion implicitly assumes full digital beamforming. Analog or hybrid beamforming schemes may achieve most of the array gain for $K = 1$ but they are less efficient than digital beamforming when spatial multiplexing is considered.

2.5 Sum-Rate Capacity Results

For the evaluation of the sum-rate capacity, we consider the simplified system model in Sec. 2.4 with the geometrical channel model in Sec. 2.3. First, we evaluate the performance of massive MIMO for i.i.d. channels, then a parametric analysis on the geometrical model is performed to assess and quantify the impact of main propagation parameters (K^{Rice}, ρ_{Rx}, etc.) on the system performance.

2.5.1 Performance in i.i.d. Channels

First, the i.i.d. case is considered for $K^{Rice} = 0$. The sum-rate capacity is represented first in Fig. 2.12(a) as a function of the SNR for $K = 12$ and a relatively small number of antennas ($M = 12$) and in (b) for $M = 32$. The goal of this representation is to underline the actual effect of the precoding strategy on the performance [158, 161].

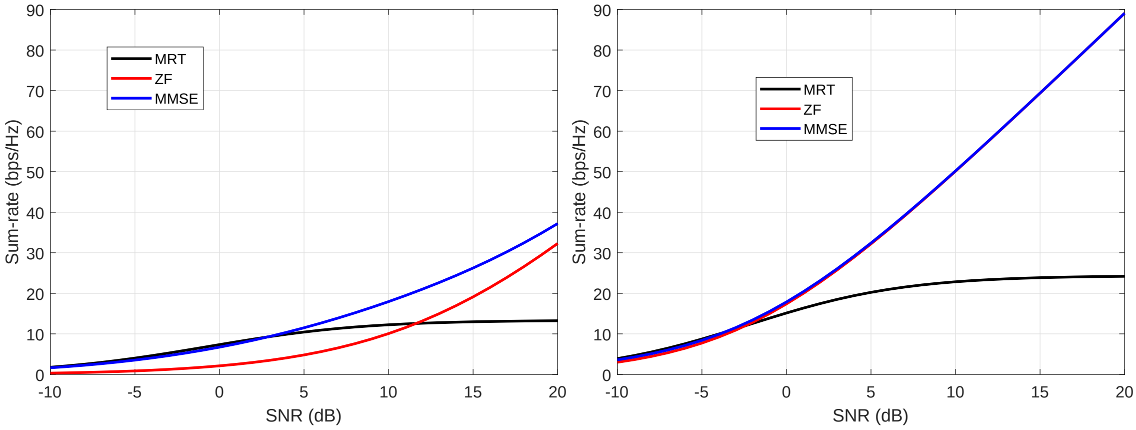

(a) **(b)**

Figure 2.12: *Comparison between MRT, ZF and MMSE for* $K = 12$ *and (a)* $M = 12$ *and (b)* $M = 32$.

To this purpose, we consider small numbers of antennas at Tx side to isolate the performance of linear precoders from the effect of massive MIMO when M is large with respect to K. It can be seen that MRT is better than ZF at low SNR when the number of antennas is not so-large ($M = 12$). Also, MMSE is proven to be a more versatile scheme combining the benefits of both schemes at high and low SNRs. From Fig. 2.12(b), the number of antennas is larger than the number of users, the massive MIMO regime kicks in and ZF performs equally well even at low SNRs and behaves similarly to MMSE as opposed to (a). The sum-rate capacity is then illustrated for a wide range of K values and SNR for MRT and ZF in Fig. 2.13.

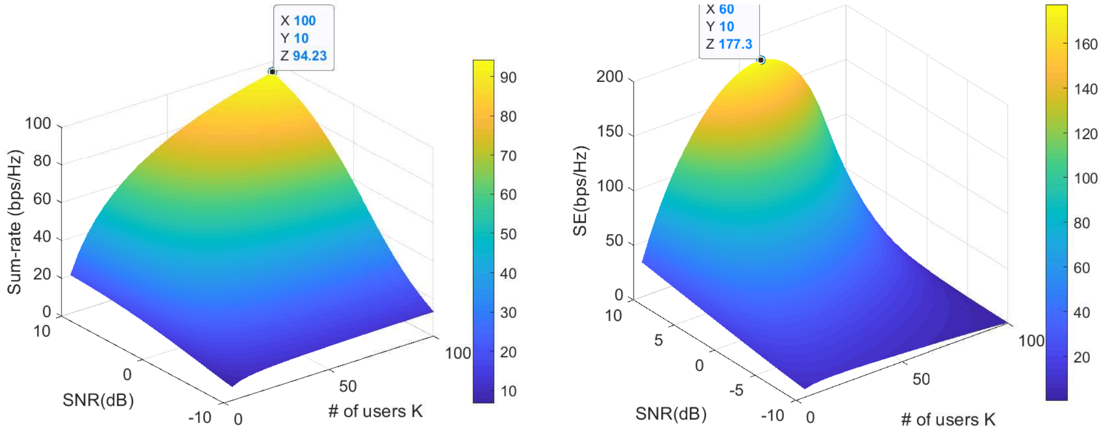

(a) **(b)**

Figure 2.13: *Massive MIMO SE for (a) MRT (b) ZF.*

Here, M= 100 antennas, $N_{obs} = 5000$, SNR values ranging from -10 to 10 dB with unit variance noise, and waterfilling power allocation is considered. From this figure, it can be seen that ZF can achieve higher sum-rates but is limited by the number of users (60 here), whereas the MRT curve increases with SNR and K. The SE increases with SNR but the performance is not only limited by this factor, especially for ZF. For higher SNRs, the maximum number of users before the drop in SE will eventually increase. It is also verified that MRT performs better at low SNR than ZF for a large number of users.

This is observed in Fig. 2.14 presenting a comparison of the three schemes for $SNR =$ 0 dB in (a) and 10 dB in (b).

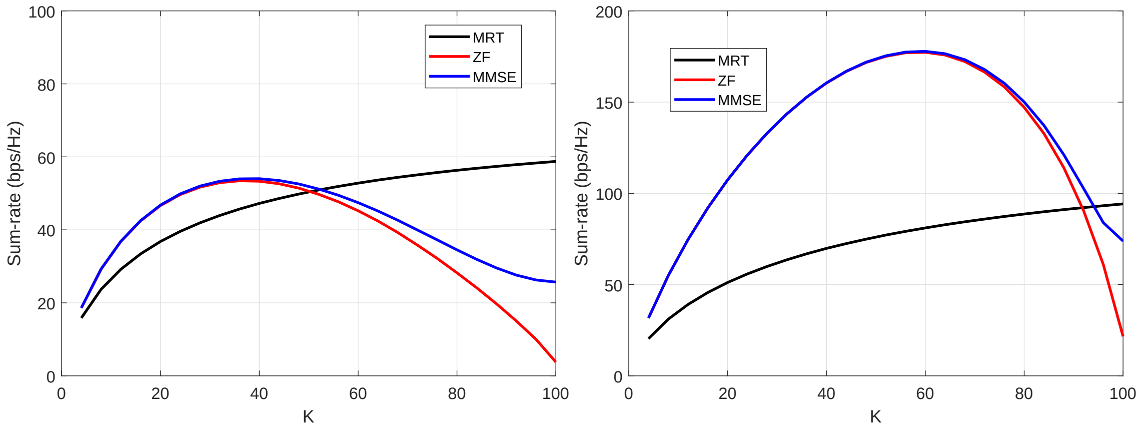

(a) **(b)**

Figure 2.14: *Massive MIMO SE for (a) 0 dB (b) 10 dB.*

MMSE performs slightly better than ZF, and both better than MRT with a limited number of users. Here, we only considered 100 antennas at Tx side, taking more elements will yield to better SEs and more served users for ZF and MMSE. We consider the number of accommodated users for a given SNR as the deflection point (where degradation begins) for the corresponding scheme. At this point, users should be dropped or multiplexed using other resource than space.

2.5.2 Parametric Analysis with the Geometrical Model

Studies addressing the influence of K^{Rice} on the achievable rates of a DL massive MIMO system are scarce in the literature. In [162], the achievable sum-rate and energy efficiency of ZF for Ricean fading channels is studied and it was found that for a ULA, with the increase of K^{Rice}, the performance of the system is reduced, the number of needed antennas M at the BS increases and the number of users K decreases. This paper also states that optimal power allocation scheme follows the waterfilling principle and that the average sum-rate can be increased in the presence of strong LOS effect in the low SNR regime. However, this model does not take into account local mechanisms such as correlation. In [163], the authors identify scenarios under which massive MIMO would potentially fail in Ricean channels and are identified by non-vanishing alignment between LOS channel vectors. Taking the model in Sec. 2.3, the massive MIMO channels are evaluated. The same scenarios than for Fig. 2.8(a) are considered. The system performance is evaluated from a parametric analysis on K, K^{Rice}, ρ_{Rx} and $\rho_{Tx,3\lambda/2}$, the last three parameters being inter-dependant as discussed from the Gram's power ratio analysis. K is varied from 1 to 100, the purpose being to quantify the limits of massive MIMO for different precoding strategies. In real scenarios, trying to serve 100 users with 100 antennas is practically impossible. In Fig. 2.15, the sum-rate is presented as a function of K for three precoding schemes: (a) MRT, (b) ZF and (c) MMSE. The SNR is 20 dB in this case. The different curves represent the different K^{Rice} values.

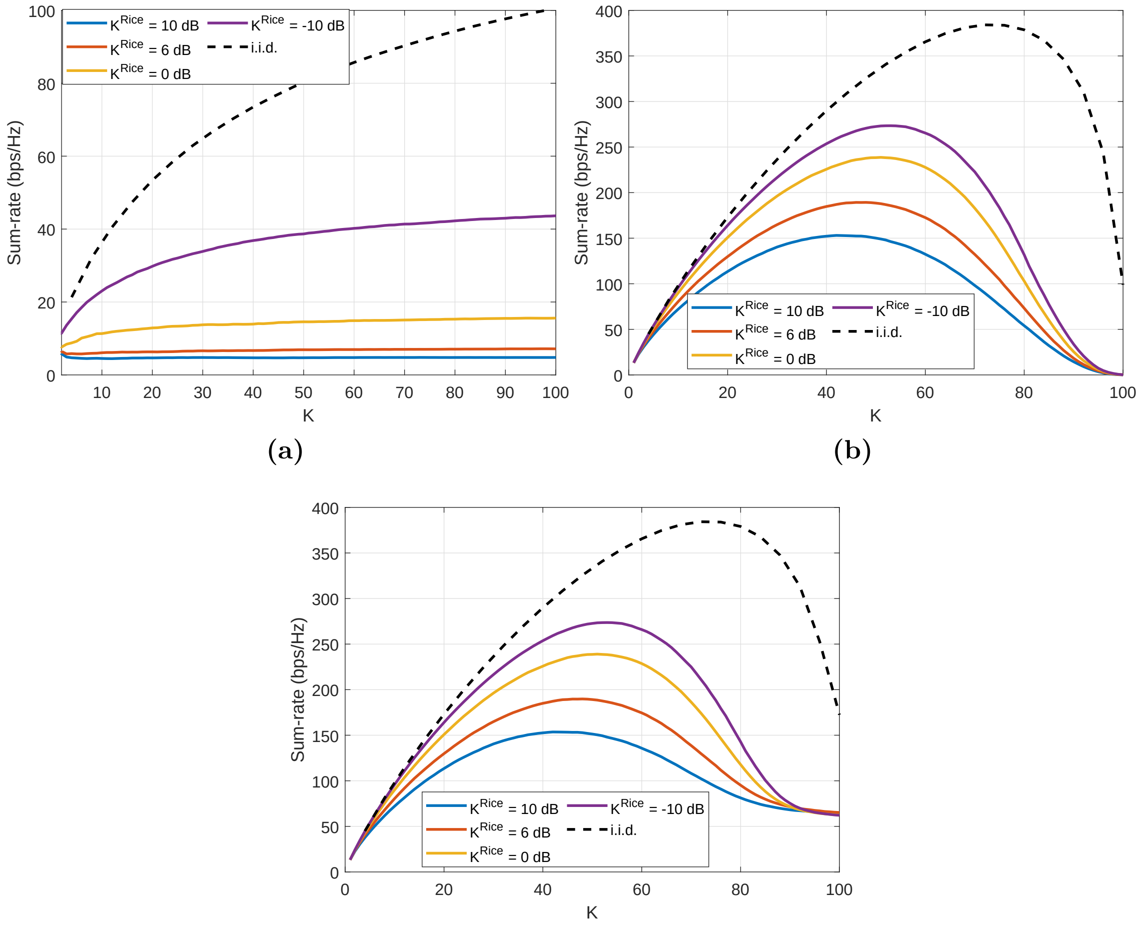

(a)

(b)

(c)

Figure 2.15: *The sum-rate capacity as a function of K: impact of K^{Rice}. (a) MRT, (b) ZF and (c) MMSE.*

It can be observed from this figure with $K^{Rice} = 10$ dB that the maximum value reached by MRT, ZF and MMSE is 5, 150 and 155 bps/Hz, respectively. The high correlation imposed by high K^{Rice} renders the use of MRT ineffective. ZF and MMSE precoding schemes both have extremum points corresponding to the maximum number of users simultaneously served before performance degradation (42 for ZF and 45 for MMSE). For small K^{Rice} values (-10 dB), the number of users increases to 56 (ZF) and 58 (MMSE). MRT exhibits better sum-rate values for small K^{Rice} values: ~45 bps/Hz for $K = 100$ and $K^{Rice} = -10$ dB compared to ~9 bps/Hz for $K = 100$ and $K^{Rice} = 6$ dB. This figure highlights the impact of strong Ricean channels that limits the spectral efficiency of massive MIMO. Strong K^{Rice} leads to high ρ_{Rx} and $\rho_{Tx,3\lambda/2}$ values, thus highlighting the influence of correlation on wireless systems. Nonetheless, it should be indicated that the considered cases are extreme and with the sole purpose of showing the limits of linear precoding.

Figure 2.16 presents the sum-rate as a function of K for (a) MRT and (b) ZF. The different curves are obtained by varying $\Delta\theta$ and $\Delta\phi$ (values chosen from the charts in Appendix D) in order to obtain the different ρ_{Rx} values: 0.2, 0,4, 0.6 and 0.8.

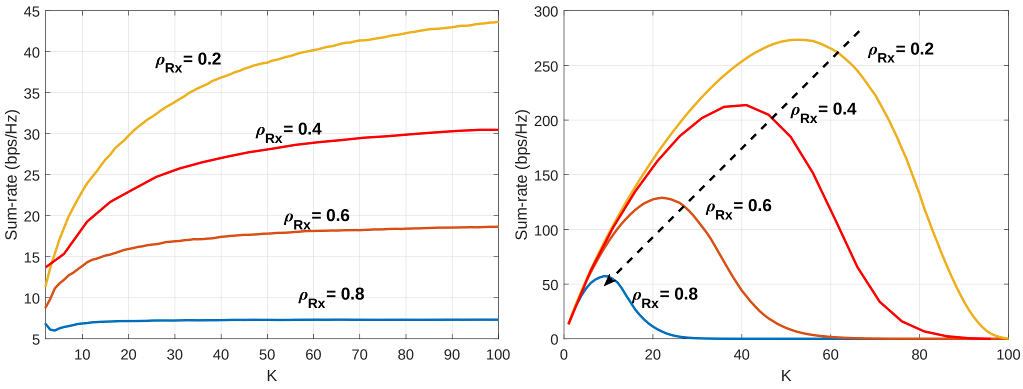

(a) **(b)**

Figure 2.16: *Impact of correlation on the sum-rate capacity for $K^{Rice} = -10$ dB as a function of K. 4 configurations of the geometrical model are considered giving correlation values ranging from 0.2 to 0.8. (a) for MRT and (b) for ZF.*

It can be seen from this figure that for large values of ρ_{Rx} (subsequently $\rho_{Tx,3\lambda/2}$ as observed in Table 2.2), and for a fixed K^{Rice} (-10 dB in this case), a clear degradation in the sum-rate results is observed. For $\rho_{Rx} = 0.2$, 56 users can be served using ZF with ~275 bps/Hz sum-rate capacity, while for $\rho_{Rx} = 0.8$ only 10 users can be served with ~55 bps/Hz. Same observation for MRT where the sum-rate capacity drops from ~45 bps/Hz to ~8 bps/Hz when $\rho_{Rx} = 0.8$. Note that ρ_{Rx} is an average spatial correlation thus reflecting the average correlation in the geometrical-based model.

It can be concluded from this analysis, that (1) ρ_{Rx}, $\rho_{Tx,3\lambda/2}$ and K^{Rice} can heavily affect the overall performance of the system. If $\rho_{Rx} = 1$(worst-case scenario, does not exist), the channels are ill-conditioned and all precoding schemes fail. For very small ρ_{Rx}, it is the i.i.d. case.

2.6 Conclusion

In this chapter, a review of SISO wireless propagation channels is presented. The characteristics of wireless channels are extended to a massive MIMO system. The latter have specific propagation characteristics and its main advantages depend on favorable propagation conditions and channel hardening. A geometrical-based massive MIMO channel model is proposed and validated with the corresponding channel metrics. K^{Rice} and channel correlation properties are shown to be crucial for massive MIMO channel characterization. Finally, in order to quantify the system performance of massive MIMO, a thorough review of precoding strategies and power allocation schemes is presented. The performance of i.i.d. channels is evaluated and a parametric analysis on the sum-rate capacity using the proposed massive MIMO channel model is presented. It confirms the importance of channel characteristics (K^{Rice}, Tx and Rx correlation) when evaluating the sum-rate capacity of a massive MIMO system.

2.7 Summary of Key Points

- For massive MIMO systems, propagation conditions are approximately considered as favorable if the channel responses $\mathbf{h_k}$ for $k = 1, 2, ..., K$ are nearly orthogonal (pairwise).
- Massive MIMO systems increase systems reliability due to channel hardening.
- Massive MIMO is not pencil beamforming. It is a high-resolution version of multi-user MISO with multiple streams to be multiplexed in the space dimension.
- Channel hardening and favorable propagation condition largely depend on K^{Rice} and correlation properties at both Tx and Rx side.
- Linear precoding schemes are affected by correlation characteristics of Rx or Tx.
- ZF and MMSE achieve very high SE, but are limited with the number of users for a given number of array elements. The maximum number of users is determined by the corresponding K^{Rice} and correlation characteristics at Tx and Rx.

Chapter 3

Polarimetric Massive MIMO Channel Measurements in an Industry 4.0

3.1 Introduction: Industry 4.0

M2M communication systems consist in a large number of separately organized devices connected through a network and can be used in different applications such as industrial automation, health care, logistics and electricity grids [164]. The requirements are many and include increase in flexibility, predictive maintenance of machines, versatility and significant increase in efficiency of warehousing and supply chain. ETSI, IEEE and 3GPP have confirmed the need to support increasing number of M2M communications in LTE [165]. 5G should be able to support the connectivity requirements in automation cells, and provide ultra-reliability with ultra-low latency (mMTC and URLLC).

From this, it is expected that 5G wireless networks will benefit the industrial automation community in the frame of Industry 4.0 [18]. More specifically, new technologies such as massive MIMO (for instance a massive MIMO AP inside an automated industry), make it possible to gather and analyze data across a big number of machines because of its capability of accommodating a large number of user equipments (UEs). A study in [166] on analytical correlated Nakagami-m fading channels demonstrated that the achieved gain with polarization diversity can be significant despite losses due to cross-polarizations. Nonetheless, massive MIMO measurements in industrial scenarios are scarce and no polarimetric studies that could help in the choice of antenna arrays in such environments were reported. Also, no capacity analysis using linear precoding schemes was performed to assess the impact of cross-polarization on massive MIMO performance for potential mMTC. For example, it is of interest to see whether the MRT precoder can be a contender for the discussed configurations, especially in scenarios from Industry 4.0 [167, 168] where data packets contain small payloads (in the range of bytes to kilobytes) [169, 170]. In these cases, nearly optimal precoders like ZF can be replaced by simpler ones like MRT. Also, the benefit of using dual-polarized antenna arrays should be evaluated for Industry 4.0.

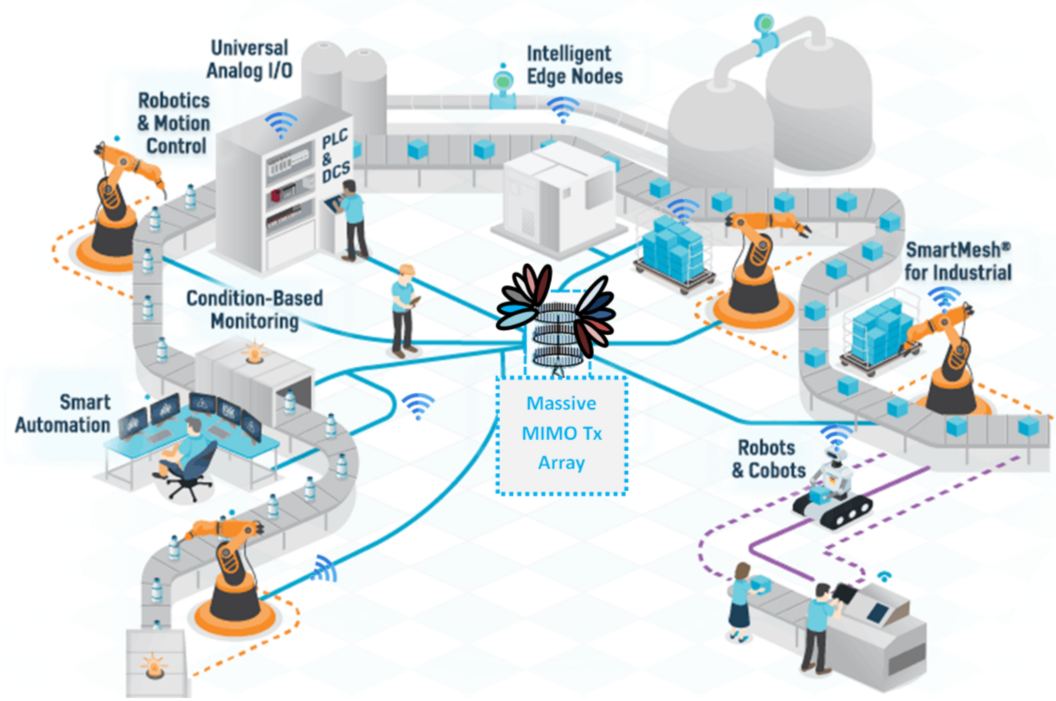

Figure 3.1: *Example of an Industry 4.0 automation cell.*

Chapter Outline

As indicated in Ch. 1, sub-6GHz bands are crucial to support most 5G scenarios [26]. Three different frequency bands were considered in this study: 1.35, 3.5 and 6 GHz. The organization of this chapter is as follows: after a thorough literature review of sounding techniques and channel measurements in Sec. 3.2, the experimental setup and geometrical configuration of the industrial experiments are presented in Sec. 3.3 and 3.4, respectively. The different propagation parameters are presented in Sec. 3.5 and used to classify the different UEs. The impact of cross-polarization is evaluated using propagation and system-based metrics such as the Gram's power ratio and sum-rate capacity in Sec. 3.6. Finally, before concluding in Sec. 3.8, a communication strategy exploiting polarization diversity is proposed and its performance is evaluated in Sec. 3.7.

3.2 Review of Massive MIMO Channel Characterization

During the last 6 years, many massive MIMO channel characterization results have been published in several frequency bands and for different use-cases and scenarios. On one hand, the objectives are to develop accurate and realistic massive MIMO channel models, and on the other hand, to quantify the massive MIMO gain under many constraints and using propagation and system-oriented metrics. In order to establish realistic channel models, channel measurements are essential. A survey on 5G channel measurements and models can be found in [171, 146] and some channel measurement settings and characteristics are presented in Table 3.1.

3.2.1 Sounding Techniques

Three main measurement techniques are considered:

- Fully physical real-time massive MIMO system (denoted R in Table 3.1) with an M-element array (can be rectangular $M_x \times M_y$ or other). This is the sole method to allow dynamic real-time channel measurements. It is also a costly approach especially if each radiating element is connected to an independent RF chain.
- Virtual Array Measurements (denoted V in Table 3.1) where an M-element array is constructed by positioning one antenna element over different X and Y coordinates. This forms a virtual massive MIMO array where mutual coupling and RF chains imperfections are overlooked. The main drawback is the time spent to span all the elements position.
- Hybrid Virtual Array where an M-element URA is constituted by positioning one vertical ULA over different horizontal coordinates. This approach is a trade-off between full physical arrays and virtual sounding techniques and is proposed and exploited [152] in J2 from the list of publications. Note that both virtual and hybrid virtual setups are not adequate for dynamic real-time measurements.

3.2.2 Review of Main Results

Here, a summary of main findings from different measurement campaigns are listed in Table 3.1:

Non-stationarity of channel parameters

One essential factor for massive MIMO arrays is the power variation across antenna elements analyzed in [77, 78]. A massive Tx array with large aperture and a large number of elements could experience spatial variability due to cluster visibility regions at the BS side [137]. Non-stationarity also occurs in delay and spatial domain over the large array size [192]. In [179], the authors indicate that channel parameters appear stationary at high frequencies over the linear array but not at low frequencies, basically due to stronger MPC at these frequencies.

Users orthogonality and channel hardening

The condition number (ratio between largest and smallest singular value) was shown to be a good indicator on the orthogonality between users [77, 185, 178]. It also depicts the channel hardening effect [141, 142].

Table 3.1: *Advances in massive MIMO Channel Measurements.*

Sc.	**F (GHz)**	**Array Size (Setup)**	**V or R**	**Channel Parameters**	**Ref.**
Outdoor	2.6	128 ULA/UCA (LOS-NLOS)	V/R	SE/Spatial Fingerprints-Condition Number WSS	[77, 172]
	2.6	128 UCA (LOS)	R	Spatial Separation	[78]
	44	48 URA (LOS)	R	ABF-AoD/AoA-Capacity	[173]
	3.7	100 URA	R	Reciprocity Calibration-Coupling	[174]
	3.7	100 URA	R	Signal Constellation-Design Parameters	[69]
	2.59	64 URA/ULA	R	SNR-Correlation Coefficient	[175]
	15	40 × 40 URA (LOS-NLOS)	V	K^{Rice}/Spatial stationary clusters	[79]
	5.2	64 URA (UMa)	V	Power, Signal-to Interference ratio	[176]
	2.53	Switched UCA (Urban)	V	Cluster Statistics/EoD-EoA	[177]
	3.5-2.35	URA/UCA (UMi)	R	Eigenvalues-Capacity statistics	[178]
	1.47	128 ULA (Stadium)	V	APS	[179]
Indoor	2-4-6	128 ULA	V	PathLoss (PL)/τ_{rms}/B_{coh}	[180]
	26	ULA/URA	V	PL/Shadow Fading τ_{rms}/B_{coh}	[181]
	94	50 × 50- URA	V	K^{Rice}/MPC-Rx,Tx Correlation	[182]
	13-17	20 × 20 URA (Hall)	V	K^{Rice}/τ_{rms}	[183]
	5.8	64 URA/ULA (Mall)	V	Singular-value-spread (SVS)/ Frequency-Dependency	[184]
	4.1	64 URA	R	SVS/Capacity-Coupling Matrix	[185]
	11	64 URA (Lobby)	V	Power,Non-Stationnary Properties	[186]
	11-16/28-38	Up to 121 × 121- ULA	V	AAS/EAS/τ_{rms}	[187]
	1.35	96 URA	**Hybrid**	Spatial Correlation XPD,K^{Rice}	[152]
O2I	2.53	Switched UCA	V	Az. and El. spread statistics/SE	[188]
	6	32 URA Tx/56 UCA Rx	R	Angular-delay spread-Capacity statistics	[189, 190]
Ind.	1.35-3.5-6	100 URA	V	Spatial Correlation-Polarization Diversity-Sum-rate	[191]

In [175], the authors report that a horizontal arrangement appears more suitable for massive MIMO and yields to low correlation values among the considered positions. Spatial separation and interference reduction between closely-located users is highlighted to be possible in [78] using singular value spread analysis. The capacity of massive MIMO to separate users is also explored for an anechoic chamber and an indoor corridor at 2.6 GHz in [193]. In [194], massive MIMO channel performance for close users in urban macro-cell scenario is evaluated using three kinds of channel models: i.i.d., GSM, and physical ray-based software.

Spectral and Energy efficiency

Large gains in spectral efficiency, using sum-rate capacity analysis and power allocation schemes, are achieved with massive MIMO [77, 124]. Energy efficiency based on consumption analysis and hardware impairments was also shown to be of great benefit for massive MIMO systems [65]. Optimal designs for MU setups with massive antenna arrays using linear precoding and heuristic power allocation techniques are discussed in [82]. Nonetheless, no polarimetric massive MIMO measurements in industrial scenarios have been reported. Moreover, the impact of dual-polarized arrays and the potential of polarization diversity strategies have not been addressed for industrial setups.

3.3 Experimental Setup

In this section, the experimental setup of an industrial environment in a concrete lab is presented and the radio channel sounding procedure is explained.

3.3.1 Radio Channel Sounding

Radio Channel sounding measurements were performed in the frequency domain using a vector network analyzer (VNA - Agilent E5071C), the virtual array acting as a transmitter (see parameters in Table 3.2). The VNA being situated in the vicinity of Tx, a 500-m optical fibers link was deployed for connecting Rx with optical/radio frequency interfaces. A power amplifier is used at Tx side with output gain of 47 dB allowing an output power of 1 W, and a LNA of 31 dB gain is inserted at the receiver end. The S_{21} scattering parameter of the VNA was calibrated by taking into account the cabling (cables, fiber optics, transducers) and the LNA as well. The power amplifier was separately characterized, allowing subsequent correction of the measured S_{21} values. The Tx array is a virtual URA[1] (see Fig. 3.2). The positioning system of the moving Tx antenna is controlled through a fiber optics link with a dedicated LabView program installed on a Windows PC. The spatial step and thus the antenna spacing of the virtual array is 0.5λ, with λ the wavelength for each

---

[1] Vertical dimension along the z axis and horizontal dimension alongside x axis. The longitudinal axis of the hall is along y.

studied central frequency. The different sounding parameters and characteristics of the Tx array are listed in Table 3.2. The mean height above ground being 6.5 m, Tx has a dominant view over the hall as it can be seen in Fig. 3.4(a).

Table 3.2: *Radio Channel Sounding Parameters and different Tx array dimensions.*

VNA	Frequencies	1.35, 3.5 and 6 GHz
	Span Bandwidth	80 MHz
	Resolution	12.5 ns
	Maximum resolvable path	3.75 m
	Number of frequency points M_f	819
	Number of observations N_{obs}	20
	Power Amplifier	47 dB
	LNA Gain	31 dB
	Tx Power	3 dBm
	Fiber/Cables Loss	30 dB
	Resolution BW	70 KHz
	Dynamic range	120 dB
Tx array	URA dimension 1.35 GHz	4×10
	Tx spacing	10 cm
	URA dimension 3.5 GHz	10×10
	Tx spacing	3.86 cm
	URA dimension 6 GHz	10×10
	Tx spacing	2.25 cm
	Tx Height	6.5 m
	Rx Height	1.6 m

3.3.2 Antennas

Identical mono-polarized patch antennas were used for $F = 3.5$ and 6 GHz with a 80 MHz bandwidth and manually rotated to get both polarizations. The antennas at 1.35 Hz are dual-polarized as indicated in Fig. 3.3. These antennas operate at the studied center frequencies with ∼80 degrees half-power beamwidth, both in azimuth and elevation and an average 7 dBi gain with typical nominal VSWR ≤ 2 in the band of interest. Main parameters of the antennas are presented in Table 3.3. The bandwidth is computed for a scattering parameter $S_{11} < -6$ dB. The radiating pattern and detailed characteristics of the antennas can be found in Appendix E.
V and H polarization were applied only at the Tx level since, from a practical point of view, the complexity of switching polarizations is reported at the Tx side for a massive MIMO system.

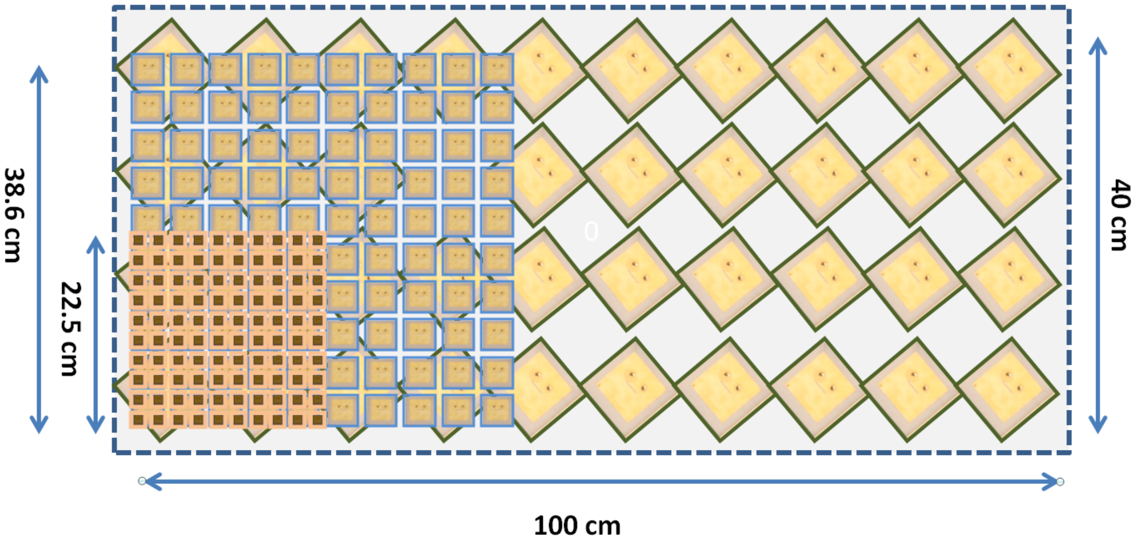

Figure 3.2: *Schematic of the created URA for 1.35, 3.5 and 6 GHz.*

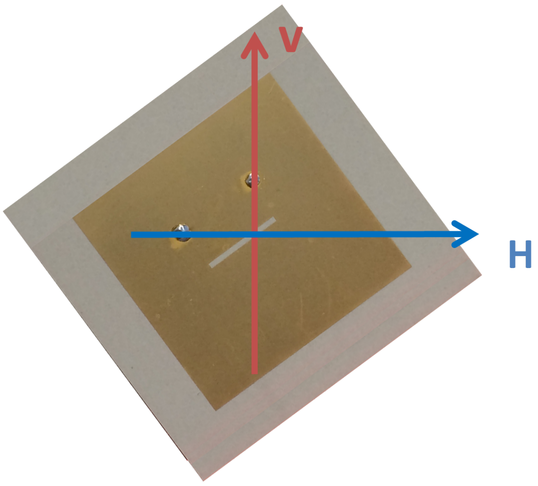

Figure 3.3: *Schematic of the dual-polarized patch antenna at 1.35 GHz.*

Table 3.3: *Main Parameters of the antennas.*

Frequency (GHz)	BW (MHz)	Patch Gain (dBi)	V/H Rejection (dB)
1.35	>80	7	18
3.5	59	6.4	30
6	>80	6.3	30

3.4 Geometrical Configuration of the Experiments

The propagation environment is a large industrial hall located in Technologiepark-Zwijnaarde, Belgium. The 21.3×77.2×12.2 m^3 hall is a research lab dedicated for testing the robustness of concrete structures. The dominant building material for walls, floor, and ceiling is concrete. The windows are located near the ceiling and a large metallic industrial door which was closed during the measurements is located at the end of the hall. Large metallic machines and measurement tools can be found in the environment, typical for automation cells in Industry 4.0. In Fig. 3.4(a), a panoramic view from the Tx array is shown.

3.4.1 Multi-User Setup

The massive MIMO scenario consists in a MU[2] setup wherein a number of single antenna UEs are distributed in the industrial hall as illustrated in Fig. 3.4(b). The machines distributed in the hall and which act as reflectors or can block the direct path between Tx and Rx are not indicated in the schematic. The positions of the different users[3] were selected to cover most of the practical configuration: LOS, strong metallic surrounding the receiving antenna as seen in Fig. 3.5(a), totally obstructed in (b), concrete structures around the UE in (c), and visible LOS UE (partially obstructed by a measurement system) in (d).

3.4.2 General Notations

3.4.2.1 Polarimetric Massive MIMO Channel Matrix

In practice, the transfer matrices were measured by successively moving an Rx antenna from one position to another one, its height remaining constant. For each UE position k, Tx antenna m and polarization link ψ, the wideband complex channel transfer function $\mathbf{h}_{k,m,\psi}(f) \in \mathbb{C}^{1\times M_f}$ is obtained from the S_{21} scattering parameter, where $k = 1, 2, ..., K$, $m = 1, 2, ..., M$, and M_f is the total number of frequency points, respectively. Note that $M = M_x \times M_y$, but vectorized in order to simplify representations and notations. ψ can be either co-polar VV or cross-polar HV, the first letter denoting Tx polarization and the second Rx polarization. The polarimetric massive MIMO channel matrix $\mathbf{H}_\psi \in \mathbb{C}^{K\times M\times M_f}$ is constructed from $\mathbf{h}_{k,m,\psi}$ for all possible k and m values.

---

[2] User or UE notations are both used to indicate a receiver with one Rx antenna.

[3] For all UEs, Tx and Rx antennas are always facing each other. The radiating patterns are parallel between the Tx and Rx antennas.

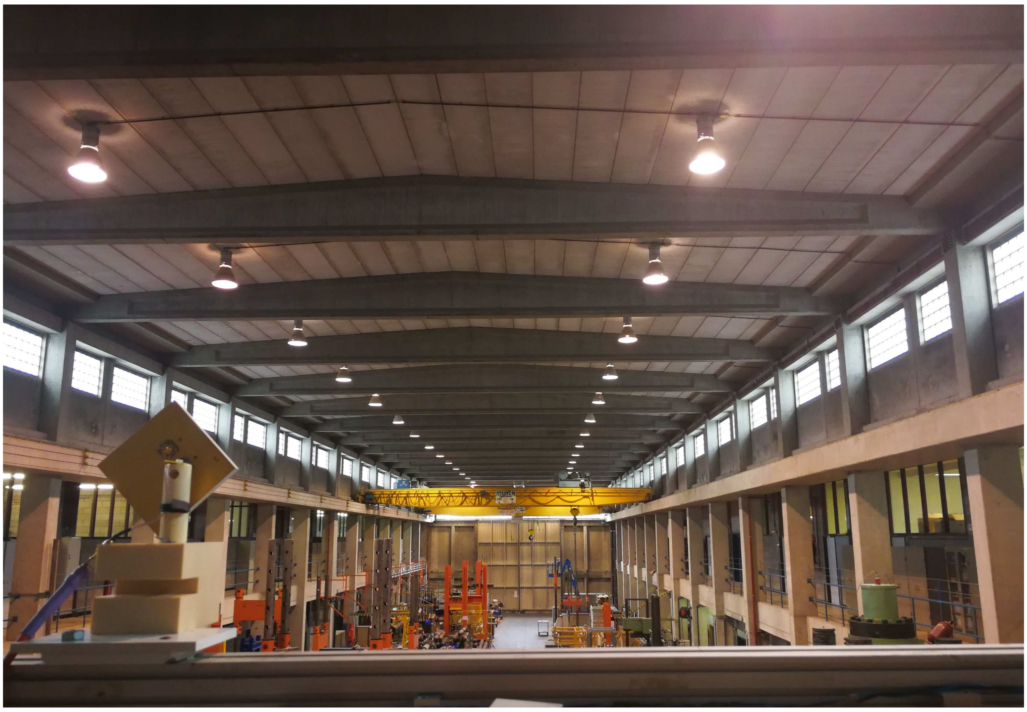

(a)

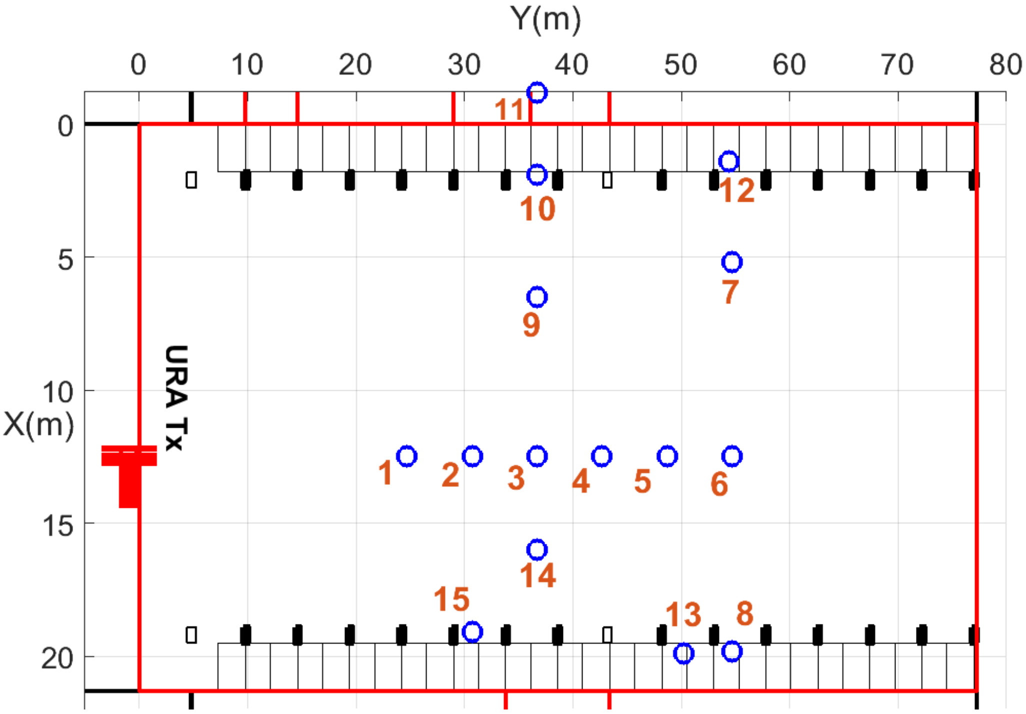

(b)

Figure 3.4: *a) Panoramic view of the industrial hall from the Tx point of view and b) Schematic from above of the distributed setup.*

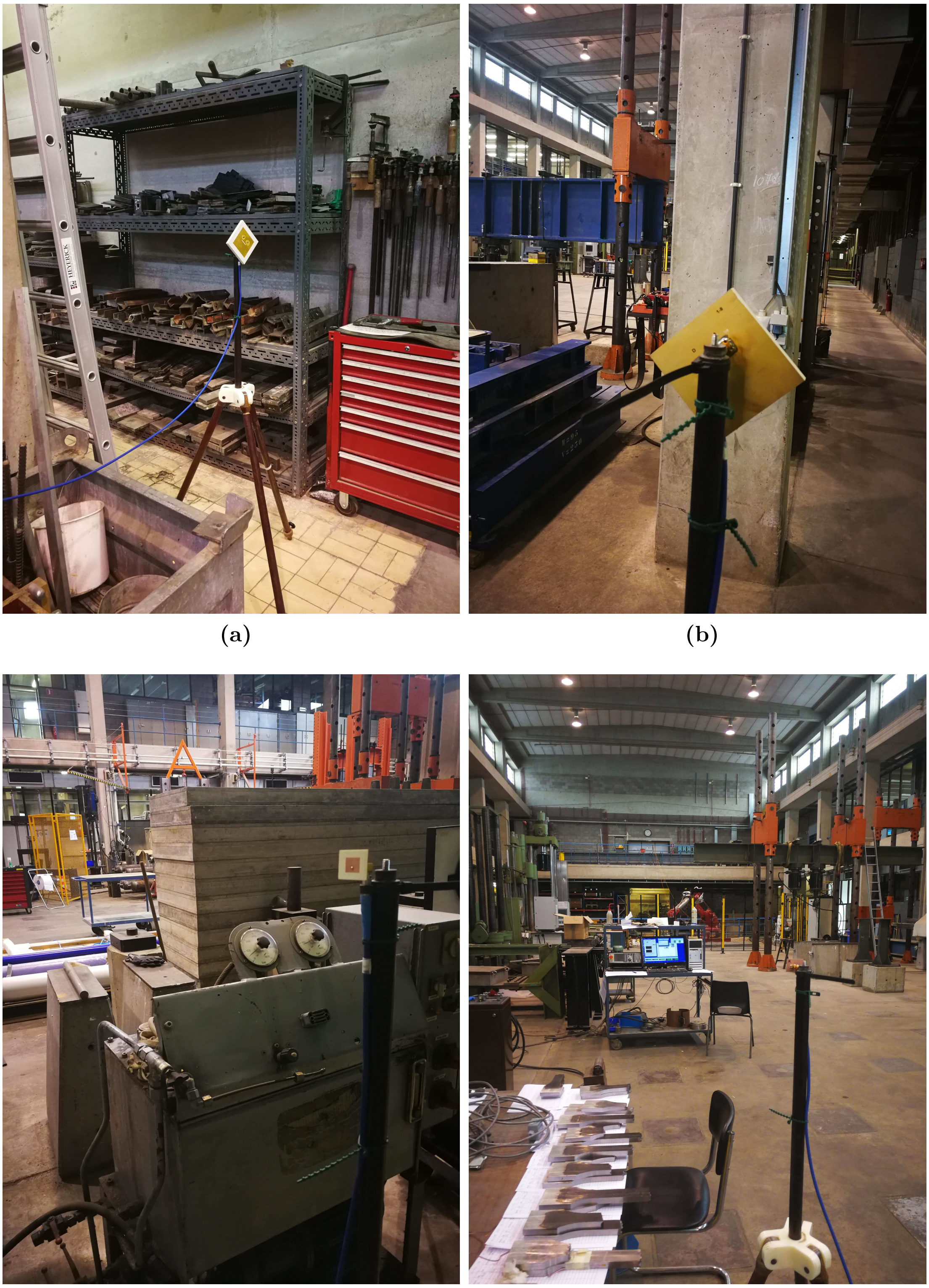

(a) **(b)**

(c) **(d)**

Figure 3.5: *Example of UE positions with metallic structures UE8 (a), totally obstructed UE11 (b), with concrete surroundings UE12 (c) and visible LOS UE5 (d).*

Channel Normalization

For sum-rate capacity analysis, channel normalization is carefully applied to keep the imbalance between both polarizations. Consider $\mathbf{H}_k$ the k^{th} $M \times M_f$ channel matrix, then the normalization is as follows:

$$\mathbf{H}^n_{k,VV} = \frac{\sqrt{MM_f}\ \mathbf{H}_{k,VV}}{||\mathbf{H}_{k,VV}||_F} \quad and \quad \mathbf{H}^n_{k,HV} = \frac{\sqrt{MM_f}\ \mathbf{H}_{k,HV}}{||\mathbf{H}_{k,VV}||_F}. \tag{3.1}$$

3.5 Propagation Channel Characteristics

3.5.1 Channel Transfer Function: Example

Figure 3.6 presents the co- and cross- $|\mathbf{h}_{k,m,\psi}(f)|^2$ for positions $k = 1$ (strong LOS) and $k = 8$ (high metal concentration around the UE, NLOS) for one Tx-Rx link to highlight the particularity of these type of environments.

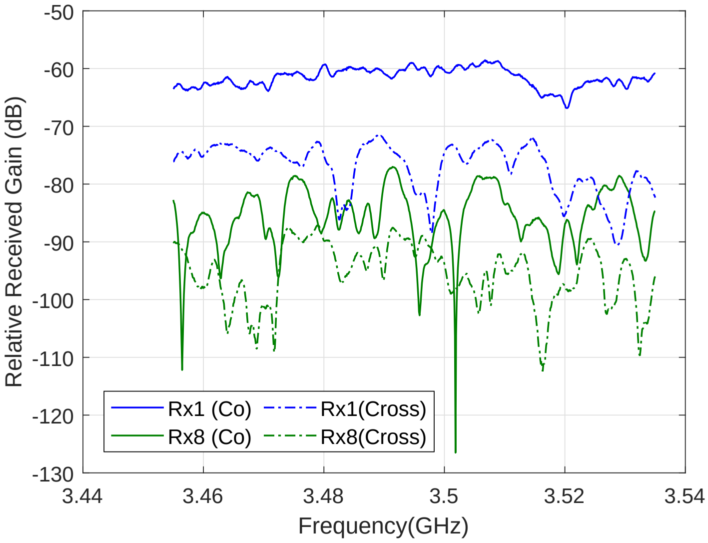

Figure 3.6: $|\mathbf{h}_{1,50,\psi}(f)|^2$ *and* $|\mathbf{h}_{8,50,\psi}(f)|^2$ *for co- and cross-polarization links.*

Indeed, the LOS scenario exhibits a co-polarized flat frequency channel whereas deep frequency fading occurs for co-polarized NLOS channel. In both cases, cross-polarized channels are frequency selective and their relative gain with respect to co-polarized channel is larger in NLOS than in LOS.

3.5.2 Average Received Gain

The median value of the LOS experimental gain at 26 m reference distance at 1.35 GHz is observed to be in agreement with the theoretical values estimated with the Friis equation as shown in Table 3.4. At the same reference distance, UE11 in NLOS scenario exhibits additional losses of ∼18.7 dB, whatever the frequencies. However, the relative NLOS additional losses at 3.5 GHz with respect to 1.35 GHz is 31 dB. This highlights the advantage of using lower frequency bands for deep indoor coverage.

Table 3.4: *Experimental Vs Theoretical Friis Gain and NLOS relative gain to UE 1 for the three frequencies.*

F (GHz)	**LOS Experimental Gain (dB)**	**Theoretical Gain (dB)**	**NLOS Additional Losses (dB)**	**Relative NLOS Additional Losses (dB)**
1.35	-50.2	-51.3	18.7	18.7
3.5	-62.9	-60.2	18.3	31
6	-65.9	-64.3	18.8	34.5

The average received gain as a function of the different discrete Tx-Rx distances (of the UEs) in co-polarization over all Tx elements is presented in Fig. 3.7(a,c,e) for 1.35, 3.5 and 6 GHz, respectively. In Fig. 3.7(b,d,f), a boxplot of the received gain is illustrated for both polarizations. The central mark is the median over the Tx antennas, the edges are the 25^{th} and 75^{th} percentiles. The whiskers extend to the most extreme data points (but not considered as outliers) and the outliers are plotted individually using red crosses.
From Fig. 3.7, gain variations across the Tx array[4] can reach large values. Looking in detail at UE 3 at 1.35 GHz, large fading of more or less 10 dB depth occurs on ∼50% of the array elements which highlights spatial variability across the array. This variability is particularly true for 1.35 GHz for which the large array size gives rise to different fading statistics. Similar observations were reported in [172].

3.5.3 Coherence BW, Ricean factor and Tx Correlation

Propagation channel characteristics such as the coherence bandwidth ($B_{c,0.7}$), estimated Ricean factor (using MLE from Matlab toolbox) and Tx correlation can be jointly used to classify the UEs, and without prior knowledge of their actual positions, according to distinct scenarios: LOS, NLOS or OLOS. This is particularly of interest when studying multiple UE positions in order to understand the impact of propagation conditions on the overall performance of the system. The median values of B_c (the subscript 0.7 is omitted), K^{Rice} and ρ_{Tx} are presented for all UEs positions in Fig. 3.8(a), (b) and (c), respectively.

Some notable conclusions can be drawn from this figure: (1) apart from some exceptions, B_c, K^{Rice} and ρ_{Tx} are similar for the three frequencies and do not appear to be frequency-dependant, (2) nonetheless, Rx 3 presents the lowest median value of B_c, K^{Rice} at 1.35 GHz, which can be explained by the physical size of the Tx

---

[4] Note that the first 10 elements of the M dimension designate the first column or vertical dimension of the URA.

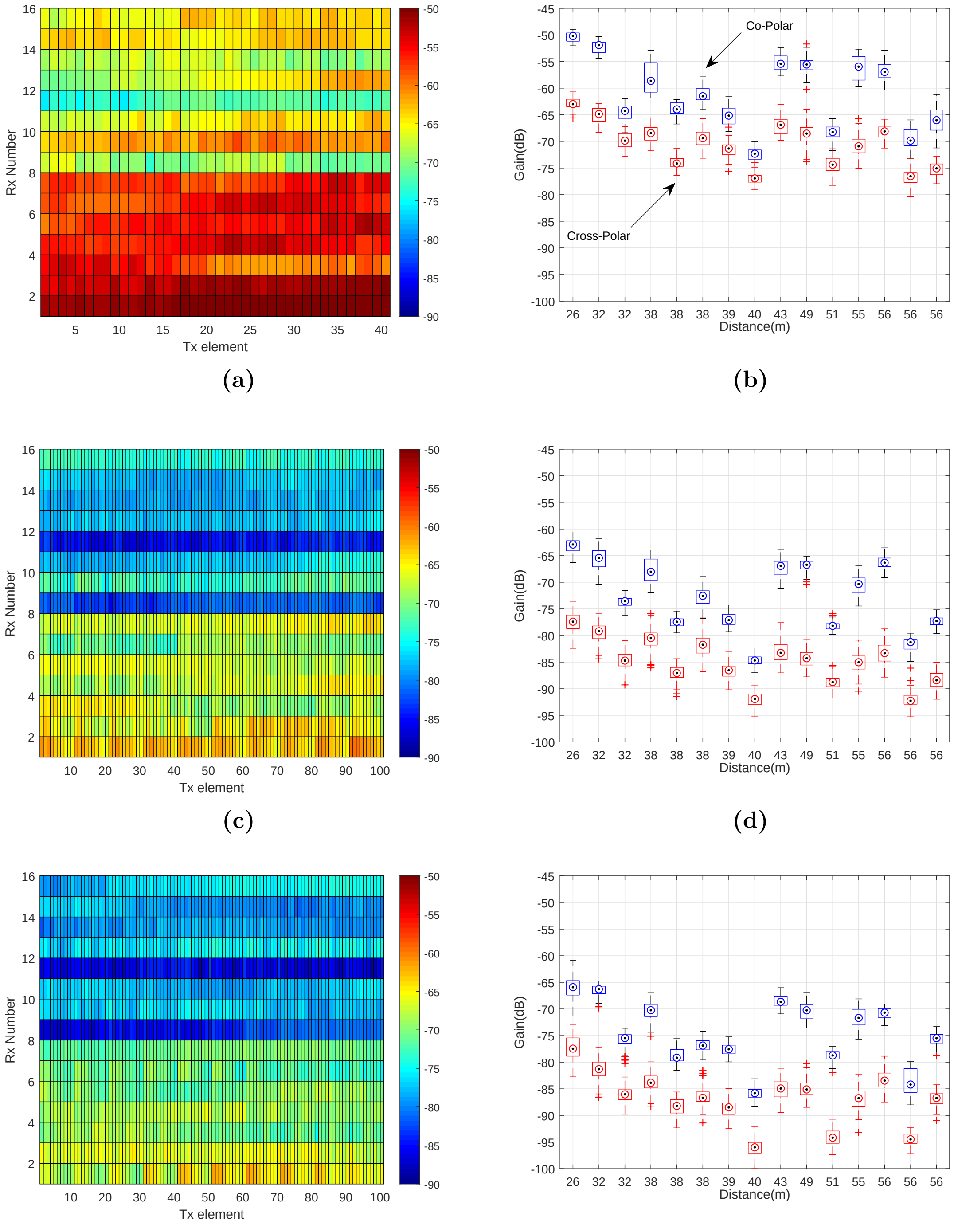

(a) (b)

(c) (d)

(e) (f)

Figure 3.7: *The average received gain in co-polarization scheme for all UEs across the Tx array at (a) 1.35 GHz, (c) 3.5 GHz, (e) 6 GHz and the boxplot of average received gain in both polarizations displaying gain variations at (b) 1.35 GHz, (d) 3.5 GHz, (f) 6 GHz.*

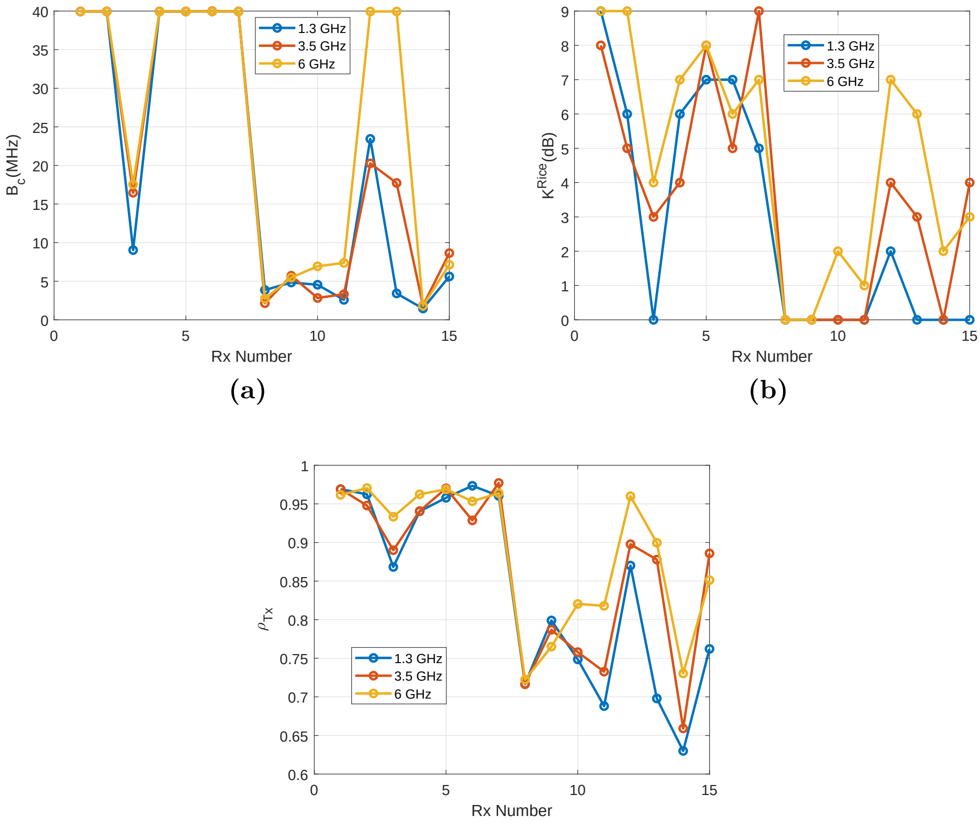

(a) **(b)**

(c)

Figure 3.8: *The median values of $B_{c,0.7}$ (a), K^{Rice}(b) and ρ_{Tx}(c) for the three studied frequency bands.*

array for which different fading statistics occur showing lower B_c and K^{Rice}, (3) Rx 12 and 13 appear to have completely different behavior for the three different frequency bands with higher B_c and K^{Rice} at higher frequencies. This observation suggests that the classification is not necessarily the same at different frequencies and will eventually depend on the Tx array size. On another note, K^{Rice} has larger variations than B_c and ρ_{Tx} across the UEs. In fact, K^{Rice} is an estimation of the real Ricean factor as already discussed and can be subject to some inaccuracies. Hence, we have decided to use B_c and ρ_{Tx} for the initial classification, and if needed, refine the results with K^{Rice}.

3.5.4 Classification

It appears from the previous analysis that the presented channel parameters are correlated and can, therefore, be thus used to obtain a relatively precise classification of the different positions. Using a rule of thumb, a LOS scenario consists in selecting UEs having B_c median values higher than 40 MHz, relatively high K^{Rice} ($\geq$ 6 dB) and ρ_{Tx} (around 0.95). Other UEs can be considered as either NLOS or OLOS. Figure 3.9 presents a scatter plot of B_c and ρ_{Tx} for the three studied frequencies. This plot supports the claim that these two parameters are correlated and it is then possible to jointly consider the B_c and Tx correlation values to create specific groups of UEs.

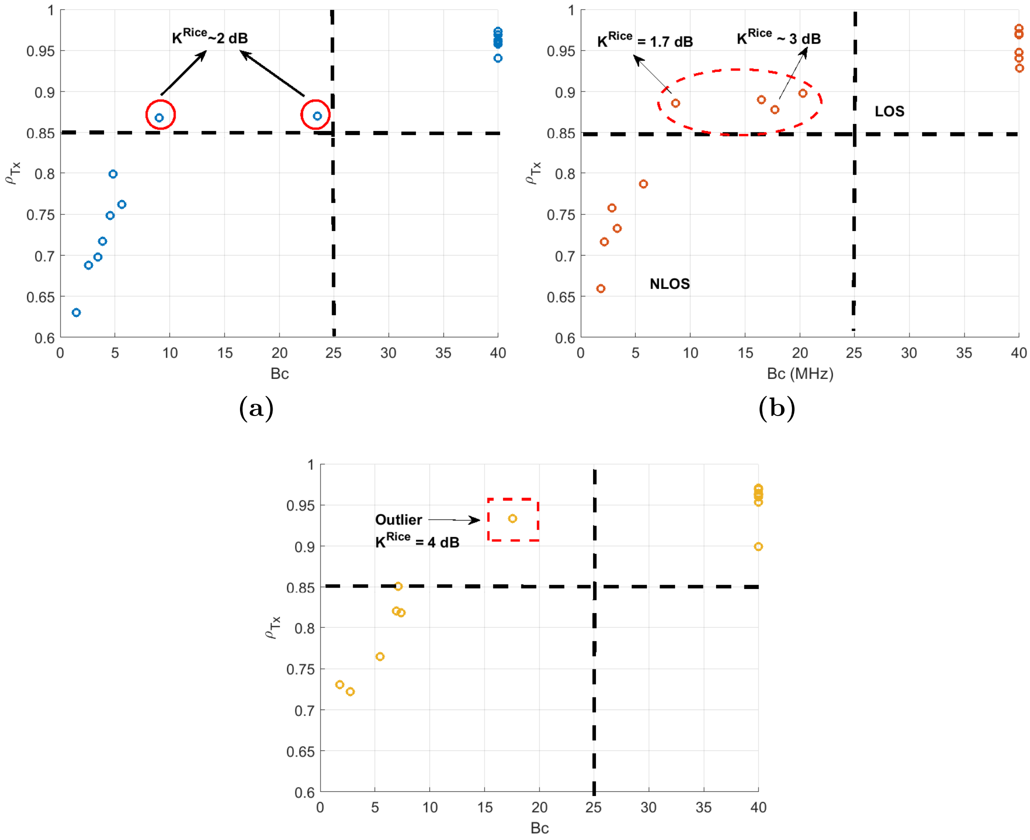

(a) **(b)**

(c)

Figure 3.9: *Classification of UEs with a scatter plot of B_c and ρ_{Tx} for (a) 1.35 GHz, (b) 3.5 GHz, (c) 6 GHz.*

This classification indicates that some UEs are "in-between" these two scenarios (at 1.35 and 3.5 GHz) and are probably considered as OLOS such as UE 3. These UEs share LOS (relatively high ρ_{Tx}) and NLOS properties (relatively lower B_c). In order to classify these UEs, the Ricean factor is used: it is considered that a UE in OLOS condition having $K^{Rice} < 3$ dB will be considered as NLOS.

As already stated, the proposed classification is different for the three frequencies. One particularity for 6 GHz is the existence of more LOS UEs than 1.35 and 3.5 GHz. This is due to the small distance spanned by the 6 GHz array, meaning lower probability of obstruction. The different results in this section were confronted and validated with the map of UEs positions. Table 3.5 presents the standard deviation and mean values across the Tx array for a LOS UE 1, OLOS UE 3 and NLOS UE 11. B_c and K^{Rice} values are in MHz and dB, respectively.

Table 3.5: *Statistics of key channel parameters over the Tx array at the studied frequencies for LOS UE 1, OLOS UE 3 and NLOS UE 11.*

		1.35 GHz			**3.5 GHz**			**6 GHz**		
		LOS	**OLOS**	**NLOS**	**LOS**	**OLOS**	**NLOS**	**LOS**	**OLOS**	**NLOS**
B_c	**Mean**	39.2	16.1	3.8	37.8	19.7	3.5	35.4	23.4	8.2
	σ	4.5	15.4	2.4	6.7	11.5	1.2	3.5	13.4	7.5
K^{Rice}	**Mean**	8.6	2.3	0.3	8	3	0.9	7.9	4.2	1.9
	σ	2.1	3.5	0.6	3	3	1.4	4.1	3	2.1
ρ_{Tx}	**Mean**	0.96	0.8	0.61	0.95	0.85	0.67	0.93	0.88	0.71
	σ	0.04	0.18	0.22	0.04	0.16	0.22	0.06	0.13	0.2

3.5.5 Selected Scenarios

Three distinct scenarios can be defined for 3.5 and 1.35 GHz:
- **LOS Scenario:** UEs 1, 2, 4, 5, 6 and 7.
- **NLOS Scenario:** UEs 3, 8, 9, 10, 11, 12, 13, 14 and 15.
- **Total Scenario:** All UEs.

And for 6 GHz:
- **LOS Scenario:** UEs 1, 2, 4, 5, 6, 7, 12 and 13.
- **NLOS Scenario:** UEs 8, 9, 10, 11, 14 and 15.
- **Total Scenario:** All UEs.

3.5.6 Parameter Cross-Correlation

The inter-dependence of channel parameters can be evaluated through a cross-correlation analysis as indicated in The WINNER II channel model [195]. The correlation between ρ_{Tx}, K^{Rice} and B_c is computed and the median value is presented in Table 3.6. OLOS and NLOS UEs were regrouped for this analysis.

Table 3.6: *Cross-correlation between channel parameters.*

	1.35 GHz		**3.5 GHz**		**6 GHz**	
	LOS	**NLOS**	**LOS**	**NLOS**	**LOS**	**NLOS**
$B_c - K^{Rice}$	0.88	0.46	0.91	0.75	0.95	0.88
$B_c - \rho_{Tx}$	0.80	0.44	0.84	0.72	0.85	0.84
$K^{Rice} - \rho_{Tx}$	0.78	0.41	0.82	0.69	0.87	0.8

The correlation between B_c and K^{Rice} slowly increases in the LOS scenario from 0.88 at 1.35 GHz to 0.95 at 6 GHz. However, with NLOS, the correlation between these parameters significantly increases from 0.46 at 1.35 GHz to 0.75 and 0.88 at 3.5 and 6 GHz, respectively. The same conclusion holds for the correlation of B_c with K^{Rice} and K^{Rice} with ρ_{Tx}. In conclusion, even though B_c, K^{Rice} and ρ_{Tx} are not frequency-dependent, the correlation of these parameters is observed to be clearly frequency-dependent since its value increases from 1.35 to 6 GHz, notably for NLOS conditions.

3.5.7 Polarimetric Channel Characteristics

Depolarization effects, illustrated by the XPD, are insightful for polarimetric channel analysis, especially in industrial scenarios where UEs experience different propagation environments. An XPD analysis helps predicting the potential impact of cross-polarization, especially on UEs correlation. This will be further detailed when analyzing favorable propagation conditions. From the previous classification and the average received gain, it is possible to deduce the XPD (defined in 2.2.2.2 from Ch. 2) variation across the Tx array and UE positions. To this purpose, we present in Fig. 3.10 the CDF of the XPD for 2 UEs: UE1 (LOS), UE11 (NLOS) at the three frequencies: (a) 1.35 GHz, (b) 3.5 GHz and (c) 6 GHz.

The observed values are well below the V/H rejection limit measured in an anechoic chamber. One interesting point is that the XPD values spread over the Tx antennas, showing that polarimetric channel characteristic also have spatial variability over the Tx array. The median values for the NLOS UE are 4.1, 7.1 and 10 dB for 1.35, 3.5 and 6 GHz, respectively, indicating that depolarization effects are more dominant at 1.35 GHz. Compared to the LOS UE with median XPD > 10 dB for all frequencies, it can be seen that channels stay strongly polarized in LOS conditions. Table 3.7 presents the median value of the XPD distribution over the Tx array for the three different frequency bands. In this table, all LOS and NLOS UEs are regrouped since similar behavior was observed.

Table 3.7: *Median XPD value at the three frequencies for LOS and NLOS scenarios.*

	XPD (dB)	
Frequency	**LOS**	**NLOS**
1.35 GHz	12.6	7.3
3.5 GHz	15.5	10.1
6 GHz	13.9	10.5

The median XPD value at 6 GHz for LOS UEs is smaller than at 3.5 GHz but higher than at 1.35 GHz. The XPD median value for both LOS and NLOS scenarios increases with frequency for the NLOS scenario indicating less depolarization effects

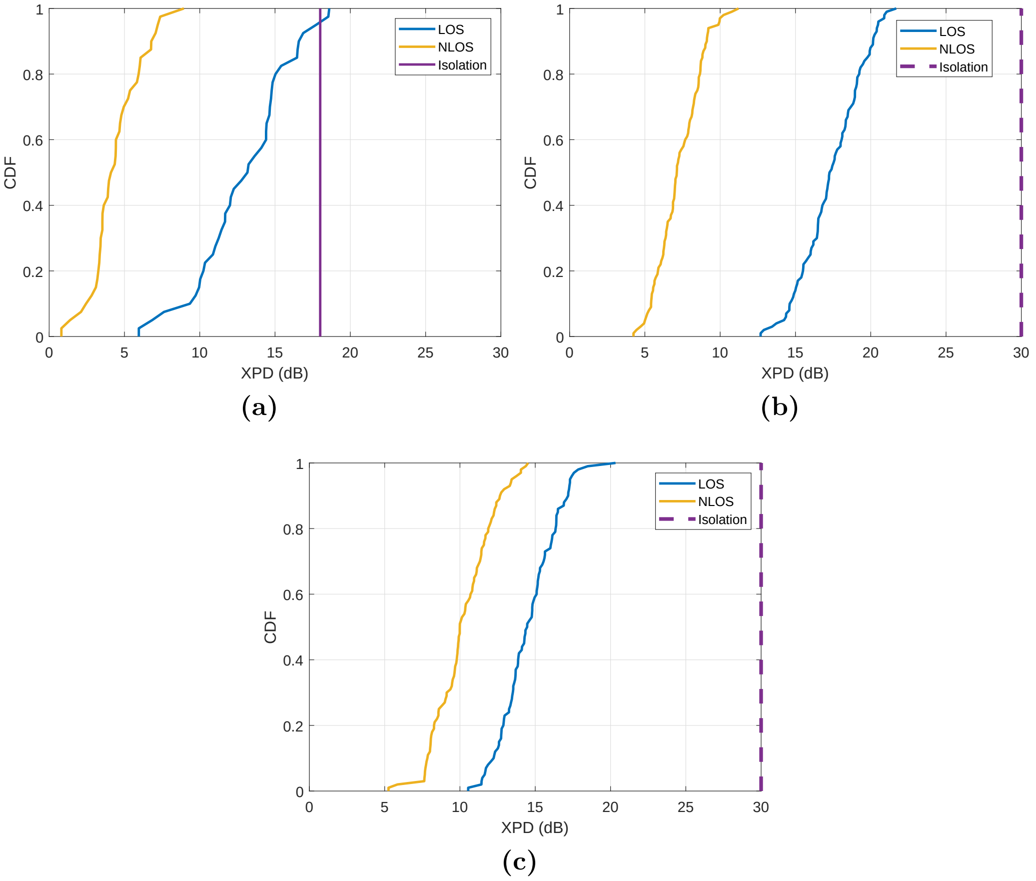

(a) **(b)** **(c)**

Figure 3.10: *CDF of the XPD factor for LOS (UE 1), NLOS (UE 11) at (a) 1.35 GHz, (b) 3.5 GHz and (c) 6 GHz.*

at higher frequencies as observed for UE 11. In the rest of this chapter, we are interested in the 3.5 GHz frequency, a potential band for indutrial IOT.

3.6 Massive MIMO System Evaluation

In this section, key parameters for the evaluation of the massive MIMO system are presented. The two pillars of massive MIMO are first illustrated using receiver spatial correlation for the favorable propagation condition and the variance of the average channel gain for channel hardening. The Gram's power ratio is used to evaluate the percentage of the total energy that is focused to the intended user. However, this ratio does not take into account the cross-polarization losses, precoding and power allocation schemes. This is achieved with the sum-rate capacity.

3.6.1 Does Channel Hardening hold ?

When increasing M, variations of the user channel gain decrease and result in channel hardening. The definition in Ch. 2 (Eq. 2.22) is adequate for asymptotic analysis but for practical purposes, it is of interest to evaluate, for a limited number of antennas, how close to asymptotic channel hardening it can get. By using a simple criterion based on the Chebyshev inequality, we use the definition in [123, 141] to evaluate channel hardening for a particular propagation environment, illustrated by $\frac{\mathbb{V}\{\|\mathbf{h}_k\|^2\}}{(\mathbb{E}\{\|\mathbf{h}_k\|^2\})^2}$ with $\mathbb{V}\{\mathbf{x}\}$the variance of $\mathbf{x}$. This expression almost surely converges to 0 when $M \rightarrow \infty$. The results of the channel gain variance are presented in Fig. 3.11 as a function of M for (a) LOS UE1, (b) OLOS UE 3 (c) NLOS UE 11 and the i.i.d. taking the same number of observations M_f for all cases.

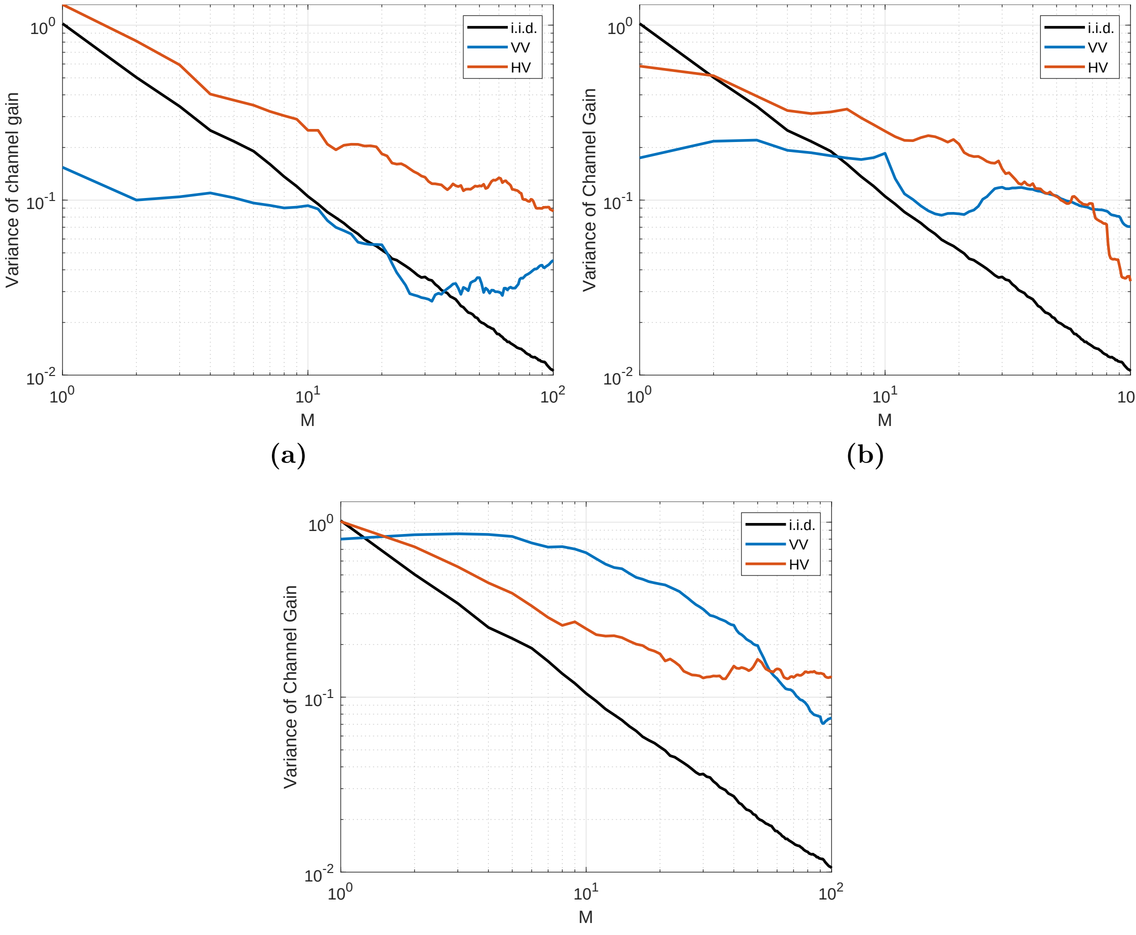

(a) **(b)**

(c)

Figure 3.11: *Channel hardening effect using* $\frac{\mathbb{V}\{\|\mathbf{h}_k\|^2\}}{(\mathbb{E}\{\|\mathbf{h}_k\|^2\})^2}$ *for (a) LOS UE1, (b) OLOS UE 3 and (c) NLOS UE 11, as a function of* M*.*

From this representation, when a given curve is below the i.i.d. case, it means that the corresponding Tx antennas experience a strong LOS component (thus large K^{Rice} values). For UE 1, it was expected that co-polarized channels with strong K^{Rice} behave better than the i.i.d., nonetheless K^{Rice} values vary across the Tx array (as in Table 3.5) even for LOS UEs. Cross-polarized channels behave worse than i.i.d. compared to co-polarized channels for UE 1. For the NLOS case, the corresponding channel hardens slower than in LOS case with an advantage of cross-polarized channels. This is rather surprising given that co-polarized channels harden faster due to the existence of LOS. Indeed, it can be explained by the position of UE 11 in strong NLOS conditions where cross-polarized schemes can be beneficial.

However, this result must be interpreted with caution because the SNR would be very low (median received gain of -92 dB). For UE 3 in OLOS conditions, one can note the variability of the channel hardening effect due to different fading statistics experienced by the Tx array for this particular UE and validated by the different channel characteristics (B_c, K^{Rice}, and ρ_{Tx}).

It is concluded that depending on the UE location and propagation conditions, the channel hardening assumption might not be true for some cases, underlining the complexity of industrial channels. Also, even for co-polarized schemes, the variance of the channel gains eventually behaves worst than the i.i.d. due to the spatial variability over the Tx array.

3.6.2 How Favorable is the Propagation ?

To illustrate this characteristic of massive MIMO, the correlation values from the total correlation matrix $\mathbf{R}_{Rx}$(averaged over frequencies) with $M = 32$ and $M = 64$ is shown in Fig. 3.12. It can be observed that, even with $M = 64$, UEs in the LOS region (UE 1 to 7) are strongly correlated, while the same UEs have lower correlation values with only $M = 32$ using cross-polarization. This figure clearly underlines the advantage of cross-polarization in the decorrelation of UEs channels. This can be further depicted looking at the definition in Ch. 2 of average spatial receiver correlation ρ_{Rx}.

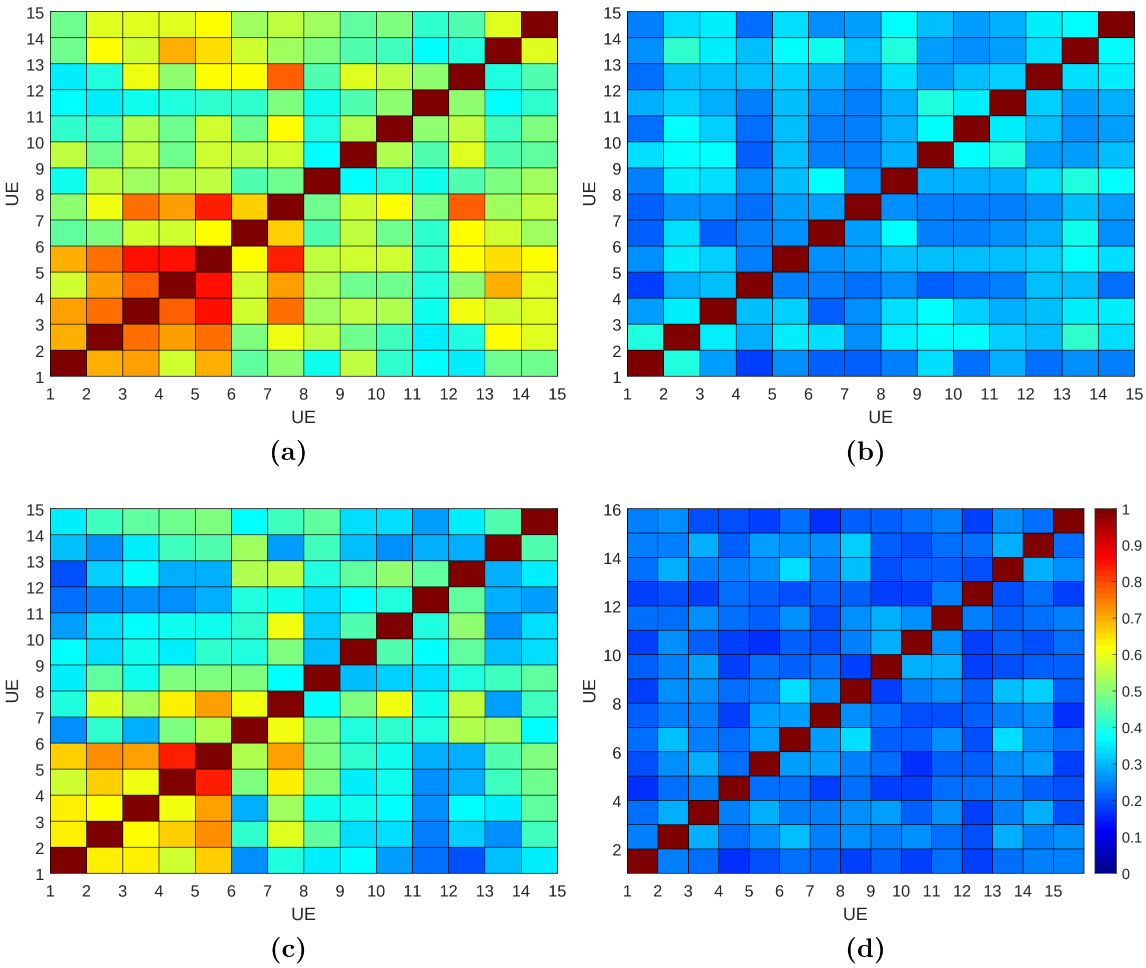

(a) (b)

(c) (d)

Figure 3.12: *Receiver Spatial Correlation matrix* $\mathbf{R}_{Rx}$ *for all UEs averaged over frequencies: Co-polarization with (a)* $M = 32$ *and (c)* $M = 64$*, Cross-polarization with (b)* $M = 32$ *and (d)* $M = 64$*.*

The evolution of ρ_{Rx} at 1.35 and 3.5 GHz for both polarizations is illustrated in Fig. 3.13 for the LOS, NLOS and total scenario with the 15 UEs. The i.i.d. curve is used for the sake of comparison.

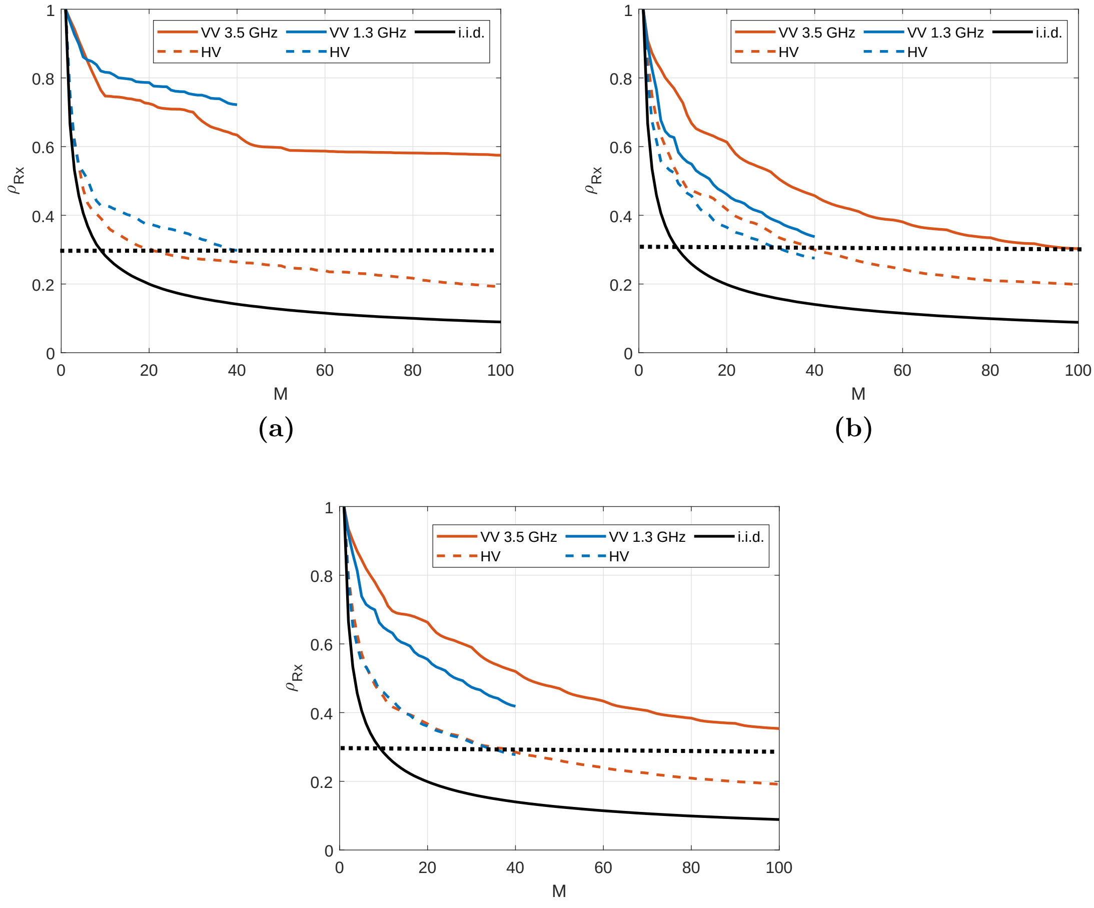

(a) **(b)**

(c)

Figure 3.13: *Average spatial correlation ρ_{Rx} evolution with M for (a) LOS scenario (b) NLOS and (c) total scenario.*

Some key points arise from the observation of ρ_{Rx}. For the total and NLOS scenarios, ρ_{Rx} for $M = 100$ is lower (0.3 in NLOS) for 3.5 GHz compared to $M = 40$ at 1.35 GHz (0.36). However, the 1.35 GHz band appears to decorrelate UEs faster with fewer antennas. This might be due to diversity richness brought by the larger Tx array at this frequency band. The largest benefits are harvested in the LOS scenario where the gap between the co- and cross-polarization schemes is more pronounced than in the NLOS case. This can be explained by the high XPD values for LOS UEs as seen in Sec. 3.5.7. Since LOS UEs have higher XPDs, the orthogonality between both polarizations is more pronounced than in NLOS. Thus, when using cross-polarization, it is suspected that the correlation curve decreases faster compared to NLOS UEs. The number of needed Tx antennas M_{min} to reach a decorrelation target value $\rho_{t,Rx} = 0.3$ (good decorrelation between users) is proposed in Table 3.8 for both polarizations.

Table 3.8: *Minimum number of Tx antennas for* $\rho_{t,Rx} = 0.3$.

Scenario	Polarization	Frequency (GHz)	
		1.35	3.5
LOS	VV	> 40	> 100
	HV	40	20
NLOS	VV	> 40	100
	HV	32	40
Total	VV	> 40	> 100
	HV	34	36

The improvement brought by the extra DoF[5] provided by cross-polarization is observed for all frequency bands and all scenarios since M_{min} is always smaller for cross-polarization schemes. In all cases, the advantages of cross-polarization are frequency-independent. It was illustrated, referring to the VV curve in LOS scenarios at 3.5 GHz, that adding more antennas does not always contribute to the decorrelation process as the curve is stable for $M > 40$. This is an example of a scenario where massive MIMO might fail because of high correlation between UEs, making simultaneous transmission a challenging task. In this case, other DoF should be used, for instance, cross-polarization. Indeed, it was indicated from this observation that massive MIMO systems in industrial scenarios can use the extra DoF from cross-polarization to lower the correlation between LOS co-polarized UEs. The same analysis was done for 6 GHz and similar results were found.

3.6.3 Gram's Power Ratio

The Gram's power ratio $\gamma(\mathbf{G})$, or the percentage of total energy toward a given intended user, is displayed for the 3.5 GHz band as a function of M. First, LOS, NLOS scenarios are compared, and then we take a closer look on the UEs power ratio for each scenario and the total scenario.

3.6.3.1 Influence of the Scenario

Normalized User Gain:

In order to understand the impact of propagation conditions, $\gamma(\mathbf{G})$ should be first compared for the same number of UEs and with corresponding normalized channels. To this purpose, UEs 3 (OLOS), 8 and 11 (strong NLOS) are omitted from the NLOS scenario for this analysis and the UE channels are normalized such that $\mathbb{E}(|\mathbf{h}_k|^2) = 1$. The average Gram's power ratio $\gamma(\mathbf{G})$ is presented for the 3.5 GHz band as a function of M in Fig. 3.14 for the LOS and NLOS UEs.

---

[5] Degrees of Freedom.

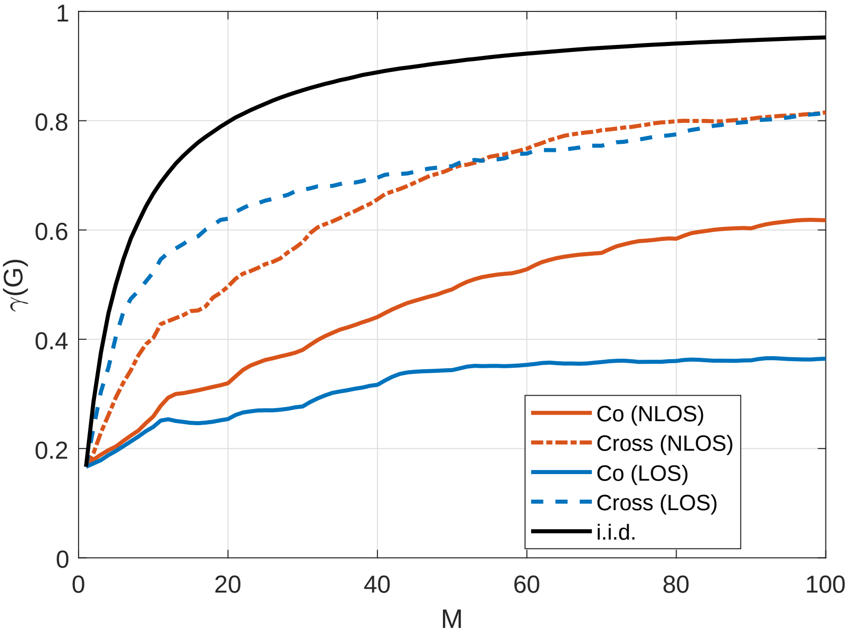

Figure 3.14: *Gram's Power Ratio* $\gamma(\mathbf{G})$ *evolution with* M *for LOS and NLOS scenarios. The UE channels are normalized to remove the effect of channel gains imbalance.*

Figure 3.14 shows that massive MIMO with cross-polar in LOS and NLOS can focus 80% of the energy toward the intended user whereas this ratio tends to 95% in i.i.d. channels. For co-polarized channels, the LOS scenario exhibits a ratio of 39% , a rather small value compared to the i.i.d. or cross-polarized case. However, for the NLOS scenario, the distribution of UEs and hence the decorrelation mechanisms will lead to a ratio of 60%. The benefit of cross-polarization is higher when dealing with LOS channels since $\gamma(\mathbf{G})$ increases from 38% to 81% when cross-polarization is applied on LOS UEs. This is less obvious for NLOS UEs where $\gamma(\mathbf{G})$ increases from 61% to 81%.

Non-Normalized User Gain: Real Case

The Gram's power ratio $\gamma(\mathbf{G})$ is plotted as a function of the UEs position for $M = 100$ and LOS and NLOS cases respectively in Fig. 3.15(a) and (b). The average $\gamma(\mathbf{G})$ for total scenario is presented in Fig. 3.15(c).

It can be globally observed from Fig. 3.15(a) and (b) that cross-polarization schemes drastically improve the Gram's Power ratio. It is also indicated from Fig. 3.15(a) that this ratio decreases with distance which was expected because the average received gain is subsequently lower. However, it still has improvement over co-polarized schemes in strong LOS scenario wherein users channels are spatially correlated and spatial separation is more challenging than in NLOS conditions as highlighted from the spatial correlation earlier.

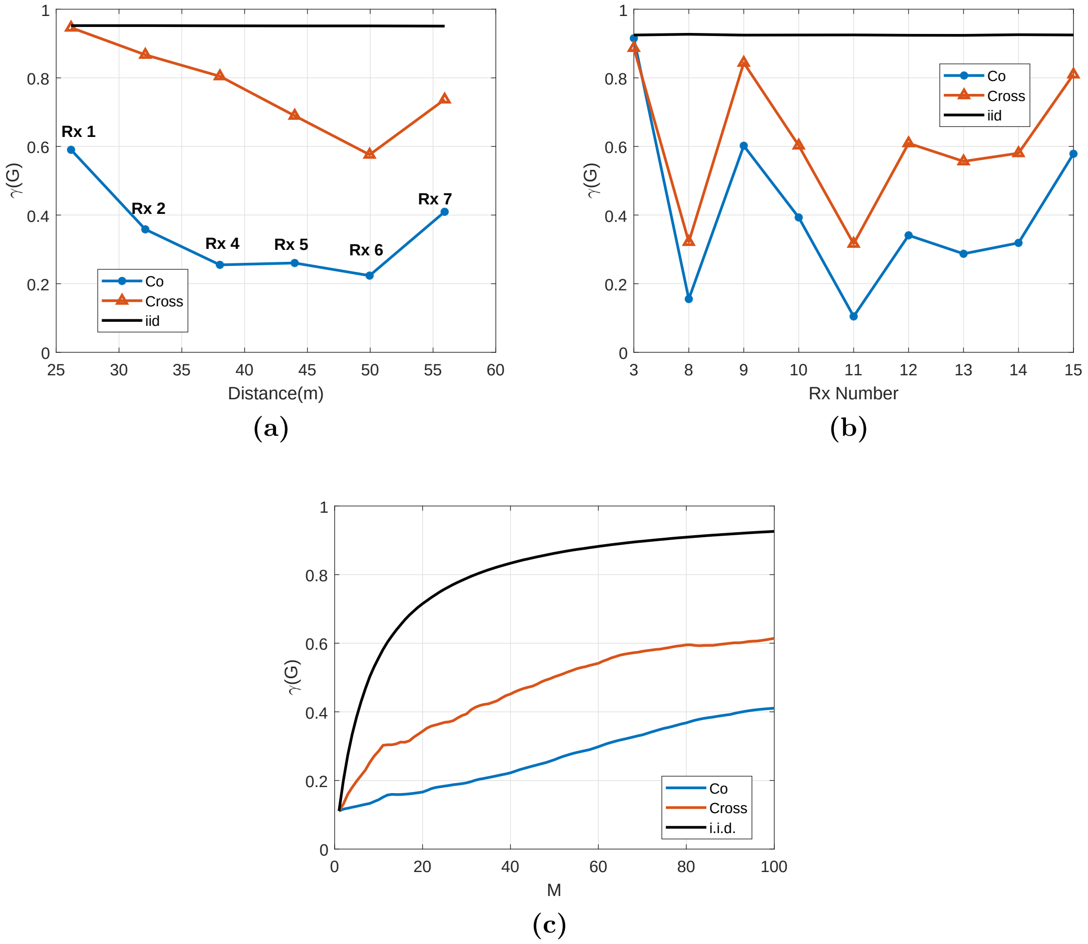

(a)

(b)

(c)

Figure 3.15: *Gram's Power Ratio $\gamma(\mathbf{G})$ evolution with UE positions for (a) LOS, (b) NLOS scenarios and (c) Average $\gamma(\mathbf{G})$ evolution in the total scenario.*

Compared to the previous paragraph (with normalized channels), this representation gives insight into the expected real performance for both LOS and NLOS scenarios. It also quantifies the Gram's power ratio for specific UE positions. In Fig. 3.15(c) (total scenario), it can be seen that the average $\gamma(\mathbf{G})$ is around 20% in co- and 52% in cross-polarization. These values are lower than for the LOS and NLOS cases which is expected since for the total scenario, each UE suffers from the sum of interferences from 14 UEs.

In conclusion, these results demonstrate that interference reduction is critical to optimize the performance of the different UEs channels. The extra DoF provided by cross-polarization is crucial to massive MIMO setups in the studied scenario. This is particularly true for strongly-correlated UEs (i.e. LOS UEs), and the use of co-polarization with an increasing M does not improve $\gamma(\mathbf{G})$. This corroborates with the results on the average spatial correlation.

3.6.4 Sum-rate Capacity:

Average spatial correlation and Gram's power ratio are both insightful parameters for massive MIMO. However, a system approach is needed to further evaluate the expected performance. Previous analysis revealed significant improvement from cross-polarization schemes. However, one downside to cross-polarization is the power penalty. In this paragraph, the trade-off between power loss and low correlation values is discussed using a sum-rate capacity analysis with different linear precoders.

Normalized User Gain:

The sum-rate of LOS and NLOS (with 6 UEs) scenarios for $M = 64$ as a function of the SNR is presented in Fig. 3.16(a) for MRT and (c) ZF. The evolution with M for $SNR = 10$ dB is presented for MRT and ZF in (b) and (d), respectively.

MRT performance:

From Fig. 3.16(a), for a SNR > 3 dB, the performance in cross-polarized channel outperforms that of the one obtained in co-polarized channels, the low correlation between UEs playing a leading part in this aspect. For $M = 64$ and $SNR = 20$ dB, it converges to ∼14 bps/Hz and ∼12 bps/Hz for NLOS and LOS scenarios, respectively. The performance as a function of M (Fig. 3.16(b)) is slowly increasing. If NLOS and cross-polarized channels are considered as the best configuration for MRT, the corresponding sum-rate capacity for $M = 64$ and $M = 100$ are 11 and 14 bps/Hz in LOS and NLOS, respectively. Lastly, the performance of MRT for $M = 100$ is only 54% of the performance in i.i.d. In the MRT case, interference is not canceled at the precoding stage, and thus, if users channels are correlated as seen from the analysis of spatial correlation in Fig. 3.13, it becomes more challenging to simultaneously transmit data. These results show that increasing the number of array elements with MRT does not contribute to drastically increase the sum-rate.

ZF performance:

From Fig. 3.16(c) and (d), the sum-rate capacity is an increasing function of SNR and M. For SNR > 5 dB, the capacity is a linear function, the best scenario being the co-polarized channel. Indeed, for an $SNR = 20$ dB and $M = 64$, the sum-rate capacity can reach ∼52 bps/Hz and ∼45 bps/Hz in NLOS and LOS scenario respectively. These values are close to the value of 60 bps/Hz obtained for i.i.d. This may be explained by the expression of the SINR in Ch. 2 (Eq. 2.47) wherein the sum-rate depends on channel gains and users interference. Using ZF, interference becomes very low such that configurations with larger received gain (co-polar schemes), reach better capacity results.

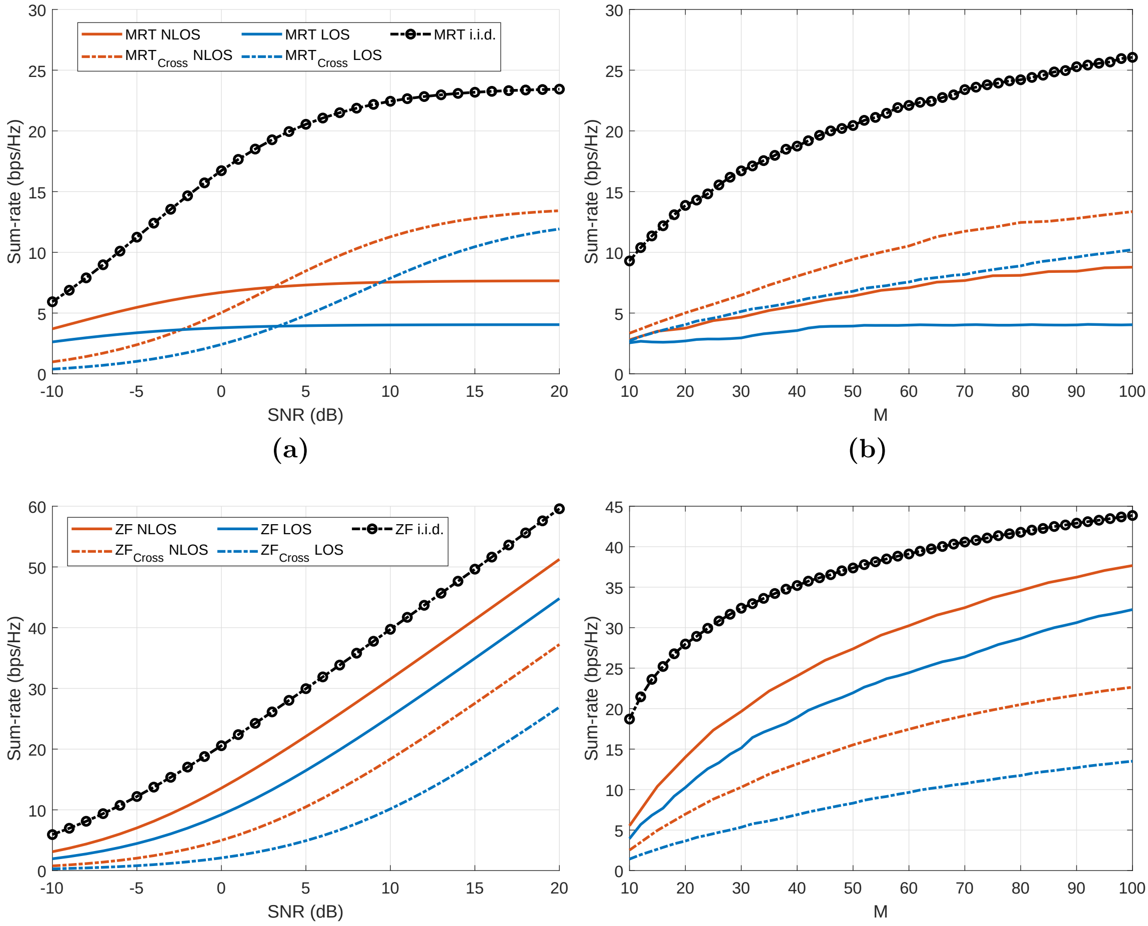

(a) **(b)** **(c)** **(d)**

Figure 3.16: *Sum-rate capacity evolution with the SNR for (a) MRT, (c) ZF for* $M = 64$ *and the evolution with* M *for a SNR of 10 dB in (b) MRT and (d) ZF. The LOS and NLOS scenarios are compared.*

.

Real Total Case

The sum-rate capacity is presented in Fig. 3.17 for the total scenario with waterfilling and $M = 64$. The UEs channels are normalized differently to account for the gain imbalance. MMSE precoding showed similar behavior than with ZF, thus, only MRT and ZF will be presented.

The conclusions formulated above remain applicable for the total scenario. The capacity with ZF and MRT are nearly similar for SNRs lower than 0 dB (MRT slightly better) but extremely low capacities with regard to the total number of elements are obtained. Beyond this, the MRT capacity in cross-polar converges to 18 bps/Hz at 20 dB for $M = 64$.

For co-polar channels, ZF precoding for which capacity increases linearly, makes

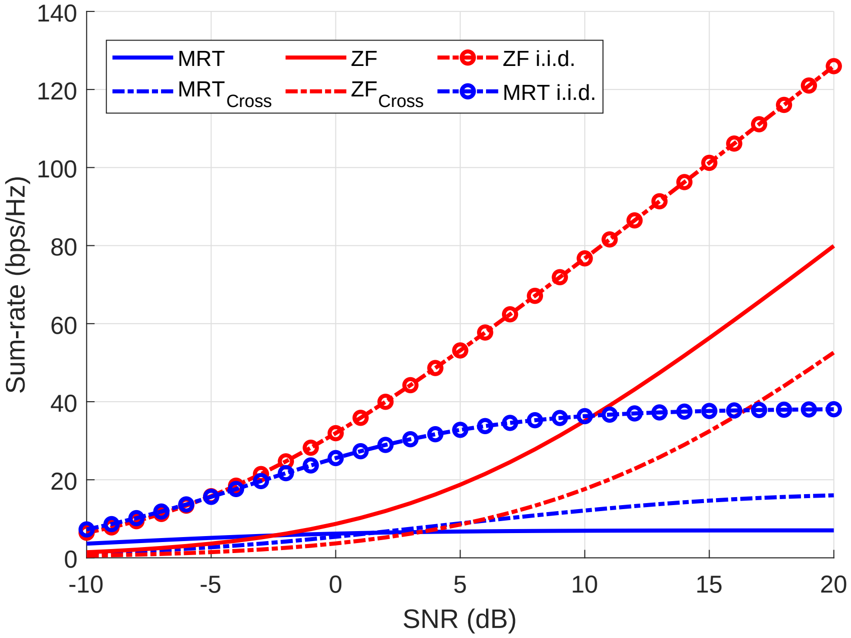

Figure 3.17: *Sum-rate capacity evolution with the SNR for the total scenario with MRT, and ZF. The results are presented for* $M = 64$.

it possible to reach 80 bps/Hz for a SNR of 20 dB. As already discussed, the advantage of MRT relies in its simplicity and energy efficiency even though ZF will almost always leads in terms of SE. Also, using waterfilling, a saturation effect for co-polarization schemes (very slow increase with the SNR in cross-polarization) appears, indicating that waterfilling is not optimal for MRT schemes. Table 3.9 summarizes the different results in this section:

Table 3.9: *Summary of Sum-rate capacity results with* $M = 64$ *and* $SNR = 20$ *dB.*

Precoder	ψ	**Sum-rate (M=64, SNR=20 dB)**	**Best Approach**	**Application**
MRT	Co	8 bps/Hz	Cross	Small Packets Less Complexity
	Cross	18.5 bps/Hz		
	i.i.d.	40 bps/Hz		
ZF	Co	80 bps/Hz	Co	High Data Rates
	Cross	54 bps/Hz		
	i.i.d.	123 bps/Hz		

From this analysis, it can be seen that cross-polarization can be of great benefit for MRT even though it results in less average received power. However, it should be noted that the values of sum-rate capacity are not very large for MRT schemes limiting their use to applications with low data rates whilst ZF appears to be a very appealing solution for high data rate applications since very good sum-rate capacity (∼43 bps/Hz for 6 UEs) are observed.

3.7 Communication Strategy Using Polarization Diversity

Until now, the extra DoF brought by cross-polarization was not exploited in any UEs allocation strategy yet. In this section, a novel communication scheme using simultaneously co- and cross-polarized channels is presented. The idea is to use $\hat{M}$ ($\hat{M} = M/2$) RF chains in co- and $\hat{M}$ in cross-polarization to simultaneously serve the different UEs. The channel is still a $K \times M$ matrix, but the UEs are served (equally or not) either via the VV link or HV link. This is illustrated in Fig. 3.18 where (a) is the full VV channel (or HV channel) and (b) general polarization diversity scheme where K_v UEs communicate over VV and K_h over the HV channel. The full channel matrix can be depicted into two parts: (1) $\mathbf{H}_{co} \in \mathbb{C}^{K_v \times \hat{M}}$ and (2) $\mathbf{H}_{cross} \in \mathbb{C}^{K_h \times \hat{M}}$.

Physical Vs Logical Configurations

Referring to [9], two features of AP can be distinguished: physical antenna arrays and logical configurations. This is equivalent to the definitions in Ch. 1 (in 1.4.2). In our case, Fig. 3.18(a) has a (10,10,1) logical structure (10 rows, 10 columns, co- or cross-polarization) while the proposed scheme in (b) has a (5,10,2) structure with both polarizations simultaneously used.

3.7.1 UEs Allocation Algorithms

The applied strategy relies on the correlation matrix defined in Ch. 2 (Eq. 2.17) and then averaging over all frequency points. Observing the different correlation values $\rho_{i,j}$, the goal is to find the couples (i, j) with large $\rho_{i,j}$. To compensate this high correlation value, the corresponding UEs are mapped to orthogonal polarizations. The allocation of UE per polarization is determined via two strategies presented in Appendix F.

- Strategy 1 will map two UEs on two different polarizations if and only if $\rho_{i,j} \geq \rho_{th}$, a specified threshold chosen to be 0.75 in this investigation. This algorithm will favor the VV channels ($K_v > K_h$). Indeed, UEs in NLOS conditions will generally have small $\rho_{i,j}$ values ($< \rho_{th}$) and will then be mapped to VV.

- Strategy 2 will always map UEs with maximum correlation coefficient on orthogonal polarizations. In this case, this algorithm will equally distribute UEs between co- and cross-polarizations ($K_v \sim K_h$) even if $\rho_{i,j}$ is not very large.

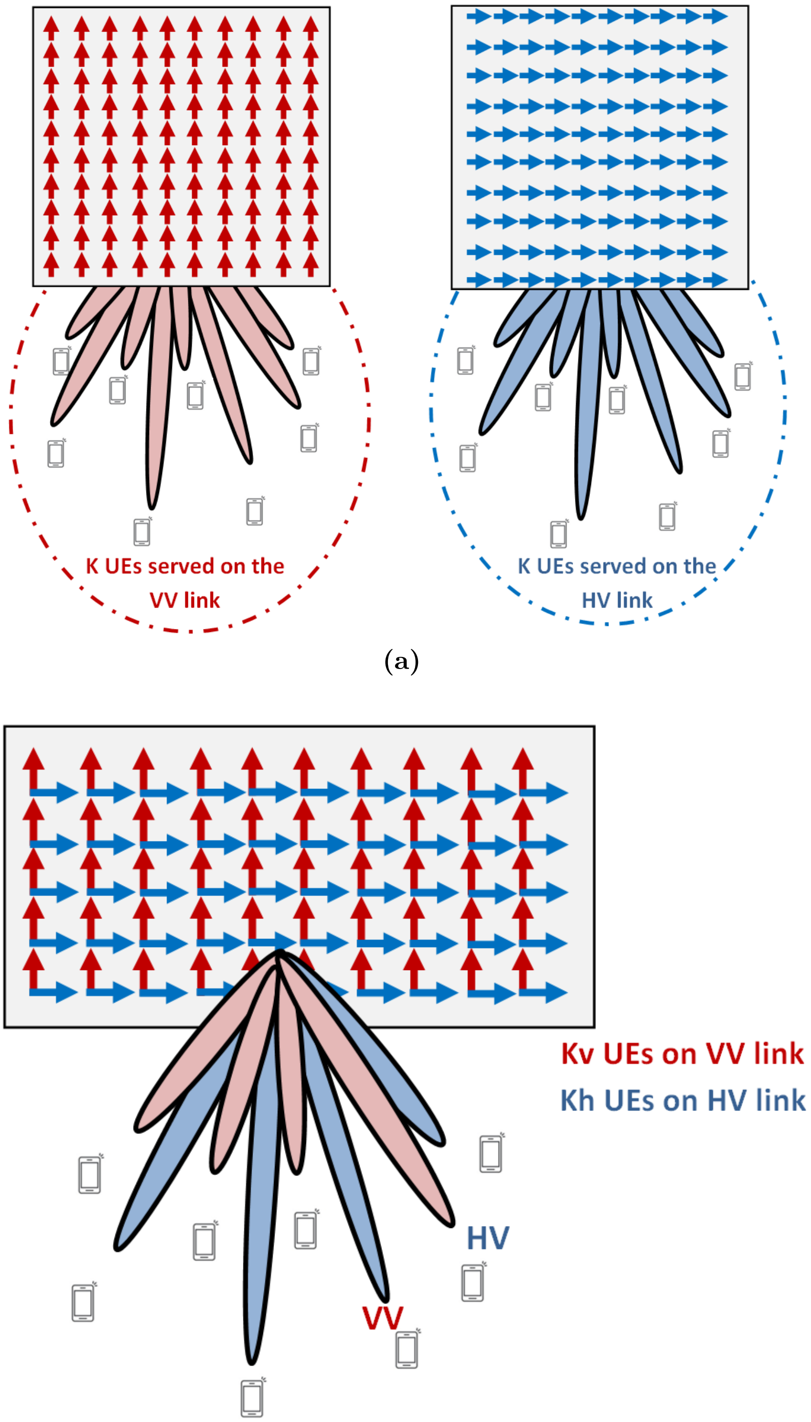

(a)

(b)

Figure 3.18: *Communication scheme with (a) Full co- or cross-polarized channel with* $M = 100$ *and (b) Diversity scheme with* $\hat{M} = 50$.

These two strategies give the following polarization maps for the different UEs:

UE	1	2	3	4	5	6	7	8	9	10	11	12	13	14	15
ψ (BS $\rightarrow$ UE)-**Str. 1**	V	H	V	V	H	V	H	V	V	V	V	V	V	V	V
ψ (BS $\rightarrow$ UE)-**Str. 2**	V	H	V	V	H	V	H	H	H	H	V	V	H	V	V

Table 3.10: *UEs polarization maps using strategy 1 and 2.*

In Strategy 1, $K_h = 3$ and $K_v = 12$. This justifies the purpose of this algorithm: a trade-off between gain optimization and polarization diversity for highly correlated users. In Strategy 2, $K_h = 7$ and justifies the purpose of this algorithm to reduce the correlation as much as possible with no consideration on channel gains.

3.7.2 Results

The sum-rate capacity is presented for $N_{RF} = 100$ (to avoid confusion with M) for full co- and cross-polarization compared to both strategies. N_{RF} is the same for diversity and full co- or cross-polarization schemes. The total scenario is considered for these results.
For MRT and $SNR < 0$ dB, both strategies give similar results compared to co-polarized channel whereas at higher SNR, performance of MRT in cross-polarized channel remains the best configuration. Figure 3.19(b) shows that the 2 proposed strategies provide the best results with $N_{RF} < 36$. Since MRT totally ignores interference, the strategy minimizing correlation between UEs (Strategy 2) presents better results. For ZF, for any SNR, the performance between Strategy 1 and the co-polarized channel gives similar sum-rates that are the highest for all configurations. ZF aims at removing interference at a power penalty cost. Hence, the strategy of using more co-polarized channels (larger gain) remains the most powerful (Strategy 1). A summary of main results is given in Table 3.11.

These results are interesting for mobile operators especially when infrastructure cost and space are considered. The main advantage of using 50 dual-polarized antennas being a smaller array size, one can expect having less channel spatial variability along the array and potentially less variations in channel gain guaranteeing channel hardening. Moreover, it was demonstrated that it is possible to use polarization diversity as an extra DoF to propose novel transmission schemes with reduced array size.

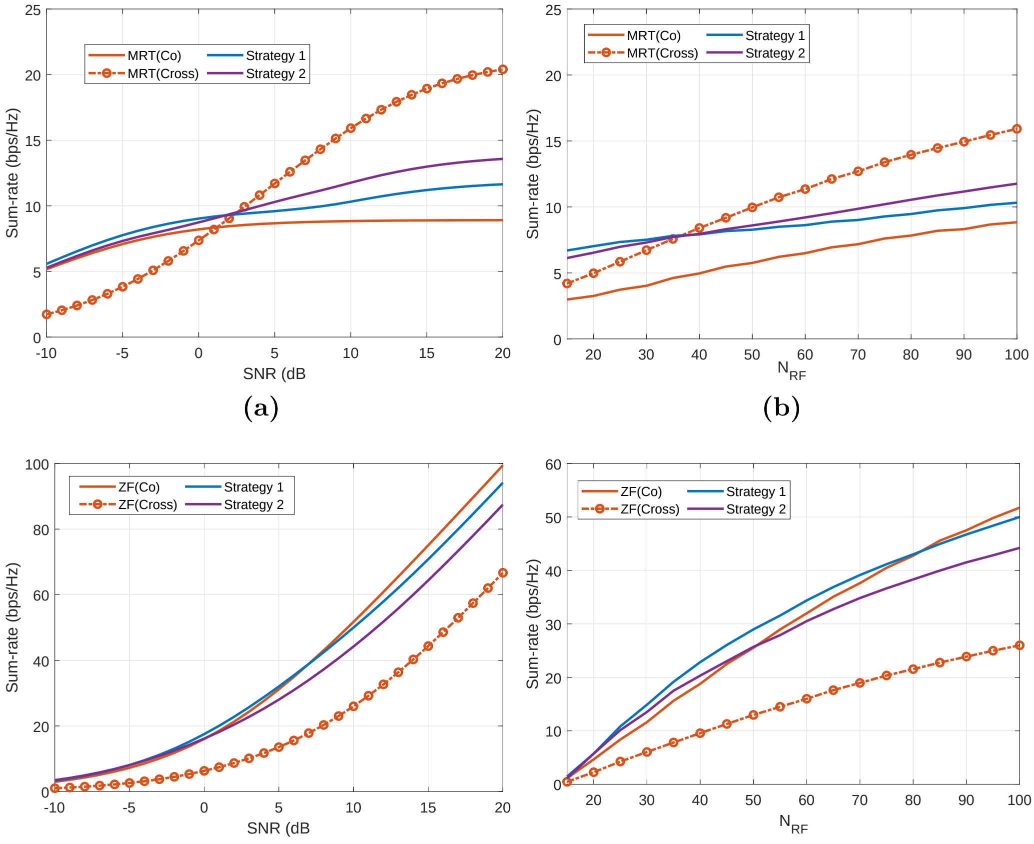

(a) (b) (c) (d)

Figure 3.19: *Sum-rate capacity evolution with the SNR for (a) MRT, (c) ZF for* $N_{RF} = 100$ *and the evolution with* N_{RF} *for a SNR of 10 dB in (b) MRT and (d) ZF.*

.

Table 3.11: *Summary of sum-rate capacity results with the proposed diversity schemes.*

Precoder	**Scheme**	**Sum-rate (N_{RF}=100, SNR=20 dB)**
MRT	Co	9 bps/Hz
	Cross	21 bps/Hz
	Strategy 1	12 bps/Hz
	Strategy 2	14 bps/Hz
ZF	Co	100 bps/Hz
	Cross	67 bps/Hz
	Strategy 1	96 bps/Hz
	Strategy 2	89 bps/Hz

3.8 Conclusion

Polarimetric channel measurements of a massive MIMO setup for an indoor industrial scenario are presented at 1.35, 3.5 and 6 GHz with 80 MHz bandwidth. The scenario consists in a massive URA transmitter and 15 distributed UEs. The industrial massive channel was evaluated using propagation metrics (average received gain, coherence bandwidth, Ricean factor, Tx correlation and Gram's power ratio) and system oriented metrics (sum-rate capacity). The propagation channel parameters were useful to classify UEs into two distinct groups: LOS and NLOS. The median correlation between users reveals strong correlation in LOS co-polarized channel whereas low correlation is obtained in all cross-polarized channels. Channel hardening allowed to point out the spatial variability along the array. In order to evaluate whether the channel is favorable for massive MIMO, the Gram's power ratio reveals that cross-polarized channel exhibits the best ratio in NLOS scenario and drastically improves the power ratio in LOS scenarios. From sum-rate capacity analysis (with the 3.5 GHz band), the best configuration for the 2 precoding techniques was presented: (a) MRT with cross-polarization can provide a sum-rate capacity of 18 bps/Hz with 64 antennas and 10 dB SNR whereas (b) ZF exhibits a sum-rate capacity of 54 bps/Hz in co-polarized channel. Cross-polarization with ZF does not improve the overall performance. The simplicity provided by MRT and the improvement offered by cross-polarization can benefit massive MIMO setups for indoor industrial environments. Finally, from previous analysis, it was concluded that increasing the number of antennas does not always improve overall results, and depending on the channel, other techniques should be considered. Two strategies exploiting polarization diversity were proposed which achieve very high sum-rate capacities (similar to co-polar in ZF) with a 50-element dual-polarized array. Compared to full co- and cross-polarization schemes, diversity schemes jointly exploiting high channel gains in co-polarization and better decorrelation in cross-polarization can achieve near-optimal results and can, therefore, be beneficial for massive MIMO setups in Industry 4.0.

3.9 Summary of Key Points

• Polarimetric massive MIMO measurements in industrial scenarios are exploited to characterize the channel with propagation-based metrics and the overall system-performance with sum-rate analysis.
• A classification method jointly using the coherence bandwidth and Tx correlation was used to categorize distinct scenarios.
• B_c, ρ_{Tx} and K^{Rice} are not frequency-dependent but these parameters cross-correlation is frequency dependent.
• Channel hardening and favorable propagation conditions are both demonstrated to be dependent on the scenarios and channel polarizations.
• The percentage of focused energy for an intended UE was shown to depend on propagation conditions. Moreover, cross-polarization schemes improve the power ratio, especially in LOS conditions.
• Sum-rate capacity quantified the impact of cross-polarization on MRT and ZF. While cross-polarization schemes are important for MRT, no improvement is noticed with ZF.
• The use of MRT is limited to applications not requiring very high sum-rate capacities whereas ZF with waterfilling is adequate for such applications.
• Polarization diversity is exploited via UEs allocation strategies. The results highlight the possibility of using dual-polarized arrays with half the number of array elements to achieve nearly the same results for co-polarized schemes in ZF.
• Polarization diversity schemes combined with UE allocation strategies and spatial diversity can achieve good results despite the inherent power imbalance between polarizations.

Chapter 4

Propagation-Based Antenna Selection Strategies

Introduction

It was demonstrated in the previous chapter that polarization diversity can greatly benefit massive MIMO setups in industrial environments. It was also observed that massive MIMO can encounter some “unfavorable” propagation conditions, especially, for UEs aligned in LOS conditions. While UE allocation strategies taking into account polarization diversity were highlighted, reduction of the number of RF chains have not been addressed yet. To this purpose, antenna selection strategies and hybrid beamforming wherein a smaller number S of RF chains is used ($S < M$) are needed. In another matter, capacity improvements in massive MIMO depend on CSIT in order to efficiently precode users signals. Originally, massive MIMO was labeled under the TDD mode. Nonetheless, motivated by spectrum regulation aspects, FDD is converging as an alternative solution. However, the complexity arising from CSI feedback in FDD-based systems is a bottleneck, and efficient estimation strategy are yet to be fully defined. This chapter addresses two following main challenges:

1. Reducing the number of reference elements at transmitter side (elements that send pilot signals) for the channel estimation in FDD mode.
2. Optimize the sum-rate capacity in the scenario, while minimizing the number of active RF chains serving simultaneously a given number of receivers.

Chapter Outline

After a thorough review of TDD and FDD-based systems in Sec. 4.1, we present another approach to decrease the overhead related to the determination of CSIT. The proposed method is evaluated for measured radio channels in an industrial scenario at 3.5 GHz and its performance is discussed in Sec. 4.1.3 before concluding in Sec. 4.1.4. A review of antenna selection strategies is then provided in Sec. 4.2 and the proposed selection strategy, selection criterion and evaluation algorithm are presented. Finally, 4.2.2 is dedicated to the strategy validation and performance results before concluding this part in 4.2.3. A general conclusion can be found at the end of the chapter.

4.1 CSI Feedback Reduction in FDD mode

Capacity improvements rely on the availability of CSIT. Massive MIMO was originally conceived using the calibrated TDD strategy, exploiting channel reciprocity to estimate the instantaneous channel from UL pilots. However, motivated by spectrum regulation issues and the far majority of currently deployed FDD-based systems, significant interest in massive MIMO-FDD versions have emerged [126, 130]. Also, FDD systems were reported to be more effective than TDD systems in specific situations with symmetric traffic and delay-sensitive applications [127, 128]. In FDD mode, fading channel reciprocity is not exploitable because UL and DL channels use different frequency bands. DL training becomes a bottleneck in FDD and CSIT generates high overhead which fundamentally limits the number of potential simultaneous data streams. In order to reduce DL training feedback overhead and materialize significant massive MIMO gains in FDD systems, FDD-based schemes solutions are necessary.

4.1.1 Context and Methodologies

4.1.1.1 Related Work

In [196], the performance of the two strategies (TDD- and FDD- based) is compared from a set of measurements at 2.6 GHz with a 128-element virtual uniform-linear array (ULA). It was reported that FDD beamforming with predetermined grid-of-beams may achieve close performance to TDD but heavily depends on advantageous propagation conditions, particularly LOS conditions and high Ricean factor values. In other cases, TDD beamforming emerges as the only alternative. Various solutions have already been proposed to cope with the limitations of FDD-based massive MIMO systems.

A simplified DL scheduling based on joint spatial division and multiplexing is studied in [130, 197, 198], the users being clustered into groups having similar channel covariances. If the user distribution is such that the channel matrix has a low rank, [199] proposes to use this property to make a joint recovery of CSIT for all scheduled users, each of them directly feeding back the pilot observation to the BS without performing channel estimation. Compressive-sensing-based approaches exploiting sparsity properties of the channel are proposed in [200, 201], while temporal-correlation based approaches using treillis-code based quantization codebooks and memory-based channel sequences to decrease CSIT estimation are described in [126]. In [202], the basic idea is to exploit the structure of the spatial channel correlation matrix (CCM) with reduced CSIT and use the dominant Eigen-space and Karhunen-Loeve representation. These models are mostly based on Rayleigh channels assuming NLOS propagation and mutually independent user channels with rich local scattering. The different proposed methods are shown to perform well provided important channel correlations but this depends on many factors as the environment, user positions, etc. It must be emphasized that results based on measured channels are quite scarce.

4.1.1.2 Preview of the Method

The channel characteristics used to validate the approach are those deduced from experimental data, as described in Ch. 3. Since measurements have been performed under static conditions, the efficiency of the proposed method is based on a comparison between results obtained with the full measured matrix to those calculated with the estimated matrix. The approach is based on successive steps:

- During the initialization process at time t, the full CSIT is measured with the classical approach using feedback of the users, allowing the determination of the full $K \times M \times M$ CCM matrix $\mathbf{R}_{Tx}(t)$.

- To get an updated estimate of CSIT at time $t+\Delta t$, the channel transfer matrix $\mathbf{H}_{ref}(t+\Delta t)$ between the UEs and only a small number of array elements, called reference antennas (ref) in the following, are measured, in order to strongly decrease the overhead time.

- An updated estimation $\hat{\mathbf{H}}(t+\Delta t)$ of CSIT is deduced at the base station (BS) from the knowledge of $\mathbf{R}_{Tx}(t)$ and $\mathbf{H}_{ref}(t+\Delta t)$.

The preview of the method is summarized in Fig. 4.1.

4.1.1.3 Framework For Channel Estimation

In this section, the fixed Tx array size is reduced from 10×10 to 9×9 URA, simply to satisfy symmetry constraints when choosing the reference elements. Results presented hereafter suppose that the occupied frequency band is 20 MHz, which is the maximum available DL bandwidth for LTE systems. Within this band, the channel transfer function is measured on M_f frequency points, with $M_f = 205$. Nevertheless, to increase the number of realizations, measurements have been made on 4 adjacent bands of 20 MHz, allowing the study of the average performance of the proposed CSIT recovery. For each position k of the Rx antenna, the wideband complex channel transfer function between Rx and any element (i, j) of the Tx array is given by $\mathbf{h}_{k,ij}(f) \in \mathbb{C}^{1\times M_f}$.

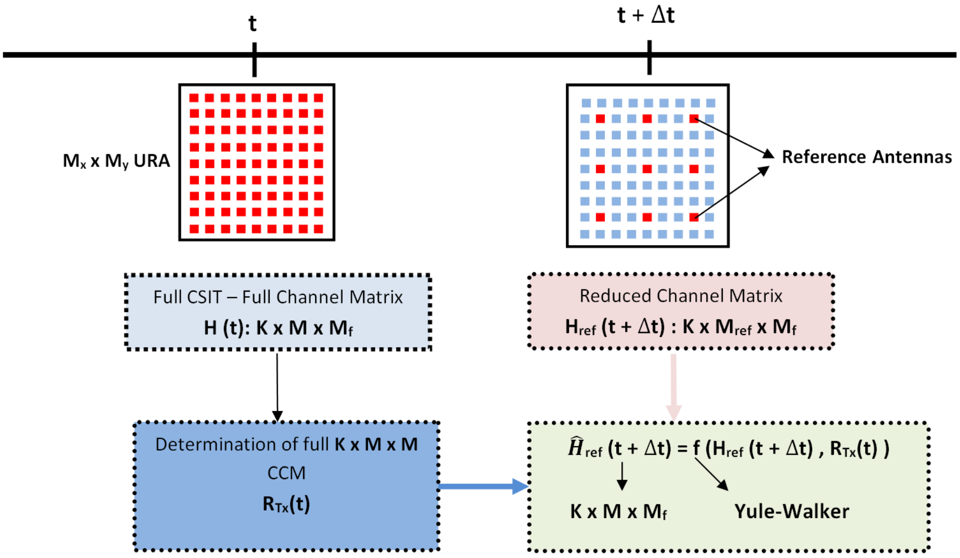

Figure 4.1: *Simplified preview of the method to estimate user channels with reduced feedback overhead.*

4.1.2 Estimation Procedure

In this section, the different guidelines for the channel estimation with the proposed method are presented. First, the importance and impact of correlation in the model is discussed, then the principle of the CSIT estimation procedure with reduced complexity is explained.

4.1.2.1 Tx Correlation

To point out the difference in terms of correlation between different scenarios, we have plotted in Fig. 4.2, the CDF of the amplitude of the Tx correlation matrix between any 2 antennas of the array and distinguishing LOS, OLOS and NLOS (grouped UEs) as explained in Ch. 3 (3.5.4).

The CDF has been calculated by considering all possible antenna element separations from d to $8d$, the minimum spacing d being equal to 0.5λ and the 4 bands of 20 MHz. Obviously, correlation values are larger in LOS scenarios, the median value of ρ_{Tx} decreasing from 0.95 to 0.67 if the UE moves from LOS to NLOS.

This can also be seen by looking at $\mathbf{R}_{Tx}$ in Fig. 4.3, for (a) LOS UE 1, (b) OLOS UE 3 and (c) NLOS UE 8.

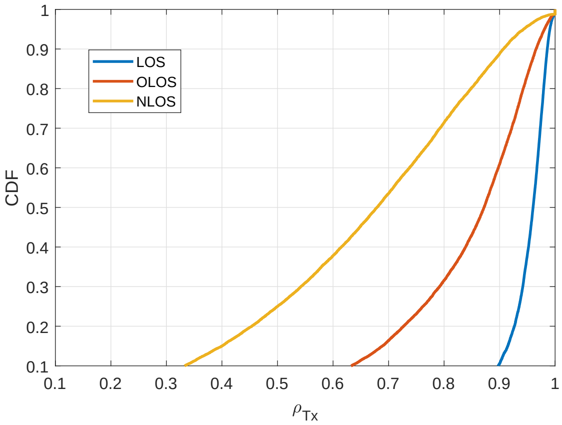

Figure 4.2: *CDF of correlation values for any inter-element spacing in the array for LOS, NLOS and OLOS scenarios.*

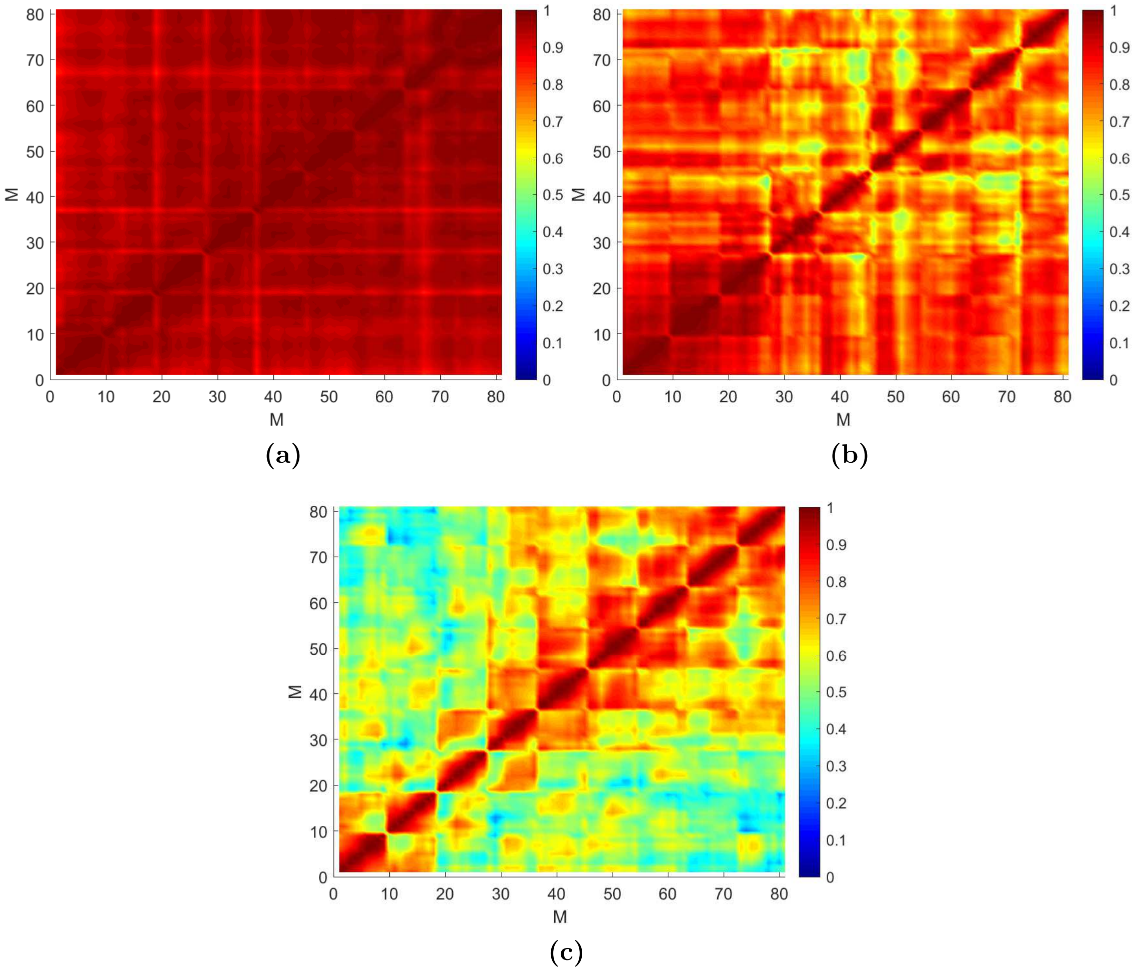

(a) **(b)**

(c)

Figure 4.3: *Colormap of the full CCM* $\mathbf{R}_{Tx}$ *for UE 1 (a), 3 (b) and 8 (c), respectively in LOS, OLOS and NLOS conditions.*

It is also noticed that the Tx correlation reflects fading characteristics of the massive MIMO channel. This is well depicted in Fig. 4.3(b) wherein the variability of fading statistics is observed across Tx antennas, especially in OLOS UE.

To highlight the antenna element-spacing influence, the CDF of $\mathbf{R}_{Tx}(t)$ is plotted in Fig. 4.4 for spacing values varying from d to $8d$. Due to the configuration of the hall where measurements took place and the relative positions of the Tx and Rx antennas, the correlation is not the same between elements aligned along an horizontal line (x axis) or a vertical line (z axis). CDF curves corresponding to these 2 cases are shown in Fig. 4.4(a) and (b), respectively, and are deduced from all values of $\mathbf{R}_{Tx}(t)$ calculated for the 15 geometrical scenarios previously described, without distinguishing LOS, OLOS and NLOS scenarios.

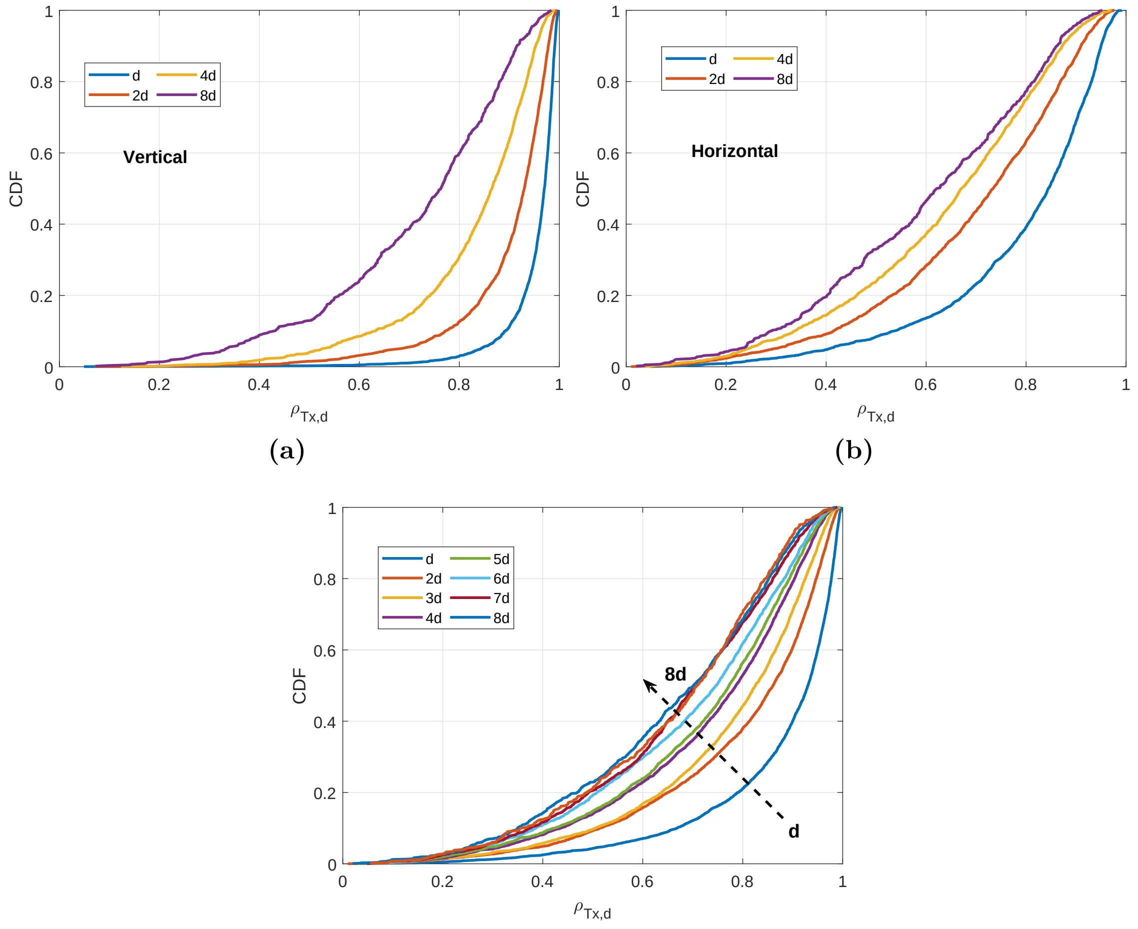

(a) (b) (c)

Figure 4.4: *CDF of Tx correlation values in vertical plane (a) and horizontal plane (b) for different antenna spacing: 2d, 4d, 6d, 8d. In (c), the correlation values of the full correlation matrix is presented for all possible spacing d and in both directions x and z merged.*

Comparison of Fig. 4.4(a) and (b) indicates that correlation is much higher in the vertical plane than in the horizontal plane. Indeed, taking the shape of the hall (scatterers in the horizontal plane) and the position of the antennas into account, all possible rays have a narrower angular spread in the elevation domain compared to the azimuth domain, thus minimizing the phase shift between them. For the horizontal correlation, the median value decreases as a function of the antenna separation, from ∼0.9 for d, to ∼0.8 for $2d$ and ∼0.6 for $8d$. Finally, the CDF of all correlation values for all spacing values along both directions (d to $8d$) is presented in Fig. 4.4(c). These results, especially the last one, will be used in the next section to optimize the parameters of the proposed approach minimizing CSIT overhead.

4.1.2.2 Principle of CSIT Estimation Procedure

In this section, to reduce the amount of notation and without loss of generality, only one UE is considered. The subscript k identifying the user is then omitted. It is assumed that, during an initialization process occurring at a time t, the DL channel transfer vector $\mathbf{h}_{ij}$ between the UE and any antenna (i, j) of the array is estimated by the UE and sent back to the BS. Hence, the question which arises is to estimate this transfer vector at time $t + \Delta t$ while minimizing the complexity of the procedure and, therefore, the number of symbols needed for this estimation. The basic idea of the proposed approach is to measure the channel between a user and only a reduced number M_{ref} of antennas, belonging to a subset of the massive array, and called reference antennas. The full transfer matrix will then be estimated owing to the knowledge of a reduced correlation vector, as detailed in the next paragraph.

4.1.2.3 Determination of the reduced correlation vector

Let (i, j) be the indices of any antenna, along the horizontal and vertical axis, respectively, and (i', j'), noted (ref) to simplify the presentation, those of the reference antenna. The channel vectors between the UE and (i, j) on one hand, and between the UE and (ref) on the other hand, are complex-valued vectors in the frequency domain noted $\mathbf{h}_{ij}$, and $\mathbf{h}_n$, respectively, their size being $(1 \times M_f)$. At time t, since the full transfer matrix has been measured, the correlation coefficient $\rho_{ij,n}$ between $\mathbf{h}_{ij}$, and $\mathbf{h}_n$, and given by Eq. 4.1, can be calculated as:

$$\rho_{ij,n} = \frac{\mathbf{h}_n \mathbf{h}_{ij}^H}{\|\mathbf{h}_n\| \|\mathbf{h}_{ij}\|}. \tag{4.1}$$

Applying Eq. 4.1 to the M_{ref} reference elements leads to a reduced correlation vector $\boldsymbol{\rho}_{ij}(t) = [\rho_{ij,1},\ \rho_{ij,2},\ ...\rho_{ij,M_{ref}}]^T$. Generalizing for all (i, j) values, the reduced correlation matrix can be computed. We suppose that, during the time interval Δt, the change in the channel characteristics are not significant and that $\boldsymbol{\rho}_{ij}(t)$, corresponding to a second order statistics, does not vary appreciably.

4.1.2.4 Estimation of the channel matrix

In a second step, we propose to estimate the channel vector $\hat{\mathbf{h}}_{ij}(t+\Delta t)$ between the UE and any array element (i,j) from the knowledge of $\mathbf{h}_n(t+\Delta t)$ and $\boldsymbol{\rho}_{ij}(t)$, by applying the Yule-Walker equations [203, 204][1].

In our case, a different approach is applied since the estimation of a given transfer function depends on its correlation with known reference elements. It can be considered as a spatial equivalent of the classical AR model since the quality of the estimation would eventually depend on the distribution of reference elements inside a Tx array. In the following, to simplify the notation and since there is no ambiguity, the time reference t or $t+\Delta t$ is omitted. In order to determine the estimate $\hat{\mathbf{h}}_{ij}$, $\boldsymbol{\alpha}_{ij}$ is first defined as:

$$\boldsymbol{\alpha}_{ij} = \mathbf{X}_{ij}^{-1}\boldsymbol{\rho}_{ij}, \tag{4.2}$$

$\mathbf{X}$ is a $M_{ref} \times M_{ref}$ Toeplitz matrix defined as:

$$\begin{bmatrix} 1 & \rho_{ij,1} & \rho_{ij,2} & \cdots & \rho_{ij,M_{ref}-1} \\ \rho_{ij,1} & 1 & \rho_{ij,1} & \cdots & \rho_{ij,M_{ref}-2} \\ \rho_{ij,2} & \rho_{ij,1} & 1 & \rho_{ij,1} & \cdots \rho_{ij,M_{ref}-3} \\ \vdots & \dots & \ddots & \dots & \vdots \\ \rho_{ij,M_{ref}-1} & \rho_{ij,M_{ref}-2} & \cdots & \cdots & 1 \end{bmatrix} \tag{4.3}$$

The estimate $\hat{\mathbf{h}}_{ij} \in \mathbb{C}^{1\times M_f}$ can be written in the following form:

$$\hat{\mathbf{h}}_{ij} = \boldsymbol{\alpha}_{ij}^T \mathbf{H}_{ref}, \tag{4.4}$$

with $\mathbf{H}_{ref}$ (ref is just a subscript and not an index), the $M_{ref} \times M_f$ channel matrix containing all measured channel vectors $\mathbf{h}_n$ of the reference elements $n = 1, 2, .., M_{ref}$.

The estimate $\hat{h}_{ij}(f)$ at frequency f can be written as:

$$\hat{h}_{ij}(f) = \sum_{n=1}^{M_{ref}} \alpha_{ij,n} h_n(f) \tag{4.5}$$

which can be generalized for M_f:

$$\hat{\mathbf{h}}_{ij} = \sum_{n=1}^{M_{ref}} \alpha_{ij,n} \mathbf{h}_n \tag{4.6}$$

The following table summarizes the sizes of the different used notations.

---

[1] The Yule-Walker equations named after Udny Yule and Gilbert Walker relate auto-regressive (AR) model parameters to the autocovariance of a random process. An AR model is used to describe a time-varying process where the output variable depends linearly on its previous values and on a stochastic term. In channel estimation, the AR model is an iterative method usually applied to minimize the mean square error of the difference between the known and estimated complex transfer function [205, 206] using time-series expansions.

Matrix or Vector	Size
$\hat{\mathbf{h}}_{ij}$	$1 \times M_f$
$\mathbf{X}_{ij}$	$M_{ref} \times M_{ref}$
$\boldsymbol{\rho}_{ij}$	$M_{ref} \times 1$
$\boldsymbol{\alpha}_{ij}$	$M_{ref} \times 1$
$\mathbf{H}_{ref}$	$M_{ref} \times M_f$
$\mathbf{h}_n$ or $\mathbf{h}_{ref}$	$1 \times M_f$

For a MU configuration with K users, this approach is repeated K times. Qualitatively, one can expect that this approach will give better results if the channel transfer function does not strongly vary from one reference antenna to its nearest one and if the related correlation coefficient remains high. Therefore, an analysis on the accuracy of the method depending on the spread of the correlation functions as a function of the antenna spacing, and on the number and choice of the reference antennas is required and discussed in the next section. The criteria chosen for evaluating the performance of the proposed approach is the accuracy to predict the channel capacity C. Links to individual SU or a global link to MU (simultaneous transmission) are considered. Fot the latter, the sum-rate capacity is calculated with two precoding techniques: MRT and ZF.

4.1.3 Optimization of the Algorithm and Performances

The channel characteristics used to validate the approach are those deduced from experimental data, as described in previous sections. Since measurements have been performed in static conditions, the efficiency of the proposed method is based on a comparison between results obtained with the full measured matrix to those calculated with the estimated matrix.

As an example, a measured channel transfer function (CTF) and the corresponding estimated function for a NLOS case (UE 8, $M_{ref} = 9$, 4 ×20 MHz adjacent bands) are presented in Fig. 4.5. The estimated CTF follows well the measured CTF.

4.1.3.1 Single-User Configuration

The ergodic capacity for any UE k, assuming equal power allocation over array antennas, and deduced from the measured channels is given by:

$$C = \log_2 \left(\det(1 + \left(\frac{SNR}{M} \mathbf{h}\mathbf{h}^H \right) \right), \tag{4.7}$$

where SNR is the mean signal-to-noise ratio and $\mathbf{h}$ is a $1 \times MM_f$ vector corresponding to a vectorization of the transfer matrix $\mathbf{H}$ for one UE of size $M \times M_f$, its columns being the vectors $\mathbf{h}_{ij}$. The capacity $\hat{C}$ calculated from the estimated channels, is obtained by replacing $\mathbf{h}^H$ (the precoding vector) in Eq. 4.7 by $\hat{\mathbf{h}}^H$ such as:

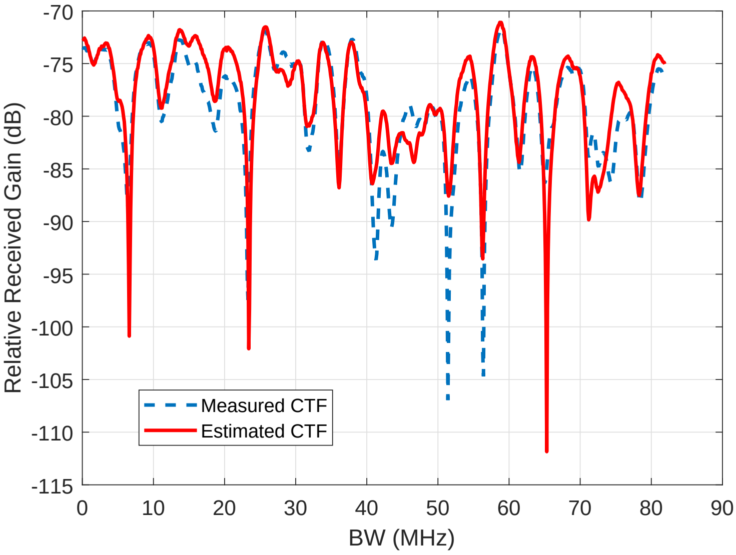

Figure 4.5: *Measured vs. Estimated transfer function for UE 8.*

$$\hat{C} = \log_2 \left(\det(1 + \frac{SNR}{M} \mathbf{h}\hat{\mathbf{h}}^H) \right), \tag{4.8}$$

Evidently, $\mathbf{h}$ is not replaced by the estimate since it is the actual channel and should not be changed. The ratio between $\hat{C}$ and C (computed from measured channels), noted β gives an idea on the performance of the proposed strategy. It is defined as:

$$\beta\ (\%) = \frac{\hat{C}}{C} \times 100. \tag{4.9}$$

Curves in Fig. 4.6 show the variation of β for different numbers of reference antennas, varying from 4 to 32, and for the 15 successive positions of the single antenna UE in the scenario. Furthermore, β is obtained by averaging its value on the 4 adjacent bands of 20 MHz. In all cases, the reference antennas are chosen in such a way that they are equally distributed amongst the array elements as illustrated in Fig. 4.1.

First, we observe in Fig. 4.6 that the performance of the channel estimator does not strongly depend on the scenarios: LOS, OLOS or NLOS. With only 9 reference elements (about 10% of the total number of Tx antennas), values of $\beta >= 90\%$ are reached. The worst case, position 11, corresponds to a severe NLOS scenario. For $M_{ref} = 9$, the separation between 2 successive reference antennas along the x or y axis is $3d$. We have seen in Section 4.1.2, Fig. 4.4(c), that for such a distance, the median value of antenna correlation is equal or greater than 0.8 whatever the Rx position. The successive steps for optimizing the choice of M_{ref} can be the following:

- From the measured full CSIT matrix at time t, calculate the matrix of correlation coefficients between array antennas,

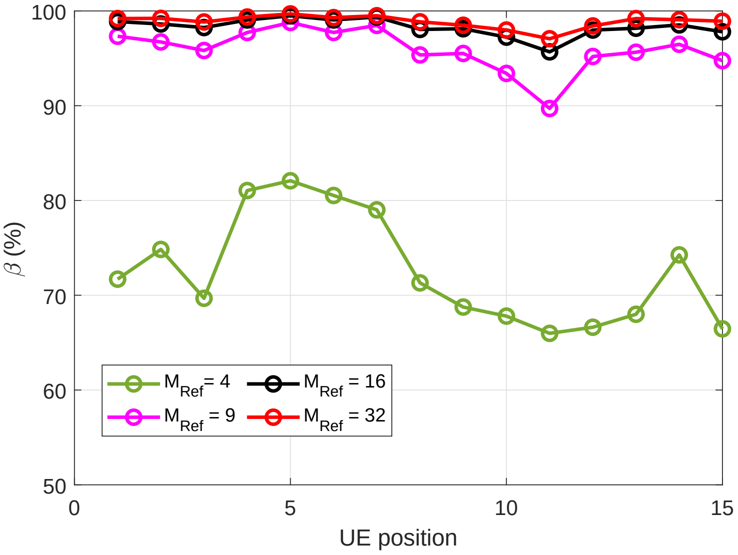

Figure 4.6: *Variation of β (in %) for different number of reference elements M_{ref} - Impact of the number of reference antennas M_{ref} on the computed channel capacity from estimated channels and for successive position of the UE.*

- Determine the antenna element separation (spacing) such that the median value of their correlation coefficient is equal or smaller than 0.8,
- Equally distribute the reference antennas among the array.

4.1.3.2 Multi-User Configuration

For massive MIMO, it is of interest to evaluate the capacity of the BS or AP to simultaneously communicate with the different UEs. This is generally quantified with the sum-rate capacity, justifying our choice of this metric as a figure of merit. In presence of $K = 15$ UEs in our scenario, the sum-rate capacity for the measured channels is given by:

$$C = \log_2 \left(\det(\mathbf{I}_K + \frac{SNR}{M}\mathbf{HW}) \right), \tag{4.10}$$

And for the estimated channels:

$$\hat{C} = \log_2 \left(\det(\mathbf{I}_K + \frac{SNR}{M}\mathbf{H}\hat{\mathbf{W}}) \right), \tag{4.11}$$

$\mathbf{H}$ is the $K \times MM_f$ massive MIMO channel matrix and $\mathbf{W}$ the normalized MRT or ZF precoding matrix given already defined in Ch. 2 (2.4.2.2). $\hat{\mathbf{W}}$ are the normalized precoding vectors for the estimated channel. β of the sum-rate capacity is given in Table 4.1 for $M_{ref} = [4,\ 9,\ 16,\ 32]$.
The convergence of ZF towards 100% is slower than for MRT, ZF being more affected by estimation errors. Nevertheless, $M_{ref} = 9$ corresponding to a median value of

Table 4.1: *β (in %) of the sum-rate capacity with MRT and ZF for different M_{ref}.*

M_{ref}	4	9	16	32
MRT	65	92	93	95
ZF	58	80	85	87

the Tx correlation of 0.8 still seems adequate in the way of choosing the number of reference antennas previously described. However, it must be kept in mind that the presented values do not mean that MRT provide higher sum-rate capacities compared to ZF, at least for the geometrical configuration presented here. Indeed, the capacity deduced from measurements of the full transfer matrix, without estimation error, is equal to 29 bps/Hz and 89 bps/Hz for MRT and ZF, respectively. This can be explained by the relatively large number of LOS UEs (7 among 15). In this case, correlation between these UEs is rather high as shown in Ch. 3 (3.13(a)), with a median value of 0.73. Since the MRT precoding technique does not take inter-user interference into account, it could be expected that its performance would be inferior to ZF. However, the presented values suggest that it is more robust than ZF in terms of estimation error. This was rather expected, since phase mismatch due to estimation errors result in misalignment and enhanced interference in some cases with ZF.

4.1.3.3 Quantifying Complexity Reduction

To complete the evaluation of the proposed strategy, we take back the constraints in 1.7.2.1 in Ch. 1, Sec. 1.7. The original FDD constraint was $K + 2M < \tau_c$ (τ_c is the coherence interval). However, with the proposed strategy and taking M_{ref}, this constraint becomes $K + 2M_{ref} < \tau_c$. Considering $M_{ref} = 9$ for the original 10×10 array[2], the new constraints on the number of estimation pilots in TDD, FDD and the proposed approach become:

- TDD: $K < \tau_c$
- FDD: $K + 2M < \tau_c$
- Channel correlation-based approach (at phase $t + \Delta t$): $K + {}^{M}\!/_{5} < \tau_c$

For the investigated scenario, FDD requires 215 pilot samples while the proposed strategy takes 33 samples compared to the 15 samples with TDD. Furthermore, to generalize, the number of resource elements required for training (number of pilot samples) is plotted as a function of M for an example of 64 UEs and is illustrated in Fig. 4.7.

---

[2] Taking 10×10 or 9×9 does not change the approach since correlation factor at Tx does not vary a lot from $6d$ to $8d$ as observed in Fig. 4.4(c).

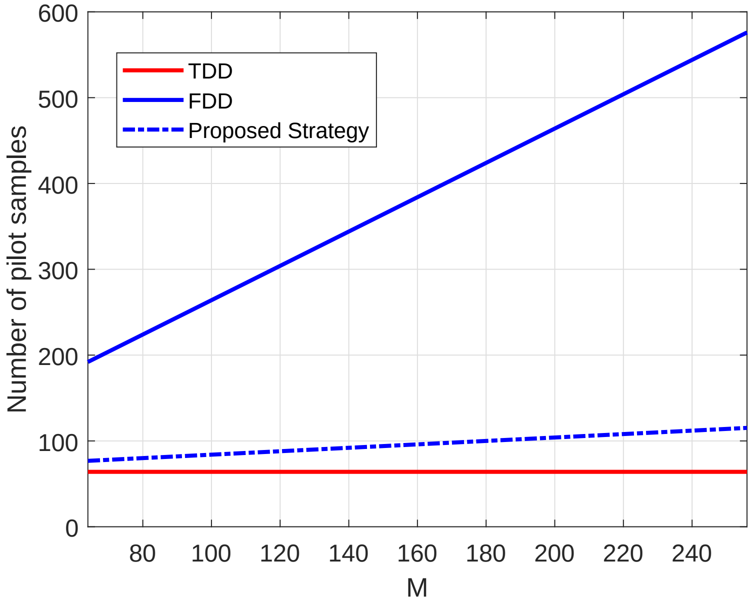

Figure 4.7: *Number of pilot samples for TDD, FDD and the correlation-based approach for feedback overhead reduction. An example for* $K = 64$ *is considered and* M *varies from 64 to 256.*

This figure validates the proposed overhead reduction strategy. It shows that for small values of M, the number of pilot samples needed is close to TDD and much less than FDD. When M increases, the number of pilot samples increases at a much slower rate than with the original FDD scheme owing to the reduced number of reference elements.

4.1.4 Conclusion

In this first part of the chapter, a correlation-based approach for feedback overhead reduction in FDD massive MIMO was proposed. It is based on measurements of transfer functions between UEs and only a few number of array elements, strongly decreasing the size of the channel matrix. The estimation of the full matrix is then obtained owing to the knowledge of the correlation matrix at the transmitter. Using ergodic capacity and sum-rate analysis with ZF and MRT, it was demonstrated in industrial environments that the prohibitive DL training feedback can be overcome with nearly ∼10% of the original number array elements, materializing massive MIMO gains with FDD-based systems.

4.2 Antenna Selection Strategies

4.2.1 Context and Methodologies

Promising performance for massive MIMO systems can be obtained at the expense of increased hardware cost and complexity arising from the sheer number of transmitting elements. To address this challenge, antenna selection strategies have been reported as an appealing solution for hybrid beamforming architectures where a number of RF chains less than the total number of antennas is selected. Indeed, unlike i.i.d. Rayleigh fading channels, where all antennas contribute equally, real propagation channels are subject to large-scale fading over the array. Architectures aiming at exploiting this aspect of massive MIMO systems are very appealing. However, these architectures are yet to be fully defined and evaluated. On another prospect, some massive MIMO base stations have already been developed and deployed with dedicated transceivers to each antenna. From this, another motivation can be that power might be saved by using a subset of the array at a time, especially for scenarios wherein the traffic load is much below the maximum system capacity. In this case, there is no compromise with the overall users throughput. In this section, we propose a novel transmit selection algorithm based on Rx spatial correlation.

4.2.1.1 Related Work

In full DBF, each antenna element is equipped with an individual RF chain. With the large increase in the number of Tx elements, hardware complexity becomes a bottleneck. To alleviate this problem, many solutions have been proposed. The general concept consists in choosing a subset of S antennas in a given M-dimension array to reduce the number of required RF chains for communication between the BS and UEs (see Fig. 4.8).

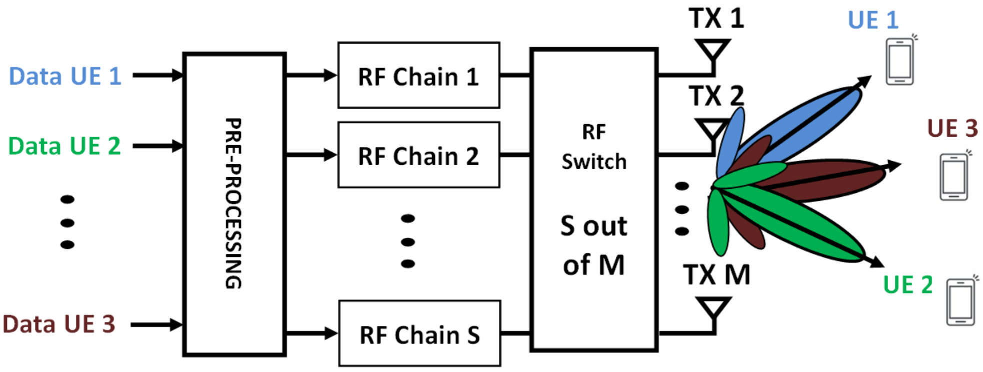

Figure 4.8: *Switching architecture example S out of M.*

The overall RF-cost can be reduced but it should be verified whether antenna diversity is maintained. This has been studied for classical MIMO systems wherein a small number of antennas is selected from the full array [207, 208, 209, 210]. These strategies are generally computationally simple. Concerning massive MIMO, it has been evaluated in measured massive MIMO channels at 2.6 GHz using the sum-rate capacity maximization obtained after a convex optimization including exhaustive search amongst different antenna subsets [211]. Nonetheless, convex optimization using DPC analysis is quite complicated for massive MIMO systems, especially when M is large. The authors have reported that selecting the best antennas boosts the performance of a cylindrical array to obtain higher performance than a linear array with higher angular resolution. In [212], the same authors compare selection schemes based on convex optimization with a very simple selection technique based on the highest relative received power (classic approach) at the antennas. Also, based on strongest channel gains, with simulated i.i.d. channels, [213] derive analytical expressions for the number of selected antennas to maximize energy efficiency. It is concluded that relatively simpler selection schemes can also provide good results. In [214], transmit antenna selection in mmW is formulated using Knapsack problems in order to determine the smallest subset of antennas to satisfy a given quality of service (QoS) for a given user. Optimal selection schemes via advanced analytical tools are proposed in [215]. In another approach, the determination of the optimal number of RF chains when considering circuit power is evaluated in [216]. In [217], the authors try to find an optimal balance between consumed power by the RF chains and total transmitted power by jointly determining the optimal number of antennas and the corresponding power allocation. More recently, several selection strategies have been also tested for secrecy performance [218]. Switching architectures and capacity bounds are also discussed for i.i.d. channels in [219]. Practical implementation issues such as insertion losses caused by switching architectures are discussed in [220]. It follows that in the existing state-of-art, most strategies are based on analytical channels (i.i.d. for instance), exhaustive DPC and/or based on relative received channel gains. Also, the implementation aspects are rarely taken into account and if they are, sub-optimal solutions are derived at the expense of the overall performance compared to full DBF. Under the same scope, hybrid transmit precoding role is to alleviate complexity issues by picking a reduced set of RF chains mapped to a larger number of radiating elements in the array. This issue is widely discussed [87, 221, 222, 223, 224, 225]. From this, antenna selection strategies and hybrid beamforming are supposed, in this thesis, as two complementary notions, even though one can exist without the other. Based on this review, simple antenna selection strategies at Tx side are yet to be fully defined and validated, especially since measurement-based strategies for massive MIMO systems are scarce. The trade-off between the number of elements and the overall performance with full-size array should also be addressed.

4.2.1.2 Antenna selection Procedure

Three general different configurations are considered for evaluation as shown in Fig. 4.9 with a URA as an example: (1) the full massive M-antenna array, (2) a sub-array (i.e. collocated elements) with S antennas ($S < M$) and (3) a distributed array with S antennas.

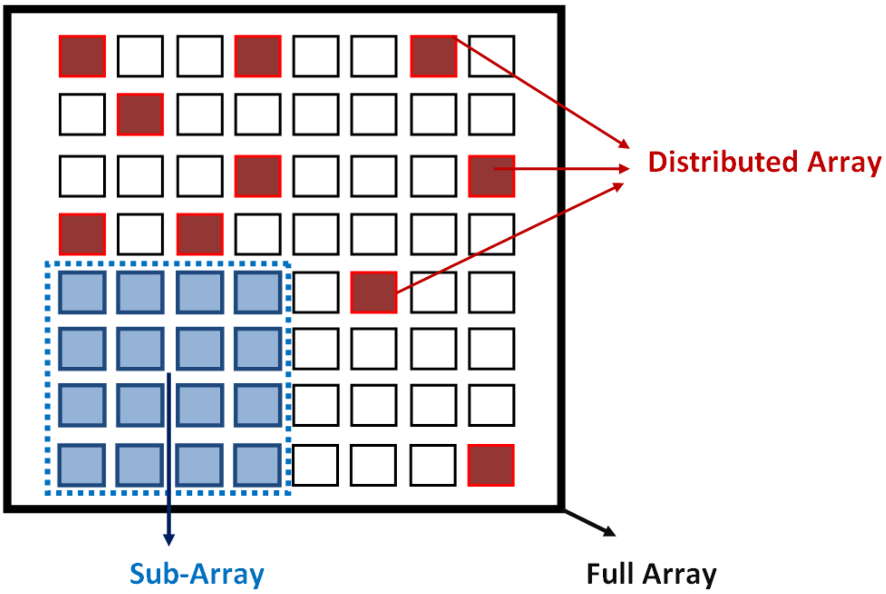

Figure 4.9: *Investigated subset configurations from a URA.*

The sub-array is used as a reference to highlight the fact that distributing the antennas within a given array is a better approach. It should be noted that the propsosed antenna selection is a digital-based switch architecture that consists in connecting S RF chains to S out of M possible antennas.

4.2.1.3 Selection criterion

The acquisition and application of Rx spatial correlation information will be key in 5G and beyond-5G systems, to take the spectral efficiency to the next level. Under this umbrella, the Rx spatial correlation ρ_{Rx} (or intercorrelation) is chosen as the selection criterion in order to select subsets. It highlights the capability of the system to simultaneously serve a number of users which is a pivotal aspect in massive MIMO. It follows that antenna selection criterion aiming at minimizing interference via spatial correlation reduction is a suitable figure of merit. It was also evaluated in Ch. 3 (3.7) for mapping high-correlated UEs to orthogonal polarizations, thus demonstrating the potential of polarization diversity with the use of dual-polarized antenna arrays.

4.2.1.4 Evaluation Algorithm

The antenna selection algorithm is presented in Fig. 4.10. Basically, N_{dist} subsets of S randomly distributed antennas are created from the massive $K \times M$ massive MIMO channel $\mathbf{H}_{FULL}$. The average spatial correlation is then computed for all subsets using Eq. 2.18. The lowest correlation value ${\rho_{min}}^{3}$ corresponds to the best selected subset (BSS) and the highest correlation value ρ_{max} to the worst selected subset (WSS). These subsets contain the indices of the best and worst selected antennas from which $\mathbf{H}_{BSS}$ and $\mathbf{H}_{WSS}$ are constructed, respectively. For the sub-array, N_{SUB} subsets of S collocated antennas $\mathbf{H}_{SUB}$ are generated from $\mathbf{H}_{FULL}$. It should be noted that the proposed approach is independent of the antenna topology, frequency band, or radio channels. Therefore, it is applicable to any desired setup. The proposed approach was assessed by investigating the propagation characteristics and system performance of arbitrary ray-traced radio channels at 6 GHz [226]. The analysis of the propagation mechanisms using channel metrics such as the power to interference ratio and condition number has validated the choice of the Rx spatial correlation. Also, sum-rate capacity was found to be nearly optimal compared to convex optimization [227]. It should be noted that in order to choose the S distributed elements, the knowledge of the full channel is still needed to compute the average spatial correlation between UEs. From this arises the importance of the proposed method in Sec. 4.1.

4.2.1.5 Investigated Scenario

For this study, the 3.5 GHz band is considered with the defined scenarios: LOS, NLOS and total. S designates the number of selected elements inside a subset. Consequently, $S = S_x \times S_y$. Nonetheless symmetric arrays are here considered (same number of elements in x and y directions) at all times. For the evaluation of the strategy, we only consider co-polarized channels . At the initialization, $N_{dist} = 1000$ were used to assess the approach. However, the convergence toward optimum decorrelation values was achieved for the 5^{th} and 10^{th} trial for NLOS and LOS scenarios, respectively. This will be further discussed later on.

4.2.2 Validation and Results

4.2.2.1 Validation based on Rx correlation

For each result, the four configurations (BSS, WSS, sub-array and full-array) are considered with $S = 36$. In Figure 4.11(a) and (b), ρ_{Rx} is presented for the LOS (a) and total scenario (b). It shows the different draws for the selection strategy.
Compared to $\rho_{Rx} = 0.37$ for $M = 100$, the BSS reaches decorrelation values of 0.35 with $S = 36$ for the full scenario. For the LOS scenario, $\rho_{Rx} = 0.59$ for $M = 100$ and 0.33 for the BSS. This comparison is crucial for the LOS scenario, underlining

---

[3] The minimum value over all generated N_{dist}. The same procedure for the maximum value.

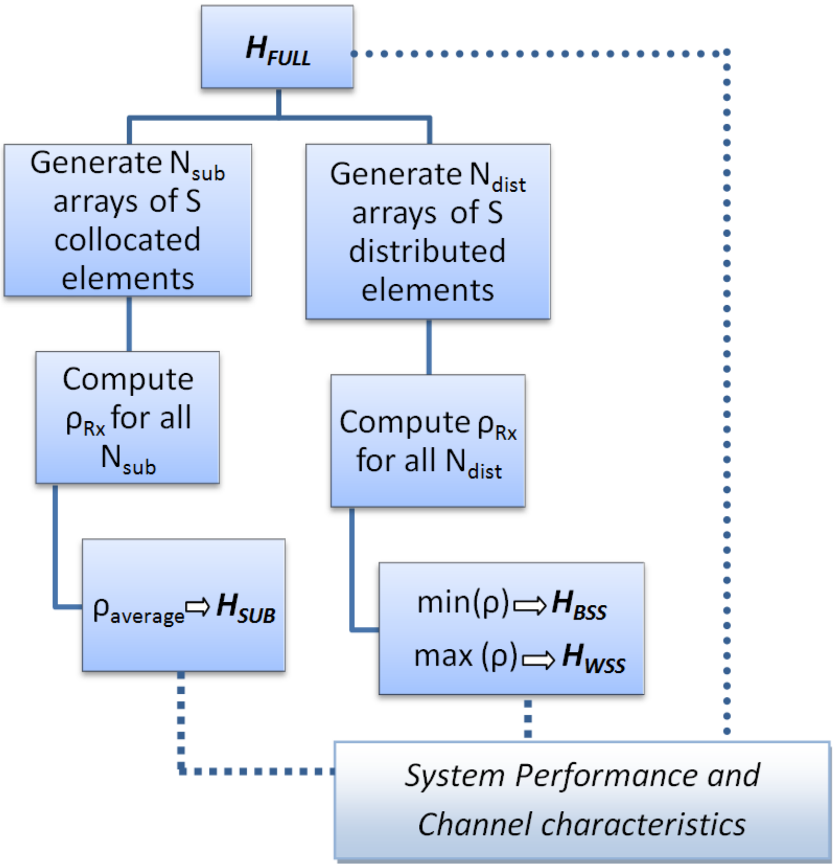

Figure 4.10: *Antenna selection evaluation algorithm.*

that the applied strategy brings significant benefits, especially to the LOS decorrelation, which is the challenging part for massive MIMO systems, especially if high correlation values exist. A similar result in Ch. 3 on the Gram's power ratio and average spatial correlation confirms this observation. One can note that with the selection strategy, the drop in correlation values is very fast compared to the sub and full-array. This is somehow expected since selecting distributed antennas at Tx leads to lower Tx correlation values (larger separations between the elements), which in turn, leads to UEs decorrelation.

This figure highlights the capability of the BSS to decorrelate users with ∼60% less antennas compared with the full array. It also performs better than the $S_x \times S_y$ sub-array. Regarding $\mathbf{H}_{SUB}$, the variance of the ρ_{Rx} values for N_{sub} arrays of collocated antennas was found to be negligible ($\simeq 0.05$). This indicates the different sub-arrays exhibit very close behavior regarding correlation mechanisms. Thus, a $\rho_{average}$ on N_{sub}, reflecting the overall behavior of the sub-arrays, was used.

It is noteworthy that, between the BSS and the WSS, there exists a family of curves with ρ_{Rx} values ranging from $\simeq 0.35$ (BSS) to $\simeq 0.42$ (WSS), for instance, for the full scenario. This variation in ρ_{Rx} strongly depends on the selected subset and, therefore, propagation mechanisms. However, the difference is not large, and in

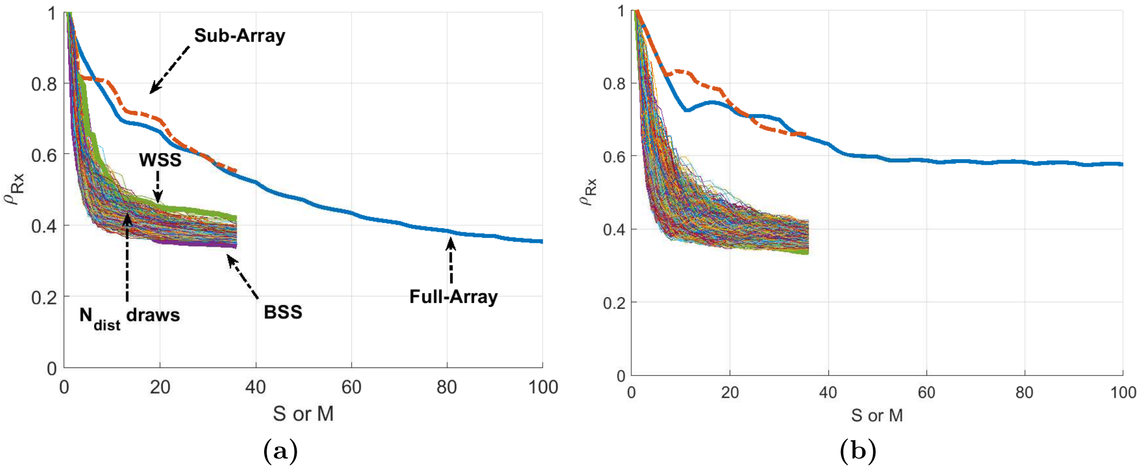

(a)

(b)

Figure 4.11: *The average spatial correlation for the different configurations, showing all the draws, for* $S = 36$*. In (a) the total scenario and (b) LOS UEs as defined in Ch. 3.*

order to lighten the presentation, only the BSS will be considered. Finally, N_{dist} was chosen large enough for the sole purpose of generating sufficient statistics but is much smaller than the total number of combinations C_M^S (which is not tractable in practice). Finally, to achieve convergence with distributed subsets and low ρ_{Rx} values, only 5, 10 and 13 draws on average are needed, therefore, considerably reducing the computational time.

4.2.2.2 Strategy Performance Evaluation and Results

From the previous paragraph, it was shown that by exploiting the spatial selectivity via the proposed strategy, the average spatial correlation can be greatly improved. However, this is not sufficient to quantify the added value of this strategy.
The trade-off between reduced complexity and less Tx antennas is assessed using (1) the Gram's power ratio and in the next section (2) the sum-rate capacity that will give good insight on the total achievable performance.

4.2.2.3 Gram's Power Ratio

The CDF of the Gram's power ratio is presented for the three configurations : full-array, sub-array and BSS with $S = 36$. An additional curve denoted PS for power selection was added. This designates a classical way of selecting antennas based on their average received gain as discussed in [212]. It simply consists in selecting S antennas with the largest gains from the M element-array. The 4 configurations are compared using the CDF of $\gamma(\mathbf{G})$ in Fig. 4.12(a) and (b) for the LOS and NLOS scenarios whereas (c) and (d) present $\gamma(\mathbf{G})$ for LOS and NLOS, respectively.

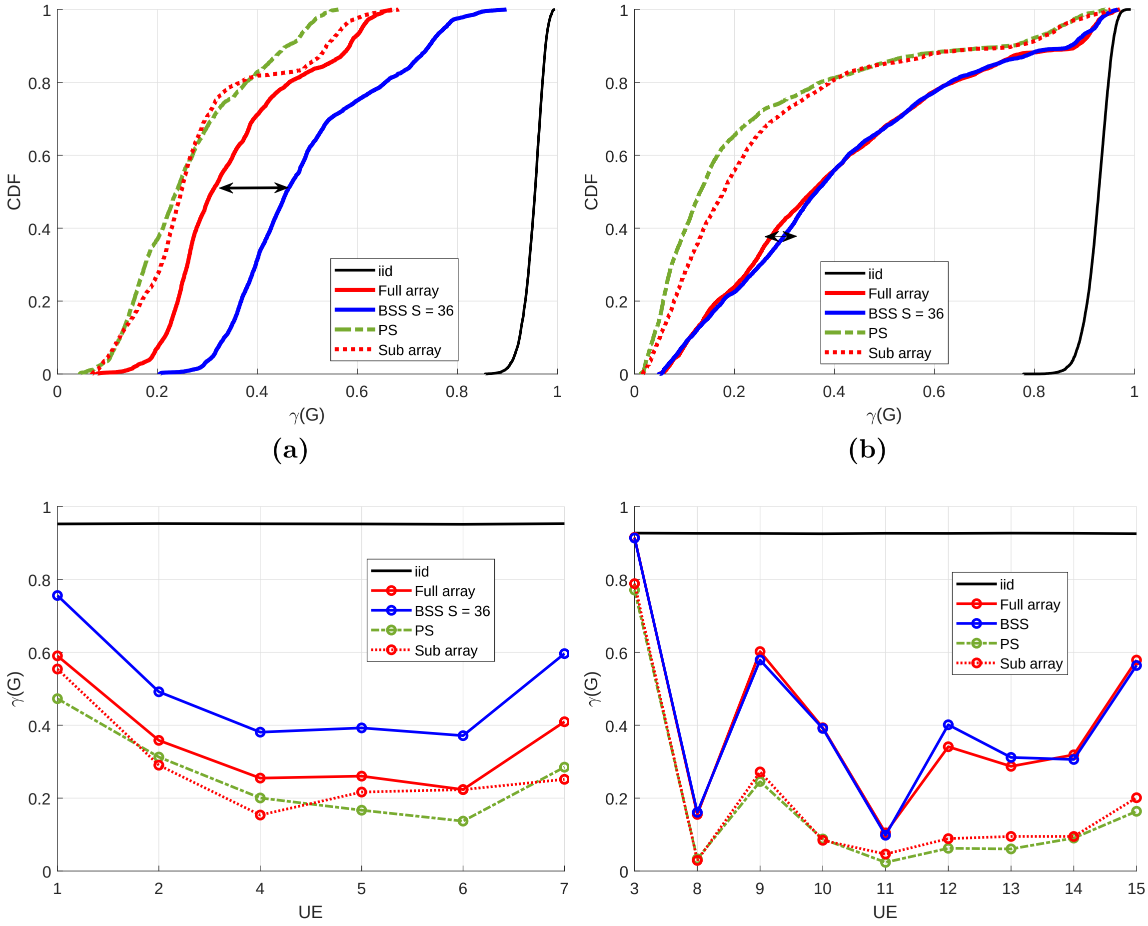

(a) **(b)** **(c)** **(d)**

Figure 4.12: *CDF of $\gamma(\mathbf{G})$ for (a) LOS and (b) NLOS scenario. The 4 different configurations ($S = 36$) are presented as well as the i.i.d. curve for the sake of comparison. The evolution of $\gamma(\mathbf{G})$ as a function of UE position is also presented in (c) and (d) for the LOS and NLOS scenario, respectively.*

The observed values for the median $\gamma(\mathbf{G})$ in Fig. 4.12(a) are ∼0.46 and 0.36 with the BSS for LOS and NLOS scenario, compared to ∼0.3 and ∼0.36 for the full array. The values of $\gamma(\mathbf{G})$ for PS and sub-array are ∼0.25 for both configurations in LOS and ∼0.1 for PS, 0.15 for sub-array in NLOS scenario. Figure 4.12(c) and (d) highlight the benefits of the strategy from a UE local point of view. It demonstrates that the benefits of the strategy are well shared between the UEs, especially in LOS.

In conclusion, this analysis suggests that the selection strategy works very well under LOS conditions since it achieves larger power ratio values with less transmitting elements as indicated by the double arrow in Fig. 4.12(a). For the NLOS case, the same performance is observed for the full and distributed array. This is

Table 4.2: *Variation of $\gamma(\mathbf{G})$ with respect to the full-array (in %) with S for LOS and NLOS scenarios. Three configurations are compared: Full, Sub-Array and BSS.*

S	9	16	25	36	49	64	81
$\gamma(\mathbf{G})$ (in %) for LOS scenario							
Full-Array ($M = 100$)	30						
Sub-Array	20	22	25	26	27	29	30
BSS	26	33	34	45	35	33	27
$\gamma(\mathbf{G})$ (in %) for NLOS scenario							
Full-Array ($M = 100$)	36						
Sub-Array	10	13	15	18	23	26	28
BSS	23	29	35	36	36	35	35

still beneficial since it indicates that the same values of $\gamma(\mathbf{G})$ can be reached with only $S = 36$ RF chains. It is also observed that the PS algorithm and sub-arrays performance are very close to each other and well below the full array and the BSS. This demonstrates that antennas reducing interference are preferred over antennas with high gain that could eventually increase interference and decrease $\gamma(\mathbf{G})$. To this purpose, the PS algorithm will be dropped for the rest of this chapter and BSS, full-array, sub-array are compared.

4.2.2.4 Parametric Analysis

It is of interest to analyze the impact of S on the overall performance. To this purpose, the values of S are chosen from the set: $[9, 16, 25, 36, 49, 64, 81]$. The median value of $\gamma(\mathbf{G})$ as a function of S is presented in Table 4.2 for the three considered configurations: Full, Sub-array and BSS.

It can be observed that increasing S does not always increase $\gamma(\mathbf{G})$. Taking for instance the LOS case, the maximum $\gamma(\mathbf{G})$ ($\sim$45%) is observed for $S = 36$ and then decreases to $\sim$27% with $S = 81$ which is the same value for $S = 9$. This is not observed for NLOS wherein the value of $\gamma(\mathbf{G})$ is nearly constant for the different values of $S > 16$.

It can be concluded that, in the LOS scenario, using massive MIMO with $M >>$ does not improve $\gamma(\mathbf{G})$ when UEs are correlated. On the contrary, more antennas could deteriorate the performance. It also suggests that there exists an optimal number of Tx antennas for which $\gamma(\mathbf{G})$ reaches its maximal value, in this case $S = 36$. Concerning NLOS, the applied strategy can alleviate the need for $M = 100$ RF chains by using a distributed array of $S = 25$ for instance. Finally, it is preferable to wisely select a reduced number of distributed elements based on the UEs correlation rather than increasing M.

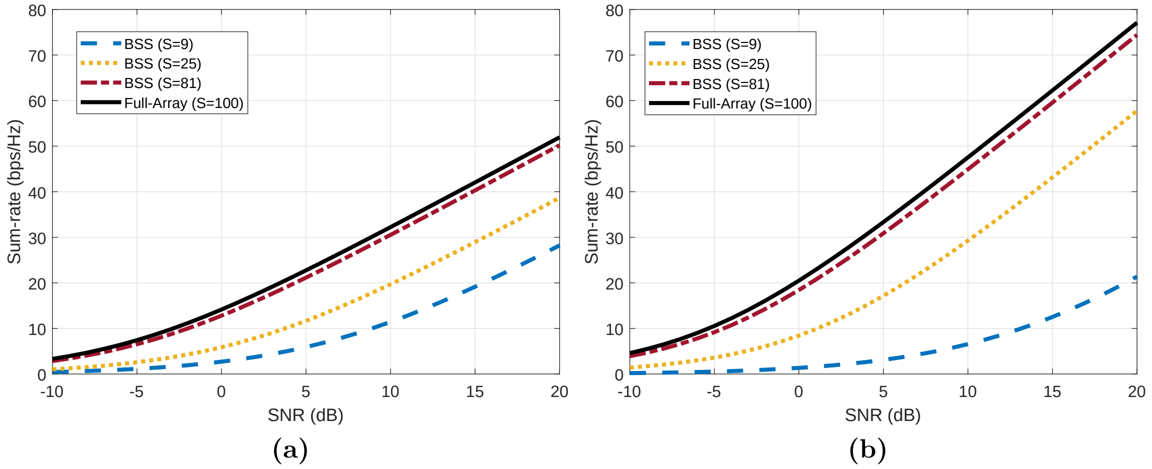

Figure 4.13: *Sum-rate capacity variation for ZF precoding with SNR for (a) LOS and (b) NLOS scenario. 3 values of S are considered: 9, 25 and 81, compared with the full-array performance.*

4.2.2.5 Sum-rate Capacity

The conclusion of the previous section is insightful regarding the reduction of the number of RF chains. Nonetheless, it does not take into consideration other systems parameter: power allocation and precoding strategies. Regarding sum-rate analysis, it is well known, from a system perspective, that increasing M generally leads to larger sum-rate capacity. In this section, our goal is to quantify the achievable overall performance of the proposed selection strategy. In other words, we try to answer the question: how closely is the performance (sum-rate capacity) of the proposed antenna selection strategy to the full-array performance, under precoding and power allocation constraints ? To this purpose, the classical system model presented in Ch. 2 (2.4.3) is considered with MRT and equal-power allocation (EP), ZF and WF. It was shown in Ch. 2 that for ZF and MRT, the best power allocation strategies were WF and EP. These precoding schemes are considered in the following.

The sum-rate capacity is presented in Fig. 4.13 with ZF as a function of the SNR. The full-array performance is compared with the BSS for $S = 9, 25, 81$. Fig. 4.13(a) illustrates the LOS and (b) the NLOS scenario.

It can be observed that with $S = 81$, the sum-rate in LOS and NLOS is respectively ∼50 and ∼75 bps/Hz compared to ∼52 and ∼78 bps/Hz for the full-array in both scenarios. This value drops to ∼ 39 and 57 bps/Hz for LOS and NLOS respectively when $S = 9$. These results indicate that a large fraction of the total sum-rate capacity can be achieved with $S << M$. The achievable sum-rate β using the BSS for instance, is presented, as follows:

$$\beta\ (\%) = \frac{C(\mathbf{H}_{BSS})}{C(\mathbf{H}_{FULL})} \times 100, \tag{4.12}$$

where $C(\mathbf{H}_{BSS})$ and $C(\mathbf{H}_{FULL})$ are the sum-rates computed with the distributed array and full-array. β variation with S is presented in Fig. 4.14 where the LOS and NLOS scenarios are compared for the BSS and sub-array. The SNR is equal to 10 dB .

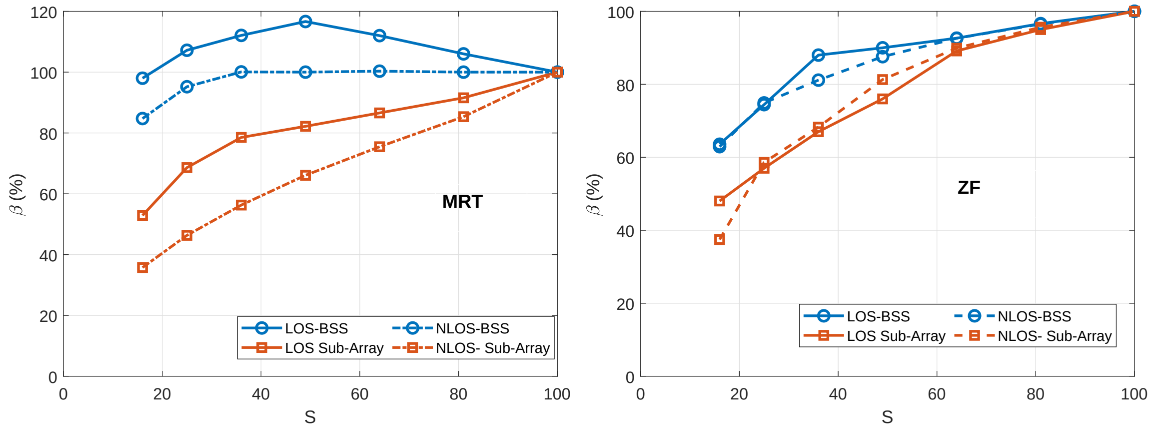

(a) **(b)**

Figure 4.14: *β (in %) variation with S for the LOS and NLOS scenarios with (a) MRT and (b) ZF. The BSS for different values of S is compared with the Sub-array.*

Starting with Fig. 4.14(b), the applied strategy reaches ∼90% of the total capacity with only $S = 36$ for both LOS and NLOS with ZF. With MRT, the achievable total sum-rate is 100% for NLOS with $S >= 36$ and reaches 110% for $S = 36$ in LOS conditions. Indeed, the MRT curve in LOS case presents a maximum for $S = 49$, showing that for LOS UEs with MRT, increasing M is not the best solution. It is observed that for $S = 36$, better achievable capacities are obtained. This is not totally surprising since the antenna selection strategy aims at minimizing the receiver correlation which corresponds to reducing interference and thus increasing capacity. Regarding the sub-arrays, their performance is always below the BSS ($S = 36$) with $\beta = 80\%$ and 65% with MRT for LOS and NLOS respectively, and β= 68% with ZF for both LOS and NLOS scenarios. Note that the absolute sum-rate capacity is lower for MRT compared to ZF.
In conclusion, this figure highlights the efficiency of the antenna selection strategy for both MRT and ZF in LOS (especially) and NLOS scenarios.
These observations agree with the previous results of the Gram's power ratio and receiver spatial correlation.

A summary of β values for LOS, NLOS is presented in Table 4.3 for MRT and ZF.

S	16	25	36	49	64	81
Precoding	**β (in %) for LOS**					
MRT	98	107	112	116	102	106
ZF	63	75	89	90	92	96
Precoding	**β (in %) for NLOS**					
MRT	84	95	100	100	100	100
ZF	63	75	81	88	93	97

Table 4.3: *Variation of β (in %) with S for LOS and NLOS. Two configurations are compared: BSS with MRT and ZF.*

In Table 4.4, β values for the total scenario are presented with the sum-rate capacity.

S	16	25	36	49	64	81
Precoding	**β (in %)**					
MRT	98	99	100	105	100	100
ZF	27	59	80	82	89	94
Precoding	**Sum-rate capacity (bps/Hz)**					
MRT	31	33	34	37	34	34
ZF	26	54	80	82	93	97

Table 4.4: *Variation of β (in %) with S for the total scenario. Two configurations are compared: BSS with MRT and ZF and the corresponding sum-rate capacity values are given.*

4.2.3 Conclusion

An original strategy to minimize the number of RF chains of massive MIMO system using a digital-based swicth architecture has been described. Basically, antennas for which user spatial correlation is low are selected. Based on experimental channel characterization, system metrics such as Gram's power ratio and sum-rate capacity are used to validate the approach. Results show that by considering MRT precoding technique, the maximum capacity obtained with a full array of 100 antennas, limited by high correlation especially in LOS scenario, can be achieved with only 36 antennas. This leads to a reduction of 64% of RF chains. ZF precoding exhibits a sum-rate capacity of 80% of the maximum capacity using these selected antennas. The proposed strategy gives near-optimal performance while reducing the complexity of massive MIMO systems, minimizing cost, maintenance, antenna coupling (since antennas are distributed) and increasing energy efficiency by decreasing the overall hardware energy consumption. Finally, the proposed strategy simplifies the task of Rx scheduling since correlated UEs can be simultaneously served.

4.3 General Conclusion

To conclude this chapter, we must draw attention to the link between the two proposed strategies. It is true that these two strategies can be applied independently since one reduces the overhead feedback for channel estimation and the other decreases the complexity by only considering S Tx antennas connected to S RF chains with $S < M$. However, these two strategies are the two faces of the same coin. Indeed, the $K \times S$ BSS channel is deduced from the $K \times M$ full-array and the knowledge of the $K \times M$ channel is necessary for the selection procedure of S. From this, without the Tx correlation-based approach to reduce feedback overhead (with FDD for instance), the Rx correlation-based approach to select the BSS would still be too complex since $K \times M$ channels should be estimated.

Chapter 5

Conclusion

THE main research subject investigated in this thesis was the evaluation of the performance of a massive MIMO setup in an industrial scenario whithin the scope of Industry 4.0. Moreover, many challenges were addressed such as CSIT feedback overhead reduction, number of RF chains reduction, polarization diversity impact and overall performance. The main contributions of this work are summarized in the next paragraphs, and future research directions are proposed.

In **Ch. 1**, we presented an overview of 5G-NR, its use-cases, spectrum-related features and gaps with previous wireless generations. 5G, in its current form, is not a revolution but an evolution of 4G and configurations using both 5G and 4G technologies will co-exist. Multiple antenna systems such as MIMO and MU-MIMO are capable of addressing many challenges using spatial multiplexing or diversity. Despite the many benefits brought by these technologies in modern wireless communication systems, it was concluded that a paradigm shift was needed to fulfill the new requirements. This leads to massive MIMO systems where the increase in the number of array elements at Tx helps in achieving both high spectral and energy efficiencies by multiplexing many UEs. Massive MIMO can be used for analog beamforming, mostly for very high data rate applications and backhaul links. Nonetheless, its full advantages are harvested with digital beamforming. The theoretical advantages of massive MIMO such as channel hardening and favorable propagation condition are now well-known to academia, and have been confirmed by some field trials by telecom operators [97, 100, 101].

Ch. 2 introduced the main characteristics of wireless channel parameters such as Ricean factor, received gain and spatial correlation. In order to understand the impact of these channel parameters on the system performance, a geometrical channel model was proposed and used to perform a parametric analysis. This model, validated with experimental results (Appendix D), quantified the impact of the different scenarios such as highly correlated users and /or highly correlated Tx elements. The two main properties of massive MIMO were evaluated, (i) channel hardening i.e. the variance of channel gain vanishing with the increasing number of array elements and (ii) favorable propagation conditions illustrated by the convergence to zero of interference between UEs. It was concluded from this analysis that channel hardening and favorable propagation condition largely depend on the Ricean factor and correlation properties at both Tx and Rx side. Finally, in order to quantify the system performance, precoding strategies and power allocation schemes were presented and a simplified system model was described. The performance of i.i.d. channels was evaluated and a parametric analysis on the sum-rate capacity using the proposed massive MIMO channel model was presented. It was shown that linear precoding schemes are affected by the Ricean factor and by correlation properties, and that ZF and MMSE achieving very high spectral efficiencies have limitations for a large number of users.

On another note, 5G aims at supporting the Industry 4.0 connectivity requirements for massive connectivity, ultra-reliability and ultra-low latency (mMTC and URLLC). Furthermore, massive MIMO could potentially lead to an increase in flexibility, versatility, productivity and resource efficiency. The various channel and system aspects of massive MIMO in industrial environments have been developed in Ch. 3.

Ch. 3 was first dedicated to the presentation of polarimetric channel measurements of a massive MIMO setup for an indoor industrial scenario at 1.35, 3.5 and 6 GHz with 80 MHz bandwidth. The scenario consists in a massive URA transmitter and 15 distributed users covering most propagation conditions. Using the propagation channel parameters introduced in Ch. 2, UEs were classified into two distinct groups: LOS and NLOS. The median correlation between users revealed strong correlation in LOS co-polarized channels whereas low correlation is obtained in all cross-polarized channels, but at the cost of power penalty especially in severe NLOS conditions. Spatial variability across the array, depending on the UE position, has been pointed out using, for instance, channel hardening. Furthermore, the Gram's power ratio showed that cross-polarized channels exhibit the best percentage of the total energy focused toward the intended users in NLOS scenario. From sum-rate capacity analysis, the best configuration for the 2 precoding techniques was cross-polarization with MRT and co-polarization with ZF and waterfilling power allocation. Finally, from previous analyses, it was shown that increasing the number of antennas does not always improve overall results and other approaches should be considered. Two strategies exploiting polarization diversity were proposed and it was demonstrated that very high sum-rate capacities (similar to co-polar in ZF) with a 50-element dual-polarized array can be achieved. Compared to full co- and cross-polarization schemes, diversity schemes jointly exploiting high channel gains in co-polarization and better decorrelation in cross-polarization can lead to near-optimal results and can, therefore, be beneficial for massive MIMO setups in Industry 4.0.

Finally, in **Ch. 4**, two original strategies are proposed to reduce the complexity of massive MIMO on two main aspects: channel estimation and number of RF chains. For the latter, we introduced an Rx-correlation based method to select antennas at Tx. Basically, antennas for which user spatial correlation is low are selected. Based on experimental channel characterization, system metrics such as the Gram's power ratio and sum-rate capacity were used to validate the approach. The results showed that the proposed strategy gives near-optimal performance while reducing the complexity of the massive MIMO systems, minimizing cost, maintenance and antenna coupling. For instance, with MRT precoding technique and the propsed selection strategy, it is possible to only use 36 RF chains (out of 100) and achieve the same capacity than with the full-array. This indicates that in some cases, wisely selecting a reduced number of antennas is by far a better approach. For these selected antennas, ZF precoding achieves 80% of the maximum capacity. However, the selection criteria, using Rx spatial correlation, depends on the knowledge of the full channel state information. FDD channel estimation becomes challenging due to substantial overhead that scales up with the number of antennas. This motivated the idea of simplifying the channel estimation procedure by proposing a Tx correlation-based approach for feedback overhead reduction in FDD massive MIMO. It is based on measurements of transfer functions between UEs and only a few number of array elements, strongly decreasing the size of the channel matrix. The estimation of the full matrix is then obtained owing to the knowledge of the correlation matrix at the transmitter. Using ergodic capacity and sum-rate analysis with ZF and MRT, it was demonstrated in industrial environments that the prohibitive DL training feedback can be overcome using only $\sim 10\%$ of the original number array elements for channel estimation. This indicates that the proposed method allows accurate feedback of channel state information in a resource-efficient manner. In terms of feedback reduction, we have demonstrated with an example that, for a Tx array of 81 elements, a rather robust estimation of CSIT is obtained by using only 9 reference antennas, reducing overhead by ~ 75 %. These two strategies provide a practical approach for FDD-based massive MIMO systems alongside complexity reduction, paving the way for enhanced massive MIMO systems.

Chapter 6

Future Research Directions

Works for Release 16 within 3GPP have already begun and some new trends for 5G are already emerging. There exists many aspects that can eventually be supported by massive MIMO such as vertical industries, non-terrestrial networks (NTN), V2X, public safety, and Industrial IoT. However, many challenges are still to be tackled before achieving the full potential of massive MIMO for different use-cases. Based on the results from this work, many future research directions and guidelines can be proposed.

- The proposed geometrical channel model, with a specific set of parameters for the Ricean factor, elevation and azimuth angles, appeared to be well suited to the simulation of industrial environment as shown in Appendix D. Nevertheless, the accuracy of this model can still be improved by including spatial variability of the Ricean factor along the URA transmitter.

- We have shown that the DMC or dense multipath components are a significant contributor to the decorrelation mechanisms between UEs at mmW bands as briefly mentioned in Sec. 1.10. Details are given in **J4** from the **List of Publications**. It was concluded that DMC should be taken into account when modeling radio channels. In an ongoing work, this phenomenon is being investigated for the massive MIMO setup in industrial environment for 1.35, 3.5 and 6 GHz. The goal of this study is to quantify the presence of DMC, its frequency-dependence and its impact on the performance of massive MIMO. This can be part of a recent study item proposed by 3GPP and dealing with industrial channel characterization.

- NOMA or non-orthogonal-multiple-access can outperform conventional orthogonal multiple access (OMA) schemes in cellular networks. There exists specific cases where NOMA can be complementary to massive MIMO, especially when UEs are highly correlated. By using power multiplexing when P_1 (received power by UE1) $\neq P_2$ (received power by UE2), as shown in Fig. 6.1, two highly correlated UEs can be separated owing to their power contributions and using successive interference cancellation (SIC). More generally, UEs can be grouped into pairs and the different pairs are spatially multiplexed using massive MIMO properties. This is referred to as a hybrid solution of NOMA and multi-user beamforming. The interest of this solution has been evaluated for analytical channels and was shown perform better than a system using only one of the two schemes as indicated in [228]. Nonetheless, an experimental approach is needed to validate this interesting approach. To this purpose, measurements would be planned to assess the feasibility of the association of NOMA to massive MIMO.

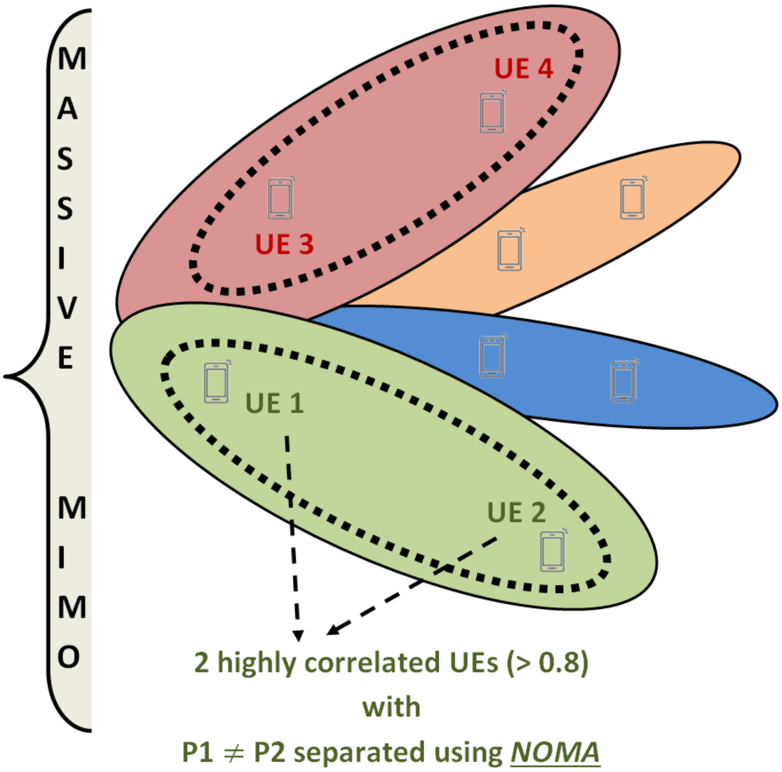

Figure 6.1: *NOMA associated to massive MIMO in highly correlated environments.*

- Results of CSIT overhead reduction in FDD mode and those of the proposed Rx correlation-based antenna selection strategy to reduce the number of RF chains are very encouraging. The next step would be to experimentally simulate dynamic conditions by introducing UE mobility and study its impact on channel estimation and on the overall performance of the selection strategy. This type of measurements would take place in the same industrial environment as that described in Ch. 3, but using a real-time channel sounder MIMOSA [229] capable of simultaneously measuring a full 16×16 channel matrix in $\sim 350 \mu s$. The channel sounder is being extended to a new version supporting massive MIMO features and a new frequency band 6 GHz. Lastly, it would be of interest to evaluate the temporal variability of the channel response and its impact on the Tx correlation between array elements since this could have an impact on the performance of the proposed CSIT estimation method.

- In **J2** from the **List of Publications**, we used an indoor virtual hybrid measurement setup at 1.35 GHz where a vertical ULA was moved along horizontal positions. In this setup, coupling and RF chains imperfections along the ULA were considered. This study compared the receiver spatial correlation with and without coupling and it was concluded that more antennas are needed to reach a given threshold of correlation when coupling is considered. The effects of coupling are well-known in MIMO systems and for analytical channels. Nonetheless, for massive MIMO, and with the proposed antenna selection strategy for RF chains reduction, it would be of interest to compare the performance of the full array and the BSS. Since the antennas are distributed within the BSS, one can expect a greater performance of the proposed strategy with respect to the full array since coupling is reduced when antennas are distributed. Also, since coupling introduces correlation between antennas at Tx, it might be interesting to check if the correlation-based approach to reduce CSIT feedback overhead can be optimized by taking less reference antennas (M_{ref}) since the correlation is higher in the array.

- In this work, a dual-polarized antenna array with half the number of elements appeared to achieve most of the sum-rate capacity of a full co-polarized antenna array. Also, the BSS using the Rx correlation-based selection strategy was shown to perform very well with only 36 antennas out of 100 for both MRT and ZF. However, this strategy was applied for the co-polarized array and the potential of jointly using antenna selection strategies and dual-polarized array would be attractive to simplify even more the complexity of massive MIMO systems.

- **Towards Massive MIMO 2.0**: The different advancements in massive MIMO systems with the addressed challenges as indicated before are paving the way towards massive MIMO 2.0, a term used by the authors in [230]. Massive MIMO 2.0 will be a key motivator for new research directions, even beyond 5G. As an example one can mention large intelligent surfaces wherein very large electromagnetically active surfaces are integrated into existing man-made structures, such as windows, towers or walls. This creates arrays with huge apertures and reconfigurable electromagnetic radiation properties. These large intelligent surfaces are sometimes labeled holographic massive MIMO [231] and could be an interesting research subject. Finally, let us mention that sub-THz communications [232] provide answers in the quest for ever-increasing data rates using very large bandwidths and application of massive MIMO to this frequency band would also be a challenge. Indeed, owing to compact arrays at high frequencies, the massive MIMO regime is reached very fast, providing huge performance gains.

Appendix A

List of Notations, Symbols and Acronyms

A.0.1 Mathematical Notations and Operators

Matrices are denoted by upper-case boldface letters ($\mathbf{A}$) while column vectors are denoted with lower-case boldface letters ($\mathbf{a}$). Scalars are denoted by lower or upper-case italic letters (a). Unless otherwise indicated, a product between two matrices is a matrix product and not element-by-element product. In the following, a list of mathematical notations:

$\mathbb{C}^{X\times Y}$	Matrix with $X \times Y$ complex-valued elements.
$\mathbb{R}_+$	The set of positive real-valued numbers.
j	$\sqrt{-1}$.
e	Euler number ($\sim$ 2.718281).
$(\mathrm{a})^*$	Conjugate of a.
$\mathcal{R}(a)$	The real part of a.
$\mathcal{I}(a)$	The imaginary part of a.
$x \in S$	x is a member of S.
$x \notin S$	x is not a member of S.
$(\mathbf{a})^T$	Transpose of $\mathbf{a}$.
$(\mathbf{a})^H$	Hermitian or conjugate-transpose of $\mathbf{a}$.
$\mathbf{a}_k$	k^{th} element of $\mathbf{a}$.
$\mathbf{A}_{k,l}$	The (k,l) element of $\mathbf{A}$.
$\mathbf{A}^{-1}$	The inverse of square matrix $\mathbf{A}$.
$tr(\mathbf{A})$	The trace of square matrix $\mathbf{A}$.
$det(\mathbf{A})$	The determinant of square matrix $\mathbf{A}$.
$rank(\mathbf{A})$	The rank of $\mathbf{A}$ or the number of non-zeros singular values.
$\mathbf{I}_M$	$M \times M$ identity matrix.
$\mathbb{E}\{x\}$	The expected value of random variable x.
$\mathbb{V}\{x\}$	$\mathbb{V}\{x\} = \mathbb{E}\{\lvert x-\mathbb{E}\{x\}\rvert^2\}$. The variance of random variable x.

$\lvert a\rvert$	The absolute value of a.
$\sqrt{a}$	The square-root of a.
$\lVert\mathbf{a}\rVert$	$\lVert\mathbf{a}\rVert = \sqrt{\sum_i \lvert\mathbf{a}_k\rvert^2}$. The Euclidean norm of $\mathbf{a}$.
$\lVert\mathbf{A}\rVert_F$	$\lVert\mathbf{A}\rVert_F = \sqrt{\sum_{k,l} \lvert\mathbf{A}_{k,l}\rvert^2}$. The Frobenius norm of $\mathbf{A}$.
$\max(a,b)$	The maximum of a and b.
$\sin(x), cos(x)$	The sine and cosine function of x.
$\log_y(x)$	logarithm of x using the base a in $\mathbb{R}_+$.
σ^2	The variance of a distribution.
$\mathcal{N}_{\mathbb{C}}(0,1)$	Circularly symmetric complex Gaussian distribution: mean 0 and variance 1.
$\mathbb{U}[a,b]$	Uniform distribution between a and b.
χ^2_N	The chi-square random variable with N degrees of freedom.
$\mathbf{A}\otimes\mathbf{B}$	Kronecker product of $\mathbf{A}$ and $\mathbf{B}$.

A.0.2 List of Specific Used Symbols

Ch. 2	
M	Number of transmitting antennas at BS or AP side.
N_{RF}	Number of RF chains.
K	Number of users or UEs.
N	Number of antennas per UE.
M_f	Number of frequency points.
N_{obs}	Number of observations.
B_c	Coherence Bandwidth (generally at 0.7).
K^{Rice}	Ricean factor in dB.
$\gamma(\mathbf{G})$	Gram's Power Ratio.
t	Absolute time.
$\Delta\tau$	Delay bin.
n	Pathloss exponent.
N_{ray}	Number of MPC.
$\mathbf{h}_k$	k^{th} user channel vector.
$\mathbf{H}$ $(K\times M\times M_f)$	Massive MIMO channel matrix.
$\mathbf{R}_{Tx,3\lambda/2}$	Tx correlation matrix for $3\lambda/2$ element separation.
$\mathbf{R}_{Rx}$	$K\times K$ UE spatial correlation matrix.
ρ_{ij}	Spatial correlation between UEs i and j, respectively.
β	Large-scale coefficient (dB).
θ	Elevation angle.
ϕ	Azimuth angle.
$(\Delta\theta, \Delta\phi)$	Elevation and Azimuth angular spread.
C_k	Capacity bound per user.
$C(\mathbf{H})$ or C	Sum-rate capacity of $\mathbf{H}$.
$\mathbf{W}$	$M\times K$ Normalized precoding matrix.

Ch. 3	
M_{min}	Minimum number of array elements to reach ρ_{th}.
ψ	Link Polarization (VV or HV).
$\hat{M}$	Number of Tx elements in each polarization.
ρ_{th}	Correlation threshold for M_{min} .
K_v	Number of UEs on VV link.
K_h	Number of UEs on HV link.

Ch. 4	
PS	Power Selection
$\mathbf{R}_{Tx}(t)$	Full channel correlation matrix.
$\mathbf{H}_{ref}(t+\Delta t)$	Reduced measured channel matrix.
$\hat{\mathbf{H}}(t+\Delta t)$	Estimate of the measured channel.
d	Array element spacing.
$\boldsymbol{\rho}(t)$	Reduced correlation vector.
M_{ref}	Number of reference elements.
ρ_{Rx}	UEs average spatial correlation.
C	Capacity from measured channels.
$\hat{C}$	Capacity from estimated channels.
β	in %: ratio of C to $\hat{C}$.
S	Number of selected antennas for the array.
N_{dist}	Number of generated subsets for antenna selection strategy.
N_{sub}	Number of generated sub-arrays.
$\mathbf{H}_{FULL}$	$K \times M$ full array channel matrix.
$\mathbf{H}_{SUB}$	$K \times S$ Sub-array channel matrix.
$\mathbf{H}_{BSS}$	$K \times S$ channel matrix of the BSS.
$\mathbf{H}_{WSS}$	$K \times S$ channel matrix of the WSS.
C(BSS)	Sum-rate capacity obtained with the BSS.
C (FULL)	Sum-rate capacity obtained with the full-array.
β	Here, it is the ratio of C(BSS) and C (FULL).

A.0.3 List of Acronyms

3GPP	3^{rd} Generation Partnership Project.
A	
ADC	Analog-to-Digital Converter.
AF	Amplify and Forward.
AoD	Angle of Departure.
AoA	Angle of Arrival.
AP	Access Point.
Arcep	Autorité de régulation des communications électroniques et des Postes.
AWGN	Additive White Gaussian Noise.
AAS	Azimuth Angular Spread.
B	
BBU	Baseband units.
BS	Base Station.
BSS	Best Selected Subset.
BW	Bandwidth.
C	
CCM	Channel Correlation Matrix.
CDF	Cumulative Distribution Function.
C-RAN	Cloud-based radio access network.
CSI	Channel State Information.
CSIT	Channel State Information at Transmitter.
CTF	Channel Transfer Function.
D	
DAC	Digital-to-Analog Converter.
DBF	Digital Beamforming.
DL	Downlink.
DoF	Degrees of Freedom.
DPC	Dirty Paper Coding.
E	
eMBB	Enhanced Mobile Broadband.
ETSI	European Telecommunications Standards Institute.
EoD	Elevation of Departure.
EoA	Elevation of Arrival.
EAS	Elevation Angular Spread.
EP	Equal Power allocation.
F	
FDD	Frequency-Division Duplexing.

G	
GSM	Global System for Mobile Communications.
H	
HETNET	Heterogeneous network.
I	
i.i.d.	Independently and identically distributed.
IEEE	Institute of Electrical and Electronics Engineers.
IoT	Internet of Things.
K	
KBSM	Kronecker-Based Stochastic Model.
L	
LDPC	Low-Density Parity-Check code
LNA	Low Noise Amplifier.
LO	Local Oscillator.
LOS	Line-of-Sight.
LTE	Long-term evolution.
M	
MGF	Moment Generating Function.
MIMO	Multiple-Input Multiple-Output.
mmW	Millimeter Wavelength.
MMSE	Minimum Mean-Squared Error.
mMTC	Massive Machine Type Communications.
MPC	Multipath Components.
MRC	Maximal Ratio Combining.
MRT	Maximal Ratio Transmitting.
M2M	Machine-to-Machine.
MU	Multi-User.
N	
NR	New Radio.
NLOS	Non Line-Of-Sight.
O	
OFDM	Orthogonal Frequency-Division Multiplexing.
P	
PDF	Probability Distribution Function.
Q	
QoS	Quality of Service.
R	
RB	Resource block.
RF	Radio-Frequency.
RRH	Remote radio heads.

S	
SDMA	Space-Division Multiple Access.
SE	Spectral Efficiency.
SINR	Signal-to-Interference and Noise Ratio.
SISO	Single-Input Single-Output.
SNR	Signal-to-Noise Ratio.
SU	Single-User.
T	
TAS	Transmit Antenna Selection.
TDD	Time-Division Duplexing.
U	
UE	User Equipment.
UL	Uplink.
ULA	Uniform Linear Array.
UMa	Urban Macro.
UMi	Urban Micro.
URA	Uniform rectangular array.
URLLC	Ultra-Reliable Low Latency Communications.
V	
VAA	Virtual Antenna Array.
VNA	Vector Network Analyzer.
V2V	Vehicle-to-Vehicle.
VSWR	Voltage Standing Wave Ratio.
W	
WINNER	Wireless World Initiative New Radio.
WF	Waterfilling.
WSS	Worst Selected Subset.
X	
XPD	Cross-Polar Discrimination.
Z	
ZF	Zero-Forcing.

Appendix B

DPC and Waterfilling

B.1 Dirty Paper Coding

Dirty paper coding is a precoding technique for efficient data transmission over a channel experiencing interference such as noise sources, crosstalk, etc. This techniques was introduced by Max Costa [57] in 1983 and consists in canceling the effect of known interferences. The paper referred to in the technique's name is the data transmission medium, the writer is the transmitter and the reader is the user or the receive antenna. However, this paper is subject to dirt (interference) and the message on the paper (data information) might be unreadable when it reaches the reader because the dirt has distorted the original message. But if (and only if) the writer already knows the positions and intensities of the dirt spots are on the paper, he could try to get around them (in this case the paper is not fully used for writing the message). He could also try to adapt his ink to convey the message, in other words write on the dirt spots the message in a way that it is understandable to the reader. In this case, the paper is fully used and the reader receives the original message. Technically speaking, the BS avoids inter-user interference by adequately choosing the transmitted codewords. The message is encoded in the direction of interference instead of avoiding it and then added to the dirt. The set of used codewords should be known to the user in order to decode the original message. In MU-MIMO, this technique achieves the optimal channel capacity without interference knowledge at the receiver and more importantly with no power penalty. Most linear precoders are compared in terms of efficiency to the DPC technique. The drawback of this technique is mainly its significant complexity which is why low-complexity suboptimal schemes were selected.

B.2 Waterfilling algorithm

In a MU-MIMO setup and time-variant scenarios, the channels linking the BS to the different users is rapidly changing. Hence, the power and resource allocation should be accordingly updated to take into consideration the channel state. The power allocation $\{p_1^*, ..., p_{min(K,M)^*}\}$ that maximizes Eq. 2.41 is given by :

$$p_k^* = \left(\mu - \frac{1}{\rho\sigma_k^2}\right), \quad k = 1, ..., min(K, M), \tag{B.1}$$

where μ is the Lagrange multiplier satisfying the power constraint in the system. For each level $\rho\sigma_k^2$ with σ_k^2 denoting the singular mode of the corresponding user channel, the power allocation is performed by filling up the mode up to the power level indicated by μ. No power is allocated to the k^{th} mode if $\rho\sigma_k^2 \leq \frac{1}{\lambda}$. The optimization of power allocation is iteratively estimated as in [133]. A counter i is incremented and the constant μ is estimated at each iteration from the power constraint:

$$\mu(i) = \frac{1}{n - i + 1}\left(1 + \sum_{k=1}^{min(K,M)} \frac{1}{\rho\sigma_k^2}\right). \tag{B.2}$$

If the allocated power to the weakest mode is negative (i.e. $p_{min(K,M)-i+1} < 0$), the corresponding allocated power is set to 0. This mode is dropped and the power for the other modes is re-calculated after incrementing i. The process is repeated until the power allocated to each mode is either null or positive. An example of this principle with 8 channels and arbitrary chosen values is illustrated in Fig. B.1.

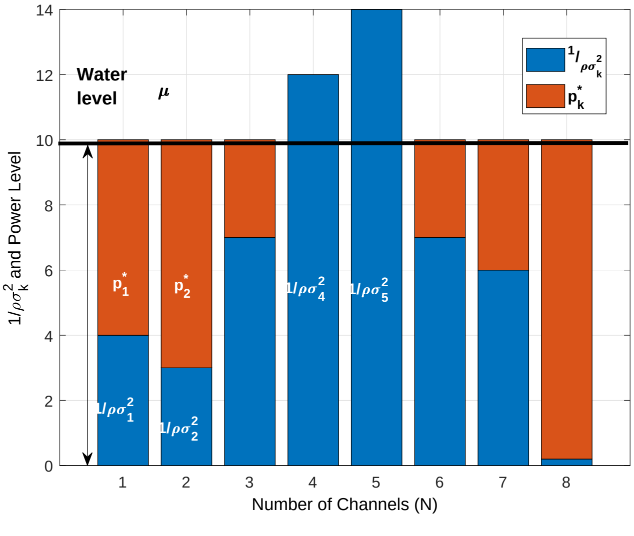

Figure B.1: *Waterfilling algorithm principle.*

Appendix C

Ricean Factor Estimation

In this appendix, a brief specification of maximum-likelihood-estimation (MLE) is discussed. In statistics, MLE is an estimation method of parameters by maximizing a likelihood function between the data in an observation set and the assumed statistical model. The point in the parameter space maximizing this function is called the maximum likelihood estimate [233]. The considered statistical model here is the Ricean Distribution with density function:

$$p(x) = \frac{x}{\sigma^2} I_0\left(\frac{Ax}{\sigma^2}\right) \exp(-\frac{x^2+\sigma^2}{2\sigma^2}), \quad x > 0 \tag{C.1}$$

and 0 otherwise. I_0 is the zero-order modified Bessel function of the first kind. A is the non-zero positive non-centrality parameter and σ a positive scale parameter. The Ricean factor is defined as:

$$K^{Rice} = \frac{A^2}{2\sigma^2}. \tag{C.2}$$

From the geometrical model presented in this manuscript, the accuracy of the MLE is evaluated. The following figure illustrates the estimated K^{Rice} with respect to the real simulated K^{Rice}.

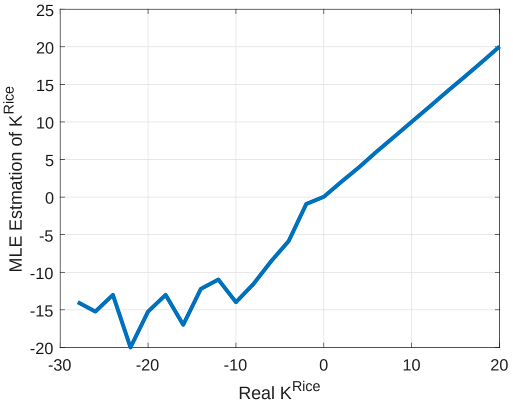

Figure C.1: *Convergence of the MLE estimator for different K^{Rice} values.*

It is concluded from this presentation that K^{Rice} is well estimated for positive values only and thus MLE cannot be used to estimate negative K^{Rice} values. Therefore, the negative values of estimated K^{Rice} values in this manuscript are thus considered as zeros due to the poor estimation accuracy.

Appendix D

Geometrical Model: Charts and Validation

In this appendix, the geometrical channel model proposed in Ch. 2 is validated using channel measurements described in Ch. 3. First, the different charts of correlation values at Rx (Fig. D.1) and Tx (Fig. D.2) are presented. These values were used for the parametric analysis in Ch. 2 as shown in Tables 2.1 and 2.2.

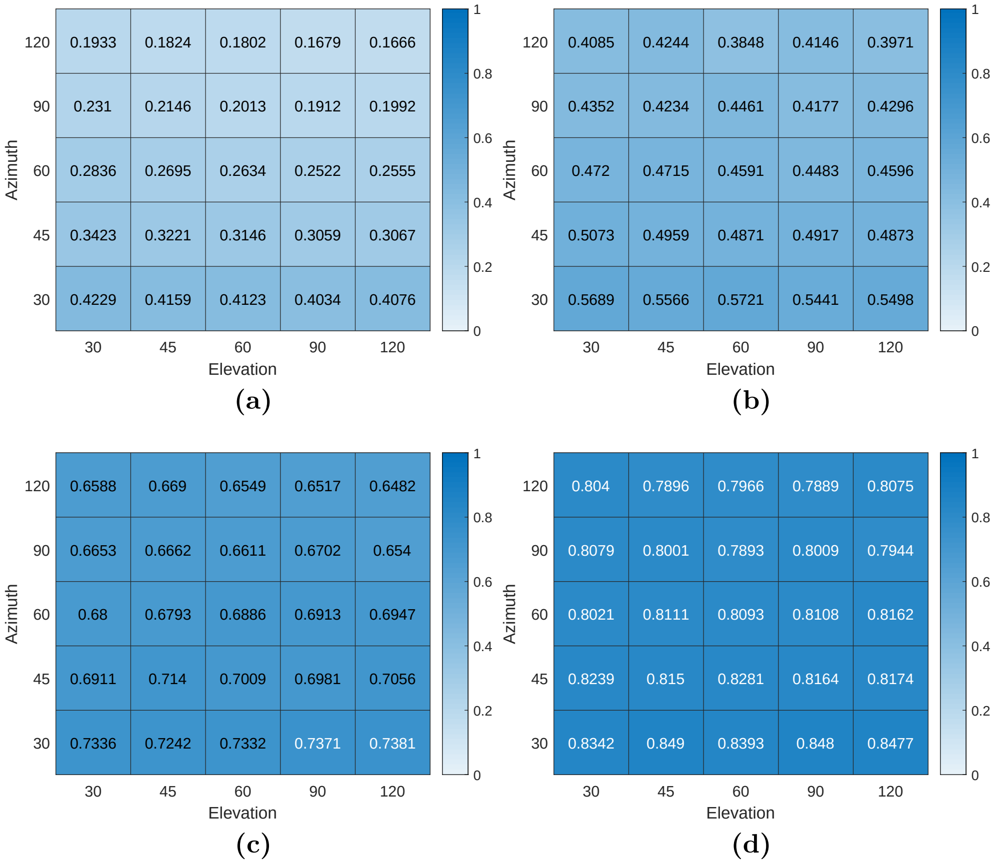

	30	45	60	90	120
120	0.1933	0.1824	0.1802	0.1679	0.1666
90	0.231	0.2146	0.2013	0.1912	0.1992
60	0.2836	0.2695	0.2634	0.2522	0.2555
45	0.3423	0.3221	0.3146	0.3059	0.3067
30	0.4229	0.4159	0.4123	0.4034	0.4076

(a)

	30	45	60	90	120
120	0.4085	0.4244	0.3848	0.4146	0.3971
90	0.4352	0.4234	0.4461	0.4177	0.4296
60	0.472	0.4715	0.4591	0.4483	0.4596
45	0.5073	0.4959	0.4871	0.4917	0.4873
30	0.5689	0.5566	0.5721	0.5441	0.5498

(b)

	30	45	60	90	120
120	0.6588	0.669	0.6549	0.6517	0.6482
90	0.6653	0.6662	0.6611	0.6702	0.654
60	0.68	0.6793	0.6886	0.6913	0.6947
45	0.6911	0.714	0.7009	0.6981	0.7056
30	0.7336	0.7242	0.7332	0.7371	0.7381

(c)

	30	45	60	90	120
120	0.804	0.7896	0.7966	0.7889	0.8075
90	0.8079	0.8001	0.7893	0.8009	0.7944
60	0.8021	0.8111	0.8093	0.8108	0.8162
45	0.8239	0.815	0.8281	0.8164	0.8174
30	0.8342	0.849	0.8393	0.848	0.8477

(d)

Figure D.1: *ρ_{Rx} values for different elevation $\Delta\theta$ and azimuth $\Delta\phi$ angles (in ^{o}) and different K^{Rice} values: (a) -10 dB, (b) 0 dB, (c) 6 dB and (d) 10 dB. These parameters are set using the geometrical model.*

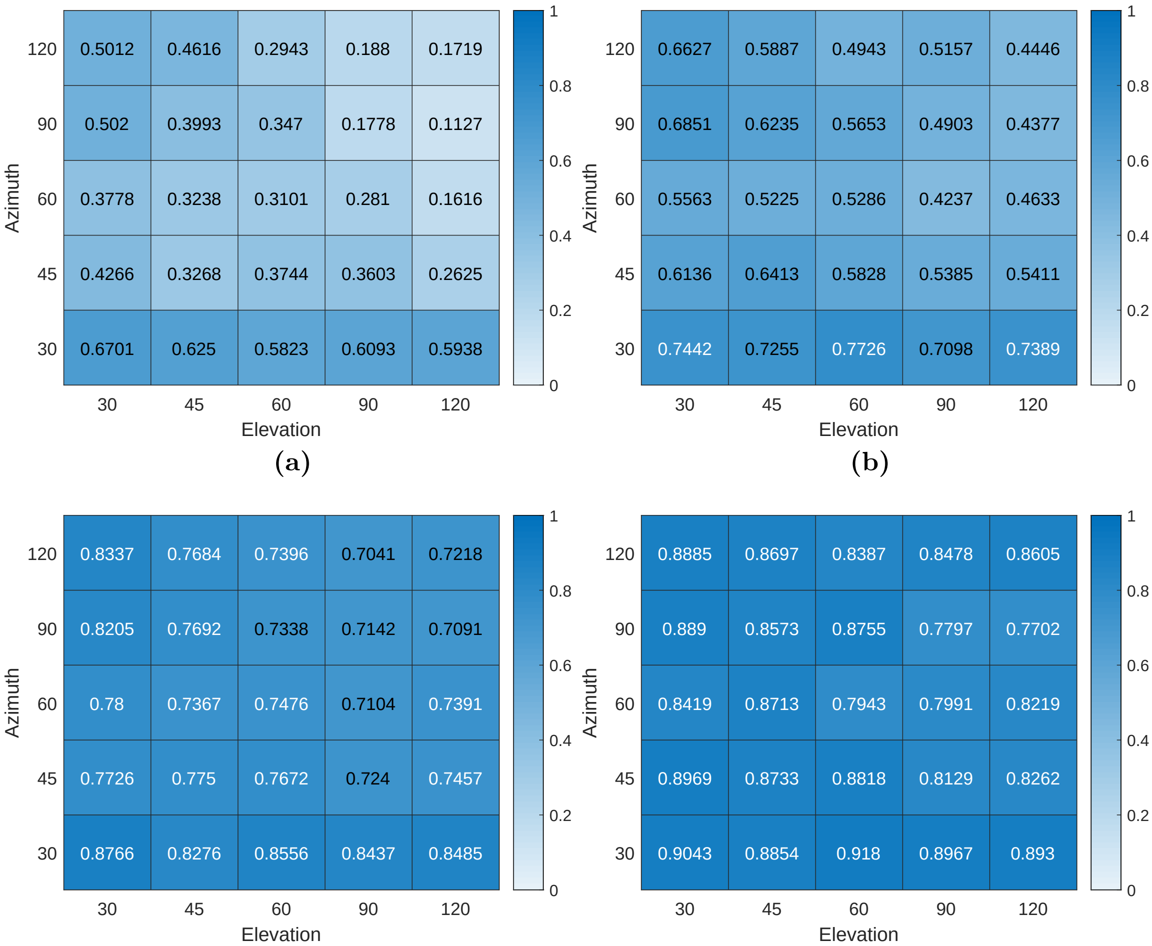

(a) **(b)**

(c) **(d)**

Figure D.2: *$\rho_{Tx,3\lambda/2}$ values for different elevation $\Delta\theta$ and azimuth $\Delta\phi$ angles (in ^{o}) and different K^{Rice} values: (a) -10 dB, (b) 0 dB, (c) 6 dB and (d) 10 dB. These parameters are set using the geometrical model.*

Experimental Vs Geometrical Model

The geometrical model parameters for this comparison are:

- LOS scenario : $K = 6$, $K^{Rice} = 6$ dB, $\Delta\theta = 25^o$ and $\Delta\phi = 30^o$.
- NLOS scenario : $K = 9$, $K^{Rice} = -3$ dB, $\Delta\theta = 45^o$ and $\Delta\phi = 90^o$.

The different CDF curves in Figs. D.3(a) and (b) show that the geometrical model fits fairly well the measured channel in the industrial scenario, especially in NLOS and for the total scenario. Also, the Tx correlation computed with the geometrical model presents a similar behavior (shape and median value of the curve) than those obtained from experimental channels. This figure gives insight into the possibility of evaluating the massive MIMO system performance using a parametric analysis.

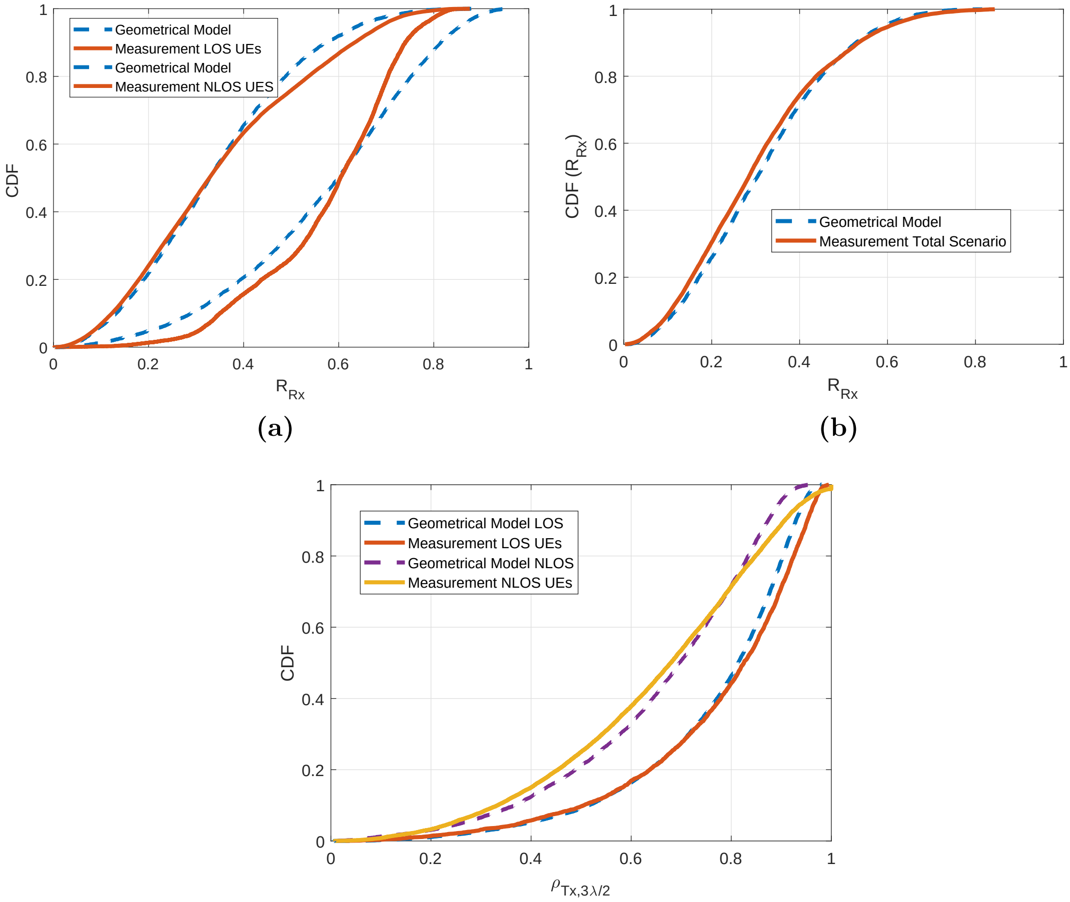

(a) (b) (c)

Figure D.3: *CDF of the spatial correlation values $\rho_{i,j}$ for all (i, j) combinations. The comparison is done for (a) LOS, NLOS scenarios of Ch. 3 and geometrical model for each case, (b) the total scenario with all UEs and (c) the correlation at Tx for inter-element spacing of $3\lambda/2$ for LOS and NLOS UE.*

Geometrical Model Validation

The different correlation characteristics were shown to be close to experimental data in the previous section.

In order to validate the geometrical model, it is possible to evaluate its performance using the Gram's power ratio and comparing $\gamma(\mathbf{G})$ for the LOS and NLOS scenarios (presented in Ch. 3).

This is illustrated in Fig. D.4. This figure highlights the evolution of $\gamma(\mathbf{G})$ with the number of array elements M and confirms that the model performance is close to the experimental channels.

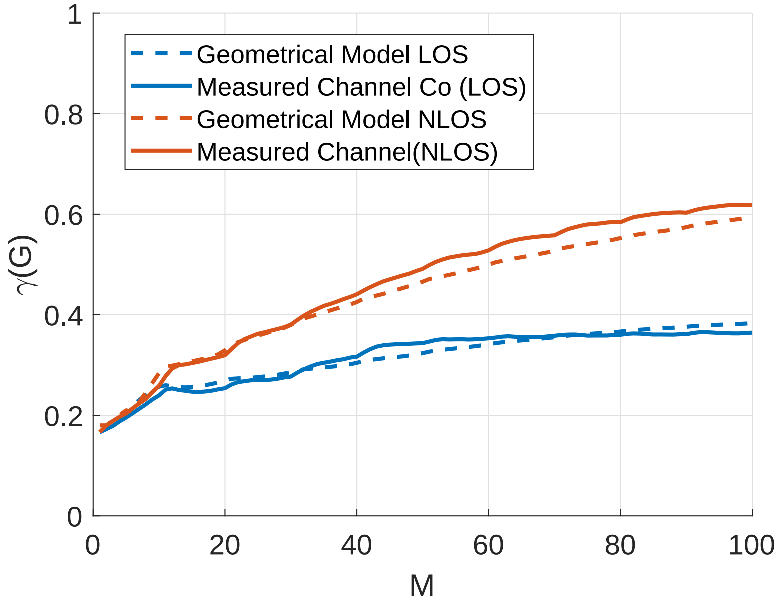

Figure D.4: *Comparison of the Gram's power ratio dependence with M between measured and geometrical channels for the LOS and NLOS scenarios. The geometrical model was tuned using the parameters defined in the previous section.*

Appendix E

Antennas Characteristics

In this appendix, the different frequency characteristics of the patch antennas at 1.35, 3.5 and 6 GHz are presented. Antennas at 1.35 GHz were designed for the MIMOSA channel sounder presented in [229]. More information about the antennas can be found in [234]. The radiation patterns of antennas at 3.5 and 6 GHz are presented for the two cuts in azimuth ϕ and elevation θ. The beamwidth at -3 dB is also indicated.

S_{11} parameter and Patch Gain

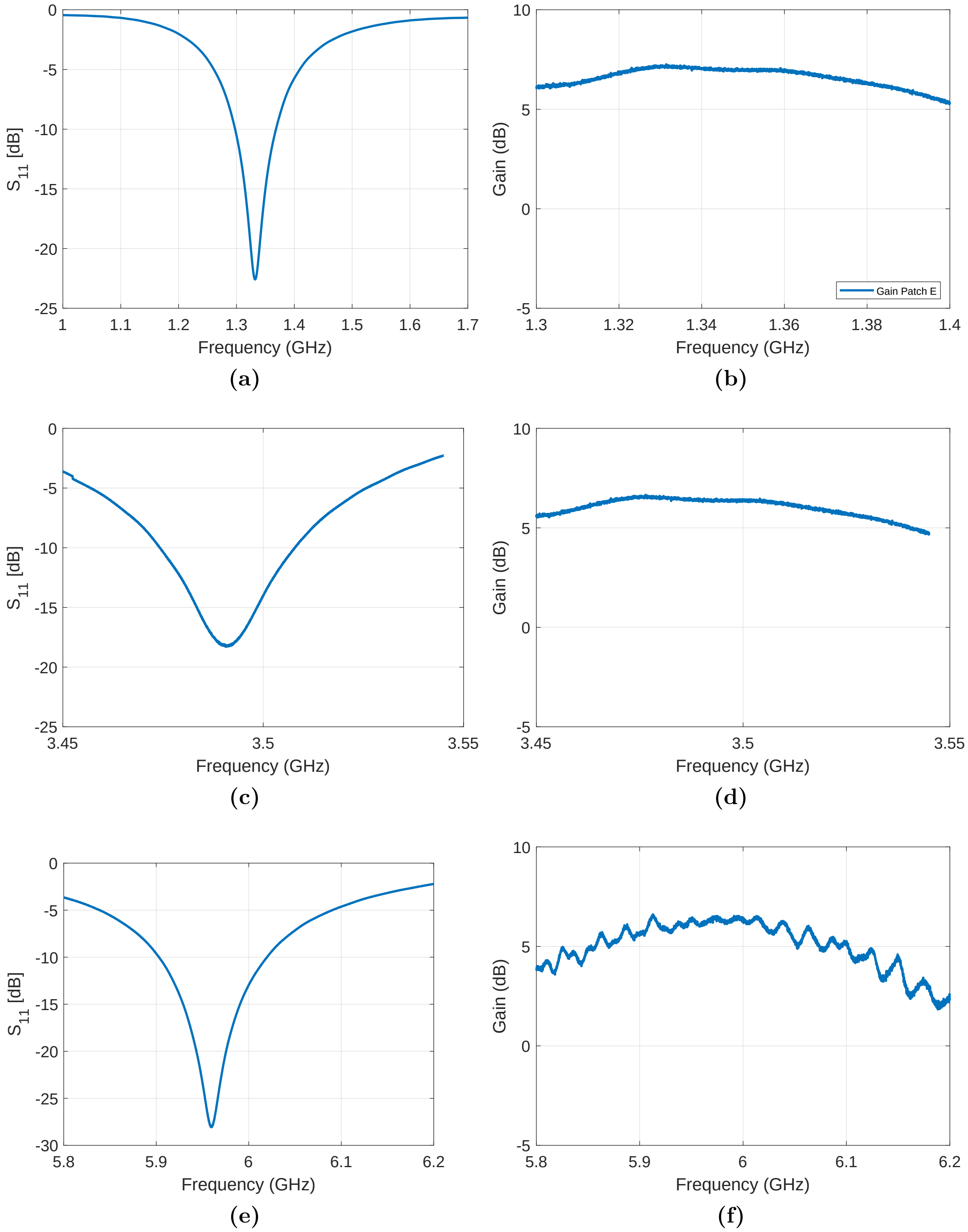

Figure E.1: *Scattering parameter* S_{11} *in dB for the three frequencies (a) 1.35 GHz, (c) 3.5 GHz and (e) 6 GHz. Patch Gain in dB for the three frequencies (b) 1.35 GHz, (d) 3.5 GHz and (f) 6 GHz.*

Radiation Pattern $G(\phi, \theta)$

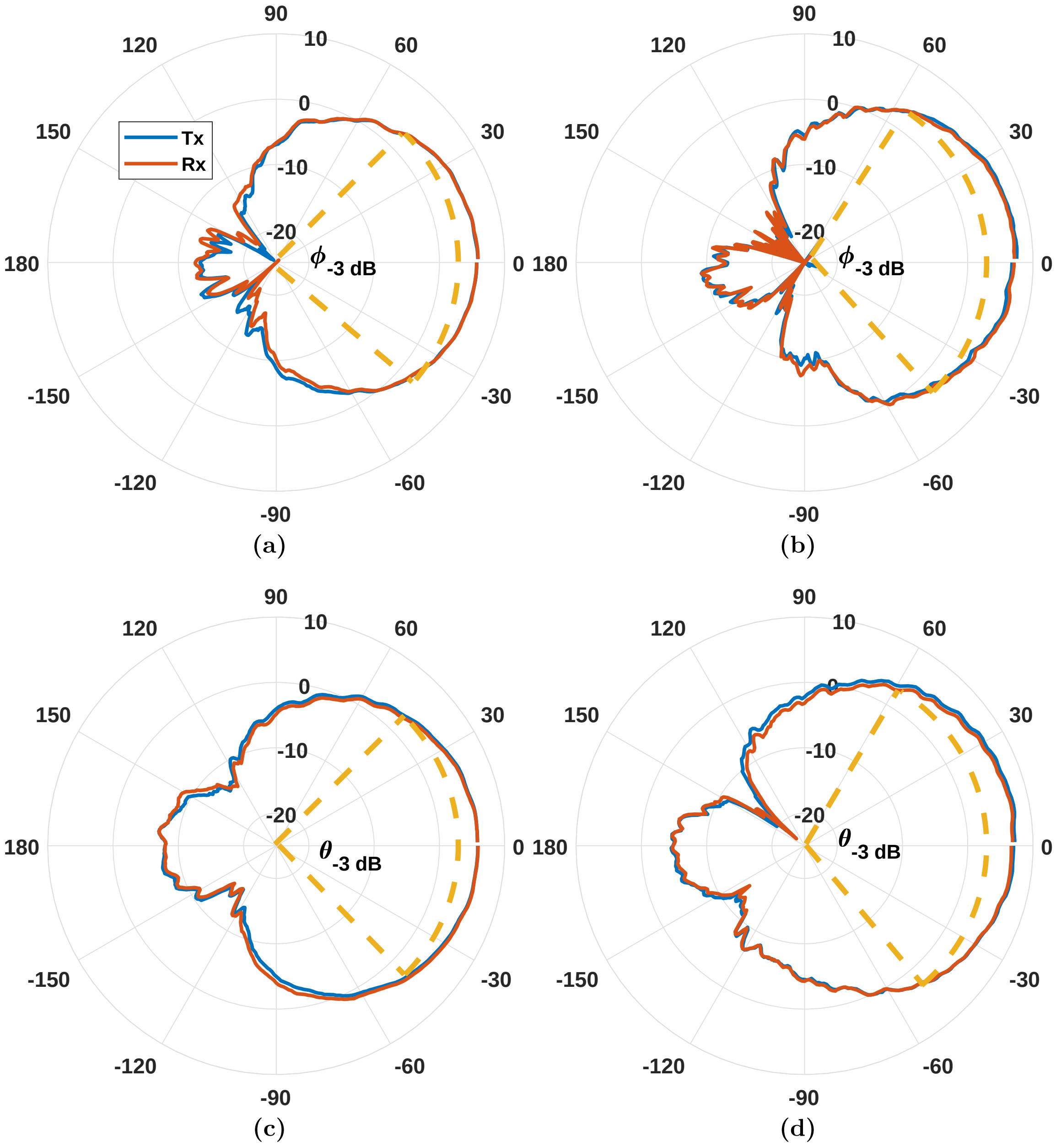

(a) (b)

(c) (d)

Figure E.2: *Radiation pattern in azimuth cut for (a) 3.5 GHz, (b) 6 GHz and in elevation cut for (c) 3.5 GHz, (d) 6 GHz.*

Radiation Pattern with Cross-Polarization

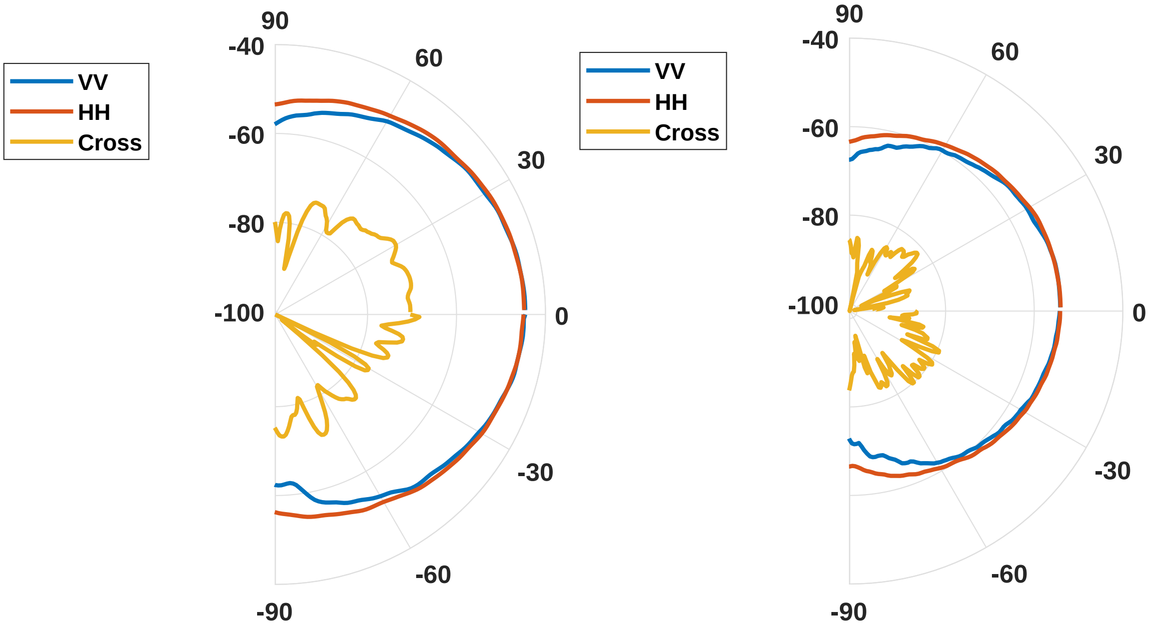

(a) (b)

Figure E.3: *Radiation pattern for co- and cross polarizations at (a) 3.5 GHz and (b) 6 GHz.*

Appendix F

UE Allocation Strategies

Algorithm 1 Minimization of $\rho_{i,j}$ for i, j couples with $\rho_{i,j} > \rho_t$

```
Compute the $K \times K$ $\mathbf{R_{Rx}}$
$i \leftarrow 1$
while $i \leq K - 1$ do
    $j \leftarrow i + 1$
    while $j \leq K$ do
        if $\rho_{i,j} \geq \rho_t$ then
            $\psi(i) \leftarrow V$
            $\psi(j) \leftarrow H$
            break
        else
            $j \leftarrow j + 1$
        end if
    end while
    $i \leftarrow i + 1$
end while
```

Algorithm 2 Minimization of $\rho_{i,j}$ for all i, j couples

```
Compute the $K \times K$ $\mathbf{R_{Rx}}$
$i \leftarrow 1$
$IndMax \leftarrow 0$
while $i \leq K - 1$ && $IndMax \neq i$ do
    $[Max, IndMax] = \arg\max(\boldsymbol{\rho}_i)$
    $\psi(i) \leftarrow V$
    $\psi(IndMax) \leftarrow H$
    $i \leftarrow i + 1$
end while
$i \leftarrow i + 1$
```

Bibliography

[1] Simon R Saunders and Alejandr Aragón Zavala. *Antennas and Propagation for Wireless Communication Systems.* John Wiley & Sons, Inc., New York, NY, USA, 1st edition, 1999.

[2] Ian F. Akyildiz, Shuai Nie, Shih-Chun Lin, and Manoj Chandrasekaran. 5G roadmap: 10 key enabling technologies. *Computer Networks*, 106:17 – 48, 2016.

[3] C. Wang, F. Haider, X. Gao, X. You, Y. Yang, D. Yuan, H. M. Aggoune, H. Haas, S. Fletcher, and E. Hepsaydir. Cellular architecture and key technologies for 5G wireless communication networks. *IEEE Communications Magazine*, 52(2):122–130, February 2014.

[4] D. Phan-Huy, M. Sternad, and T. Svensson. Making 5G Adaptive Antennas Work for Very Fast Moving Vehicles. *IEEE Intelligent Transportation Systems Magazine*, 7(2):71–84, Summer 2015.

[5] A. Osseiran, F. Boccardi, V. Braun, K. Kusume, P. Marsch, M. Maternia, O. Queseth, M. Schellmann, H. Schotten, H. Taoka, H. Tullberg, M. A. Uusitalo, B. Timus, and M. Fallgren. Scenarios for 5G mobile and wireless communications: the vision of the METIS project. *IEEE Communications Magazine*, 52(5):26–35, May 2014.

[6] A. Gupta and R. K. Jha. A Survey of 5G Network: Architecture and Emerging Technologies. *IEEE Access*, 3:1206–1232, 2015.

[7] *CISCO Global Cloud Index (GCI).* `http://www.cisco.com/c/dam/en/us/solutions/collateral/service-provider/global-cloud-index-gci/white-paper-c11-738085.pdf`.

[8] M. Agiwal, A. Roy, and N. Saxena. Next Generation 5G Wireless Networks: A Comprehensive Survey. *IEEE Communications Surveys Tutorials*, 18(3):1617–1655, thirdquarter 2016.

[9] NOKIA Bell Labs. 5G New Radio (NR) : Physical Layer Overview and Performance. `http://ctw2018.ieee-ctw.org/files/2018/05/5G-NR-CTW-final.pdf`, 2018. IEEE Communication Theory Workshop - 2018.

[10] Xingqin Lin, Jingya Li, Robert Baldemair, Thomas Cheng, Stefan Parkvall, Daniel Larsson, Havish Koorapaty, Mattias Frenne, Sorour Falahati, Asbjörn Grövlen, and Karl Werner. 5G New Radio: Unveiling the Essentials of the Next Generation Wireless Access Technology. *CoRR*, abs/1806.06898, 2018.

[11] S. Parkvall, E. Dahlman, A. Furuskar, and M. Frenne. NR: The New 5G Radio Access Technology. *IEEE Communications Standards Magazine*, 1(4):24–30, Dec 2017.

[12] 3G-PPP. 3GPP Technical Report Technical Specification Group Radio Access Network; Study on NR Industrial Internet of Things (IoT); (Release 16) available at:. `https://www.3gpp.org/ftp/Specs/archive/38_series/38.825/`.

[13] 5G-PPP. The 5G Infrastructure Public Private Partnership (5G-PPP) Technical Report, February 2016, 5G empowering vertical industries, available at:. `https://5g-ppp.eu/wp-content/uploads/2016/02/BROCHURE_5PPP_BAT2_PL.pdf`, 2018. Accessed: 2018-05-28.

[14] A. Osseiran, F. Boccardi, V. Braun, K. Kusume, P. Marsch, M. Maternia, O. Queseth, M. Schellmann, H. Schotten, H. Taoka, H. Tullberg, M. A. Uusitalo, B. Timus, and M. Fallgren. Scenarios for 5G mobile and wireless communications: the vision of the METIS project. *IEEE Communications Magazine*, 52(5):26–35, May 2014.

[15] ERICSSON. Designing for the future: the 5G NR physical layer. `https://www.ericsson.com/assets/local/publications/ericsson-technology-review/docs/2017/designing-for-the-future---the-5g-nr-physical-layer.pdf`, 2017. Accessed: 2019-03-01.

[16] M. R. Palattella, M. Dohler, A. Grieco, G. Rizzo, J. Torsner, T. Engel, and L. Ladid. Internet of Things in the 5G Era: Enablers, Architecture, and Business Models. *IEEE Journal on Selected Areas in Communications*, 34(3):510–527, March 2016.

[17] R. Ratasuk, A. Prasad, Z. Li, A. Ghosh, and M. A. Uusitalo. Recent advancements in M2M communications in 4G networks and evolution towards 5G. In *2015 18th International Conference on Intelligence in Next Generation Networks*, pages 52–57, Feb 2015.

[18] Sriganesh K. Rao and Ramjee Prasad. Impact of 5G Technologies on Industry 4.0. *Wirel. Pers. Commun.*, 100(1):145–159, May 2018.

[19] M. N. Tehrani, M. Uysal, and H. Yanikomeroglu. Device-to-device communication in 5G cellular networks: challenges, solutions, and future directions. *IEEE Communications Magazine*, 52(5):86–92, May 2014.

[20] N. A. Johansson, Y. . E. Wang, E. Eriksson, and M. Hessler. Radio access for ultra-reliable and low-latency 5G communications. In *2015 IEEE International Conference on Communication Workshop (ICCW)*, pages 1184–1189, June 2015.

[21] P. Schulz, M. Matthe, H. Klessig, M. Simsek, G. Fettweis, J. Ansari, S. A. Ashraf, B. Almeroth, J. Voigt, I. Riedel, A. Puschmann, A. Mitschele-Thiel, M. Muller, T. Elste, and M. Windisch. Latency Critical IoT Applications in 5G: Perspective on the Design of Radio Interface and Network Architecture. *IEEE Communications Magazine*, 55(2):70–78, February 2017.

[22] KEYSIGHT Technologies. Field Testing in 5G NR. `https://literature.cdn.keysight.com/litweb/pdf/5992-3299EN.pdf?id=3013192`, 2018. Accessed: 2019-03-05.

[23] ARCEP. *French regulator likely to award 5G frequencies by mid-2019*, 2019. `https://www.rcrwireless.com/20180914/5g/french-regulator-likely-award-5g-frequencies-mid-2019`.

[24] 3GPP, Dubrovnik, Croatia. *RP-170855 : New WID on new radio access technology*, March 2017. `https://www.3gpp.org/ftp/TSG_RAN/TSG_RAN/TSGR_75/Docs/RP-170855.zip`.

[25] HUAWEI. 5G Spectrum/ Public Policy Position. `http://www-file.huawei.com/-/media/CORPORATE/PDF/public-policy/public_policy_position_5g_spectrum.pdf`, 2017. Accessed: 2018-05-20.

[26] Huawei. 5G Spectrum, 2018. `https://www-file.huawei.com/-/media/CORPORATE/PDF/public-policy/public_policy_position_5g_spectrum.pdf`.

[27] S. Salous, V. Degli Esposti, F. Fuschini, R. S. Thomae, R. Mueller, D. Dupleich, K. Haneda, J. Molina Garcia-Pardo, J. Pascual Garcia, D. P. Gaillot, S. Hur, and M. Nekovee. Millimeter-Wave Propagation: Characterization and modeling toward fifth-generation systems. [wireless corner]. *IEEE Antennas and Propagation Magazine*, 58(6):115–127, Dec 2016.

[28] T. S. Rappaport, S. Sun, R. Mayzus, H. Zhao, Y. Azar, K. Wang, G. N. Wong, J. K. Schulz, M. Samimi, and F. Gutierrez. Millimeter Wave Mobile Communications for 5G Cellular: It Will Work! *IEEE Access*, 1:335–349, 2013.

[29] W. Roh, J. Seol, J. Park, B. Lee, J. Lee, Y. Kim, J. Cho, K. Cheun, and F. Aryanfar. Millimeter-wave beamforming as an enabling technology for 5G cellular communications: theoretical feasibility and prototype results. *IEEE Communications Magazine*, 52(2):106–113, February 2014.

[30] D. T. Phan-Huy, A. Tolli, N. Rajatheva, and E. De Carvalho. DFT based spatial multiplexing and maximum ratio transmission for mm-wave large MIMO. In *2014 IEEE Wireless Communications and Networking Conference (WCNC)*, pages 913–918, April 2014.

[31] J. G. Andrews, S. Buzzi, W. Choi, S. V. Hanly, A. Lozano, A. C. K. Soong, and J. C. Zhang. What Will 5G Be? *IEEE Journal on Selected Areas in Communications*, 32(6):1065–1082, June 2014.

[32] C. Jarray, A. Bouabid, and B. Chibani. Enabling and challenges for 5G Technologies. In *Information Technology and Computer Applications Congress (WCITCA), 2015 World Congress on*, pages 1–9, June 2015.

[33] S. Chen and J. Zhao. The requirements, challenges, and technologies for 5G of terrestrial mobile telecommunication. *IEEE Communications Magazine*, 52(5):36–43, May 2014.

[34] M. J. Marcus. WRC-19 Issues: A Survey. *IEEE Wireless Communications*, 24(1):2–3, February 2017.

[35] M. J. Marcus. Spectrum Policy and Regulatory Issues. *IEEE Wireless Communications*, 26(1):9–9, February 2019.

[36] F. Boccardi, R. W. Heath, A. Lozano, T. L. Marzetta, and P. Popovski. Five disruptive technology directions for 5G. *IEEE Communications Magazine*, 52(2):74–80, February 2014.

[37] C-ran the Road towards Green Ran.

[38] *Cloud RAN Architecture for 5G*. `https://www.metis2020.com/documents/deliverables/`.

[39] E. G. Larsson, O. Edfors, F. Tufvesson, and T. L. Marzetta. Massive MIMO for next generation wireless systems. *IEEE Communications Magazine*, 52(2):186–195, February 2014.

[40] Wenjia Liu, Shengqian Han, and Chenyang Yang. Is Massive MIMO Energy Efficient? *CoRR*, abs/1505.07187, 2015.

[41] C. E. Shannon. A mathematical theory of communication. *The Bell System Technical Journal*, 27(3):379–423, July 1948.

[42] I. Emre Telatar. Capacity of multi-antenna Gaussian channels. *EUROPEAN TRANSACTIONS ON TELECOMMUNICATIONS*, 10:585–595, 1999.

[43] A. J. Paulraj and C. B. Papadias. Space-time processing for wireless communications. *IEEE Signal Processing Magazine*, 14(6):49–83, Nov 1997.

[44] P. Pagani, R. Hashmat, A. Schwager, D. Schneider, and W. Baschlin. European MIMO PLC field measurements: Noise analysis. In *2012 IEEE International Symposium on Power Line Communications and Its Applications*, pages 310–315, March 2012.

[45] R. Hashmat, P. Pagani, A. Zeddam, and T. Chonavel. Mimo communications for inhome plc networks: Measurements and results up to 100 mhz. In *ISPLC2010*, pages 120–124, March 2010.

[46] D. Schneider, A. Schwager, W. Baschlin, and P. Pagani. European MIMO PLC field measurements: Channel analysis. In *2012 IEEE International Symposium on Power Line Communications and Its Applications*, pages 304–309, March 2012.

[47] P. Viswanath and D. N. C. Tse. Sum capacity of the vector Gaussian broadcast channel and uplink-downlink duality. *IEEE Transactions on Information Theory*, 49(8):1912–1921, Aug 2003.

[48] Q. H. Spencer, C. B. Peel, A. L. Swindlehurst, and M. Haardt. An introduction to the multi-user MIMO downlink. *IEEE Communications Magazine*, 42(10):60–67, Oct 2004.

[49] E. Castaneda, A. Silva, A. Gameiro, and M. Kountouris. An Overview on Resource Allocation Techniques for Multi-User MIMO Systems. *IEEE Communications Surveys Tutorials*, 19(1):239–284, Firstquarter 2017.

[50] A. Sibille. Diversity combining for enhanced Multi-user throughput in pulse based UWB communications. In *11th European Wireless Conference 2005 - Next Generation wireless and Mobile Communications and Services*, pages 1–6, April 2006.

[51] S. C. Swales, M. A. Beach, D. J. Edwards, and J. P. McGeehan. The performance enhancement of multibeam adaptive base-station antennas for cellular land mobile radio systems. *IEEE Transactions on Vehicular Technology*, 39(1):56–67, Feb 1990.

[52] J. Winters. Optimum Combining for Indoor Radio Systems with Multiple Users. *IEEE Transactions on Communications*, 35(11):1222–1230, November 1987.

[53] P. Zetterberg and B. Ottersten. The spectrum efficiency of a base station antenna array system for spatially selective transmission. In *Proceedings of IEEE Vehicular Technology Conference (VTC)*, pages 1517–1521 vol.3, June 1994.

[54] S. Anderson, M. Millnert, M. Viberg, and B. Wahlberg. An adaptive array for mobile communication systems. *IEEE Transactions on Vehicular Technology*, 40(1):230–236, Feb 1991.

[55] D. Gesbert, M. Kountouris, R. W. Heath, C. Chae, and T. Salzer. Shifting the MIMO Paradigm. *IEEE Signal Processing Magazine*, 24(5):36–46, Sep. 2007.

[56] Verdu, Sergio. *Multiuser Detection.* Cambridge University Press, New York, NY, USA, 1st edition, 1998.

[57] M. Costa. Writing on dirty paper (corresp.). *IEEE Transactions on Information Theory*, 29(3):439–441, May 1983.

[58] N. Jindal and A. Goldsmith. Dirty paper coding vs. TDMA for MIMO broadcast channels. In *2004 IEEE International Conference on Communications (IEEE Cat. No.04CH37577)*, volume 2, pages 682–686 Vol.2, June 2004.

[59] K. Gomadam, V. R. Cadambe, and S. A. Jafar. A Distributed Numerical Approach to Interference Alignment and Applications to Wireless Interference Networks. *IEEE Transactions on Information Theory*, 57(6):3309–3322, June 2011.

[60] C. Suh, M. Ho, and D. N. C. Tse. Downlink Interference Alignment. *IEEE Transactions on Communications*, 59(9):2616–2626, September 2011.

[61] A. Tarighat, M. Sadek, and A. H. Sayed. A multi user beamforming scheme for downlink MIMO channels based on maximizing signal-to-leakage ratios. In *Proceedings. (ICASSP '05). IEEE International Conference on Acoustics, Speech, and Signal Processing, 2005.*, volume 3, pages iii/1129–iii/1132 Vol. 3, March 2005.

[62] M. Codreanu, A. Tolli, M. Juntti, and M. Latva-aho. Joint Design of Tx-Rx Beamformers in MIMO Downlink Channel. *IEEE Transactions on Signal Processing*, 55(9):4639–4655, Sept 2007.

[63] A. Marzetta T.L., Ashikhmin. MIMO systems having a plurality of service antennas for data transmission and reception and method thereof, 2011.

[64] T. L. Marzetta. Noncooperative Cellular Wireless with Unlimited Numbers of Base Station Antennas. *IEEE Transactions on Wireless Communications*, 9(11):3590–3600, November 2010.

[65] E. Björnson, J. Hoydis, M. Kountouris, and M. Debbah. Massive MIMO Systems With Non-Ideal Hardware: Energy Efficiency, Estimation, and Capacity Limits. *IEEE Transactions on Information Theory*, 60(11):7112–7139, Nov 2014.

[66] J. Jose, A. Ashikhmin, T. L. Marzetta, and S. Vishwanath. Pilot Contamination and Precoding in Multi-Cell TDD Systems. *IEEE Transactions on Wireless Communications*, 10(8):2640–2651, August 2011.

[67] Thomas L. Marzetta, Erik G. Larsson, Hong Yang, and Hien Quoc Ngo. *Fundamentals of Massive MIMO*. Cambridge University Press, 2016.

[68] Trinh Van Chien and Emil Björnson. *Massive MIMO Communications*, pages 77–116. Springer International Publishing, Cham, 2017.

[69] J. Vieira, S. Malkowsky, K. Nieman, Z. Miers, N. Kundargi, L. Liu, I. Wong, V. ¨Owall, O. Edfors, and F. Tufvesson. A flexible 100-antenna testbed for Massive MIMO. In *2014 IEEE Globecom Workshops (GC Wkshps)*, pages 287–293, Dec 2014.

[70] J. Hoydis, S. ten Brink, and M. Debbah. Massive MIMO in the UL/DL of Cellular Networks: How Many Antennas Do We Need? *IEEE Journal on Selected Areas in Communications*, 31(2):160–171, February 2013.

[71] S. K. Mohammed and E. G. Larsson. Per-Antenna Constant Envelope Precoding for Large Multi-User MIMO Systems. *IEEE Transactions on Communications*, 61(3):1059–1071, March 2013.

[72] H. Yang and T. L. Marzetta. Performance of Conjugate and Zero-Forcing Beamforming in Large-Scale Antenna Systems. *IEEE Journal on Selected Areas in Communications*, 31(2):172–179, February 2013.

[73] L. Lu, G. Y. Li, A. L. Swindlehurst, A. Ashikhmin, and R. Zhang. An Overview of Massive MIMO: Benefits and Challenges. *IEEE Journal of Selected Topics in Signal Processing*, 8(5):742–758, Oct 2014.

[74] E. Björnson, E. G. Larsson, and M. Debbah. Massive MIMO for Maximal Spectral Efficiency: How Many Users and Pilots Should Be Allocated? *IEEE Transactions on Wireless Communications*, 15(2):1293–1308, Feb 2016.

[75] H. Huh, G. Caire, H. C. Papadopoulos, and S. A. Ramprashad. Achieving "Massive MIMO" Spectral Efficiency with a Not-so-Large Number of Antennas. *IEEE Transactions on Wireless Communications*, 11(9):3226–3239, Sep. 2012.

[76] G. N. Kamga, M. Xia, and S. Aïssa. Spectral-Efficiency Analysis of Massive MIMO Systems in Centralized and Distributed Schemes. *IEEE Transactions on Communications*, 64(5):1930–1941, May 2016.

[77] X. Gao, O. Edfors, F. Rusek, and F. Tufvesson. Massive MIMO Performance Evaluation Based on Measured Propagation Data. *IEEE Transactions on Wireless Communications*, 14(7):3899–3911, July 2015.

[78] J. Flordelis, X. Gao, G. Dahman, F. Rusek, O. Edfors, and F. Tufvesson. Spatial separation of closely-spaced users in measured massive multi-user MIMO channels. In *2015 IEEE International Conference on Communications (ICC)*, pages 1441–1446, June 2015.

[79] J. Chen, X. Yin, X. Cai, and S. Wang. Measurement-Based Massive MIMO Channel Modeling for Outdoor LoS and NLoS Environments. *IEEE Access*, 5:2126–2140, 2017.

[80] P. Gandotra and R. K. Jha. Next generation cellular networks and green communication. In *2018 10th International Conference on Communication Systems Networks (COMSNETS)*, pages 522–524, Jan 2018.

[81] S. Buzzi, C. I, T. E. Klein, H. V. Poor, C. Yang, and A. Zappone. A Survey of Energy-Efficient Techniques for 5G Networks and Challenges Ahead. *IEEE Journal on Selected Areas in Communications*, 34(4):697–709, April 2016.

[82] E. Björnson, L. Sanguinetti, J. Hoydis, and M. Debbah. Optimal Design of Energy-Efficient Multi-User MIMO Systems: Is Massive MIMO the Answer? *IEEE Transactions on Wireless Communications*, 14(6):3059–3075, June 2015.

[83] V. Venkateswaran and A. van der Veen. Analog Beamforming in MIMO Communications With Phase Shift Networks and Online Channel Estimation. *IEEE Transactions on Signal Processing*, 58(8):4131–4143, Aug 2010.

[84] Z. Gao, L. Dai, D. Mi, Z. Wang, M. A. Imran, and M. Z. Shakir. MmWave massive-MIMO-based wireless backhaul for the 5G ultra-dense network. *IEEE Wireless Communications*, 22(5):13–21, October 2015.

[85] T. E. Bogale and L. B. Le. Massive MIMO and mmWave for 5G Wireless HetNet: Potential Benefits and Challenges. *IEEE Vehicular Technology Magazine*, 11(1):64–75, March 2016.

[86] F. Sohrabi and W. Yu. Hybrid Digital and Analog Beamforming Design for Large-Scale Antenna Arrays. *IEEE Journal of Selected Topics in Signal Processing*, 10(3):501–513, April 2016.

[87] A. F. Molisch, V. V. Ratnam, S. Han, Z. Li, S. L. H. Nguyen, L. Li, and K. Haneda. Hybrid Beamforming for Massive MIMO: A Survey. *IEEE Communications Magazine*, 55(9):134–141, Sep. 2017.

[88] T. E. Bogale and L. B. Le. Beamforming for multiuser massive MIMO systems: Digital versus hybrid analog-digital. In *2014 IEEE Global Communications Conference*, pages 4066–4071, Dec 2014.

[89] T. E. Bogale, L. B. Le, and X. Wang. Hybrid Analog-Digital Channel Estimation and Beamforming: Training-Throughput Tradeoff. *IEEE Transactions on Communications*, 63(12):5235–5249, Dec 2015.

[90] Ehab Ali, Mahamod Ismail, Rosdiadee Nordin, and Nor Fadzilah Abdulah. Beamforming techniques for massive MIMO systems in 5G: overview, classification, and trends for future research. *Frontiers of Information Technology & Electronic Engineering*, 18(6):753–772, Jun 2017.

[91] S. Malkowsky, J. Vieira, L. Liu, P. Harris, K. Nieman, N. Kundargi, I. C. Wong, F. Tufvesson, V. Öwall, and O. Edfors. The World's First Real-Time Testbed for Massive MIMO: Design, Implementation, and Validation. *IEEE Access*, 5:9073–9088, 2017.

[92] P. Harris, S. Zang, A. Nix, M. Beach, S. Armour, and A. Doufexi. A Distributed Massive MIMO Testbed to Assess Real-World Performance and Feasibility. In *2015 IEEE 81st Vehicular Technology Conference (VTC Spring)*, pages 1–2, May 2015.

[93] Hans Steyskal. Digital beamforming antennas - An introduction. *Microwave Journal*, 30:107, 12 1986.

[94] W. Zhang, J. Xiang, Y. N. R. Li, Y. Wang, Y. Chen, P. Geng, and Z. Lu. Field trial and future enhancements for TDD massive MIMO networks. In *2015 IEEE 26th Annual International Symposium on Personal, Indoor, and Mobile Radio Communications (PIMRC)*, pages 2339–2343, Aug 2015.

[95] *TitanMIMO*. `https://www.nutaq.com/5g-massive-mimo-testbed`.

[96] P. Harris, W. B. Hasan, S. Malkowsky, J. Vieira, S. Zhang, M. Beach, L. Liu, E. Mellios, A. Nix, S. Armour, A. Doufexi, K. Nieman, and N. Kundargi. Serving 22 Users in Real-Time with a 128-Antenna Massive MIMO Testbed. In *2016 IEEE International Workshop on Signal Processing Systems (SiPS)*, pages 266–272, Oct 2016.

[97] DeutscheAG. Berlin trial shows throughput boost. `https://www.telekom.com/en/media/media-information/consumer-products/berlin-trial-shows-throughput-boost-503698`, 2018. Accessed: 2018-05-08.

[98] Samsung. *Samsung and Sprint Conduct Real-World Massive MIMO Testing at Mobile World Congress Fall 2017*, 2017. https://insights.samsung.com/2017/09/11/samsung-and-sprint-conduct-real-world-massive-mimo-testing-at-mobile-world-congress-fall-2017/.

[99] M. Shafi, A. F. Molisch, P. J. Smith, T. Haustein, P. Zhu, P. De Silva, F. Tufvesson, A. Benjebbour, and G. Wunder. 5G: A Tutorial Overview of Standards, Trials, Challenges, Deployment, and Practice. *IEEE Journal on Selected Areas in Communications*, 35(6):1201–1221, June 2017.

[100] Ericsson. Ericsson and MTS to deliver superior mobile broadband experiences for football fans at tournament in Russia. `https://www.ericsson.com/en/press-releases/2018/6/ericsson-and-mts-to-deliver-superior-mobile-broadband\-experiences-for-football-fans-at-tournament-in-russia`, 2018. Accessed: 2018-07-08.

[101] Telkomsel and ZTE. Telkomsel and ZTE complete FDD-LTE Massive MIMO field trial. `https://www.telegeography.com/products/commsupdate/articles/2017/07/14/telkomsel-and-zte-complete-fdd-lte-massive-mimo-field-trial/`, 2018. Accessed: 2018-04-30.

[102] A. Pitarokoilis, S. K. Mohammed, and E. G. Larsson. On the Optimality of Single-Carrier Transmission in Large-Scale Antenna Systems. *IEEE Wireless Communications Letters*, 1(4):276–279, August 2012.

[103] H. Yin, D. Gesbert, M. Filippou, and Y. Liu. A Coordinated Approach to Channel Estimation in Large-Scale Multiple-Antenna Systems. *IEEE Journal on Selected Areas in Communications*, 31(2):264–273, February 2013.

[104] C. Studer and E. G. Larsson. PAR-Aware Large-Scale Multi-User MIMO-OFDM Downlink. *IEEE Journal on Selected Areas in Communications*, 31(2):303–313, February 2013.

[105] A. Pitarokoilis, S. K. Mohammed, and E. G. Larsson. Effect of oscillator phase noise on uplink performance of large MU-MIMO systems. In *2012 50th Annual Allerton Conference on Communication, Control, and Computing (Allerton)*, pages 1190–1197, Oct 2012.

[106] X. Artiga, B. Devillers, and J. Perruisseau-Carrier. Mutual coupling effects in multi-user massive MIMO base stations. In *Proceedings of the 2012 IEEE International Symposium on Antennas and Propagation*, pages 1–2, July 2012.

[107] P. S. Taluja and B. L. Hughes. Diversity Limits of Compact Broadband Multi-Antenna Systems. *IEEE Journal on Selected Areas in Communications*, 31(2):326–337, February 2013.

[108] E. Bjornson, J. Hoydis, M. Kountouris, and M. Debbah. Hardware impairments in large-scale MISO systems: Energy efficiency, estimation, and capacity limits. In *Digital Signal Processing (DSP), 2013 18th International Conference on*, pages 1–6, July 2013.

[109] X. Gao, O. Edfors, F. Tufvesson, and E. G. Larsson. Massive MIMO in Real Propagation Environments: Do All Antennas Contribute Equally? *IEEE Transactions on Communications*, 63(11):3917–3928, Nov 2015.

[110] O. Elijah, C. Y. Leow, T. A. Rahman, S. Nunoo, and S. Z. Iliya. A Comprehensive Survey of Pilot Contamination in Massive MIMO 5G System. *IEEE Communications Surveys Tutorials*, 18(2):905–923, Secondquarter 2016.

[111] R. R. Müller, L. Cottatellucci, and M. Vehkaperä. Blind Pilot Decontamination. *IEEE Journal of Selected Topics in Signal Processing*, 8(5):773–786, Oct 2014.

[112] K. T. Truong and R. W. Heath. Effects of channel aging in massive MIMO systems. *Journal of Communications and Networks*, 15(4):338–351, Aug 2013.

[113] E. Björnson, M. Matthaiou, and M. Debbah. Massive MIMO with Non-Ideal Arbitrary Arrays: Hardware Scaling Laws and Circuit-Aware Design. *IEEE Transactions on Wireless Communications*, 14(8):4353–4368, Aug 2015.

[114] E. Björnson, M. Matthaiou, and M. Debbah. Massive MIMO systems with hardware-constrained base stations. In *2014 IEEE International Conference on Acoustics, Speech and Signal Processing (ICASSP)*, pages 3142–3146, May 2014.

[115] V. P. Tran and A. Sibille. Influence of mutual coupling on MIMO channel capacity. In *11th International Symposium on Antenna Technology and Applied Electromagnetics [ANTEM 2005]*, pages 1–4, June 2005.

[116] S. Biswas, C. Masouros, and T. Ratnarajah. On the effect of antenna correlation and coupling on energy-efficiency of massive MIMO systems. In *2014 IEEE 25th Annual International Symposium on Personal, Indoor, and Mobile Radio Communication (PIMRC)*, pages 497–501, Sept 2014.

[117] S. Vishwanath, N. Jindal, and A. Goldsmith. Duality, achievable rates, and sum-rate capacity of Gaussian MIMO broadcast channels. *IEEE Transactions on Information Theory*, 49(10):2658–2668, Oct 2003.

[118] Hoon Huh, Giuseppe Caire, Haralabos C. Papadopoulos, and Sean A. Ramprashad. Achieving "Massive MIMO" Spectral Efficiency with a Not-so-Large Number of Antennas. *CoRR*, abs/1107.3862, 2011.

[119] R. Janaswamy. Effect of element mutual coupling on the capacity of fixed length linear arrays. *IEEE Antennas and Wireless Propagation Letters*, 1(1):157–160, 2002.

[120] H. Q. Ngo, E. G. Larsson, and T. L. Marzetta. Aspects of favorable propagation in Massive MIMO. In *2014 22nd European Signal Processing Conference (EUSIPCO)*, pages 76–80, Sep. 2014.

[121] T. L. Marzetta. How Much Training is Required for Multiuser Mimo? In *2006 Fortieth Asilomar Conference on Signals, Systems and Computers*, pages 359–363, Oct 2006.

[122] F. Rusek, D. Persson, B. K. Lau, E. G. Larsson, T. L. Marzetta, O. Edfors, and F. Tufvesson. Scaling Up MIMO: Opportunities and Challenges with Very Large Arrays. *IEEE Signal Processing Magazine*, 30(1):40–60, Jan 2013.

[123] H. Q. Ngo and E. G. Larsson. No Downlink Pilots Are Needed in TDD Massive MIMO. *IEEE Transactions on Wireless Communications*, 16(5):2921–2935, May 2017.

[124] E. Björnson, J. Hoydis, and L. Sanguinetti. *Massive MIMO Networks: Spectral, Energy, and Hardware Efficiency.* now, 2017.

[125] Stefania Sesia, Issam Toufik, and Matthew Baker. *LTE, The UMTS Long Term Evolution: From Theory to Practice.* Wiley Publishing, 2009.

[126] J. Choi, D. J. Love, and P. Bidigare. Downlink Training Techniques for FDD Massive MIMO Systems: Open-Loop and Closed-Loop Training With Memory. *IEEE Journal of Selected Topics in Signal Processing*, 8(5):802–814, Oct 2014.

[127] Z. Jiang, A. F. Molisch, G. Caire, and Z. Niu. Achievable Rates of FDD Massive MIMO Systems With Spatial Channel Correlation. *IEEE Transactions on Wireless Communications*, 14(5):2868–2882, May 2015.

[128] X. Rao and V. K. N. Lau. Distributed Compressive CSIT Estimation and Feedback for FDD Multi-User Massive MIMO Systems. *IEEE Transactions on Signal Processing*, 62(12):3261–3271, June 2014.

[129] 3G-PPP. 3GPP Technical Report TR38.913, ver. 14.2.0, Release 14, March 2017, Study on scenarios and requirements for next generation access technologies available at:. `https://portal.3gpp.org/desktopmodules/Specifications/SpecificationDetails.aspx?specificationId=2996`.

[130] A. Adhikary, J. Nam, J. Ahn, and G. Caire. Joint Spatial Division and Multiplexing-The Large-Scale Array Regime. *IEEE Transactions on Information Theory*, 59(10):6441–6463, Oct 2013.

[131] H. Boche and M. Schubert. A general duality theory for uplink and downlink beamforming. In *Proceedings IEEE 56th Vehicular Technology Conference*, volume 1, pages 87–91 vol.1, Sep. 2002.

[132] S. Mukherjee, S. S. Das, A. Chatterjee, and S. Chatterjee. Analytical Calculation of Rician K-Factor for Indoor Wireless Channel Models. *IEEE Access*, 5:19194–19212, 2017.

[133] Arogyaswami Paulraj, Rohit Nabar, and Dhananjay Gore. *Introduction to Space-Time Wireless Communications.* Cambridge University Press, New York, NY, USA, 1st edition, 2008.

[134] C. Tepedelenlioglu, A. Abdi, and G. B. Giannakis. The Ricean K factor: estimation and performance analysis. *IEEE Transactions on Wireless Communications*, 2(4):799–810, July 2003.

[135] Theodore S. Rappaport. *Wireless communications : principles and practice.* Prentice Hall PTR, Upper Saddle River, N.J., 2002.

[136] J. Sijbers, A. J. den Dekker, P. Scheunders, and D. Van Dyck. Maximum-likelihood estimation of Rician distribution parameters. *IEEE Transactions on Medical Imaging*, 17(3):357–361, June 1998.

[137] X. Gao, F. Tufvesson, and O. Edfors. Massive MIMO channels: Measurements and models. In *2013 Asilomar Conference on Signals, Systems and Computers*, pages 280–284, Nov 2013.

[138] H. Cramer. *Random Variables and Probability Distributions.* Cambridge Tracts in Mathematics. Cambridge University Press, 1970.

[139] J. F. Diouris and J. Zeidler. Performance analysis of a compact array receiver for cdma cellular communications. In *IEEE Military Communications Conference. Proceedings. MILCOM 98 (Cat. No.98CH36201)*, volume 1, pages 182–186 vol.1, Oct 1998.

[140] B. M. Hochwald, C. B. Peel, and A. L. Swindlehurst. A vector-perturbation technique for near-capacity multiantenna multiuser communication-part II: perturbation. *IEEE Transactions on Communications*, 53(3):537–544, March 2005.

[141] S. Gunnarsson, J. Flordelis, L. Van der Perre, and F. Tufvesson. Channel Hardening in Massive MIMO-A Measurement Based Analysis. In *2018 IEEE 19th International Workshop on Signal Processing Advances in Wireless Communications (SPAWC)*, pages 1–5, June 2018.

[142] Á. O. Martínez, E. De Carvalho, and J. O. Nielsen. Massive MIMO properties based on measured channels: Channel hardening, user decorrelation and channel sparsity. In *2016 50th Asilomar Conference on Signals, Systems and Computers*, pages 1804–1808, Nov 2016.

[143] Hien Quoc Ngo, Erik G. Larsson, and Thomas L. Marzetta. Aspects of Favorable Propagation in Massive MIMO. *CoRR*, abs/1403.3461, 2014.

[144] X. Wu, N. C. Beaulieu, and D. Liu. On Favorable Propagation in Massive MIMO Systems and Different Antenna Configurations. *IEEE Access*, 5:5578–5593, 2017.

[145] Y. Sun, L. Tian, J. Zhang, L. Wu, and P. Zhang. On asymptotic favorable propagation condition for massive MIMO with co-located user terminals. In *2014 International Symposium on Wireless Personal Multimedia Communications (WPMC)*, pages 706–711, Sep. 2014.

[146] Kan Zheng, Suling Ou, and Xuefeng Yin. Massive mimo channel models: A survey, 2014.

[147] L. Bai, C. Wang, S. Wu, C. F. Lopez, X. Gao, W. Zhang, and Y. Liu. Performance comparison of six massive MIMO channel models. In *2017 IEEE/CIC International Conference on Communications in China (ICCC)*, pages 1–5, Oct 2017.

[148] S. Wu, C. Wang, Y. Yang, W. Wang, and X. Gao. Performance comparison of massive MIMO channel models. In *2016 IEEE/CIC International Conference on Communications in China (ICCC)*, pages 1–6, July 2016.

[149] S. Noh, M. D. Zoltowski, Y. Sung, and D. J. Love. Pilot Beam Pattern Design for Channel Estimation in Massive MIMO Systems. *IEEE Journal of Selected Topics in Signal Processing*, 8(5):787–801, Oct 2014.

[150] E. Riegler and G. Taricco. Asymptotic Statistics of the Mutual Information for Spatially Correlated Rician Fading MIMO Channels With Interference. *IEEE Transactions on Information Theory*, 56(4):1542–1559, April 2010.

[151] 3G-PPP. 3GPP Technical Report Technical Specification Group Radio Access Network; Study on NR Industrial Internet of Things (IoT); (Release 16) available at:. `https://www.3gpp.org/ftp/Specs/archive/38_series/38.825/`.

[152] Frederic Challita, Pierre Laly, Martine Lienard, Emmeric Tanghe, Wout Joseph, and Davy Gaillot. Hybrid Virtual Polarimetric Massive MIMO Measurements at 1.35 GHz. *IET Microwaves, Antennas & Propagation*, May 2019.

[153] C. Shannon. The zero error capacity of a noisy channel. *IRE Transactions on Information Theory*, 2(3):8–19, Sep. 1956.

[154] C. Oestges and B. Clerckx. *MIMO Wireless Communications: From Real-World Propagation to Space-Time Code Design*. Elsevier Science, 2010.

[155] Thomas M. Cover and Joy A. Thomas. *Elements of Information Theory (Wiley Series in Telecommunications and Signal Processing)*. Wiley-Interscience, 2006.

[156] Chen-Nee Chuah, J. M. Kahn, and D. Tse. Capacity of multi-antenna array systems in indoor wireless environment. In *IEEE GLOBECOM 1998 (Cat. NO. 98CH36250)*, volume 4, pages 1894–1899 vol.4, 1998.

[157] N. Jindal and A. Goldsmith. Dirty-paper coding versus TDMA for MIMO Broadcast channels. *IEEE Transactions on Information Theory*, 51(5):1783–1794, May 2005.

[158] E. Björnson, M. Bengtsson, and B. Ottersten. Optimal Multiuser Transmit Beamforming: A Difficult Problem with a Simple Solution Structure . *IEEE Signal Processing Magazine*, 31(4):142–148, July 2014.

[159] M. Joham, W. Utschick, and J. A. Nossek. Linear transmit processing in MIMO communications systems. *IEEE Transactions on Signal Processing*, 53(8):2700–2712, Aug 2005.

[160] C. B. Peel, B. M. Hochwald, and A. L. Swindlehurst. A vector-perturbation technique for near-capacity multiantenna multiuser communication-part I: channel inversion and regularization. *IEEE Transactions on Communications*, 53(1):195–202, Jan 2005.

[161] E. Björnson and E. Jorswieck. *Optimal Resource Allocation in Coordinated Multi-Cell Systems.* now, 2013.

[162] C. Kong, C. Zhong, M. Matthaiou, and Z. Zhang. Performance of downlink massive mimo in ricean fading channels with zf precoder. In *2015 IEEE International Conference on Communications (ICC)*, pages 1776–1782, June 2015.

[163] Michail Matthaiou, Senior, Peter J. Smith, Hien Quoc Ngo, and Member. Does massive mimo fail in ricean channels? *IEEE Wireless Communications Letters*, 8:61–64, 2019.

[164] Y. Zhang, R. Yu, M. Nekovee, Y. Liu, S. Xie, and S. Gjessing. Cognitive machine-to-machine communications: visions and potentials for the smart grid. *IEEE Network*, 26(3):6–13, May 2012.

[165] CISCO. *Cisco Visual Networking Index: Global Mobile Data Traffic Forecast Update, 2016-2021.*

[166] J. Jootar, J. F. Diouris, and J. R. Zeidler. Performance of polarization diversity in correlated nakagami-m fading channels. *IEEE Transactions on Vehicular Technology*, 55(1):128–136, Jan 2006.

[167] A. Frotzscher, U. Wetzker, M. Bauer, M. Rentschler, M. Beyer, S. Elspass, and H. Klessig. Requirements and current solutions of wireless communication in industrial automation. In *2014 IEEE International Conference on Communications Workshops (ICC)*, pages 67–72, June 2014.

[168] A. Varghese and D. Tandur. Wireless requirements and challenges in Industry 4.0. In *2014 International Conference on Contemporary Computing and Informatics (IC3I)*, pages 634–638, Nov 2014.

[169] B. Holfeld, D. Wieruch, L. Raschkowski, T. Wirth, C. Pallasch, W. Herfs, and C. Brecher. Radio channel characterization at 5.85 GHz for wireless M2M communication of industrial robots. In *2016 IEEE Wireless Communications and Networking Conference*, pages 1–7, April 2016.

[170] F. Schaich, T. Wild, and Y. Chen. Waveform Contenders for 5G - Suitability for Short Packet and Low Latency Transmissions. In *2014 IEEE 79th Vehicular Technology Conference (VTC Spring)*, pages 1–5, May 2014.

[171] C. Wang, J. Bian, J. Sun, W. Zhang, and M. Zhang. A Survey of 5G Channel Measurements and Models. *IEEE Communications Surveys Tutorials*, 20(4):3142–3168, Fourthquarter 2018.

[172] S. Payami and F. Tufvesson. Channel measurements and analysis for very large array systems at 2.6 GHz. In *2012 6th European Conference on Antennas and Propagation (EUCAP)*, pages 433–437, March 2012.

[173] A. Taira, H. Iura, K. Nakagawa, S. Uchida, K. Ishioka, A. Okazaki, S. Suyama, T. Obara, Y. Okumura, and A. Okamura. Performance Evaluation of 44GHz Band Massive MIMO Based on Channel Measurement. In *2015 IEEE Globecom Workshops (GC Wkshps)*, pages 1–6, Dec 2015.

[174] J. Vieira, F. Rusek, and F. Tufvesson. Reciprocity calibration methods for massive MIMO based on antenna coupling. In *2014 IEEE Global Communications Conference*, pages 3708–3712, Dec 2014.

[175] M. Gauger, J. Hoydis, C. Hoek, H. Schlesinger, A. Pascht, and S. t. Brink. Channel Measurements with Different Antenna Array Geometries for Massive MIMO Systems. In *SCC 2015; 10th International ITG Conference on Systems, Communications and Coding*, pages 1–6, Feb 2015.

[176] K. Maruta, A. Ohta, S. Kurosaki, T. Arai, and M. Iizuka. Experimental investigation of space division multiplexing on Massive Antenna Systems. In *2015 IEEE International Conference on Communications (ICC)*, pages 2042–2047, June 2015.

[177] S. Sangodoyin, V. Kristem, C. U. Bas, M. Käske, J. Lee, C. Schneider, G. Sommerkorn, J. Zhang, R. Thomä, and A. F. Molisch. Cluster-based analysis of 3D MIMO channel measurement in an urban environment. In *MILCOM 2015 - 2015 IEEE Military Communications Conference*, pages 744–749, Oct 2015.

[178] Y. Yu, J. Zhang, M. Shafi, P. A. Dmochowski, M. Zhang, and J. Mirza. Measurements of 3D channel impulse response for outdoor-to-indoor scenario: Capacity predictions for different antenna arrays. In *2015 IEEE 26th Annual International Symposium on Personal, Indoor, and Mobile Radio Communications (PIMRC)*, pages 408–413, Aug 2015.

[179] W. Li, L. Liu, C. Tao, Y. Lu, J. Xiao, and P. Liu. Channel measurements and angle estimation for massive MIMO systems in a stadium. In *2015 17th International Conference on Advanced Communication Technology (ICACT)*, pages 105–108, July 2015.

[180] J. Li, B. Ai, R. He, K. Guan, Q. Wang, D. Fei, Z. Zhong, Z. Zhao, D. Miao, and H. Guan. Measurement-Based Characterizations of Indoor Massive MIMO Channels at 2 GHz, 4 GHz, and 6 GHz Frequency Bands. In *2016 IEEE 83rd Vehicular Technology Conference (VTC Spring)*, pages 1–5, May 2016.

[181] B. Ai, K. Guan, R. He, J. Li, G. Li, D. He, Z. Zhong, and K. M. S. Huq. On Indoor Millimeter Wave Massive MIMO Channels: Measurement and Simulation. *IEEE Journal on Selected Areas in Communications*, 35(7):1678–1690, July 2017.

[182] F. Challita, M. Martinez-Ingles, M. Liénard, J. Molina-Garcia-Pardo, and D. P. Gaillot. Line-Of-Sight Massive MIMO Channel Characteristics in an Indoor Scenario at 94 GHz. *IEEE Access*, pages 1–1, 2018.

[183] J. Chen, X. Yin, and S. Wang. Measurement-based massive MIMO channel modeling in 13-17 GHz for indoor hall scenarios. In *2016 IEEE International Conference on Communications (ICC)*, pages 1–5, May 2016.

[184] A. O. Martinez, E. De Carvalho, J. O. Nielsen, and L. Jing. Frequency Dependence of Measured Massive MIMO Channel Properties. In *2016 IEEE 83rd Vehicular Technology Conference (VTC Spring)*, pages 1–5, May 2016.

[185] Y. Yu, P. Cui, J. She, Y. Liu, X. Yang, W. Lu, S. Jin, and H. Zhu. Measurement and empirical modeling of massive MIMO channel matrix in real indoor environment. In *2016 8th International Conference on Wireless Communications Signal Processing (WCSP)*, pages 1–5, Oct 2016.

[186] J. Li, B. Ai, R. He, M. Yang, Z. Zhong, Y. Hao, and G. Shi. The 3D Spatial Non-Stationarity and Spherical Wavefront in Massive MIMO Channel Measurement. In *2018 10th International Conference on Wireless Communications and Signal Processing (WCSP)*, pages 1–6, Oct 2018.

[187] J. Huang, C. Wang, R. Feng, J. Sun, W. Zhang, and Y. Yang. Multi-Frequency mmWave Massive MIMO Channel Measurements and Characterization for 5G Wireless Communication Systems. *IEEE Journal on Selected Areas in Communications*, 35(7):1591–1605, July 2017.

[188] V. Kristem, S. Sangodoyin, C. U. Bas, M. Käske, J. Lee, C. Schneider, G. Sommerkorn, C. J. Zhang, R. S. Thomä, and A. F. Molisch. 3D MIMO Outdoor-to-Indoor Propagation Channel Measurement. *IEEE Transactions on Wireless Communications*, 16(7):4600–4613, July 2017.

[189] Y. Zhang, L. Tian, Y. Yu, Q. Zheng, J. Zhang, and Y. Zhang. 3D MIMO Channel Characteristics and Capacity Evaluation for Different Dynamic Ranges in Outdoor-to-Indoor Scenario for 6 GHz. In *2016 IEEE 84th Vehicular Technology Conference (VTC-Fall)*, pages 1–6, Sep. 2016.

[190] Q. Zheng, J. Zhang, H. Yu, Y. Zhang, and L. Tian. Propagation statistic characteristic of 3D MIMO channel in outdoor-to-indoor scenario with different antenna heights. In *2016 19th International Symposium on Wireless Personal Multimedia Communications (WPMC)*, pages 411–416, Nov 2016.

[191] F. Challita, P. Laly, M. Lienard, W. Joseph E. Tanghe, M.Yusuf, and D.P.Gaillot. Impact of Polarization Diversity in Massive MIMO for Industry 4.0. In *2019 European Conference on Networks and Communications (EuCNC)*, pages 1–2, Oct 2019.

[192] Dan Fei, Ruisi He, Bo Ai, Bei Zhang, Ke Guan, and Zhangdui Zhong. Massive MIMO channel measurements and analysis at 3.33 GHz. In *2015 10th International Conference on Communications and Networking in China (ChinaCom)*, pages 194–198, Aug 2015.

[193] C. Chen, V. Volskiy, A. Chiumento, L. Van der Perre, G. A. E. Vandenbosch, and S. Pollin. Exploration of User Separation Capabilities by Distributed Large Antenna Arrays. In *2016 IEEE Globecom Workshops (GC Wkshps)*, pages 1–6, Dec 2016.

[194] M. Z. Aslam, Y. Corre, E. Bjoernson, and Y. Lostanlen. Massive MIMO Channel Performance Analysis Considering Separation of Simultaneous Users. In *WSA 2018; 22nd International ITG Workshop on Smart Antennas*, pages 1–6, March 2018.

[195] Pekka Kyösti, Juha Meinilä, Lassi Hentilä, Xiongwen Zhao, Tommi Jämsä, Christian Schneider, Milan Narandzic, Marko Milojevic, Aihua Hong, Juha Ylitalo, Veli-Matti Holappa, Mikko Alatossava, Robert J. C. Bultitude, Yvo L. C. De Jong, Terhi Rautiainen, Juha Ebitg, Meinilä, Xiongwen Ebitg, Zhao, Mikko Uoulu, Alatossava, Veli-Matti Uoulu, Holappa, Robert Crc, Bultitude, and Crc Yvo De Jong. WINNER II Channel Models Part I Channel Models.

[196] J. Flordelis, F. Rusek, F. Tufvesson, E. G. Larsson, and O. Edfors. Massive MIMO Performance: TDD Versus FDD: What Do Measurements Say? *IEEE Transactions on Wireless Communications*, 17(4):2247–2261, April 2018.

[197] J. Nam, J. Ahn, A. Adhikary, and G. Caire. Joint spatial division and multiplexing: Realizing massive MIMO gains with limited channel state information. In *2012 46th Annual Conference on Information Sciences and Systems (CISS)*, pages 1–6, March 2012.

[198] J. Nam, A. Adhikary, J. Ahn, and G. Caire. Joint Spatial Division and Multiplexing: Opportunistic Beamforming, User Grouping and Simplified Downlink Scheduling. *IEEE Journal of Selected Topics in Signal Processing*, 8(5):876–890, Oct 2014.

[199] W. Shen, L. Dai, B. Shim, S. Mumtaz, and Z. Wang. Joint CSIT Acquisition Based on Low-Rank Matrix Completion for FDD Massive MIMO Systems. *IEEE Communications Letters*, 19(12):2178–2181, Dec 2015.

[200] X. Rao and V. K. N. Lau. Distributed Compressive CSIT Estimation and Feedback for FDD Multi-User Massive MIMO Systems. *IEEE Transactions on Signal Processing*, 62(12):3261–3271, June 2014.

[201] P. Kuo, H. T. Kung, and P. Ting. Compressive sensing based channel feedback protocols for spatially-correlated massive antenna arrays. In *2012 IEEE Wireless Communications and Networking Conference (WCNC)*, pages 492–497, April 2012.

[202] J. Joung, E. Kurniawan, and S. Sun. Channel Correlation Modeling and its Application to Massive MIMO Channel Feedback Reduction. *IEEE Transactions on Vehicular Technology*, 66(5):3787–3797, May 2017.

[203] J. A. Cadzow. Spectral estimation: An overdetermined rational model equation approach. *Proceedings of the IEEE*, 70(9):907–939, Sep. 1982.

[204] B. Friedlander and B. Porat. The Modified Yule-Walker Method of ARMA Spectral Estimation. *IEEE Transactions on Aerospace and Electronic Systems*, AES-20(2):158–173, March 1984.

[205] L. Ros and E. Simon. Second-order modeling for Rayleigh flat fading channel estimation with Kalman Filter. In *2011 17th International Conference on Digital Signal Processing (DSP)*, pages 1–6, July 2011.

[206] H. Hijazi and L. Ros. Joint data QR-detection and Kalman estimation for OFDM time-varying Rayleigh channel complex gains. *IEEE Transactions on Communications*, 58(1):170–178, January 2010.

[207] A. F. Molisch and M. Z. Win. Mimo systems with antenna selection. *IEEE Microwave Magazine*, 5(1):46–56, Mar 2004.

[208] A. F. Molisch, M. Z. Win, Yang-Seok Choi, and J. H. Winters. Capacity of mimo systems with antenna selection. *IEEE Transactions on Wireless Communications*, 4(4):1759–1772, July 2005.

[209] S. Sanayei and A. Nosratinia. Antenna selection in mimo systems. *IEEE Communications Magazine*, 42(10):68–73, Oct 2004.

[210] C. Jiang and L. J. Cimini. Antenna selection for energy-efficient mimo transmission. *IEEE Wireless Communications Letters*, 1(6):577–580, December 2012.

[211] X. Gao, O. Edfors, J. Liu, and F. Tufvesson. Antenna selection in measured massive mimo channels using convex optimization. In *2013 IEEE Globecom Workshops (GC Wkshps)*, pages 129–134, Dec 2013.

[212] X. Gao, O. Edfors, F. Tufvesson, and E. G. Larsson. Massive mimo in real propagation environments: Do all antennas contribute equally? *IEEE Transactions on Communications*, 63(11):3917–3928, Nov 2015.

[213] S. Asaad, A. M. Rabiei, and R. R. Müller. Massive mimo with antenna selection: Fundamental limits and applications. *IEEE Transactions on Wireless Communications*, 17(12):8502–8516, Dec 2018.

[214] R. Husbands, Q. Ahmed, and J. Wang. Transmit antenna selection for massive mimo: A knapsack problem formulation. In *2017 IEEE International Conference on Communications (ICC)*, pages 1–6, May 2017.

[215] S. Asaad, A. Bereyhi, M. A. Sedaghat, R. Mueller, and A. M. Rabiei. Asymptotic performance analysis of spatially reconfigurable antenna arrays. In *WSA 2017; 21th International ITG Workshop on Smart Antennas*, pages 1–6, March 2017.

[216] Yiyang Pei, The-Hanh Pham, and Y. C. Liang. How many rf chains are optimal for large-scale mimo systems when circuit power is considered? In *2012 IEEE Global Communications Conference (GLOBECOM)*, pages 3868–3873, Dec 2012.

[217] R. Hamdi and W. Ajib. Joint optimal number of rf chains and power allocation for downlink massive mimo systems. In *2015 IEEE 82nd Vehicular Technology Conference (VTC2015-Fall)*, pages 1–5, Sept 2015.

[218] S. Asaad, A. Bereyhi, R. R. Mueller, R. F. Schaefer, and A. M. Rabiei. Optimal number of transmit antennas for secrecy enhancement in massive mimome channels. In *GLOBECOM 2017 - 2017 IEEE Global Communications Conference*, pages 1–6, Dec 2017.

[219] Y. Gao, H. Vinck, and T. Kaiser. Massive mimo antenna selection: Switching architectures, capacity bounds, and optimal antenna selection algorithms. *IEEE Transactions on Signal Processing*, 66(5):1346–1360, March 2018.

[220] A. Garcia-Rodriguez, C. Masouros, and P. Rulikowski. Efficient large scale antenna selection by partial switching connectivity. In *2017 IEEE International Conference on Acoustics, Speech and Signal Processing (ICASSP)*, pages 6269–6273, March 2017.

[221] H. Lin, F. Gao, S. Jin, and G. Y. Li. A new view of multi-user hybrid massive mimo: Non-orthogonal angle division multiple access. *IEEE Journal on Selected Areas in Communications*, 35(10):2268–2280, Oct 2017.

[222] G. Zhu, K. Huang, V. K. N. Lau, B. Xia, X. Li, and S. Zhang. Hybrid beamforming via the kronecker decomposition for the millimeter-wave massive mimo systems. *IEEE Journal on Selected Areas in Communications*, 35(9):2097–2114, Sept 2017.

[223] S. Park, J. Park, R. W. Heath, and A. Yazdan. Hybrid precoding using long-term channel statistics for massive mimo systems. In *2017 IEEE International Conference on Acoustics, Speech and Signal Processing (ICASSP)*, pages 3449–3453, March 2017.

[224] S. Park, J. Park, A. Yazdan, and R. W. Heath. Exploiting spatial channel covariance for hybrid precoding in massive mimo systems. *IEEE Transactions on Signal Processing*, 65(14):3818–3832, July 2017.

[225] L. Liang, W. Xu, and X. Dong. Low-complexity hybrid precoding in massive multiuser mimo systems. *IEEE Wireless Communications Letters*, 3(6):653–656, Dec 2014.

[226] F. Challita, M. Martinez-Ingles, M. Liénard, J. Molina-Garcia-Pardo, and D. P. Gaillot. Evaluation of an Antenna Selection Strategy for Reduced Massive MIMO Complexity. In *5th MCM and 5th Technical meeting, Cartagena, Spain*, 2018.

[227] F. Challita, M. Martinez-Ingles, M. Liénard, J. Molina-Garcia-Pardo, and D. P. Gaillot. Evaluation of an Antenna Selection Strategy for Reduced Massive MIMO Complexity. In *2018 12th European Conference on Antennas and Propagation (EuCAP 2018)* , 2018.

[228] K. Senel, H. V. Cheng, E. Bjornson, and E. G. Larsson. What Role can NOMA Play in Massive MIMO? *IEEE Journal of Selected Topics in Signal Processing*, 13(3):597–611, June 2019.

[229] Pierre Laly. *Sondeur de canal MIMO temps reel et applications*. PhD thesis, Université de Lille, 2016.

[230] Luca Sanguinetti, Emil Björnson, and Jakob Hoydis. Towards Massive MIMO 2.0: Understanding spatial correlation, interference suppression, and pilot contamination. *arXiv e-prints*, page arXiv:1904.03406, Apr 2019.

[231] Emil Björnson, Luca Sanguinetti, Henk Wymeersch, Jakob Hoydis, and Thomas L. Marzetta. Massive MIMO is a Reality – What is Next? Five Promising Research Directions for Antenna Arrays. *arXiv e-prints*, page arXiv:1902.07678, Feb 2019.

[232] Sona Carpenter Thomas Emanuelsson Yinggang Li Herbert Zirath Jonas Edstam, Jonas Hansryd. *Microwave backhaul evolution – reaching beyond 100GHz*. ERICSSON, 2017. `https://www.ericsson.com/assets/local/publications/ericsson-technology-review/docs/2017/etr-beyond-100ghz.pdf`.

[233] G. Alastair Young. Mathematical Statistics: An Introduction to Likelihood Based Inference Richard J. Rossi John Wiley & Sons, 2018, xv. *International Statistical Review*, 87(1):178–179, 2019.

[234] Shiqi Cheng. *Characterization and modeling of the polarimetric MIMO radio channel for highly diffuse scenarios*. PhD thesis, 2016. Thèse de doctorat dirigée par Liénard, Martine et Gaillot, Davy Micro et nano technologies, acoustique et télécommunications Lille 1 2016.